

# Synthesis and characterization of $\gamma$ -, $\beta$ -, and $\delta$ -phases of bismuth oxide

**Dissertation**

zur Erlangung des Doktorgrades der Naturwissenschaften

-Dr. rer. nat.-

Vorgelegt dem Promotionsausschuss  
des Fachbereichs 02 (Biologie/Chemie)  
der Universität Bremen



von

Md Imran Hossain

Chemische Kristallographie fester Stoffe

Universität Bremen, Germany

Bremen, im Dezember 2024

Datum der Disputation: Februar 14, 2025

Diese Arbeit wurde in der Arbeitsgruppe "Chemische Kristallographie fester Stoffe" von Herrn Prof. Dr. Thorsten M. Gesing an der Universität Bremen im Zeitraum von Januar 2021 bis November 2024 angefertigt.

Begutachtung des schriftlichen Teils:

**1. Gutachter:** Prof. Dr. Reinhard X. Fischer, University of Bremen

**2. Gutachter:** Prof. Dr. Claus Rüscher, Leibniz Universität Hannover

# Synthesis and characterization of $\gamma$ -, $\beta$ -, and $\delta$ -phases of bismuth oxide

**Dissertation**

to obtain the doctoral degree in natural sciences

-Dr. rer. nat.-

Submitted to the doctoral committee

of Faculty 02 (Biology / Chemistry)

at the University of Bremen



from

Md Imran Hossain

Institute of Inorganic Chemistry and Crystallography

University of Bremen, Germany

Bremen, December 2024

Date of Defence: February 14, 2025

This work was carried out in the working group "Institute of Inorganic Chemistry and Crystallography" by Prof. Dr. Thorsten M. Gesing at the University of Bremen from January 2021 to November 2024.

Assessment of the written part:

**1st reviewer:** Prof. Dr. Reinhard X. Fischer, University of Bremen

**2nd reviewer:** Prof. Dr. Claus Rüscher, Leibniz Universität Hannover



## Acknowledgments

First and foremost, I would like to express my sincere gratitude to Prof. Dr. Thorsten M. Gesing for giving me the opportunity to work in his group, for his unwavering support, and for his insightful suggestions throughout my research. My heartfelt thanks also go to my advisor, Prof. Dr. M. Mangir Murshed, for his valuable guidance, thought-provoking discussions, and constructive feedback on my manuscripts and research.

I am also deeply grateful to Dr. Lars Robben and Mrs. Gabriele Ebert for their kind assistance and support during my time in the group.

I am truly honored that Prof. Dr. Reinhard X. Fischer and Prof. Dr. Claus Rüscher have agreed to serve as reviewers for my dissertation. I appreciate their time, effort, and the helpful suggestions they provided to enhance my work.

For the collaborative work, I thank Prof. Dr. Claudia Weidenthaler (Max-Planck-Institut für Kohlenforschung, Mülheim an der Ruhr) for her invaluable contribution and support.

I am indebted to my colleagues, both past and present, in the AG Gesing group for their friendship and collaboration. Special thanks to Kowsik Ghosh and Mathias Gogolin for the enriching scientific discussions and for the enjoyable times we shared.

I would also like to thank Dr. Michael Wendschuh, Dr. Iris Spiess, and Dr. Johannes Birkenstock from the University of Bremen for their expert management and training on the X-ray diffractometers.

For their financial support, I am grateful to the University of Bremen and Agentur für Arbeit Göttingen for enabling me to carry out my research.

Last but certainly not least, I am deeply thankful to my family for their constant encouragement, love, and support throughout this journey.

Ort, Datum: Bremen, 01.12.2024

### **Erklärungen zur elektronischen Version und zur Überprüfung einer Dissertation**

Hiermit betätige ich gemäß §7, Abs. 7, Punkt 4, dass die zu Prüfungszwecken beigelegte elektronische Version meiner Dissertation identisch ist mit der abgegebenen gedruckten Version.


Ich bin mit der Überprüfung meiner Dissertation gemäß §6 Abs. 2, Punkt 5 mit qualifizierter Software im Rahmen der Untersuchung von Plagiatsvorwürfen einverstanden.



Unterschrift

## Declaration

I hereby declare that this submission is my own work and that, to the best of my knowledge and belief, it contains no material previously published or written by another person nor material which to a substantial extent has been accepted for the award of any other degree or diploma of the university or other institute of higher learning, except where due acknowledgment has been made in the text.

Signature:  \_\_\_\_\_ Date: 01.12.2024

# Declaration

## Versicherung an Eides Statt

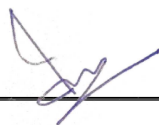
Hiermit versichere ich, Md Imran Hossain,

Albrecht-Thaer-Weg 22g, Zi.-Nr. 11, 37075 Göttingen, Deutschland

an Eides statt durch meine Unterschrift, dass ich die vorstehende Arbeit mit dem Titel "*Synthesis and characterization of  $\gamma$ ,  $\beta$ , and  $\delta$ -phases of bismuth oxide*" selbständig und ohne fremde Hilfe angefertigt und alle Stellen, die ich wörtlich dem Sinne nach aus Veröffentlichungen entnommen habe, als solche kenntlich gemacht habe, mich auch keiner anderen als der angegebenen Literatur oder sonstiger Hilfsmittel bedient habe.

Ich versichere an Eides statt, dass ich die vorgenannten Angaben nach bestem Wissen und Gewissen gemacht habe und dass die Angaben der Wahrheit entsprechen und ich nichts verschwiegen habe.

Die Strafbarkeit einer falschen eidesstattlichen Versicherung ist mir bekannt, namentlich die Strafandrohung gemäß § 156 StGB bis zu drei Jahren Freiheitsstrafe oder Geldstrafe bei vorsätzlicher Begehung der Tat bzw. gemäß § 161 Abs. 1 StGB bis zu einem Jahr Freiheitsstrafe oder Geldstrafe bei fahrlässiger Begehung.



---

Md Imran Hossain

Bremen, 01.12.2024

## Table of Contents

Acknowledgments	5
Declaration	7
Publications	10
List of Abbreviations	11
Zusammenfassung	12
Summary	15
Thesis structure	17
Chapter 1	18
Introduction	
Chapter 2	26
Experimental methods	
Details of declarations on own contribution to the publication	30
Chapter 3	33
Indium containing sillenite semiconductor: synthesis, structural, spectroscopic and thermogravimetric analysis	
Chapter 4	64
Stabilization of $(\text{Bi}_{1-x}\text{M}_x)_2\text{O}_3$ delta phase with rare-earth cations: structural, spectroscopic and thermal investigations for $M = \text{Y, Gd, Tb, Dy, Ho, Er, Tm, Yb, and Lu}$	
Chapter 5	115
Impact of $M^{n+}$ charge and size on $\delta$ -phases formation: structural and spectroscopic investigations with $M = \text{Cr and Ta}$	
Chapter 6	141
Synthesis of $\delta$ -phase $(\text{Bi}_{1-x}\text{M}^{n+}_x)_2\text{O}_{3+(n-3)x}$ : exploring suitable foreign cation for $\text{Bi}^{3+}$ substitution	
Outlook	152
Appendix	154
Curriculum Vitae	155

## **Publications**

**M. I. Hossain**, M. M. Murshed, Th. M. Gesing, Indium containing sillenite semiconductor: Synthesis, structural, spectroscopic and thermogravimetric analysis, J. Am. Ceram. Soc. 106(10) (2023) 6268-6278. DOI: 10.1111/jace.19231

## List of Abbreviations

RE	Rare-earth cation
LEP	Lone electron pair
WLE	Wang-Liebau eccentricity
BVS	Bond valence sum
XRPD	X-ray powder diffraction
SEM	Scanning electron microscopy
EDX	Energy dispersive X-ray spectroscopy
XPS	X-ray photoelectron spectroscopy
DASF	Derivative absorption spectrum fitting
TGA	Thermogravimetric analysis
DSC	Differential scanning calorimetry

## Zusammenfassung

Die Polymorphie von  $\text{Bi}_2\text{O}_3$  ist thermisch getrieben, wobei die Hochtemperatur  $\delta$ -Phase die vielversprechendste für die Verwendung als Festoxid-Elektrolyt in der Brennstoffzellentechnologie darstellt. Das Hauptziel dieser Arbeit ist es, die  $\delta$ -Phase bei Umgebungsbedingungen zu stabilisieren, indem  $\text{Bi}^{3+}$  durch andere Kationen ersetzt wird. Diese Dissertation konzentriert sich auf die Synthese verschiedener  $\text{Bi}^{3+}$ -substituierter Serien und die Untersuchung der strukturellen Beziehungen zwischen den Phasen, mit besonderem Augenmerk auf die Unordnung in der  $\delta$ -Phase.

Der Effekt von anionischen und kationischen Fehlstellen sowie dem einsamen Elektronenpaar von  $\text{Bi}^{3+}$  auf strukturelle Modifikationen wird durch den Austausch von  $\text{Bi}^{3+}$  mit  $\text{In}^{3+}$ -Kationen (Kapitel 3) [1] untersucht. Eine Reihe von Sillenit-Verbindungen mit der Formel  $\text{Bi}_{12}(\text{Bi}^{3+}_{4/5-3x}\text{In}^{3+}_{5x}\text{O}_{19,2+3x}\text{O}_{0,8-3x})$  ( $x = 0,03 - 0,27$ ) wird synthetisiert, um zu verstehen, wie sich die  $\text{In}^{3+}$ -Substitution auf die Eigenschaften des Materials auswirkt. Die Festkörpersynthese wird verwendet, und die Proben werden durch Röntgenbeugung (XRD), Raman-Spektroskopie, UV/Vis diffuse Reflexion und thermogravimetrische Analyse charakterisiert. Die Röntgenpulverdaten zeigen, dass für  $x = 0,03 - 0,08$  phasenreine Proben erhalten werden, während  $\text{In}_2\text{O}_3$  für  $x > 0,08$  als Nebenphase erscheint. Der Gitterparameter verringert sich mit zunehmender  $\text{In}^{3+}$  Konzentration, was darauf hinweist, dass die kleineren  $\text{In}^{3+}$  Kationen  $\text{Bi}^{3+}$  ersetzen. Die einsamen Elektronenpaare von  $\text{Bi}^{3+}$  und Kationen-Fehlstellen verändern die Bindungslängen und Raman-Spektren zeigen eine Phononenverhärtung bei reduzierten Fehlstellen. Die Bandlücke nimmt mit steigendem In-Gehalt zu, und zusätzliche Absorptionsbänder werden für  $x = 0,03 - 0,08$  beobachtet. Stärkere In-O Bindungen verbessern die thermische Stabilität, was durch thermogravimetrische Daten bestätigt wird. Der Austausch von  $\text{Bi}^{3+}$  mit Lanthanoid-Kationen (Kapitel 4) eignet sich für die Bildung der  $\delta$ -Phase bei



verschiedenen Substitutionslevel, wobei die Bildung vom Kationenradius abhängt. Es wird eine Serie hochsymmetrischer  $\delta$ -( $\text{Bi}_{1-x}\text{M}_x$ ) $_2\text{O}_3$ -Phasen, mit  $M = \text{Y, Gd, Tb, Dy, Ho, Er, Tm, Yb}$  und  $\text{Lu}$ , mittels der Festkörpersynthesemethode synthetisiert, dabei reicht  $x$  von 0,05 bis 0,25. Rietveld-Verfeinerungen der Röntgenbeugungsdaten werden verwendet, um jede Probe zu charakterisieren. Die Art des  $\text{M}^{3+}$ -Kations und die Zusammensetzung ( $x$ ) beeinflussen erheblich die Transformation von der niedrigsymmetrischen  $\beta$ -Phase zur hochsymmetrischen  $\delta$ -Phase. Der Austausch von  $\text{Bi}^{3+}$  durch kleinere  $\text{M}^{3+}$ -Kationen verringert den Gitterparameter. Raman-Spektren bestätigen das Vorhandensein der  $\delta$ -Phase und zeigen charakteristische Merkmale wie Bandverbreiterung und Blauverschiebungen. Die direkte Bandlücke erreicht 2,75(4) eV, mit zusätzlichen Absorptionsbändern, die auf anionische Defekte hinweisen. Die thermische Stabilität wird durch Veränderungen der  $\text{Bi/M-O}$ -Bindungsstärke erklärt, wobei ein endothermer Peak auf Ordnungs-Unordnungs-Übergänge in der  $\delta$ -Phase hinweist. Die komplexen strukturellen Modifikationen in der  $\delta$ -Phase werden weiter untersucht, indem  $\text{Bi}^{3+}$  mit  $\text{Cr}^{3+}$  und  $\text{Ta}^{5+}$ -Kationen (Kapitel 5) substituiert wird. Zwei Serien werden untersucht: die Cr-Serie ( $x = 0,15$  bis  $0,30$ ) und die Ta-Serie ( $x = 0,05$  bis  $0,30$ ). Während der Synthese bei 1273 K wird  $\text{Cr}^{3+}$  zu  $\text{Cr}^{6+}$  oxidiert, was zu einem gemischten Oxidationszustand führt, der durch Röntgenphotoelektronenspektroskopie identifiziert wird. Die Cr-Serie zeigt eine stabile  $\delta$ -Phase mit konstantem Gitterparameter, während die Ta-Serie mit zunehmendem  $x$  von der  $\beta$ -Phase zur  $\delta$ -Phase übergeht. Raman-Spektroskopie und Rietveld-verfeinerte Röntgenbeugungsdaten bestätigen die Phasen. Die Bandlückenenergie beträgt 2,27(2) eV für die Cr-Serie und 2,93(2) eV für die Ta-Serie bei  $x = 0,25$ . Defektbezogene Absorptionsbänder zeigen Sauerstofffehlstellen in beiden Serien und bestätigen damit die strukturellen Modifikationen in der  $\delta$ -Phase.

## References

- [1] M.I. Hossain, M.M. Murshed, T.M. Gesing, Indium containing sillenite semiconductor: Synthesis, structural, spectroscopic and thermogravimetric analysis, *J. Am. Ceram. Soc.* 106(10) (2023) 6268-6278. Doi:10.1111/jace.19231

## Summary

The polymorphism of  $\text{Bi}_2\text{O}_3$  is thermally driven, with the high-temperature  $\delta$ -phase being the most promising for use as a solid oxide electrolyte in fuel cell technology. The main goal of this work is to stabilize the  $\delta$ -phase at ambient conditions by substituting  $\text{Bi}^{3+}$  with other cations. This dissertation focuses on synthesizing various  $\text{Bi}^{3+}$  substituted series and investigating the structural relationships between phases, with particular attention to the disorder present in the  $\delta$ -phase.

The effect of anionic and cationic vacancies, along with the lone electron pair of  $\text{Bi}^{3+}$ , on structural modifications is studied by substituting  $\text{Bi}^{3+}$  with  $\text{In}^{3+}$  cations (Chapter 3) [1]. A series of sillenite compounds with the formula  $\text{Bi}_{12}(\text{Bi}^{3+}_{4/5-3x}\text{In}^{3+}_{5x}\text{O}_{19.2+3x}\text{V}_{0.8-3x})$  ( $x = 0.03 - 0.27$ ) is synthesized to understand how  $\text{In}^{3+}$  substitution affects the material's properties. Solid-state synthesis is used, and the samples are characterized by X-ray diffraction (XRD), Raman spectroscopy, UV/Vis diffuse reflectance, and thermogravimetric analysis. X-ray powder refinement reveals phase-pure samples for  $x = 0.03 - 0.08$ , with  $\text{In}_2\text{O}_3$  appearing as a minor phase for  $x > 0.08$ . The lattice parameter decreases with increasing  $\text{In}^{3+}$  concentration, indicating that smaller  $\text{In}^{3+}$  cations replace  $\text{Bi}^{3+}$ . The lone electron pairs of  $\text{Bi}^{3+}$  and cation vacancies modify bond lengths, and Raman spectra show phonon hardening with reduced vacancies. The bandgap increases with In content, and additional absorption bands are observed for  $x = 0.03 - 0.08$ . Stronger In-O bond enhances thermal stability, as confirmed by thermogravimetric data. The substitution of  $\text{Bi}^{3+}$  with rare earth metal cations (Chapter 4) is suitable for the formation of the  $\delta$ -phase at various substitution levels, with the formation depending on the cationic radius. A series of high-symmetric  $\delta\text{-(Bi}_{1-x}\text{M}_x)_2\text{O}_3$  phases, where  $M = \text{Y, Gd, Tb, Dy, Ho, Er, Tm, Yb, and Lu}$ , are synthesized using the solid-state method, with  $x$  ranging from 0.05 to 0.25. XRD data Rietveld refinement is used to characterize each sample.

The type of  $M^{3+}$  cation and the composition ( $x$ ) significantly influence the transformation from the low-symmetric  $\beta$ -phase to the high-symmetric  $\delta$ -phase. Substitution of  $\text{Bi}^{3+}$  with smaller  $M^{3+}$  cations decreases the lattice parameter. Raman spectra confirm the presence of the  $\delta$ -phase and show distinct features, such as band broadening and blue shifts. The direct bandgap reaches 2.75(4) eV, with additional absorption band indicating anionic defect. Thermal stability is explained by changes in Bi/ $M$ -O bond strength, with an endothermic peak indicating order-disorder transitions in the  $\delta$ -phase. The complex structural modifications in the  $\delta$ -phase are further studied by substituting  $\text{Bi}^{3+}$  with  $\text{Cr}^{3+}$  and  $\text{Ta}^{5+}$  cations (Chapter 5). Two series are studied: the Cr-series ( $x = 0.15$  to  $0.30$ ) and the Ta-series ( $x = 0.05$  to  $0.30$ ). During synthesis at 1273 K,  $\text{Cr}^{3+}$  is oxidized to  $\text{Cr}^{6+}$ , resulting in a mixed oxidation state, identified by X-ray photoelectron spectroscopy. The Cr-series shows a stable  $\delta$ -phase with a constant lattice parameter, while the Ta-series transitions from the  $\beta$ -phase to the  $\delta$ -phase as  $x$  increases. Raman spectroscopy and XRD data Rietveld refinement confirm the phases. The bandgap energy is 2.27(2) eV for the Cr-series and 2.93(2) eV for the Ta-series at  $x = 0.25$ . Defect-related absorption band indicate oxygen vacancies in both series, further confirming the structural modifications in the  $\delta$ -phase.

## References

- [1] M.I. Hossain, M.M. Murshed, T.M. Gesing, Indium containing sillenite semiconductor: Synthesis, structural, spectroscopic and thermogravimetric analysis, *J. Am. Ceram. Soc.* 106(10) (2023) 6268-6278. Doi:10.1111/jace.19231

## Thesis structure

This dissertation presents cumulative research on the polymorphism and stabilization of the  $\delta$ -phase of  $\text{Bi}_2\text{O}_3$ , focusing on its crystal structures, applications, and stabilization at ambient conditions. **Chapter 1** discusses the temperature-dependent polymorphism of  $\text{Bi}_2\text{O}_3$ , with particular emphasis on the  $\delta$ -phase. **Chapter 2** outlines the experimental methods for synthesis and characterization used throughout the research. **Chapter 3** explores indium-containing sillenite semiconductors, detailing their synthesis, structural, spectroscopic, and thermogravimetric properties, with results published in a peer-reviewed journal (DOI: 10.1111/jace.19231). **Chapter 4** investigates the stabilization of the  $\delta$ -phase in  $(\text{Bi}_{1-x}\text{M}_x)_2\text{O}_3$  using rare-earth cations ( $M = \text{Y, Gd, Tb, Dy, Ho, Er, Tm, Yb, and Lu}$ ), employing structural, spectroscopic, and thermal analyses. **Chapter 5** examines the impact of  $M^{n+}$  charge and size on  $\delta$ -phase formation, focusing on  $M = \text{Cr and Ta}$ . **Chapter 6** further explores potential cations for  $\text{Bi}^{3+}$  substitution to stabilize the  $\delta$ -phase, supported by structural investigations. Each chapter includes the relevant references at the end.

# Chapter 1

## Introduction

Bismuth oxide is versatile material with significant applications in areas such as piezoelectric device [1, 2], ferroelectric [3], electro-optic [4], high-temperature superconductor [5, 6], and catalyst [7, 8]. Among the various polymorphic phases of  $\text{Bi}_2\text{O}_3$ , the  $\delta$ -phase stands out due to its unique properties, particularly its high oxide ion conductivity (OIC) [5]. This high OIC is attributed to the substantial number of oxygen vacancies within its structure, which enable the efficient movement of oxygen ions ( $\text{O}^{2-}$ ) through the lattice [5]. This characteristic makes the  $\delta$ -phase a promising candidate for applications in solid oxide fuel cell [6] and other high-temperature electrochemical processes [5]. The  $\delta$ -phase of  $\text{Bi}_2\text{O}_3$  adopts a face-centered cubic structure, commonly referred to as the  $\text{CaF}_2$ -type structure, with a space group of  $Fm\bar{3}m$  (no. 225) and a lattice parameter of 566.07(7) pm [9]. In this phase, the  $\text{Bi}^{3+}$  ions are surrounded by oxygen vacancies within the oxygen sublattice [9], significantly contributing to the high OIC [9-12]. Additionally, the  $\text{Bi}^{3+}$  ions possess  $6s^2$  lone-pair electrons (LEP), which enhance the polarizability of the cations, further facilitating the mobility of oxygen ions [12-14]. However, the  $\delta$ -phase is only stable within a narrow temperature range of approximately 1002 K – 1097 K [9]. Beyond this range, it transitions to other phases, such as the  $\beta$ -phase (tetragonal) or  $\gamma$ -phase (cubic) [15, 16]. At ambient conditions,  $\text{Bi}_2\text{O}_3$  predominantly exists in the  $\alpha$ -phase, which is monoclinic in structure [17]. The transformation from  $\alpha$ -phase to  $\delta$ -phase is driven thermally [5, 11]. A key challenge for the practical use of the  $\delta$ -phase is its limited temperature stability [5]. Above  $\sim 1097$  K, the  $\delta$ -phase melts, while below  $\sim 1002$  K, it transforms into the  $\gamma$ - or  $\beta$ -phase [11, 15, 18]. These metastable phases can occur under specific conditions, such as rapid cooling or high-temperature treatments, where the stability of the structure is influenced by temperature, pressure, and composition [5, 18-38]. This highlights

the importance of controlled synthesis to achieve the desired properties for practical applications.

The  $\alpha$ -phase has lattice parameters of  $a = 584.44(2)$  pm,  $b = 815.74(3)$  pm, and  $c = 750.32(3)$  pm, with  $\beta = 112.97(1)$  [17]. In this phase, the  $\text{Bi}^{3+}$  ions are located in a highly distorted anion environment, where they occupy two Wyckoff sites near the center of a distorted square pyramid of  $\text{O}^{2-}$  ions. In the  $\beta$ -phase, the lattice parameters are  $a = 774.39(3)$  pm and  $c = 562.87(3)$  pm [9]. In this phase, only one Wyckoff site for  $\text{Bi}^{3+}$  is observed, forming a distorted square pyramidal geometry ( $\text{BiO}_5$ ). Both the  $\alpha$ - and  $\beta$ -phases accommodate the LEP of the  $\text{Bi}^{3+}$  ions in such a way that they are centered within an irregular octahedron of anions, with one vertex left vacant due to the orientation of the LEP [9]. The  $\delta$ -phase and  $\beta$ -phase are closely related in terms of their  $\text{Bi}^{3+}$  cation sublattice, with the  $\delta$ -phase being slightly more distorted than the  $\beta$ -phase [9]. However, the anionic sublattice in the  $\beta$ -phase differs significantly from that in the  $\delta$ -phase, where extensive dynamic disorder is observed in the latter [12-14]. Another metastable phase of  $\text{Bi}_2\text{O}_3$  is the  $\gamma$ -phase, also known as sillenite. This phase has a lattice parameter of  $a = 1025.01(5)$  pm [39]. The  $\text{Bi}^{3+}$  cations in the  $\gamma$ -phase occupy two distinct Wyckoff sites, forming  $\text{BiO}_5E$  nido-octahedra and  $\text{BiO}_3E$  nido-tetrahedra [39, 40]. Additionally, cation vacancies are present in the central position of the  $\text{BiO}_3E$  nido-tetrahedra, which contributes to structural modifications within the  $\gamma$ -phase [40]. The impact of LEP and cation vacancies on the structure of the  $\gamma$ -phase is further discussed in **chapter 3**.

Stabilizing the  $\delta$ -phase of  $\text{Bi}_2\text{O}_3$  often requires significant substitution of  $\text{Bi}^{3+}$  cations, which can result in grain boundary resistance and microstructural non-uniformity [41, 42]. Excessive doping may also reduce the polarizability of the cations, negatively impacting the OIC [43]. To enhance the stability of the  $\delta$ -phase over a broader temperature range,  $\text{Bi}^{3+}$  substitution with rare earth metals such as  $\text{Gd}^{3+}$ ,  $\text{Dy}^{3+}$ ,  $\text{Ho}^{3+}$ , and  $\text{Er}^{3+}$  is commonly used [40, 44-46]. The ionic

radius of the substituted cation is crucial in stabilizing the cubic structure, with smaller ionic radii like those of  $\text{Gd}^{3+}$  and  $\text{Dy}^{3+}$  being particularly effective [47]. The lattice parameter of the  $\delta$ -phase typically ranges from 540 pm to 551 pm [41, 43, 46-48], though this can vary depending on the level of substitution and preparation conditions. Substituting  $\text{Bi}^{3+}$  with elements like yttrium (Y), tungsten (W), and vanadium (V) has been shown to improve the thermal stability of the  $\delta$ -phase [42, 49, 50]. The polarizability of the substituted cations, which affects the local electron cloud of oxygen, also plays a significant role in phase stabilization. Cations with high polarizability, such as  $\text{Yb}^{3+}$ , tend to enhance the stability of the  $\delta$ -phase. Several series of  $(\text{Bi}_{1-x}\text{M}_x)_2\text{O}_3$ , where  $M$  includes elements like Y, Gd, Tb, Dy, Ho, Er, Tm, Yb, and Lu, have been studied to determine the conditions for pure  $\delta$ -phase formation and to assess the influence of disorder in the oxygen sublattice. These studies are discussed in **chapter 4**. Other series, including Sc, Ti, Cr, Zr, Mo, Ta, W, Al, Ga, Ge, Sn, Sb, Te, La, Ce, and Eu, are explored briefly in **chapters 5 and 6**. Notably, the substitution of  $\text{Bi}^{3+}$  with  $\text{Cr}^{3+}$  complicates  $\delta$ -phase formation due to the easy oxidation of  $\text{Cr}^{3+}$  to  $\text{Cr}^{6+}$  [51]. X-ray diffraction analysis reveals faint extra peaks, particularly at low  $2\theta$  angles, indicating three-dimensional incommensurate modulation in the  $\delta$ -phase [51], a trend also observed in Mo and W series [52, 53]. The disorder in the oxygen sublattice can be tracked using Raman spectroscopy [54], where peak broadening in the high-frequency Raman band suggests distortion in the  $\text{BiO}_x$  polyhedra [40, 54-57]. Thermal analysis supports these structural modifications, showing that metastable phases undergo complex thermal decomposition, transitioning to stable phases through intermediate amorphous or crystalline states [18]. These findings highlight the role of metastable melts in influencing defective structures.



## References

- [1] P.S. Halasyamani, K.R. Poeppelmeier, Noncentrosymmetric oxides, *Chem. Mater.* 10(10) (1998) 2753-2769. Doi:10.1021/cm980140w
- [2] H. Nagata, T. Takenaka, Lead-Free Piezoelectric Ceramics of  $(\text{Bi}_{1/2}\text{Na}_{1/2})\text{TiO}_3\text{-KNbO}_3\text{-}1/2(\text{Bi}_2\text{O}_3\cdot\text{Sc}_2\text{O}_3)$  System, *Jpn. J. Appl. Phys.* 37(9S) (1998) 5311. Doi:10.1143/JJAP.37.5311
- [3] E. Subbarao, A family of ferroelectric bismuth compounds, *J. Phys. Chem. Solids* 23(6) (1962) 665-676. Doi:10.1016/0022-3697(62)90526-7
- [4] N.M. Khusayfan, Coumarin: GO doped  $\text{Bi}_2\text{O}_3$  composites/p-type silicon hybrid photodiodes, *Synth. Met.* 222 (2016) 299-308. Doi:10.1016/j.synthmet.2016.11.003
- [5] V.V. Kharton, E.N. Naumovich, A.A. Yaremchenko, F.M. Marques, Research on the electrochemistry of oxygen ion conductors in the former Soviet Union: IV. Bismuth oxide-based ceramics, *J. Solid State Electrochem.* 5 (2001) 160-187. Doi:10.1007/s100080000141
- [6] S. Hui, J. Roller, S. Yick, X. Zhang, C. Decès-Petit, Y. Xie, R. Maric, D. Ghosh, A brief review of the ionic conductivity enhancement for selected oxide electrolytes, *J. Power Sources* 172(2) (2007) 493-502. Doi:10.1016/j.jpowsour.2007.07.071
- [7] C.-H. Ho, C.-H. Chan, Y.-S. Huang, L.-C. Tien, L.-C. Chao, The study of optical band edge property of bismuth oxide nanowires  $\alpha\text{-Bi}_2\text{O}_3$ , *Opt. Express* 21(10) (2013) 11965-11972. Doi:10.1364/OE.21.011965
- [8] J. Yang, P. Jiang, M. Yue, D. Yang, R. Cong, W. Gao, T. Yang,  $\text{Bi}_2\text{Ga}_4\text{O}_9$ : An undoped single-phase photocatalyst for overall water splitting under visible light, *J. Catal.* 345 (2017) 236-244. Doi:10.1016/j.jcat.2016.11.007
- [9] S. Hull, S.T. Norberg, M.G. Tucker, S.G. Eriksson, C.E. Mohn, S. Stølen, Neutron total scattering study of the  $\delta$  and  $\beta$  phases of  $\text{Bi}_2\text{O}_3$ , *Dalton Trans.* (40) (2009) 8737-8745. Doi:10.1039/B910484B
- [10] N. Sammes, G. Tompsett, H. Näfe, F. Aldinger, Bismuth based oxide electrolytes—structure and ionic conductivity, *J. Eur. Ceram. Soc.* 19(10) (1999) 1801-1826. Doi:10.1016/S0955-2219(99)00009-6
- [11] P. Shuk, H.-D. Wiemhöfer, U. Guth, W. Gijpeld, M. Greenblatt, Oxide ion conducting solid electrolytes based on  $\text{Bi}_2\text{O}_3$ , *Solid State Ionics* 89 (1996) 179-196. Doi:10.1016/0167-2738(96)00348-7
- [12] D.S. Aidhy, J.C. Nino, S.B. Sinnott, E.D. Wachsman, S.R. Phillpot, Vacancy-ordered structure of cubic bismuth oxide from simulation and crystallographic analysis, *J. Am. Ceram. Soc.* 91(7) (2008) 2349-2356. Doi:10.1111/j.1551-2916.2008.02463.x
- [13] C.E. Mohn, M. Krynski, Collective diffusion within the superionic regime of  $\text{Bi}_2\text{O}_3$ , *Phys. Rev. B* 101(10) (2020) 104309. Doi:10.1103/PhysRevB.101.104309

- [14] C.E. Mohn, S. Stølen, S.T. Norberg, S. Hull, Oxide-ion disorder within the high temperature  $\delta$  phase of  $\text{Bi}_2\text{O}_3$ , *Phys. Rev. Lett.* 102(15) (2009) 155502. Doi:10.1103/PhysRevLett.102.155502
- [15] H.A. Harwig, J.W. Weenk, Phase relations in bismuthsesquioxide, *Z. anorg. allg. Chem.* 444 (1978) 167-177. Doi:10.1002/zaac.19784440119
- [16] H.A. Harwig, On the structure of bismuthsesquioxide: the  $\alpha$ ,  $\beta$ ,  $\gamma$ , and  $\delta$ -phase, *Z. anorg. allg. Chem.* 444 (1978) 151-166. Doi:10.1002/zaac.19784440118
- [17] S. Ivanov, R. Tellgren, H. Rundlo, V. Orlov, Structural studies of  $\alpha$ - $\text{Bi}_2\text{O}_3$  by neutron powder diffraction, *Powder Diffr.* 16(4) (2001) 227-230. Doi:10.1154/1.1401200
- [18] V. Zhreb, V. Skorikov, Metastable states in bismuth-containing oxide systems, *Inorg. Mater.* 39 (2003) S121-S145. Doi:10.1023/B:INMA.0000008890.41755.90
- [19] Y.-C. Wu, Y.-T. Huang, H.-Y. Yang, Crystallization mechanism and photocatalytic performance of vanadium-modified bismuth oxide through precipitation processes at room temperature, *CrystEngComm* 18(36) (2016) 6881-6888. Doi:10.1039/C6CE00954A
- [20] H. Sudrajat, Chemical state and local structure of V species incorporated in  $\delta$ - $\text{Bi}_2\text{O}_3$  photocatalysts, *J. Mater. Sci.* 53(2) (2018) 1088-1096. Doi:10.1007/s10853-017-1565-9
- [21] Y. Lu, L. Chen, Y. Huang, H. Cheng, S.I. Kim, H.J. Seo, Optical properties and visible light-driven photocatalytic activity of  $\text{Bi}_{11}\text{VO}_{19}$  nanoparticles with  $\delta$ - $\text{Bi}_2\text{O}_3$ -structure, *J. Alloys Compd.* 640 (2015) 226-232. Doi:10.1016/j.jallcom.2015.04.046
- [22] H. Sudrajat, S. Hartuti, Boosting electron population in  $\delta$ - $\text{Bi}_2\text{O}_3$  through iron doping for improved photocatalytic activity, *Advanced Powder Technology* 30(5) (2019) 983-991. Doi:10.1016/j.appt.2019.02.012
- [23] X. Liu, A. Staubitz, T.M. Gesing, Thermochromic behavior of yttrium-substituted bismuth oxides, *ACS Appl. Mater. Interfaces* 11(36) (2019) 33147-33156. Doi:10.1021/acsami.9b11450
- [24] R.K. Datta, J.P. Meehan, The system  $\text{Bi}_2\text{O}_3$ - $\text{R}_2\text{O}_3$  (R= Y, Gd), *Z. Anorg. Allg. Chem.* 383(3) (1971) 328-337.
- [25] Y.-C. Wu, Y.-W. Chang, S.-F. Wang, Electrical properties and microstructural analysis of aliovalent-ion ( $\text{Y}^{3+}$ ,  $\text{Nb}^{5+}$ )-doped bismuth-based solid-oxide electrolyte, *Ferroelectrics* 455(1) (2013) 123-128. Doi:10.1080/00150193.2013.845486
- [26] T. Kikuchi, Y. Kitami, M. Yokoyama, H. Sakai, Pseudo-binary system  $\text{Bi}_2\text{O}_3$ - $\text{TeO}_2$  in air, *J. Mater. Sci.* 24 (1989) 4275-4278. Doi:10.1007/BF00544499
- [27] G.A. Lovas, I. Dódonny, L. Pöppl, Z. Szaller, On the phase transitions of  $\text{Bi}_2\text{Te}_4\text{O}_{11}$ , *J. Solid State Chem.* 135(2) (1998) 175-181. Doi:10.1006/jssc.1997.7594
- [28] S.E. Lin, W.C.J. Wei, Long-term degradation of  $\text{Ta}_2\text{O}_5$ -doped  $\text{Bi}_2\text{O}_3$  systems, *J. Eur. Ceram. Soc.* 31(16) (2011) 3081-3086. Doi:10.1016/j.jeurceramsoc.2011.04.015

- [29] M. Gambino, F. Giannici, A. Longo, S.D. Tommaso, F. Labat, A. Martorana, Dopant clusterization and oxygen coordination in Ta-doped bismuth oxide: a structural and computational insight into the mechanism of anion conduction, *J. Phys. Chem. C* 119(47) (2015) 26367-26373. Doi:10.1021/acs.jpcc.5b09449
- [30] L. Bourja, B. Bakiz, A. Benlhachemi, M. Ezahri, J.C. Valmalette, S. Villain, J.R. Gavarrı, Structural and raman vibrational studies of CeO<sub>2</sub>-Bi<sub>2</sub>O<sub>3</sub> oxide system, *Adv. Mater. Sci. Eng.* 2009 (2009) 1-4. Doi:10.1155/2009/502437
- [31] Y. Huang, G. Zhou, D. Wei, Z. Fan, H.J. Seo, Phase-formation and luminescence properties of Eu<sup>3+</sup>-doped Bi<sub>2</sub>O<sub>3</sub> on synthetic process, *J. Lumin.* 220 (2020) 116970. Doi:10.1016/j.jlumin.2019.116970
- [32] N.O. Kalaycioglu, E. Çırçır, Measurement and properties of the oxide ionic conductivity of  $\beta$ - and  $\delta$ -Phases in the binary (Bi<sub>2</sub>O<sub>3</sub>)<sub>1-x</sub>(Tb<sub>4</sub>O<sub>7</sub>)<sub>x</sub> system, *Synthesis and Reactivity in Inorganic, Metal-Organic, and Nano-Metal Chemistry* 42(3) (2012) 398-401. Doi:10.1080/15533174.2011.611565
- [33] S. Bandyopadhyay, A. Dutta, Thermal, optical and dielectric properties of phase stabilized  $\delta$ -Dy-Bi<sub>2</sub>O<sub>3</sub> ionic conductors, *J. Phys. Chem. Solids* 102 (2017) 12-20. Doi:10.1016/j.jpcs.2016.11.001
- [34] A. Concha-Balderrama, H.A. Martinez-Rodriguez, G. Rojas-George, H.E. Esparza-Ponce, V. Orozco-Carmona, P. Pizá-Ruiz, M.H. Bocanegra-Bernal, A. Reyes-Rojas, Enhanced Ionic transport and compressive residual stress in Er-doped Bi<sub>2</sub>O<sub>3</sub> with lower Er<sup>3+</sup> concentrations, *J. Electron. Mater.* 47 (2018) 5422-5432. Doi:10.1007/s11664-018-6441-0
- [35] A. Dapčević, D. Poleti, J. Rogan, A. Radojković, M. Radović, G. Branković, A new electrolyte based on Tm<sup>3+</sup>-doped  $\delta$ -Bi<sub>2</sub>O<sub>3</sub>-type phase with enhanced conductivity, *Solid State Ionics* 280 (2015) 18-23. Doi:10.1016/j.ssi.2015.08.004
- [36] H.O. Torun, S. Cakar, E. Ersoy, O. Turkoglu, The bulk electrical conductivity properties of  $\delta$ -Bi<sub>2</sub>O<sub>3</sub> solid electrolyte system doped with Yb<sub>2</sub>O<sub>3</sub>, *J. Therm. Anal. Calorim.* 122 (2015) 525-536. Doi:10.1007/s10973-015-4785-8
- [37] E. Öztürk, N.O. Kalaycioglu, Synthesis, characterization and oxide ionic conductivity of binary  $\delta$ -(Bi<sub>2</sub>O<sub>3</sub>)<sub>1-x</sub>(Lu<sub>2</sub>O<sub>3</sub>)<sub>x</sub> system, *J. Chin. Chem. Soc.* 60(6) (2013) 605-607. Doi:10.1002/jccs.201200540
- [38] P. Meenakshi, K. Promila, U. Sitharaman, R. Nagarajan, Evaluation of solid solution formation between ThO<sub>2</sub> and  $\delta$ -Bi<sub>2</sub>O<sub>3</sub> by molecular precursor route, *Mater. Res. Bull.* 107 (2018) 66-73. Doi:10.1016/j.materresbull.2018.07.001
- [39] S.F. Radaev, V.I. Simonov, Structural features of  $\gamma$ -phase Bi<sub>2</sub>O<sub>3</sub> and its place in the sillenite family, *Acta Cryst.* B48 (1992) 604-609. Doi:10.1107/S0108768192003847
- [40] M.I. Hossain, M.M. Murshed, T.M. Gesing, Indium containing sillenite semiconductor: Synthesis, structural, spectroscopic and thermogravimetric analysis, *J. Am. Ceram. Soc.* 106(10) (2023) 6268-6278. Doi:10.1111/jace.19231

- [41] M. Tian, H. Cao, L. Liu, J. Xu, Phases, stabilities, and oxide ion conductions of multiple lanthanide and tungsten co-doped  $\delta$ -Bi<sub>2</sub>O<sub>3</sub>-based materials: From low to high configuration entropy, *Ceram. Int.* (2024) 26548–26557. Doi:10.1016/j.ceramint.2024.04.383
- [42] A.H. Ibrahim, Y.M. Abbas, M.H. Ali, H. Ayoub, M. Aldoori, Influence of vanadium and dysprosium co-doping on phase stability, microstructure, and electrical properties of Bi<sub>2</sub>O<sub>3</sub>, *J. Mater. Sci.: Mater. Electron.* 35(10) (2024) 676. Doi:10.1007/s10854-024-12371-4
- [43] M.A. Payveren, M. Balci, B. Saatci, M. Ari, Investigation of the structural, thermo-electrical, and morphological properties of the Bi<sub>2</sub>O<sub>3</sub> ceramics co-doped with rare earths, *Appl. Phys. A* 130(10) (2024) 1-12. Doi:10.1007/s00339-024-07837-5
- [44] J.C. Boivin, G. Mairesse, Recent material developments in fast oxide ion conductors, *Chem. Mater.* 10(10) (1998) 2870-2888. Doi:10.1021/cm980236q
- [45] J. Ducke, M. Trömel, D. Hohlwein, P. Kizler, Yttrium and titanium bismuthates with structures related to  $\beta$ -Bi<sub>2</sub>O<sub>3</sub>, *Acta Cryst.* 52(6) (1996) 1329-1331. Doi:10.1107/S0108270195011267
- [46] M. Balci, Structural, thermal, surface, and electrical properties of Bi<sub>2</sub>O<sub>3</sub> ceramics co-doped with Er–Ho–Tb rare earths, *J. Aust. Ceram. Soc.* 60(2) (2024) 385-397. Doi:10.1007/s41779-024-01007-9
- [47] A.H. Ibrahim, Y.M. Abbas, H. Ayoub, M.H. Ali, M. Aldoori, Novel synthesis of stabilized Bi<sub>1-x-y</sub>Gd<sub>x</sub>Dy<sub>y</sub>O<sub>1.5</sub> solid electrolytes with enhanced conductivity for intermediate temperature solid oxide fuel cells (SOFCs), *J. Rare Earths* 42(10) (2024) 1903-1911. Doi:10.1016/j.jre.2023.10.003
- [48] E. Elbaev, N. Matskevich, S. Luk'yanova, V. Zaitsev, E. Tkachev, Enthalpy of Formation and Lattice Enthalpy of Erbium-Substituted Bismuth Oxide, *Russ. J. Phys. Chem. A* 98(9) (2024) 1941-1944. Doi:10.1134/S003602442470105X
- [49] P.D. Battle, C.R.A. Catlow, J. Drennan, A.D. Murray, The structural properties of the oxygen conducting  $\delta$  phase of Bi<sub>2</sub>O<sub>3</sub>, *J. Phys. C: Solid State Phys.* 16(17) (1983) L561-L566. Doi:10.1088/0022-3719/16/17/003
- [50] P.D. Battle, C.R.A. Catlow, J.W. Heap, L.M. Moroney, Structural and dynamical studies of  $\delta$ -Bi<sub>2</sub>O<sub>3</sub> oxide ion conductors: I. The structure of (Bi<sub>2</sub>O<sub>3</sub>)<sub>1-x</sub>(Y<sub>2</sub>O<sub>3</sub>)<sub>x</sub> as a function of x and temperature, *J. Solid State Chem.* 63(1) (1986) 8-15. Doi:10.1016/0022-4596(86)90146-5
- [51] S. Esmaeilzadeh, S. Lundgren, U. Hålenius, J. Grins, Bi<sub>1-x</sub>Cr<sub>x</sub>O<sub>1.5+1.5x</sub>, 0.05 ≤ x ≤ 0.15: A New High-Temperature Solid Solution with a Three-Dimensional Incommensurate Modulation, *J. Solid State Chem.* 156(1) (2001) 168-180. Doi:10.1006/jssc.2000.8978
- [52] M. Valldor, S. Esmaeilzadeh, C. Pay-Gomez, J. Grins, A new high-temperature cubic fluorite-type phase Mo<sub>0.16</sub>Bi<sub>0.84</sub>O<sub>1.74</sub> with a rare three-dimensional incommensurate modulation, *J. Solid State Chem.* 152(2) (2000) 573-576. Doi:10.1006/jssc.2000.8742

- [53] W. Zhou, Defect fluorite superstructures in the  $\text{Bi}_2\text{O}_3\text{-WO}_3$  system, *J. Solid State Chem.* 108 (1994) 381-394. Doi:10.1006/jssc.1994.1056
- [54] R. Sharma, N. Benshalom, M. Asher, T.M. Brenner, A. Kossi, O. Yaffe, R. Korobko, Dynamic disorder in Bi sub-lattice of  $\delta\text{-Bi}_2\text{O}_3$ , *Cond-mat.mtrl-sci* (2022) 1-6. Doi:10.48550/arXiv.2205.13289
- [55] R.J. Betsch, W.B. White, Vibrational spectra of bismuth oxide and the sillenite-structure bismuth oxide derivatives, *Spectrochim. Acta A Mol. Biomol. Spectrosc.* 34(5) (1978) 505-514. Doi:10.1016/0584-8539(78)80047-6
- [56] A. Rubbens, M. Drache, P. Roussel, J.P. Wignacourt, Raman scattering characterization of bismuth based mixed oxides with  $\text{Bi}_2\text{O}_3$  related structures, *Mater. Res. Bull.* 42(9) (2007) 1683-1690. Doi:10.1016/j.materresbull.2006.11.036
- [57] F. D.Hardcastle, I. E.Wachs, The molecular structure of bismuth oxide by Raman spectroscopy, *J. Solid State Chem.* 97(2) (1992) 319-331. Doi:10.1016/0022-4596(92)90040-3

## Chapter 2

### Experimental methods

#### 2.1. Synthesis

The compounds are synthesized using a solid-state method, where stoichiometric amounts of metal oxides and bismuth oxide are mixed in an agate mortar and heated in corundum crucible. For the  $\delta$ - and  $\beta$ -phases, the mixture is heated at 923 K for 24 h, followed by air quenching, and then further heated at 1073 K for 24 h with another quenching step. The  $\gamma$ -phase is synthesized by mixing metal nitrates and oxides with glycerin, followed by heating at 363 K for one hour and 473 K for another hour under stirring. The mixture is then ground and heated at 973 K for 30 h, followed by 1073 K for 24 h. For mixed phases, metal oxides and bismuth oxide are heated at 923 K for 24 h, followed by intermediate grinding and heating at 1073 K for various times, often with air quenching between stages. For specific compositions like  $(\text{Bi}_{1-x}\text{Sn}_x)_2\text{O}_{3+x}$ , heating occurs in two stages, first at 923 K for 24 h and then at 1073 K for 24 h, with an ice-water quenching step. Other compositions, such as  $(\text{Bi}_{1-x}\text{Sb}_x)_2\text{O}_3$ , are heated in multiple stages at different temperatures (923 K, 983 K, and 1213 K), with intermediate grinding and quenching. Compositions like  $(\text{Bi}_{1-x}\text{Te}_x)_2\text{O}_{3+x}$  are heated at 983 K for 18 h, while  $(\text{Bi}_{1-x}\text{Sc}_x)_2\text{O}_3$  is heated at 1073 K for 24 h.  $(\text{Bi}_{1-x}\text{Ti}_x)_2\text{O}_{3+x}$  is heated at 1073 K for 18 h, and  $(\text{Bi}_{1-x}\text{Zr}_x)_2\text{O}_{3+x}$  is heated at 923 K and 1073 K for 24 h, with intermediate grinding and quenching. Finally,  $(\text{Bi}_{1-x}\text{Mo}_x)_2\text{O}_{3+3x}$  and  $(\text{Bi}_{1-x}\text{W}_x)_2\text{O}_{3+3x}$  are heated at 923 K for 24 h, followed by 1073 K for eight days, with intermediate grinding and air quenching. The synthesis process of each compound is described in detail in **chapter 3 to 6**.

## 2.2. Microscopy

Scanning electron microscopy (SEM) is performed using a JMS-6510 (JEOL) with a X-Flash 410-M detector (Bruker) for energy dispersive X-ray spectroscopy (EDX) analysis. Samples are placed on conducting carbon tabs, gold-sputtered for 20 s with a JFC-1200 coater (JEOL), and then inserted into the SEM chamber.

## 2.3. X-ray photoelectron spectroscopy

X-ray photoelectron spectroscopy (XPS) measurement has been performed on a Specs GmbH customized spectrometer, equipped with a Phoibos 150 hemispherical electron analyzer and a 1D-DLD Detector. Monochromatized Al radiation ( $E = 1486.6$  eV) operated at 15 kV and 200 W has been used for excitation, and the pressure in the analysis chamber was about  $10^{-10}$  mbar. An electron flood gun has been used to compensate for charging. All spectra have been referenced to the C1s peak at a value of 284.5 eV. The spectrometer was operated in Medium Area Mode. The survey spectrum has been collected at a pass energy of 50 eV, and the high-resolution spectra were measured at 20 eV.

## 2.4. Powder X-ray diffraction

X-ray powder diffraction (XRPD) patterns are recorded on a Bruker D8 Discover powder diffractometer using Bragg-Brentano geometry with  $\text{CuK}_{\alpha 1,2}$  ( $\lambda_{\text{K}\alpha 1} = 154.05929(5)$  pm,  $\lambda_{\text{K}\alpha 2} = 154.4414(2)$  pm) radiation. The measurements are taken at ambient condition with a step size of  $0.0167^\circ$  and a total data collection time of 75 s/step. The fundamental parameter approach, where the fundamental parameters are fitted against a  $\text{LaB}_6$  standard material, is applied for the Rietveld refinement using 'Diffrac<sup>Plus</sup>Topas 6' software (Bruker AXS GmbH, Karlsruhe, Germany). During Rietveld refinements, the background, sample displacement, atomic coordinates, and occupancy parameters are optimized. The average crystallite size

(ACS) and microstrain (MS) are calculated from the observed all X-ray reflections, using the fundamental approach, where ACS and MS are defined as  $L_{Vol}(IB)$  and  $\epsilon_0$  by the TOPAS software [1].

## 2.5. Bond valence sum

The bond valence sum (BVS) is a method [2] derived from Pauling's second rule. The BVS method is derived from a large number of crystal structures and is based on structural chemistry principles. In this theory, the valence of an atom is distributed across each bond it forms, and each bond has a specific bond valence  $S_i$ . The bond valence is related to the bond length through the equation:

$$S_i = \exp \left[ \frac{(R_0 - R_i)}{B} \right]$$

where  $R_i$  is the observed bond length,  $R_0$  is the ideal bond length for the atom [3] when it has the exact valence, and  $B$  is an empirical constant, typically 37.0 pm. If the coordination environment of an atom is known, the BVS is calculated as:

$$BVS = \sum_i S_i$$

## 2.6. Raman spectroscopy

Raman spectra are recorded on a LabRam ARAMIS (Horiba JobinYvon, New Jersey) confocal Raman microscope with an excitation energy of 784 nm and 532 nm laser, respectively. Where suitable laser (transparent region) is identified by the UV/Vis diffuse reflectance spectrum. A 50× objective, a moving grating of 1800 grooves/mm and a thermodynamically cooled CCD detector (Synapse, 1024×256 pixels) provide the spectral width of about 1  $\text{cm}^{-1}$  for 784 nm laser and 3  $\text{cm}^{-1}$  for the 532 nm laser. The spectral positions are calibrated against the Raman mode of silicon at 520.7  $\text{cm}^{-1}$  before the measurement.



## 2.7. UV/Vis diffuse reflectance spectroscopy

UV/Vis diffuse reflectance spectra are recorded at room temperature on a Shimadzu UV-2600 (Shimadzu, Kyoto, Japan) spectrometer. Data are collected in the range between 190 nm to 850 nm with a step size of 1 nm. BaSO<sub>4</sub> powder is used as the reference standard for baseline correction. The bandgap energies and the types of transition are determined using the RATD method described elsewhere [4].

## 2.8. Thermogravimetric analysis

TGA/DSC measurements are carried out using TGA/DSC 3<sup>+</sup>STARe System of Mettler Toledo. Each sample is measured with a heating rate of 10 K/min and a continuous N<sub>2</sub> flow of 20 mL/min from 298 K to 1473 K. An amount of 10.0(1) mg of power sample is measured relative to an empty Al<sub>2</sub>O<sub>3</sub> crucible reference. The drift correction to the data is applied using an empty crucible measurement.

## References

- [1] D. Balzar, N. Audebrand, M.R. Daymond, A. Fitch, A. Hewat, J.I. Langford, A.L. Bail, D. Louër, O. Masson, C.N. McCowan, N.C. Popa, P.W. Stephens, B.H. Toby, Size-strain line-broadening analysis of the ceria round-robin sample, *J. Appl. Crystallogr.* 37(6) (2004) 911-924. Doi:10.1107/s0021889804022551
- [2] I.D. Brown, *The chemical bond in inorganic chemistry: the bond valence model*, Oxford University Press 2016.
- [3] N.E. Brese, M. O'keeffe, Bond-valence parameters for solids, *Acta Cryst.* B47(2) (1991) 192-197. Doi:10.1107/S0108768190011041
- [4] T.M. Gesing, M.M. Murshed, S. Schuh, O. Thüringer, K. Krämer, T. Neudecker, C.B. Mendive, L. Robben, Nano-crystalline precursor formation, stability, and transformation to mullite-type visible-light photocatalysts, *J. Mater. Sci.* (2022) 1-20. Doi:10.1007/s10853-022-07854-w

## **Details of declaration on own contributions to the publications**

The results presented in this dissertation were obtained in collaboration with other groups. In this section, I specifically highlight my individual contributions to the publication.

### **Chapter 3**

The work presented in chapter 3 has been published in a pre-review journal titled: M. I. Hossain, M. M. Murshed, Th. M. Gesing, Indium containing sillenite semiconductor: Synthesis, structural, spectroscopic and thermogravimetric analysis, J. Am. Ceram. Soc. 106(10) (2023) 6268-6278. DOI: 10.1111/jace.19231

I conducted the following tasks:

- Writing of the main manuscript (co-operation with Prof. Dr. Thorsten M. Gesing and Prof. Dr. Mangir Murshed).
- Generation of the figures (Fig. 3.1; co-operation with Prof. Dr. Thorsten M. Gesing).
- Solid state synthesis of the samples.
- Perform the measurements of XRPD, Raman and UV/Vis diffuse reflectance spectroscopy as well as their evaluation and interpretation, structure determination, and Rietveld refinements.
- Evaluation of TGA data and their interpretation.

I did not conduct the following tasks:

- Analysis of the data and corresponding figure generation for Figs. 3.3, 3.5, 3.8, and 3.9 (done by Prof. Dr. Thorsten M. Gesing).
- TGA/DSC measurements (carried out by Oliver Thüringer).
- Scanning electron microscopy (carried out by Dr. Sindu Shree).

## **Details of declaration on own contributions to the chapters**

### **Chapter 4**

I conducted the following tasks:

- Writing of the chapter.
- Generation of the figures.
- Solid state synthesis of the samples.
- Perform the measurements of XRPD, Raman and UV/Vis diffuse reflectance spectroscopy as well as their evaluation and interpretation, structure determination, and Rietveld refinements.
- Conduct TGA/DSC measurements, followed by the analysis and interpretation of the data.

I did not conduct the following tasks:

- Scanning electron microscopy (carried out by Christopher Reuter)

### **Chapter 5**

I conducted the following tasks:

- Writing of the chapter.
- Generation of the figures.
- Solid state synthesis of the sample.
- Perform the measurements of XRPD, Raman and UV/Vis diffuse reflectance spectroscopy as well as their evaluation and interpretation, structure determination, and Rietveld refinements.

I did not conduct the following tasks:

- X-ray photoelectron spectroscopy (done by Prof. Dr. Claudia Weidenthaler).
- Scanning electron microscopy and energy dispersive X-ray spectroscopy (carried out by Dr. Sindu Shree).

## **Chapter 6**

I conducted the following tasks:

- Writing of the chapter.
- Generation of the figures.
- Solid state synthesis of the sample.
- Perform the measurements of XRPD as well as their evaluation and interpretation.

I did not conduct the following tasks:

- Solid state synthesis of the La-, Ce-, and Eu-series (done by MS student Patrick Weitkämper).

## Chapter 3

### **Indium containing sillenite semiconductor: synthesis, structural, spectroscopic and thermogravimetric analysis**

A published paper “Reproduced with permission from The American Ceramic Society”.  
<https://ceramics.onlinelibrary.wiley.com/doi/full/10.1111/jace.19231>. Copy right permission site: <https://www.wiley.com/network/researchers/latest-content/how-to-clear-permissions-for-a-thesis-or-dissertation>

Md. Imran Hossain<sup>1</sup>, M. Mangir Murshed<sup>1,2\*</sup>, Thorsten M. Gesing<sup>1,2</sup>

<sup>1</sup>University of Bremen, Institute of Inorganic Chemistry and Crystallography, Leobener Straße 7, D-28359 Bremen, Germany

<sup>2</sup>MAPEX Center for Materials and Processes, Bibliothekstraße 1, D-28359 Bremen, Germany

\*Corresponding author: e-mail address: [murshed@uni-bremen.de](mailto:murshed@uni-bremen.de), phone: +49 (0)421 218 63144, fax: +49 421 218 63145.

#ORCID:

MIH: 0000-0002-2499-8456  
MMM: 0000-0002-9063-372X  
TMG: 0000-0002-4119-2219

## Abstract

Sillenite-type ceramics are non-centrosymmetric phases of ongoing research interest because of their structural defects and optoelectronic properties. We report a series of sillenite compounds with a general composition  $\text{Bi}_{12}(\text{Bi}^{3+}_{4/5-3x}\text{In}^{3+}_{5x}\square_{1/5-2x})\text{O}_{19.2+3x}\square_{0.8-3x}$  for  $x = 0.03 - 0.27$  to understand how the crystal-physico-chemical properties change with a successive filling of empty  $\text{Bi}^{3+}$  positions in the tetrahedral site by  $\text{In}^{3+}$  cation. Conventional solid-state synthesis method is used to prepare the micro-crystalline samples. Each sample is characterized by X-ray diffraction, Raman, UV/Vis diffuse reflectance spectroscopy and thermogravimetry (TG/DSC). X-ray powder data Rietveld refinement reveals that phase-pure samples can be obtained for  $x = 0.03 - 0.08$  in the space group  $I23$ . Appearance of starting  $\text{In}_2\text{O}_3$  as minor phases with the final products for  $0.10 < x < 0.27$  suggests for  $x_{\text{max}} = 0.08$ . The successive decrease of the lattice parameter indicates the incorporation of smaller  $\text{In}^{3+}$  cations in the structure. The effect of the lone electron pairs of  $\text{Bi}^{3+}$  and the structural cation vacancies lead to modification of the interatomic bond lengths. At least one Raman active phonon mode shows hardening for decreasing cation vacancy concentration in the system. The bandgap energy increases with increasing indium content. An additional absorption band at lower energy for  $x = 0.03 - 0.08$  complements the theoretical study, which completely disappears for  $x > 0.08$ . The stronger In-O bonds play pivotal roles in thermal stability of the phases studied by TGA/DSC analysis.

**Keywords:** Sillenite ceramic, ion-vacancy, crystal structure, bandgap, thermal stability

## 1. Introduction

Most sillenite-type ceramics crystallize in the space group  $I23$ . The non-centrosymmetry of this space group is a precondition for piezoelectricity and second-harmonic generation [1]. The sillenite representative of  $\text{Bi}_2\text{O}_3$  ceramics is  $\gamma\text{-Bi}_2\text{O}_3$  [2] –a metastable high-temperature phase. Based on intensive crystal structural studies [3-9], the structural formula of  $\gamma\text{-Bi}_2\text{O}_3$  [2] can be written as  $\text{Bi}_{12}[\text{Bi}^{3+}\text{O}_3E]_{0.8}[\square\text{O}_4]_{0.2}\text{O}_{16}$  for  $Z = 2$ , where the centroid of the  $\square\text{O}_4$  tetrahedra is occupied by a cation vacancy ( $\square$ ). The centroid of both  $\text{Bi}^{3+}\text{O}_3E$  tetrahedra and  $\text{Bi}^{3+}\text{O}_5E$  octahedra keeps a stereochemically active  $6s^2$  lone electron pair (LEP;  $E$  in formula) instead of one ligand oxygen. The crystal structure [10, 11] and the appearances of different polyhedra are depicted in **figure 3.1**. The  $\text{Bi}^{3+}$  cations locate on both  $24f$  and  $2a$  sites comprising of  $\text{BiO}_5E$  nido-octahedra and  $\text{BiO}_3E$  nido-tetrahedra, respectively. The  $\text{BiO}_5E$  polyhedra share the common edge  $\text{O}(1^{\text{II}})\text{-O}(1^{\text{III}})$  link (superscripted Roman numerals refer to three different  $\text{Bi}(1)\text{-O}(1)$  bond distances). The other corners are connected to  $\text{BiO}_3E$  tetrahedra sharing the common vertices  $\text{O}(3)$  atoms. According to the Wang-Liebau eccentricity (WLE) parameter [12, 13], the  $\text{Bi}^{3+}$  cation on the  $2a$  site possesses much stronger stereochemical activity than those on the  $24f$  site. As such, the  $\text{BiO}_5E$  polyhedra can be regarded as a distorted octahedron with axial  $\text{O}(1^{\text{I}})$  and  $E$ , where the equatorial plane is formed by  $\text{O}(1^{\text{II}})$ ,  $\text{O}(1^{\text{III}})$ ,  $\text{O}(2)$  and  $\text{O}(3)$  atoms [14]. In ideal sillenites such as  $\text{Bi}_{12}\text{GeO}_{20}$  [14], the tetrahedrally coordinated  $2a$  site is fully occupied by  $\text{Ge}^{4+}$  cations due to charge and size, showing regular  $\text{GeO}_4$  tetrahedra (e.g., Fig. 1c) without any vacancies.  $\text{Ti}^{4+}$  cations, on the other hand, exceed the optimum size, giving rise to a certain local stress in the structure with distorted  $\text{TiO}_4$  tetrahedra [14]. Phase pure  $\text{M}^{3+}$  sillenites can possess both oxygen and cation vacancies on the tetrahedral sites [15], and their physico-chemical properties depend on the  $2a$  site substitution [14].

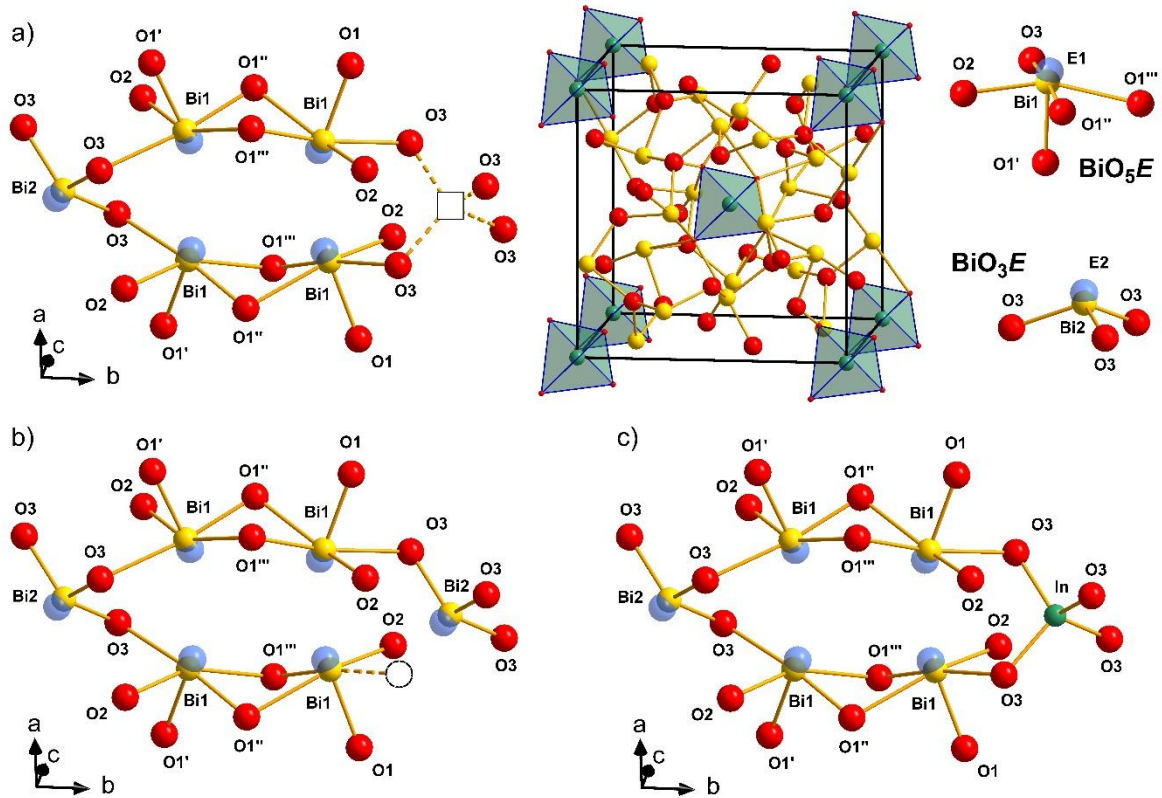


**Figure 3.1:** Crystal structure of  $\text{In}^{3+}$  containing sillenite  $\text{Bi}_{12}(\text{Bi}^{3+}_{4/5-3x}\text{In}^{3+}_{5x}\square_{1/5-2x})\text{O}_{19.2+3x}$  for  $x = 0.05$  with  $\text{BiO}_5E$  and  $\text{BiO}_3E$  (top right) or  $(\text{Bi},\text{In},\square)\text{O}_4$  polyhedral linkages, showing three possible configurations: (a) cation vacancy as  $\square\text{O}_4$  tetrahedra, (b) oxygen vacancy as dashed circle and (c) without oxygen/cation vacancies. The  $6s^2$  lone electron pairs of  $\text{Bi}^{3+}$  cations with possible orientations are shown as transparent half-circles.

Sillen as early as in 1937 [16] proposed the possibility of stabilizing metastable  $\gamma\text{-Bi}_2\text{O}_3$  with incorporation of small amount of other cations. The prediction can be well judged from the follow-up studies on sillenite-type structures with numerous  $\text{M}^{n+}$  cations (e.g.,  $\text{Al}^{3+}$ ,  $\text{Si}^{4+}$ ,  $\text{P}^{5+}$ ,  $\text{Ti}^{4+}$ ,  $\text{V}^{5+}$ ,  $\text{Mn}^{4+}$ ,  $\text{Fe}^{3+}$ ,  $\text{Zn}^{2+}$ ,  $\text{Ge}^{4+}$ ,  $\text{As}^{5+}$ ,  $\text{Cd}^{2+}$ ,  $\text{Tl}^{3+}$ ) [11, 14, 15, 17-23] mainly on the  $2a$  site. Craig *et al.* [24], however, proposed the presence of  $\text{Bi}^{5+}$  on the  $2a$  site although  $\text{Bi}^{5+}$  is known to be unstable at high temperatures [15, 18]. As such, debates on the chemical compositions and the crystal structures of some sillenites are still open [25]. The degree of  $\text{Bi}^{3+}$  substitution and the associated vacancies depend on the size and formal valance of the cations. Indeed, for  $\gamma\text{-Bi}_2\text{O}_3$  the structural formula  $\text{Bi}_{12}[\text{Bi}_{8/10}\square_{2/10}][\text{O}_{19.2}\square_{0.5+3/10}]$  keeps, beside the charge balancing



anion voids ( $\square_{0.5}$ ), both cation deficiency ( $\square_{2/10}$ ) and anion vacancy ( $\square_{3/10}$ ). Incorporation of other cations without LEP on the vacant sites can import necessary oxygen for charge compensation, leading to formation of unstable  $\text{Bi}^{3+}\text{O}_4$  polyhedra. An additional oxygen anion into the  $8c$  site is only possible when the  $\text{O}(3)$  concentration or the stereochemically activity of LEPs is decreased. This condition limits the chemical substitution of  $\text{Bi}^{3+}$  cation on the  $2a$  sites of sillenites. Based on the structural conditions required for the isomorphous substitution in sillenites Valant *et al.* [15] proposed a general formula  $\text{Bi}_{12}(\text{Bi}^{3+}_{4/5-nx}\text{M}^{n+}_{5x}\square_{1/5-(5-n)x})\text{O}_{19.2+nx}$  for  $\gamma\text{-Bi}_2\text{O}_3$ , which conveniently serves for substitution of a given cation of valence  $n = 2 - 5$ . The upper limit of substitution ( $x_{\text{max}}$ ) depends on how the vacancies in the tetrahedra are filled by oxygen. That is, based on this upper limit (zero vacancy for  $1/5 - 2x = 0$ ), substitution of a trivalent cation in the tetrahedral site allows  $x_{\text{max}} \sim 0.1$ . As such, for the present investigation we follow the chemical formula  $\text{Bi}_{12}(\text{Bi}^{3+}_{4/5-3x}\text{M}^{n+}_{5x}\square_{1/5-2x})\text{O}_{19.2+3x}$  for a successive substitution of  $\text{Bi}^{3+}$  by  $\text{In}^{3+}$  in the  $2a$  site. This study particularly emphasizes on how the crystal-physico-chemical properties change upon successive replacement of LEP-containing  $\text{Bi}^{3+}$  by  $\text{In}^{3+}$  (without LEP) on the  $2a$  site of a solid solution of  $\text{Bi}_{12}(\text{Bi}^{3+}_{4/5-3x}\text{In}^{3+}_{5x}\square_{1/5-2x})\text{O}_{19.2+3x}$  ceramics.

## 2. Experimental

### 2.1. Synthesis

All samples are prepared by mixing stoichiometric amount of  $\text{Bi}(\text{NO}_3)_3 \cdot 5\text{H}_2\text{O}$  (98%, Thermo Scientific) and  $\text{In}_2\text{O}_3$  (99.99%, Thermo Scientific) with 20 wt.% glycerin into a glass beaker and heated at 363 K under constant stirring for an hour, followed by further heated at 473 K for another hour. Afterward, the fluffy mass is ground in an agate mortar and put into a corundum crucible. Finally, the samples are sequentially heated with a heating rate of 200 K/h at 973 K for 30 h and at 1073 K for 24 h.

## 2.2. Microscopy

Scanning electron microscopy (SEM) is carried out using a JMS-6510 (JEOL) equipped with an X-Flash 410-M detector (Bruker) for energy dispersive X-ray spectroscopy. A small amount of sample is taken on conducting carbon tabs and sputtered with gold for 20 s with a JFC-1200 coater (JEOL) followed by inserting them into the SEM chamber.

## 2.3. X-ray diffraction

X-ray powder diffraction (XRPD) pattern are recorded on a Bruker D8 Discover powder diffractometer using Bragg-Brentano geometry with  $\text{CuK}_{\alpha 1,2}$  ( $\lambda_{\text{K}\alpha 1} = 154.05929(5)$  pm,  $\lambda_{\text{K}\alpha 2} = 154.4414(2)$  pm) radiation. The measurements are taken at ambient condition with a step size of  $0.0167^\circ$  and a total data collection time of 75 s/step. The fundamental parameter approach, where the fundamental parameters are fitted against a  $\text{LaB}_6$  standard material, is applied for the Rietveld refinement using ‘Diffrac<sup>Plus</sup>Topas 6’ software (Bruker AXS GmbH, Karlsruhe, Germany). The starting lattice parameters and atomic coordinates are taken from the crystal structure of  $\gamma\text{-Bi}_2\text{O}_3$  [2] (ICSD Coll. Code 71917). During Rietveld refinements, the background, sample displacement, atomic coordinates and lattice parameters are optimized. In all cases, the isotropic displacement parameters are constrained between atoms located at the same Wyckoff site ( $\text{Bi}^{3+}/\text{In}^{3+}$ ), and their occupancy parameters are refined. The WLE parameter is the absolute value of the sum of the vectors ( $\Phi_i$ ) as defined by Wang and Liebau [12], which measures the deformation density of the LEP. The direction of each  $\Phi_i$  is considered along the line from the cation nucleus to the approximate center of the deformation density of the LEP. The bond valence sum of a given cation has been calculated using the formula suggested by Brown [26], where the bond valence parameter has been taken from Brese and O'keeffe [27].

#### **2.4. Raman spectroscopy**

Raman spectra are recorded on a LabRam ARAMIS (Horiba JobinYvon, New Jersey) confocal Raman microscope with a 785 nm exciting laser. The spectra are collected from 100 to 1000  $\text{cm}^{-1}$ . A 50 $\times$  objective, a moving grating of 1800 grooves/mm and a thermodynamically cooled CCD detector (Synapse, 1024 $\times$ 256 pixels) provide the spectral width of about 1.1  $\text{cm}^{-1}$ . The spectral positions are calibrated against the Raman mode of silicon at 520.7  $\text{cm}^{-1}$  before the measurement.

#### **2.5. UV/Vis diffuse reflectance spectroscopy**

UV/Vis diffuse reflectance spectra are recorded at room temperature on a Shimadzu UV-2600 (Shimadzu, Kyoto, Japan) spectrometer. Data are collected in the range between 190 to 850 nm with a step size of 1 nm. BaSO<sub>4</sub> powder is used as the reference standard for baseline correction. The bandgap energies and the types of transition are determined using the RATD method described elsewhere [28].

#### **2.6. Thermogravimetric analysis**

TGA/DSC measurements are carried out using TGA/DSC 3<sup>+</sup>STARe System of Mettler Toledo. Each sample is measured with a heating rate of 10 K/min and a continuous N<sub>2</sub> flow of 20 mL/min from 298 K to 1473 K. An amount of 11.3(1) mg of power sample is measured relative to an empty Al<sub>2</sub>O<sub>3</sub> crucible reference. The drift correction to the data is applied using an empty crucible measurement.

### 3. Results and Discussion

#### *Crystal structure*

Each  $\text{In}^{3+}$ -containing sillenite exhibits distinctive color, as shown in **figure S3.1** (Supplementary Information). The scanning electron micrographs are shown in **figure S3.2**, depicting the distribution of average micrometer-sized particles. The XRPD patterns of  $\text{Bi}_{12}(\text{Bi}^{3+}_{4/5-3x}\text{In}^{3+}_{5x}\square_{1/5-2x})\text{O}_{19.2+3x}$  for  $x = 0.03 - 0.27$  are shown in **figure S3.3 – S3.6**. XRPD data Rietveld refinements confirm that for  $x = 0.03 - 0.08$  the samples are phase pure. A representative Rietveld refinement plot for  $x = 0.05$  is shown in **figure 3.2**, and the crystal structure parameters are given in **table 3.1**.

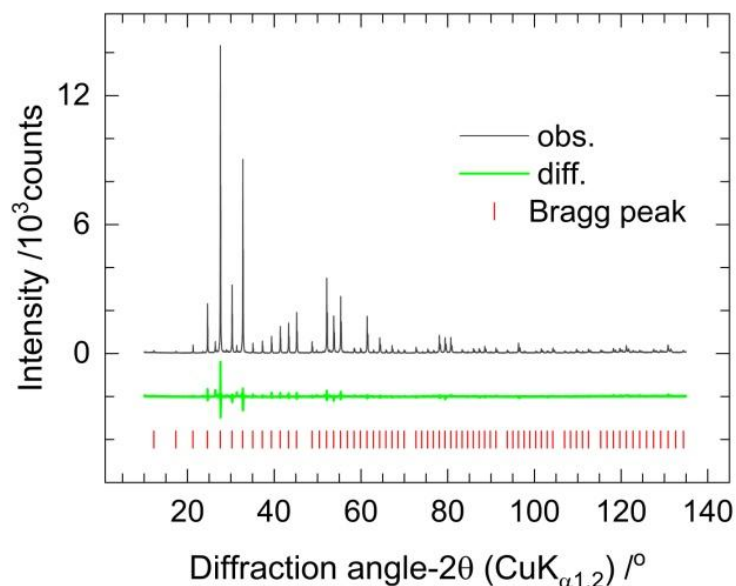


**Figure 3.2:** X-ray powder diffraction data Rietveld plot of  $\text{Bi}_{12}(\text{Bi}^{3+}_{4/5-3x}\text{In}^{3+}_{5x}\square_{1/5-2x})\text{O}_{19.2+3x}$  with  $x = 0.05$ .

During the Rietveld refinements, bismuth has been found both on  $24f$  (Bi1) and  $2a$  (Bi2) Wyckoff positions. Taking  $\text{In}^{3+}$  to be co-shared with  $\text{Bi}^{3+}$  on the  $24f$  site the refinement results in negative values for either the occupancy or the isotropic displacement parameters. Successive refinement trials reveal mixed occupancy of  $\text{In}^{3+}$  and  $\text{Bi}^{3+}(2)$  on the  $2a$  site with a better convergence statistics (e.g., improved  $R_{wp}$ ) for the  $(\text{Bi},\text{In})\text{O}_4$  tetrahedral geometry. While

$\text{In}^{3+}$  cations are mostly found with six coordination, purely  $\text{InO}_4$  tetrahedral coordination is also not rare in crystalline compounds. For instance, fourfold coordination of  $\text{In}^{3+}$  cation in  $\text{Na}_{26}\text{O}_3[\text{InO}_4]_4$  ( $Z = 4$ ) are known from single crystal X-ray data refinements [29]. The sharp decrease of the lattice parameter, as shown in **figure 3.3**, indicates the incorporation of smaller  $\text{In}^{3+}$  cations on the  $2a$  position of the sillenite structure.

**Table 3.1:** X-ray powder diffraction data Rietveld refined structural parameter for  $x = 0.03 - 0.10$  in  $\text{Bi}_{12}(\text{Bi}^{3+}_{4/5-3x}\text{In}^{3+}_{5x}\square_{1/5-2x})\text{O}_{19.2+3x}$  in the cubic space group  $I\bar{2}3$ .

$x = 0.03; R_{\text{wp}} = 5.20, R_{\text{p}} = 3.79, R_{\text{B}} = 3.67$						
Atom	Site	Occupancy	$x$	$y$	$z$	$B / 10^{-4} \text{ pm}^2$
Bi1	$24f$	1	0.177(2)	0.318(2)	0.011(2)	1.34(1)
Bi/In2	$2a$	0.81/0.19(1)	0	0	0	2.18(2)
O1	$8c$	1	0.141(2)	0.257(2)	0.489(3)	0.88(2) <sup>a</sup>
O2	$24f$	1	0.172(2)	0.172(2)	0.172(2)	0.88(2) <sup>a</sup>
O3	$8c$	1	0.869(2)	0.869(2)	0.869(2)	0.88(2) <sup>a</sup>
$x = 0.05; R_{\text{wp}} = 5.77, R_{\text{p}} = 4.20, R_{\text{B}} = 4.07$						
Bi1	$24f$	1	0.176(2)	0.319(1)	0.013(1)	1.35(2)
Bi/In2	$2a$	0.61/0.39(1)	0	0	0	2.09(2)
O1	$8c$	1	0.130(2)	0.250(2)	0.484(3)	1.08(2) <sup>b</sup>
O2	$24f$	1	0.183(2)	0.183(2)	0.183(2)	1.08(2) <sup>b</sup>
O3	$8c$	1	0.883(2)	0.883(2)	0.883(2)	1.08(2) <sup>b</sup>
$x = 0.08; R_{\text{wp}} = 5.27, R_{\text{p}} = 3.84, R_{\text{B}} = 3.72$						
Bi1	$24f$	1	0.176(2)	0.319(1)	0.013(1)	0.89(2)
Bi/In2	$2a$	0.57/0.43(1)	0	0	0	1.93(1)
O1	$8c$	1	0.131(2)	0.254(2)	0.483(3)	1.33(1) <sup>c</sup>
O2	$24f$	1	0.183(2)	0.183(2)	0.183(2)	1.33(1) <sup>c</sup>
O3	$8c$	1	0.889(2)	0.889(2)	0.889(2)	1.33(1) <sup>c</sup>
$x = 0.10; R_{\text{wp}} = 6.73, R_{\text{p}} = 4.90, R_{\text{B}} = 4.75$						
Bi1	$24f$	1	0.177(2)	0.319(1)	0.013(1)	0.91(2)
Bi/In2	$2a$	0.53/0.47(1)	0	0	0	2.80(1)
O1	$8c$	1	0.126(2)	0.248(2)	0.471(3)	2.81(2) <sup>d</sup>
O2	$24f$	1	0.179(2)	0.179(2)	0.179(2)	2.81(2) <sup>d</sup>
O3	$8c$	1	0.889(2)	0.889(2)	0.889(2)	2.81(2) <sup>d</sup>

<sup>a,b,c,d</sup>Isotropic displacement parameter ( $B$ ) of O(1), O(2) and O(3) with the same letter are linearly constraint to each other.

An abrupt change of the metric parameter behavior can be seen at  $x = 0.10$  with a further slightly increase of the lattice parameter and the concomitant appearance of  $\text{In}_2\text{O}_3$  as secondary phase which increases with increasing  $x$ . At this stage, why the lattice parameter increases again with increasing indium concentration remains unclear.

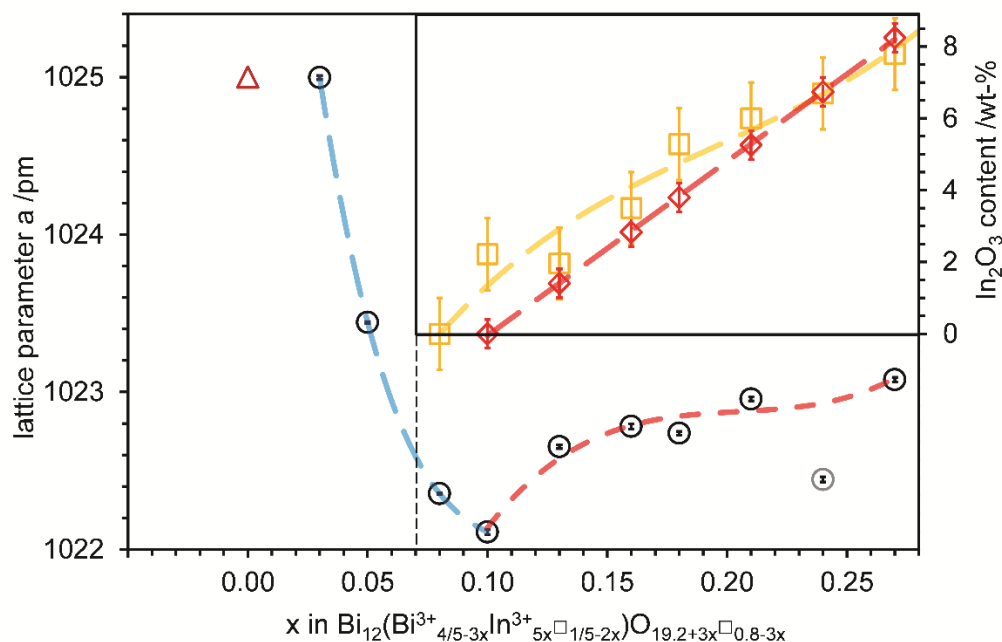


**Figure 3.3:** Evolution of metric parameter in changing the compositional  $x$  in  $\text{Bi}_{12}(\text{Bi}^{3+}_{4/5-3x}\text{In}^{3+}_{5x}\text{O}_{19.2+3x})$ , where the value  $x = 0$  is taken from Radaev *et al.* [2]. The excess  $\text{In}_2\text{O}_3$  obtained (square) and theoretical ones (diamond) is given in the inset, together with respective guideline to the eye.

Either indium further replaces bismuth on the  $\text{Bi}(2)$  position which is expected to further decrease the lattice parameter, or indium replaces bismuth on the  $\text{Bi}(1)$  position which leads to a reduction of the influence of the stereochemically active lone pairs. We assume that the latter one is the case, leading to less distortion of the nido-octahedra by shifting the equatorial plane further away from the apex  $\text{O}(1^1)$  atom, as the strength of the LEP  $E1$  decreases (**Fig. 3.1**). This might trigger slightly a spatial requirement at the cost of an enlarged lattice parameter. The cation vacancy and the orientation of LEP in  $\text{BiO}_3E$  tetrahedra play significant structural roles for the averaged  $\langle \text{Bi-O} \rangle$  bond distances both for the  $\text{BiO}_5E$  nido-octahedra and  $\text{BiO}_3E$  nido-

tetrahedra [2]. The  $\langle\text{Bi}(2)\text{--O}(3)\rangle$  bond length decreases with increasing In-content in the structure, as shown in **figure 3.4** due to smaller cationic size of  $\text{In}^{3+}$  cation than that of the  $\text{Bi}^{3+}$  cation [30]. As such, the number of  $\text{InO}_4$  tetrahedra increases with successive decrease of the cation vacancy and the  $\text{BiO}_3E$  tetrahedra as well.

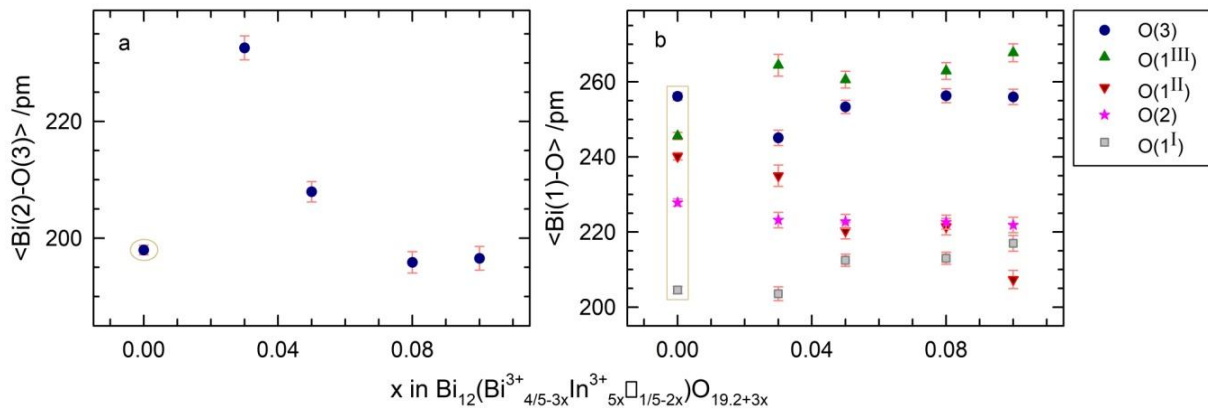


**Figure 3.4:** Evaluation of (a)  $\langle\text{Bi}(2)\text{--O}\rangle$  and (b)  $\langle\text{Bi}(1)\text{--O}\rangle$  bond distances in  $\text{BiO}_3E$  and  $\text{BiO}_5E$  polyhedra, respectively for the compositional  $x$  in  $\text{Bi}_{12}(\text{Bi}^{3+}_{4/5-3x}\text{In}^{3+}_{5x}\square_{1/5-2x})\text{O}_{19.2+3x}$ , where the value of  $x = 0$  is taken from Radaev *et al.* [2].

The apparent saturation of the  $\langle\text{Bi}(2)\text{--O}(3)\rangle$  bond length at about 197(2) pm between  $x = 0.08$  and  $x = 0.10$  can be explained in terms of the theoretical limit of the cation vacancy. In the octahedra, the  $\langle\text{Bi}(1)\text{--O}(3)\rangle$  slightly increases, which, however, remains almost constant including  $x = 0$  [2]. The octahedral  $\langle\text{Bi}(1)\text{--O}(1^{\text{III}})\rangle$  and  $\langle\text{Bi}(1)\text{--O}(1^{\text{I}})\rangle$  bond distances linearly increase (**Fig. 3.4b**). An opposite trend is observed for  $\langle\text{Bi}(1)\text{--O}(2)\rangle$  and  $\langle\text{Bi}(1)\text{--O}(1^{\text{II}})\rangle$  bond distances, which slightly and sharply decrease, respectively. The change of the  $\langle\text{Bi}(1)\text{--O}(3)\rangle$  bond distance in  $\text{BiO}_5E$  can be explained in terms of concomitant decrease of cation vacancy concentration and LEP-effect as the vacancies on Bi(2) site are filled by  $\text{In}^{3+}$ . The saturation of the bond-length changes above  $x = 0.08$ , indicating to a maximum incorporation of indium on this position. The linking  $\langle\text{Bi}(1)\text{--O}(3)\rangle$  bond distance increases up to a saturation of about 256(2) pm, keeping the  $\langle\text{Bi}(1)\text{--Bi}(2)\rangle$  distance around 373(1) pm at the expense of the change of the  $\text{Bi}(1)\text{--O}(3)\text{--Bi}(2)$  angle. The significant decrease of the  $\langle\text{Bi}(1)\text{--O}(1^{\text{II}})\rangle$  bond length can

be related to the rearrangement of the LEPS and the associated  $\text{Bi}(1)\text{O}_5E(1)$  geometry. Here,  $E(1)$  is the active LEP at  $\text{Bi}(1)$  and  $E(2)$  those of  $\text{Bi}(2)$ . Because,  $E(2)$ ,  $\text{O}(1^{\text{II}})$ ,  $\text{O}(1^{\text{III}})$  and  $\text{O}(2)$  are on a (pseudo-)plane where the  $\langle \text{Bi}(1)-\text{O}(1^{\text{II}}) \rangle$  bond distance is strongly influenced by  $E(2)$ .

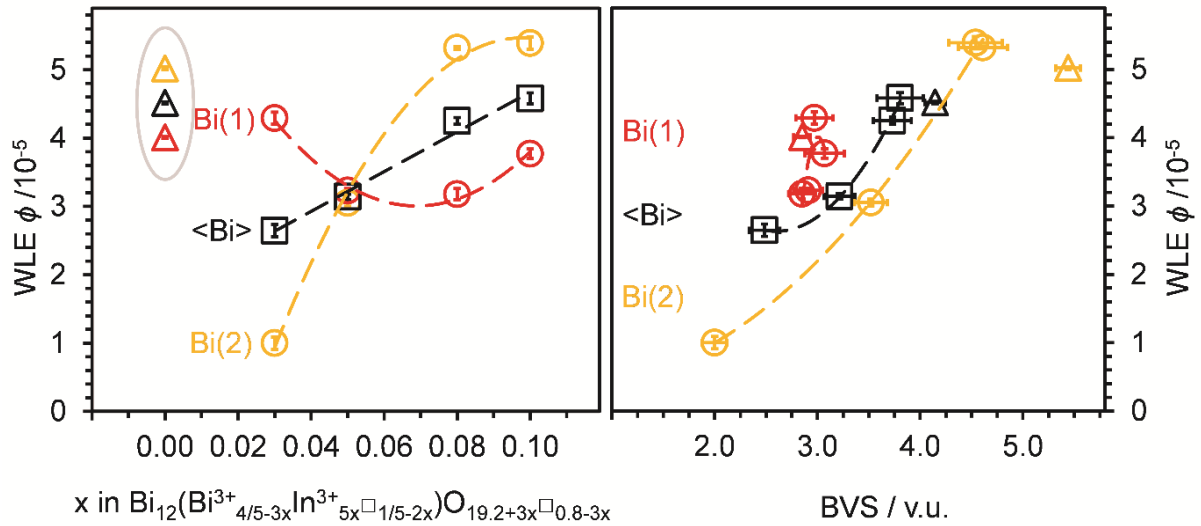


**Figure 3.5:** Change of (a) the absolute value of the WLE parameter ( $\Phi$ ) of  $\text{Bi}^{3+}$  cation on the  $2a$  ( $\text{Bi}2$ ) and  $24f$  ( $\text{Bi}1$ ) sites with respect to the compositional  $x$  in  $\text{Bi}_{12}(\text{Bi}^{3+}_{4/5-3x}\text{In}^{3+}_{5x}\square_{1/5-2x})\text{O}_{19.2+3x}$ . (b) The correlation between the average WLE parameter and bond valence sum (BVS) of the  $\text{BiO}_3E/\text{InO}_4$  polyhedra. Respective values for  $x = 0$  (triangles) are taken from Radaev *et al.* [2].

The saturation of the mentioned bond distances apparently suggests that the  $\text{In}^{3+}$  cations fill the  $2a$  site's cation vacancies, which is approximately limited to  $x = 0.10$ , instead of replacing the  $\text{Bi}^{3+}$  cations in the  $\text{Bi}(2)\text{O}_3E(2)$  tetrahedra.

The calculated WLEs and BVS show a non-linear trend with respect to the indium content, as shown in **figure 3.5**. The reported  $\gamma$ - $\text{Bi}_2\text{O}_3$  [2] possesses WLE parameters of  $5.0 \times 10^{-5}$  and  $4.0 \times 10^{-5}$  for the  $\text{BiO}_3E$  and  $\text{BiO}_5E$  polyhedra, respectively. A slight incorporation of indium ( $x = 0.03$ ) changes the local distortion of the polyhedra (WLE) of  $4.3 \times 10^{-5}$  and  $1.0 \times 10^{-5}$  for the  $\text{BiO}_5E$  and  $\text{BiO}_3E$  polyhedra, respectively, which might be originated from the stereochemical activity of the associated LEPS. Upon further indium incorporation the eccentricity shows a minimum plateau between  $x = 0.05$  and  $0.08$  for  $\text{Bi}(1)\text{O}_5E$  octahedra. In contrast, in the



Bi(2)O<sub>3E(2)</sub> polyhedra significant drop of the WLE can be seen when slightly a small amount (x = 0.03) of indium be found on the 2a site. This significant drop can be explained if only the □O<sub>4</sub> tetrahedra be replaced by the InO<sub>4</sub> tetrahedra, leading to a new structural configuration (**Fig. 3.1c**). Indeed, if Bi(2)O<sub>3E</sub> be substituted by InO<sub>4</sub>, the WLE should decrease. We, however, find an opposite behavior as WLE parameter strongly increases with further increase of indium incorporation (**Fig. 3.5a**). It additionally confirms that the amount of In<sup>3+</sup> incorporation depends on the number of cation vacancy. That is, once the indium is in the structure, the existing BiO<sub>3E</sub> tetrahedra experiences more stereochemical distortion due to relaxation of geometric strains for cation vacancy. And, this behavior is observed up to x = 0.08 and stays at the same values for x = 0.10. The overall behavior between the averaged WLE and BVS (**Fig. 3.5b**) supports the Wang-Liebau model [13] due to change of the Bi(1)O<sub>5E(1)</sub> polyhedron and the associated <Bi(1)–O> bond lengths. For instance, the <Bi(1)–O(3)> bond distance significantly changes from 245(2) pm to 256(2) pm, respectively, for x = 0.03 to x = 0.08, leading to less contribution to the BVS.

### *Spectroscopy*

Group-theoretical analysis predicts 40 zone-center phonons (8A+8E+25F) and their symmetry classification according to the irreducible representations of the crystal symmetry of sillenites [31, 32]. Since the acoustic modes belong to F-modes, the rest 24 F-modes are optically active. The A-modes are totally symmetric, E-modes are doubly degenerate, and F-modes are triply degenerate optical phonons. First-order phonons belonging to all three symmetries are Raman active, and only the F-modes are infrared active. A stack plot of the Raman spectra is shown in **figure 3.6**. The spectra could be separated into two regions: Raman shifts above and below 230 cm<sup>-1</sup>. The bands observed at 114 - 230 cm<sup>-1</sup> wavenumbers are sharper than those at the

high-frequency region. The intense modes are identified in some early studies [31, 33, 34] along with the mode symmetry, assignments and intensity [31].

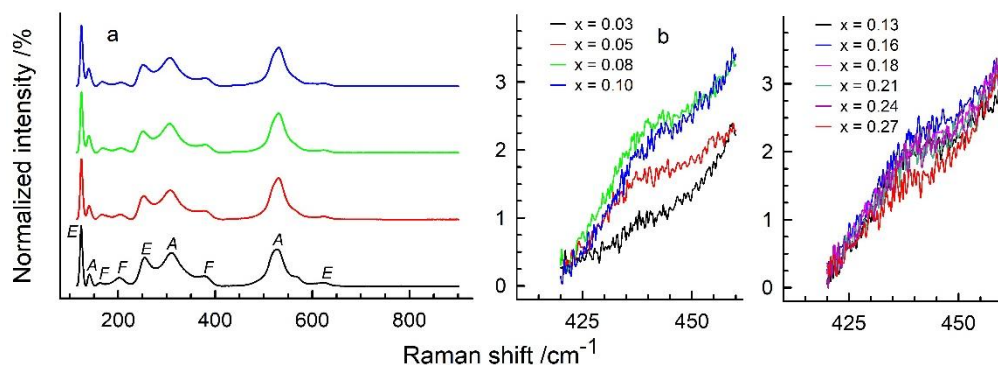


**Figure 3.6:** (a) Raman spectra of  $x = 0.03 - 0.10$  for compositional  $x$  in  $\text{Bi}_{12}(\text{Bi}^{3+}_{4/5-3x}\text{In}^{3+}_{5x}\square_{1/5-2x})\text{O}_{19.2+3x}$ , showing the mode assignment (see text). (b) The magnified spectral region assigned to In–O(3) stretching band are shown for better clarity.

The bandwidths (*FWHM*) is reported to be one of the indications for structural distortions in  $\text{BiO}_5E$  polyhedra [35], which separates the Bi–O stretching modes into more localized vibrations. The Raman peak maxima convoluted at 123, 140, 162, 204, 253, 307, 380, 530 and  $623\text{ cm}^{-1}$  can be compared with those of other sillenites [31, 32, 34, 36-38]. The peak maxima at 123, 253 and  $623\text{ cm}^{-1}$  correspond to E-modes. The bands at 162, 204 and  $380\text{ cm}^{-1}$  are assigned to F-modes, and the rest observed at 140, 307 and  $530\text{ cm}^{-1}$  belong to A-modes. The In–O(3) stretching band [39] have been identified at  $436(2)\text{ cm}^{-1}$  (**Fig. 3.6b**), which intensity (normalized to E-mode at  $123\text{ cm}^{-1}$ ) shows an increase with respect to the compositional  $x$ -value. This increase saturates between  $x = 0.08$  and  $0.10$ . Thereafter, it slightly decreases again up to  $x = 0.27$ . This mode behavior corresponds to the change of the lattice parameters (**Fig. 3.3**). The band at  $162(1)\text{ cm}^{-1}$  ( $FWHM = 9(1)\text{ cm}^{-1}$ ) belongs to the breathing of Bi- and O-atoms and,  $253(1)\text{ cm}^{-1}$  ( $FWHM = 18(1)\text{ cm}^{-1}$ ) to O(2) breathing and weak Bi(1)–O(1) rocking [38, 40]. The change of frequencies of these bands (162 and  $253\text{ cm}^{-1}$ ) is shown in

**figure 3.7**, where former one sharply increases and the later one decreases, followed by a saturation at the appearance of  $\text{In}_2\text{O}_3$  as secondary phase.

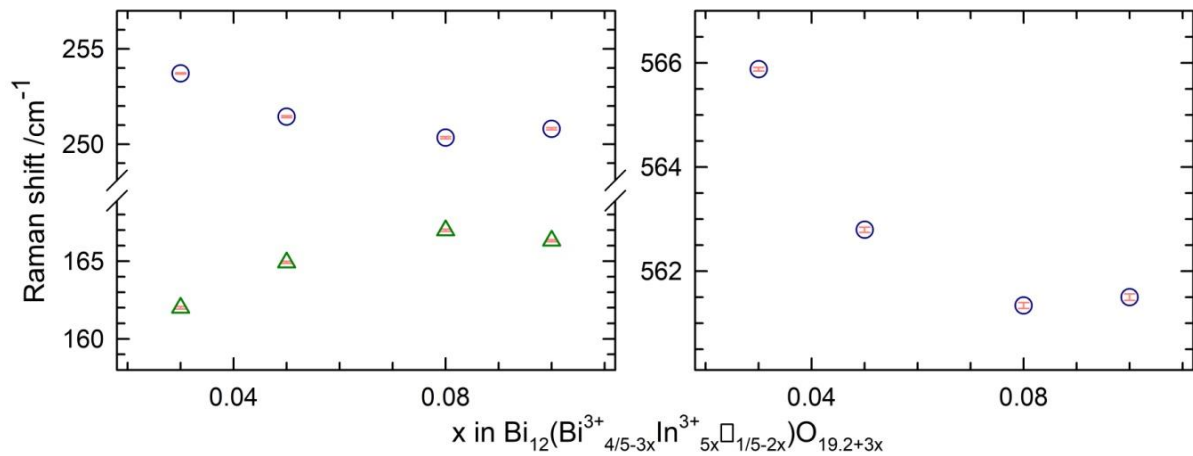


**Figure 3.7:** Change of selected Raman mode frequencies with respect to compositional  $x$  in  $\text{Bi}_{12}(\text{Bi}^{3+}_{4/5-3x}\text{In}^{3+}_{5x}\square_{1/5-2x})\text{O}_{19.2+3x}$ .

The red-shift of approximately  $5(2) \text{ cm}^{-1}$  for the mode at  $162 \text{ cm}^{-1}$  for  $x = 0.03$  (**Fig. 3.7a**) can be related to the elongations of the  $\langle \text{Bi}(1)\text{--O}(3) \rangle$  and  $\langle \text{Bi}(1)\text{--O}(1^{\text{III}}) \rangle$  bond lengths (**Fig. 3.4b**). Indeed, the  $\langle \text{Bi}(1)\text{--O}(3) \rangle$  was also earlier reported to be influenced by the cation vacancies on the  $2a$  sites [2, 41]. In this regard, the change of each  $\langle \text{Bi}(1)\text{--O} \rangle$  bond distance differently influences the respective vibrational frequency as the LEP effect is orientation dependent. As such, the blue shift ( $\sim \text{ca. } 6(1) \text{ cm}^{-1}$ ) of the mode at about  $253 \text{ cm}^{-1}$  for  $x = 0.03$  may be related to the shortening of the  $\langle \text{Bi}(1)\text{--O}(2) \rangle$  and  $\langle \text{Bi}(1)\text{--O}(1^{\text{II}}) \rangle$  bond lengths (**Fig. 3.4b**). Since XRPD suggests that the  $\text{In}^{3+}$  cations locate only on the  $\text{Bi}(2)\text{O}_4$  tetrahedral sites, we particularly emphasize our discussion on the high-frequency region accordingly. Venugopalan *et al.* [31] considered  $\text{MO}_4$  units (e.g.,  $\text{GeO}_4$ ,  $\text{SiO}_4$ ) as a tightly bound structural motif, and categorized the optical phonons into two classes: (I) normal modes and (II) lattice modes where the entire  $\text{MO}_4$  unit vibrates against the other atoms in the crystal. A regular  $\text{MO}_4$  tetrahedron as an isolated unit comprises of  $T_d$  symmetry with  $A_1 + E + 2F_2$  normal modes. The translations and rotations of the free unit belong to  $F_2$  and  $F_1$  modes, respectively. However, the symmetry

becomes lower ( $T$  symmetry) once the  $\text{MO}_4$  tetrahedron be explained as a structural unit of the sillenites, and two additional F-modes should be considered. A mode frequency at  $623\text{ cm}^{-1}$  was assigned for the Bi–O stretching in the  $\text{BiO}_4$  tetrahedra [31, 42] for  $\gamma\text{-Bi}_2\text{O}_3$ . Wojdowski [32] fitted the Bi–O asymmetric vibrational frequencies against the Bi–O bond distances, leading to a linear equation: frequency [ $\text{cm}^{-1}$ ] =  $878(18) - 1.36(7) \cdot \text{bond length [pm]}$ . Our observed data lie close to the fit line. As such, the frequencies observed (**Fig. S3.8**) at 489, 526, 566 and  $600\text{ cm}^{-1}$  can be assigned to the asymmetric stretching of four different Bi–O bond lengths. Since Bi(2) and In atoms share the same Wyckoff position, any change of the frequency can be correlated to the indium incorporation on this site. Following the trend, the mode at  $566\text{ cm}^{-1}$  can be assigned to the Bi(2)–O(3) vibrations for the bond length of about  $233(2)\text{ pm}$ . In increasing the indium concentration in the structure, the mode shifts to lower frequency (**Fig. 3.7b**) due to dominating force constant.

A representative evaluation of the UV/Vis diffuse reflectance spectra using the RATD method is shown in **figure 3.8** for  $x = 0.03$ , and the RATD plots for  $x = 0.05 - 0.10$  in **figure S3.9**. The electronic bandgap for each indium substituted composition has been calculated using both Tauc's [43] and DASF [44] evaluation techniques. The comparison between them, as implemented in the RATD analysis [28], enables to determine the transition type and the bandgap energy, as listed in **table 3.2**. A direct bandgap  $E_g = 2.81(3)\text{ eV}$  for  $x = 0.03$  calculated by the DASF can be compared with that of direct transition  $E_d = 2.86(3)\text{ eV}$  suggested by Tauc's analysis. The possible indirect transition bandgap energy  $E_i = 2.57(3)\text{ eV}$  lies significantly away from that of  $E_g$ . Comparing the respective values for all the compositions (**Tab. 3.2**) one can assume that the transition type is direct for the investigated samples. This contrasts with the theoretically calculated bandgap energy of  $1.87\text{ eV}$  [45] for an indirect transition in  $\gamma\text{-Bi}_2\text{O}_3$ , however, corresponds to earlier experimental findings [46].

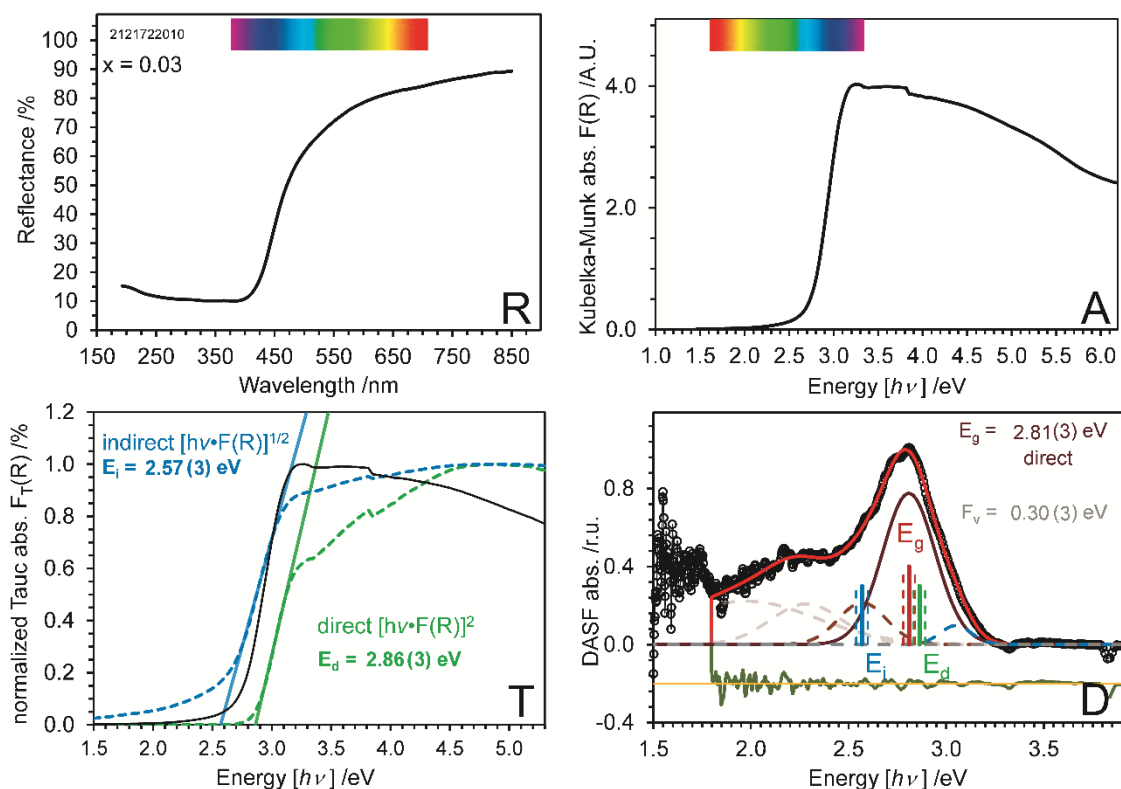


**Figure 3.8:** UV/Vis RATD plot containing reflectance spectrum (R), calculated absorbance spectrum (A), bandgap energies ( $E_g$ ) determined using the DASF method (D) and Tauc analysis (T) for direct ( $E_d$ ) and indirect ( $E_i$ ) transitions for  $x = 0.03$  in  $\text{Bi}_{12}(\text{Bi}^{3+}_{4/5-3x}\text{In}^{3+}_{5x}\square_{1/5-2x})\text{O}_{19.2+3x}$ .

The bandgap energy slightly increases with increasing indium content up to  $x = 0.10$  in the structure, as shown in **figure 3.9**. Deng *et al.* [45] demonstrated a comparable change of bandgap energies due to filling the oxygen vacancies. In the DASF plots, as shown in **figure S3.9**, additional absorption bands at lower energies can be seen between 2.57(9) eV and 2.64(13) eV for  $x = 0.03 - 0.08$ , and at higher energies between 3.04(2) eV and 3.05(3) eV as well. Theoretical calculation for sillenite structures [45] suggests an additional band at lower energy for the presence of oxygen vacancy, which was assigned to anion defect transition energy  $E^d$ . The appearance of this absorption band for  $x = 0.03 - 0.08$  supports the theoretical study [43], where the associated vacancy starts to be filled for these compositions.

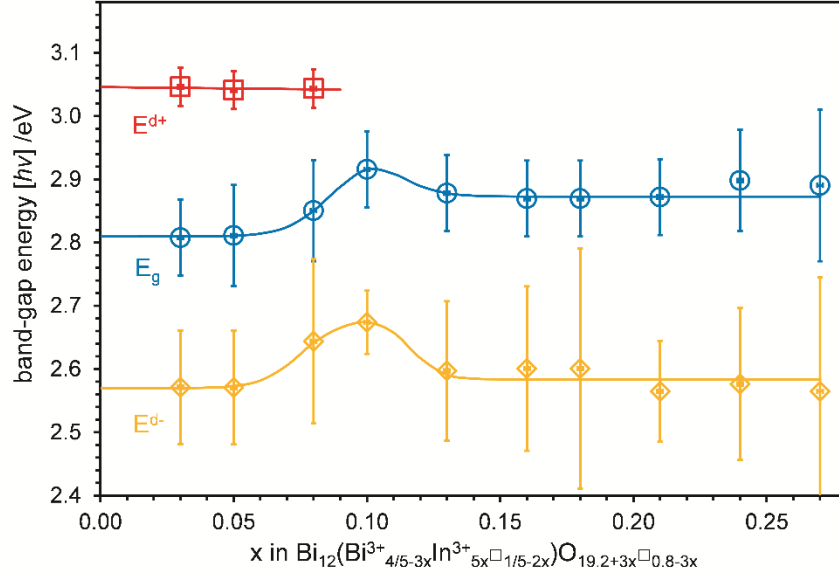


**Figure 3.9:** Determined (RATD method)  $E_g$  (circle, bandgap),  $E^{d-}$  (diamond, anionic defect) and  $E^{d+}$  (square, cationic defect) transition energies for the  $\text{Bi}_{12}(\text{Bi}^{3+}_{4/5-3x}\text{In}^{3+}_{5x}\square_{1/5-2x})\text{O}_{19.2+3x}\square_{0.8-3x}$  solid solution. Guidelines for the eye are additionally given fitted using double sigmoidal curves for  $E_g$  and  $E^{d-}$ .

**Table 3.2:** Bandgap energies calculated from UV/Vis diffuse reflectance spectroscopic data of  $\text{Bi}_{12}(\text{Bi}^{3+}_{4/5-3x}\text{In}^{3+}_{5x}\square_{1/5-2x})\text{O}_{19.2+3x}$  using the RATD methods [28]. Respective value for  $x = 0$  are taken from the given literature.

x	DASF fitting				Tauc fitting		Type
	$E_g$	$F_v$	$E^{d-}$	$E^{d+}$	$E_d$	$E_i$	
0	--	--	--	--	--	1.87 [45]	Indirect
0	--	--	--	--	2.63 [46]	--	Direct
0.03	2.81(3)	0.30(3)	2.57(9)	3.05(3)	2.86(3)	2.57(3)	Direct
0.05	2.82(4)	0.30(3)	2.57(9)	3.04(3)	2.86(3)	2.55(3)	Direct
0.08	2.85(4)	0.26(6)	2.64(13)	3.04(2)	2.90(3)	2.57(3)	Direct
0.10	2.92(2)	0.29(2)	2.67(5)	--	2.87(3)	2.52(3)	Direct

$E_g$ ,  $E^{d-}$ ,  $E^{d+}$  and  $F_v$  refer to bandgap energy, anionic defect transition, cationic defect transition and band flatness in eV, respectively, obtained from the fitting of the DASF plots. The  $E_d$  and  $E_i$ , respectively represent direct and indirect transition in eV determined from the Tauc plots.

Indeed, this transition band cannot be observed for  $x = 0.10$  (**Fig. 3.9**), where all cation voids are filled with indium cations. Further increase of the indium content in the samples lead to a drop of the bandgap ( $E_g$ ) and the anionic defect band ( $E^{d-}$ ). The changes can be analyzed using

a double sigmoidal approach for non-linear ascending and descending values. For higher indium content, the defect band remains slightly an elevated horizontal line at 2.57(3) eV than that of pure  $\gamma$ -Bi<sub>2</sub>O<sub>3</sub> (extrapolated). Concomitantly, the E<sub>g</sub>-plateau is found to be at 2.87(1) eV which is again slightly higher than that of  $\gamma$ -Bi<sub>2</sub>O<sub>3</sub> (2.81(1) eV extrapolated for x = 0). The maximum E<sub>g</sub>-value is found to be 2.92(2) eV for x = 0.10. All the calculated bandgap energies of In<sup>3+</sup> sillenites are comparable with those of the reported values (Tauc analysis: 2.76 - 2.95 eV) of other sillenites [36, 47].

### ***Thermal analysis***

Thermogravimetric analysis and respective DSC curves are shown in **figure 3.10**. Initially, a weight loss of 0.2 % for x = 0.03 can be explained in terms of the associated loss of CO<sub>2</sub>. Because, sillenites were found to react with atmospheric CO<sub>2</sub> due to oxygen vacancy [36].

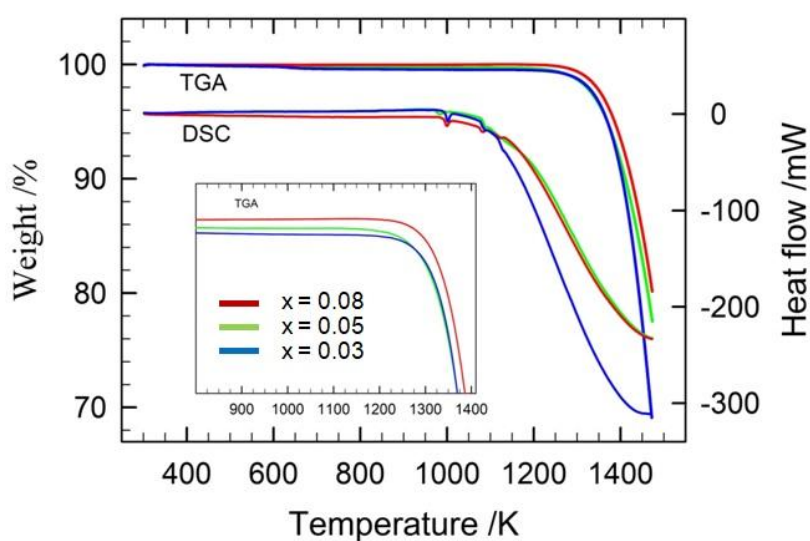


**Figure 3.10:** Thermogravimetric analysis of x = 0.03, 0.05 and 0.08 in this Bi<sub>12</sub>(Bi<sup>3+</sup><sub>4/5-3x</sub>In<sup>3+</sup><sub>5x</sub>□<sub>1/5-2x</sub>)O<sub>19.2+3x</sub>.

Sample x = 0.03 was left at ambient conditions for 86 days, which contains as much as 6 wt.-% of Bi<sub>2</sub>O<sub>2</sub>CO<sub>3</sub>, obtained from XRDP data Rietveld refinements, as shown in **figure S3.11**.

The second point of inflection (onset temperature) is identified as the decomposition

temperature of 1334(2) K, 1338(2) K and 1345(2) K, respectively, for  $x = 0.03$ ,  $0.05$  and  $0.08$  (**Fig. 3.10**). The decomposition temperature slightly increases with increasing  $\text{In}^{3+}$  concentration, which can be understood due to higher bond strength of  $\text{In-O}$  (360(21) kJ/mol) than that of  $\text{Bi-O}$  (343(6) kJ/mol) [48]. The heat flow curves show endothermic peaks between 1000 K and 1084 K without mass loss, which can be associated with the transformation to the higher symmetric  $\delta\text{-Bi}_2\text{O}_3$  phase [49].

#### 4. Conclusions

The incorporation of  $\text{In}^{3+}$  cation in the sillenite structure type of the composition  $\text{Bi}_{12}(\text{Bi}^{3+}_{4/5-3x}\text{In}^{3+}_{5x}\square_{1/5-2x})\text{O}_{19.2+3x}$  is mainly limited to the Bi-cation vacancy in the tetrahedral site. The reported maximum indium incorporation ( $x = 0.10$ ) cannot be realized from a detailed structural and spectroscopic analysis carried out in the present report. Instead, a small part of the indium cations above  $x = 0.08$  might have been replaced in the octahedral site. This study demonstrates how the crystal chemical properties of sillenite type  $\text{Bi}_2\text{O}_3$  ceramics change with a subtle change of the indium concentration. The stereochemical activity of the lone electron pair of  $\text{Bi}^{3+}$  cation shows to be the possible origin of distortions in the polyhedral sites, which is characterized by the Wang-Liebau eccentricity parameter and complemented by the bond valence sums of the associated cations and the Raman shift. The change of optical bandgap with respect to  $\text{In}^{3+}$  content in the sillenites confirms the substitution behavior, which may help understand the relevant optoelectronic properties.

#### Acknowledgements

We gratefully acknowledge the German science foundation (DFG) for financial support within grant GE1981/13-1. MIH gratefully thanks the University of Bremen for the financial supports.



## References

- [1] P.S. Halasyamani, K.R. Poeppelmeier, Noncentrosymmetric oxides, *Chem. Mater.* 10(10) (1998) 2753-2769. Doi:10.1021/cm980140w
- [2] S.F. Radaev, V.I. Simonov, Structural features of  $\gamma$ -phase  $\text{Bi}_2\text{O}_3$  and its place in the sillenite family, *Acta Cryst.* B48 (1992) 604-609. Doi:10.1107/S0108768192003847
- [3] B. Aurivillius, L.G. Sillén, Polymorphy of bismuth trioxide, *Nature* 155(3932) (1945) 305-306. Doi:10.1038/155305a0
- [4] H.A. Harwig, On the structure of bismuthsesquioxide: the  $\alpha$ ,  $\beta$ ,  $\gamma$ , and  $\delta$ -phase, *Z. anorg. allg. Chem.* 444 (1978) 151-166. Doi:10.1002/zaac.19784440118
- [5] S.C. Abrahams, J.L. Bernstein, C. Svensson, Crystal structure and absolute piezoelectric  $d_{14}$  coefficient in laevorotatory  $\text{Bi}_{12}\text{SiO}_{20}$ , *J. Chem. Phys.* 71(2) (1979) 788-792. Doi:10.1063/1.438368
- [6] C. Svensson, S.C. Abrahams, J.L. Bernstein, Laevorotatory  $\text{Bi}_{12}\text{GeO}_{20}$ : remeasurement of the structure, *Acta Cryst.* B35(11) (1979) 2687-2690. Doi:10.1107/S0567740879010190
- [7] S.F. Radaev, L.A. Muradyan, Y.F. Kargin, V.A. Sarin, E.È. Rider, V.I. Simonov, Atomic structure  $\text{Bi}_{25}\text{CaO}_{39}$  and the interpretation of selenite-type crystal structure, *Dokl. Akad. Nauk SSSR* 306(3) (1989) 624-627.
- [8] S.F. Radaev, L.A. Muradyan, Y.F. Kargin, V.A. Sarin, E.È. Rider, V.I. Simonov, Single crystal atomic structure of the  $\text{Bi}_{12}(\text{Fe,P})\text{O}_{20}$  solid solution, *Dokl. Akad. Nauk SSSR* 307(6) (1989) 1381-1384.
- [9] S.F. Radaev, L.A. Muradyan, V.A. Sarin, V.N. Kanepit, A.N. Yudin, A.A. Mar'in, V.I. Simonov, Neutron diffraction study of the atomic structure of single crystals  $\text{Bi}_{12}(\text{V,Bi})\text{O}_{20+x}$ , *Dokl. Akad. Nauk SSSR* 307(3) (1989) 606-610.
- [10] T.I. Mel'nikova, G.M. Kuz'micheva, N.B. Bolotina, V.B. Rybakov, Y.V. Zubavichus, N.V. Sadovskaya, E.A. Mar'ina, Structural features of compounds of the sillenite family, *Crystallogr. Rep.* 59(3) (2014) 353-361. Doi:10.1134/s1063774514030134
- [11] S.F. Radaev, M. Trömel,  $\text{Bi}_{12}(\text{Bi}^{\text{III}}_{0.5}\text{Tl}^{\text{III}}_{0.5})\text{O}_{19.50}$ , *Acta Cryst.* C50 (1994) 656-659. Doi:10.1107/S0108270193011205
- [12] X. Wang, F. Liebau, Influence of lone-pair electrons of cations on bond-valence parameters, *Z. Kristallogr. Cryst. Mater.* 211(7) (1996) 437-439. Doi:10.1524/zkri.1996.211.7.437
- [13] X. Wang, F. Liebau, Influence of polyhedron distortions on calculated bond-valence sums for cations with one lone electron pair, *Acta Cryst.* B63 (2007) 216-228. Doi:10.1107/S0108768106055911
- [14] S.F. Radaev, V.I. Simonov, Atomic structure and isomorphism of sillenites  $\text{Bi}_{12}\text{M}_x\text{O}_{20\pm\delta}$ , *Butll. Soc. Cat. Cien.* 12(2) (1991) 247-263.
- [15] M. Valant, D. Suvorov, A stoichiometric model for sillenit, *Chem. Mater.* 14 (2002) 3471-3476. Doi:10.1021/cm0211731
- [16] L.G. Sillen, *Ark. Kemi. Mineral. Geol.* 12A(18) (1937) 1-13.

- [17] J.-C. Champarnaud-Mesjard, B. Frit, A structural model for the  $\text{Bi}_{1-x}\text{Cd}_x\text{O}_{1.5-x/2}$  ( $0 \leq x \leq 0.0256$ ) sillenite-type solid solution, *Comptes Rendus de l'Académie des Sciences-Series IIC-Chemistry* 2(7-8) (1999) 369-374. Doi:10.1016/S1387-1609(00)88547-3
- [18] S.F. Radaev, L.A. Muradyan, V.I. Simonov, Atomic structure and crystal chemistry of sillenites:  $\text{Bi}_{12}(\text{Bi}^{3+}_{0.50}\text{Fe}^{3+}_{0.50})\text{O}_{19.50}$  and  $\text{Bi}_{12}(\text{Bi}^{3+}_{0.67}\text{Zn}^{2+}_{0.33})\text{O}_{19.33}$ , *Acta Cryst.* B47(1) (1991) 1-6. Doi:10.1107/S0108768190007492
- [19] H.S. Horowitz, A.J. Jacobson, J.M. Newsam, J.T. Lewandowski, M.E. Leonowicz, Solution synthesis and characterization of sillenite phases,  $\text{Bi}_{24}\text{M}_2\text{O}_{40}$  ( $\text{M} = \text{Si}, \text{Ge}, \text{V}, \text{As}, \text{P}$ ), *Solid State Ionics* 32 (1989) 678-690. Doi:10.1016/0167-2738(89)90344-5
- [20] D.C.N. Swindells, J.L. Gonzalez, Absolute configuration and optical activity of laevorotatory  $\text{Bi}_{12}\text{TiO}_{20}$ , *Acta Cryst.* B44(1) (1988) 12-15. Doi:10.1107/S0108768187010267
- [21] U. Delicat, S.F. Radaev, M. Trömel, P. Behrens, Y.F. Kargin, A.A. Mar'in, Tetrahedral coordination of Mn (IV) by oxygen in manganese sillenite  $\text{Bi}_{12}\text{MnO}_{20}$ , *J. Solid State Chem.* 110(1) (1994) 66-69. Doi:10.1006/jssc.1994.1136
- [22] A. Watanabe, H. Kodama, S. Takenouchi, Nonstoichiometric phase with sillenite-type structure in the system  $\text{Bi}_2\text{O}_3\text{-P}_2\text{O}_5$ , *J. Solid State Chem.* 85(1) (1990) 76-82. Doi:10.1016/S0022-4596(05)80062-3
- [23] A. Watanabe, S. Takenouchi, P. Conflant, J.P. Wignacourt, M. Drache, J.C. Boivin, Preparation of a nonstoichiometric sillenite-type phase in the system  $\text{Bi}_2\text{O}_3\text{-As}_2\text{O}_5$ , *J. Solid State Chem.* 103(1) (1993) 57-62. Doi:10.1006/jssc.1993.1078
- [24] D.C. Craig, N.C. Stephenson, Structural studies of some body-centered cubic phases of mixed oxides involving  $\text{Bi}_2\text{O}_3$ : the structures of  $\text{Bi}_{25}\text{FeO}_{40}$  and  $\text{Bi}_{38}\text{ZnO}_{60}$ , *J. Solid State Chem.* 15 (1975) 1-8. Doi:10.1016/0022-4596(75)90264-9
- [25] N. Rangavittal, T.N.G. Row, C.N.R. Rao, A study of cubic bismuth oxides of the type  $\text{Bi}_{26-x}\text{M}_x\text{O}_{40-8}$  ( $\text{M} = \text{Ti}, \text{Mn}, \text{Fe}, \text{Co}, \text{Ni}$  or  $\text{Pb}$ ) related to  $\gamma\text{-Bi}_2\text{O}_3$ , *Adv. Chem. Ser.* (2003) 95-108. Doi:10.1142/9789812835734\_0009
- [26] I.D. Brown, *The chemical bond in inorganic chemistry: the bond valence model*, Oxford University Press 2016.
- [27] N.E. Brese, M. O'keeffe, Bond-valence parameters for solids, *Acta Cryst.* B47(2) (1991) 192-197. Doi:10.1107/S0108768190011041
- [28] T.M. Gesing, M.M. Murshed, S. Schuh, O. Thüringer, K. Krämer, T. Neudecker, C.B. Mendive, L. Robben, Nano-crystalline precursor formation, stability, and transformation to mullite-type visible-light photocatalysts, *J. Mater. Sci.* (2022) 1-20. Doi:10.1007/s10853-022-07854-w
- [29] M. Lulei, R. Hoppe, Zur Überwindung von Vorurteilen: Das erste basische Oxindat,  $\text{Na}_2\text{O}_3[\text{InO}_4]_4$ , *Z. anorg. allg. Chem.* 620(7) (1994) 1179-1184. Doi:10.1002/zaac.19946200709
- [30] R.D. Shannon, Revised effective ionic radii and systematic studies of interatomic distances in halides and chalcogenides, *Acta Cryst.* A32 (1976) 751-767. Doi:10.1107/S0567739476001551

- [31] S. Venugopalan, A.K. Ramdas, Raman Spectra of Bismuth Germanium Oxide and Bismuth Silicon Oxide, *Phys. Rev. B* 5(10) (1972) 4065-4079. Doi:10.1103/PhysRevB.5.4065
- [32] W. Wojdowski, Vibrational modes in  $\text{Bi}_{12}\text{GeO}_{20}$  and  $\text{Bi}_{12}\text{SiO}_{20}$  crystals *Phys. Status Solidi B* 130(1) (1985) 121-130. Doi:10.1002/pssb.2221300109
- [33] A.V. Egorysheva, V.I. Burkov, V.S. Gorelik, Y.F. Kargin, A.V. Chervyakov, Raman scattering in sillenite-type crystals, *Crystallogr. Rep.* 46(3) (2001) 461–467. Doi:10.1134/1.1376478
- [34] A.V. Egorysheva, V.I. Burkov, Y.F. Kargin, V.G. Plotnichenko, V.V. Koltashev, E.D. Obraztsova, S.V. Terekhov, Atomic structure features of sillenite crystals as probed by Raman spectroscopy, *Zh. Neorg. Khim* 50(2) (2005) 278-286.
- [35] R.J. Betsch, W.B. White, Vibrational spectra of bismuth oxide and the sillenite-structure bismuth oxide derivatives, *Spectrochim. Acta A Mol. Biomol. Spectrosc.* 34(5) (1978) 505-514. Doi:10.1016/0584-8539(78)80047-6
- [36] M. Weber, R.D. Rodriguez, D.R.T. Zahn, M. Mehring, Gamma- $\text{Bi}_2\text{O}_3$  -To Be or Not To Be? Comparison of the Sillenite gamma- $\text{Bi}_2\text{O}_3$  and Isomorphous Sillenite-Type  $\text{Bi}_{12}\text{SiO}_{20}$ , *Inorg. Chem.* 57(14) (2018) 8540-8549. Doi:10.1021/acs.inorgchem.8b01249
- [37] B. Mihailova, M. Gospodinov, L. Konstantinov, Raman spectroscopy study of sillenites. I. comparison between  $\text{Bi}_{12}(\text{Si},\text{Mn})\text{O}_{20}$  single crystals, *J. Phys. Chem. Solids* 60 (1999) 1821-1827. Doi:10.1016/S0022-3697(99)00194-8
- [38] D.J. Arenas, T. Jegorel, C. Knab, L.V. Gasparov, C. Martin, D.M. Pajeroski, H. Kohno, M.W. Lufaso, Raman spectroscopy evidence of inhomogeneous disorder in the bismuth-oxygen framework of  $\text{Bi}_{25}\text{InO}_{39}$  and other sillenites, *Phys. Rev. B* 86(14) (2012). Doi:10.1103/PhysRevB.86.144116
- [39] D.M. Adams, A.J. Carty, P. Carty, D.G. Tuck, Co-ordination chemistry of indium. Part VI. Far-infrared spectra of indium trihalide adducts with neutral donors, *J. Chem. Soc. A* (1968) 162-164. Doi:10.1039/J19680000162
- [40] L. Wiehl, A. Friedrich, E. Haussühl, W. Morgenroth, A. Grzechnik, K. Friese, B. Winkler, K. Refson, V. Milman, Structural compression and vibrational properties of  $\text{Bi}_{12}\text{SiO}_{20}$  sillenite from experiment and theory, *J. Phys.: Condens. Matter* 22(50) (2010) 505401. Doi:10.1088/0953-8984/22/50/505401
- [41] U.D. Wdowik, G. Jagło, D. Legut, Effect of cation-vacancy superstructure on the phonon dynamics in  $\text{KNi}_2\text{Se}_2$ , *Phys. Rev. B* 101(4) (2020) 045125. Doi:10.1103/PhysRevB.101.045125
- [42] A.J. Salazar-Pérez, M.A. Camacho-López, R.A. Morales-Luckie, V. Sánchez-Mendieta, F. Ureña-Núñez, J. Arenas-Alatorre, Structural evolution of  $\text{Bi}_2\text{O}_3$  prepared by thermal oxidation of bismuth nano-particles, *Superficies y vacío* 18(3) (2005) 4-8.
- [43] J. Tauc, R. Grigorovici, A. Vanacu, Optical properties and electronic structure of amorphous germanium, *Phys. Status Solidi B* 15(2) (1966) 627-637. Doi:10.1002/pssb.19660150224
- [44] D. Souri, Z.E. Tahan, A new method for the determination of optical band gap and the nature of optical transitions in semiconductors, *Appl. Phys. B* 119(2) (2015) 273-279. Doi:10.1007/s00340-015-6053-9

- [45] H. Deng, W. Hao, H. Xu, C. Wang, Effect of intrinsic oxygen vacancy on the electronic structure of  $\gamma$ - $\text{Bi}_2\text{O}_3$ : First-principles calculations, *J. Phys. Chem. C* 116(1) (2012) 1251-1255. Doi:10.1021/jp2086895
- [46] R. Nagarajan, V. Shrivastava, J. Pandey, Optical, electrical, and catalytic (photo-and sono-) properties of indium doped  $\gamma$ - $\text{Bi}_2\text{O}_3$  with sillenite structure, *J. Alloys Compd.* 887 (2021) 161466. Doi:10.1016/j.jallcom.2021.161466
- [47] A.V. Egorysheva, O.M. Gaitko, T.B. Kuvshinova, S.V. Golodukhina, V.A. Lebedev, K.E. Erova, Targeted synthesis ultrafine  $\alpha$ - and  $\gamma$ - $\text{Bi}_2\text{O}_3$  having different morphologies, *Russ. J. Inorg. Chem.* 62(11) (2017) 1426-1434. Doi:10.1134/s0036023617110055
- [48] J.G. Speight, *Lange's handbook of chemistry*, 17 ed., McGraw-Hill Education 2017.
- [49] A.D. Murray, C.R.A. Catlow, F. Beech, J. Drennan, A neutron powder diffraction study of the low-and high-temperature structures of  $\text{Bi}_{12}\text{PbO}_{19}$ , *J. Solid State Chem.* 62(3) (1986) 290-296. Doi:10.1016/0022-4596(86)90243-4

## Supplementary Information

### **Indium containing sillenite semiconductor: synthesis, structural, spectroscopic and thermogravimetric analysis**

**Md. Imran Hossain<sup>1</sup>, M. Mangir Murshed<sup>1,2\*</sup>, Thorsten M. Gesing<sup>1,2</sup>**

<sup>1</sup>University of Bremen, Institute of Inorganic Chemistry and Crystallography, Leobener Straße 7, D-28359 Bremen, Germany

<sup>2</sup>MAPEX Center for Materials and Processes, Bibliothekstraße 1, D-28359 Bremen, Germany

\*Corresponding author: e-mail address: [murshed@uni-bremen.de](mailto:murshed@uni-bremen.de), phone: +49 (0)421 218

63144

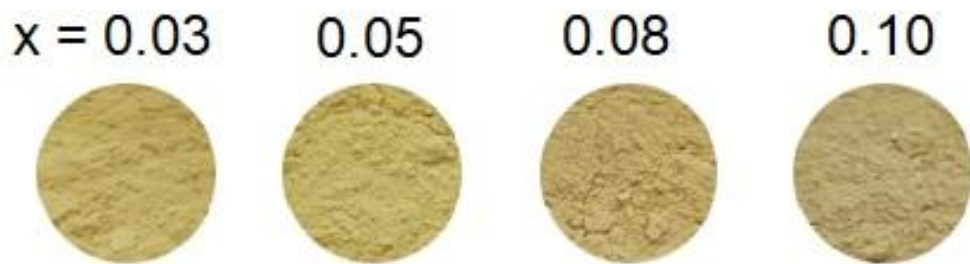


**Figure S3.1:** Sample color variation in  $\text{Bi}_{12}(\text{Bi}^{3+}_{4/5-3x}\text{In}^{3+}_{5x}\square_{1/5-2x})\text{O}_{19.2+3x}$  for  $x = 0.03 - 0.10$ .

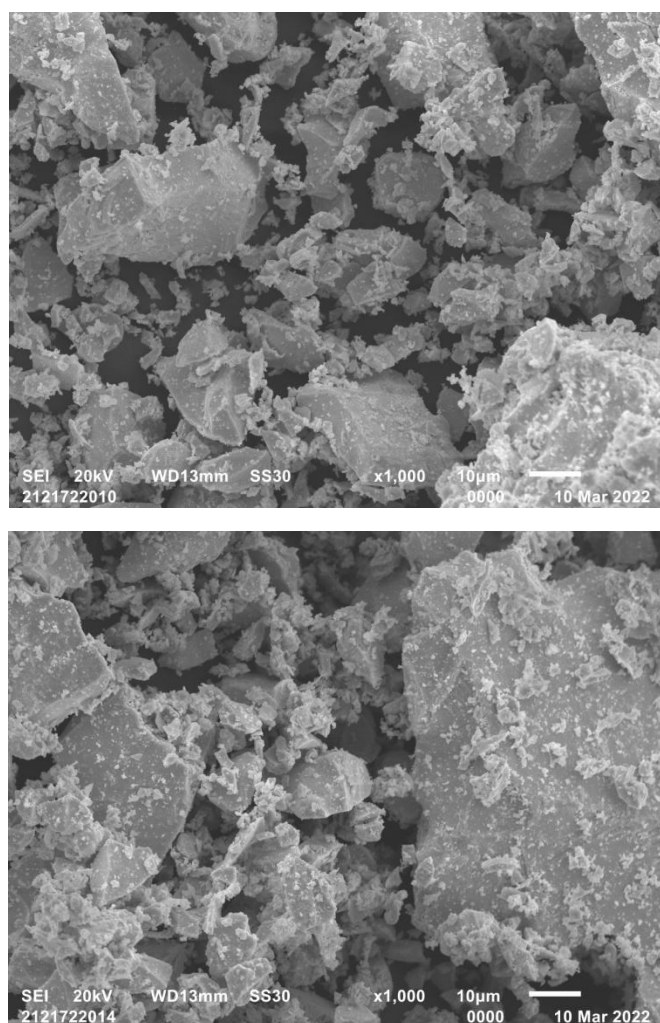


**Figure S3.2:** Scanning electron micrographs of  $x = 0.03$  (up) and  $x = 0.08$  (down) in  $\text{Bi}_{12}(\text{Bi}^{3+}_{4/5-3x}\text{In}^{3+}_{5x}\square_{1/5-2x})\text{O}_{19.2+3x}$  solid solution.

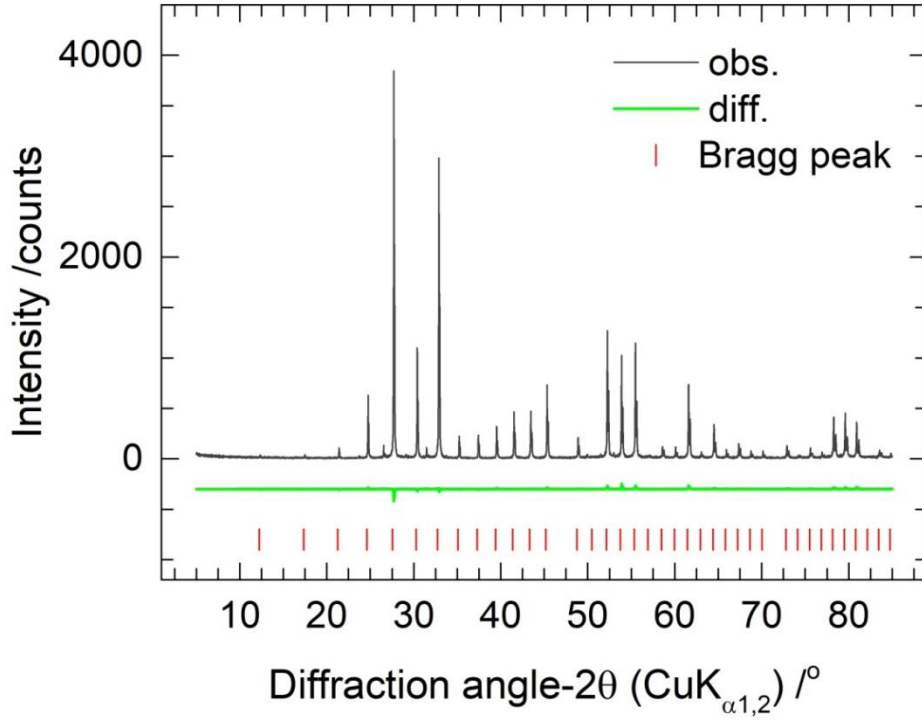


**Figure S3.3:** X-ray powder diffraction data Rietveld pattern for  $x = 0.03$  in  $\text{Bi}_{12}(\text{Bi}^{3+}_{4/5-3x}\text{In}^{3+}_{5x}\text{O}_{19.2+3x})$ .

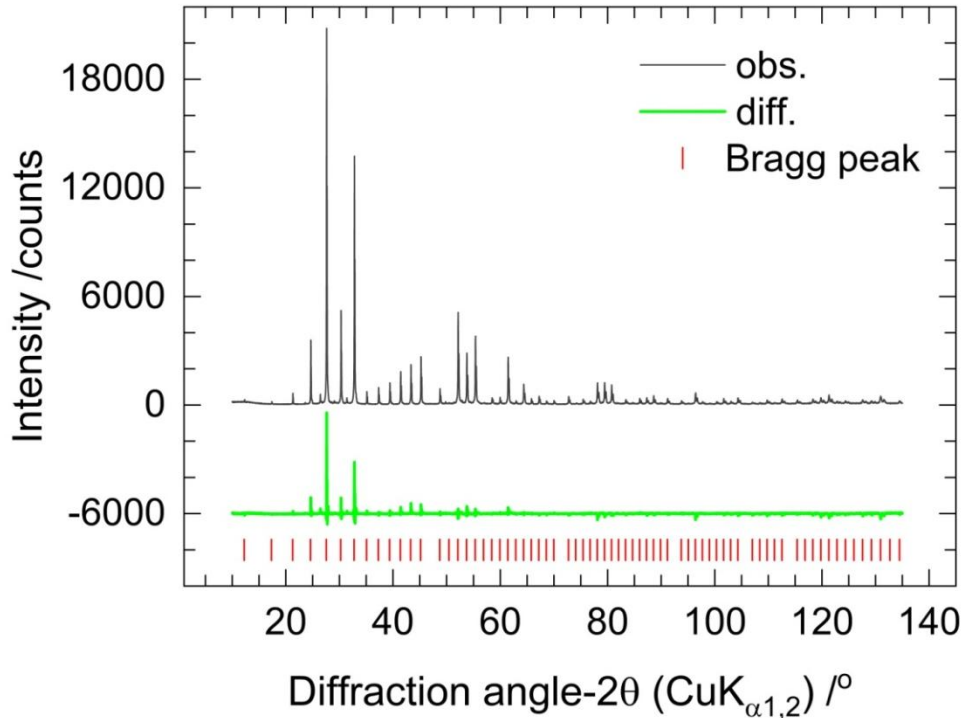


**Figure S3.4:** X-ray powder diffraction data Rietveld pattern for  $x = 0.08$  in  $\text{Bi}_{12}(\text{Bi}^{3+}_{4/5-3x}\text{In}^{3+}_{5x}\text{O}_{19.2+3x})$ .

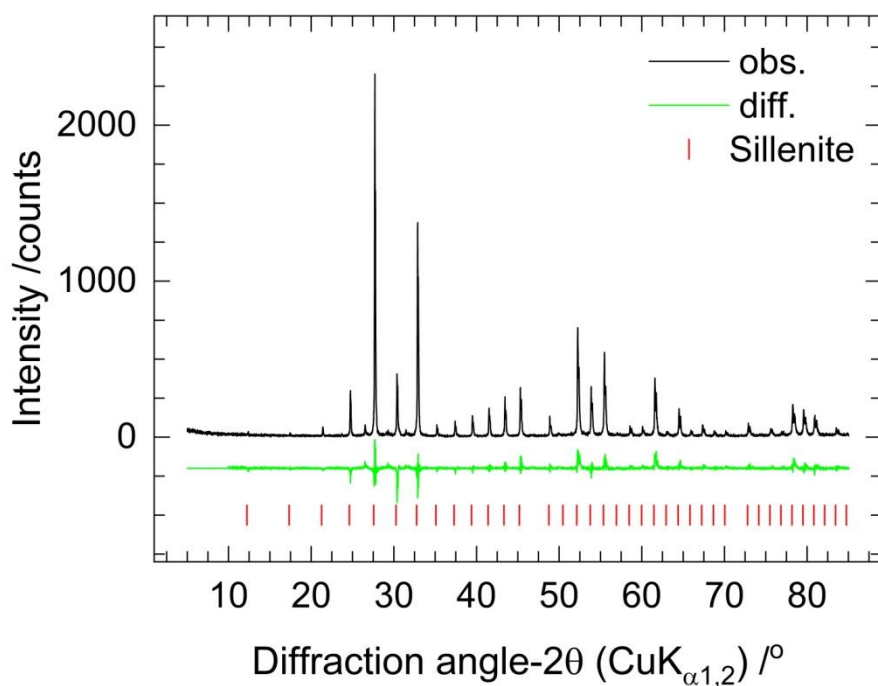


**Figure S3.5:** X-ray powder diffraction data Rietveld pattern for  $x = 0.10$  in  $\text{Bi}_{12}(\text{Bi}^{3+}_{4/5-3x}\text{In}^{3+}_{5x}\square_{1/5-2x})\text{O}_{19.2+3x}$ .

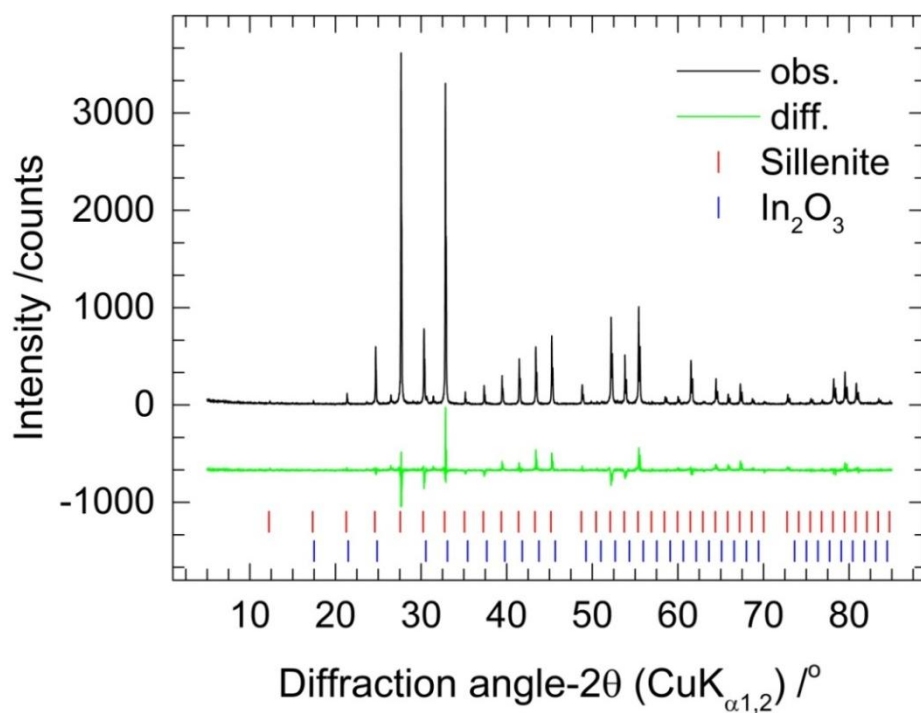


**Figure S3.6:** X-ray powder diffraction data Rietveld pattern for  $x = 0.13$  in  $\text{Bi}_{12}(\text{Bi}^{3+}_{4/5-3x}\text{In}^{3+}_{5x}\square_{1/5-2x})\text{O}_{19.2+3x}$ .



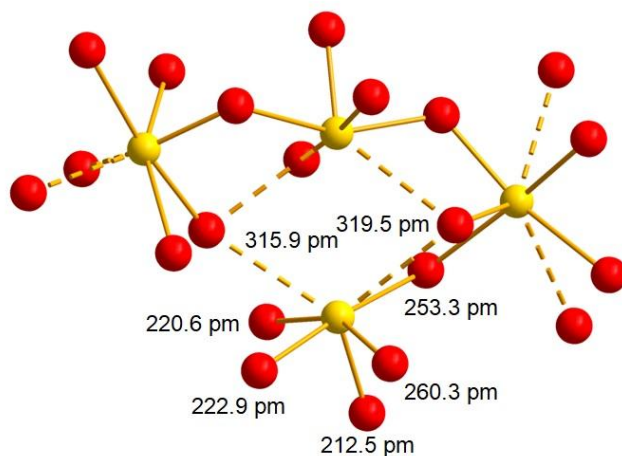


**Figure S3.7:** Evaluation of  $\langle \text{Bi}(1)\text{-O} \rangle$  bond distances in  $\text{BiO}_5E$  polyhedra for the compositional  $x = 0.05$  in  $\text{Bi}_{12}(\text{Bi}^{3+}_{4/5-3x}\text{In}^{3+}_{5x}\square_{1/5-2x})\text{O}_{19.2+3x}$ .

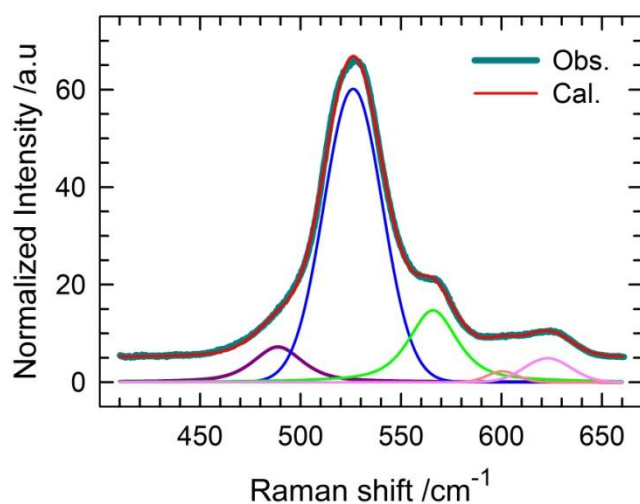


**Figure S3.8:** Representative Raman spectrum peak fitting of Bi–O asymmetric stretching vibrations for  $x = 0.03$  compositional value in  $\text{Bi}_{12}(\text{Bi}^{3+}_{4/5-3x}\text{In}^{3+}_{5x}\square_{1/5-2x})\text{O}_{19.2+3x}$ .

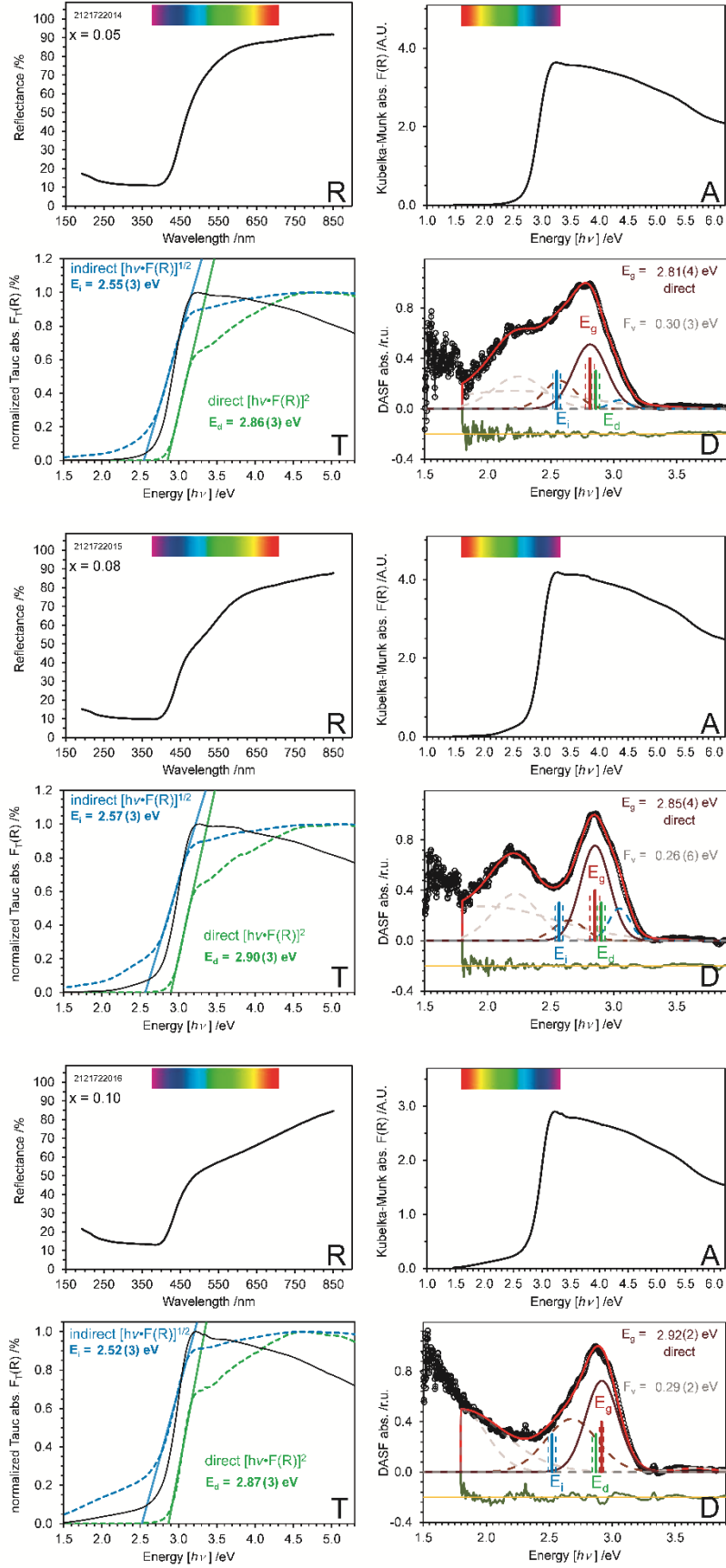
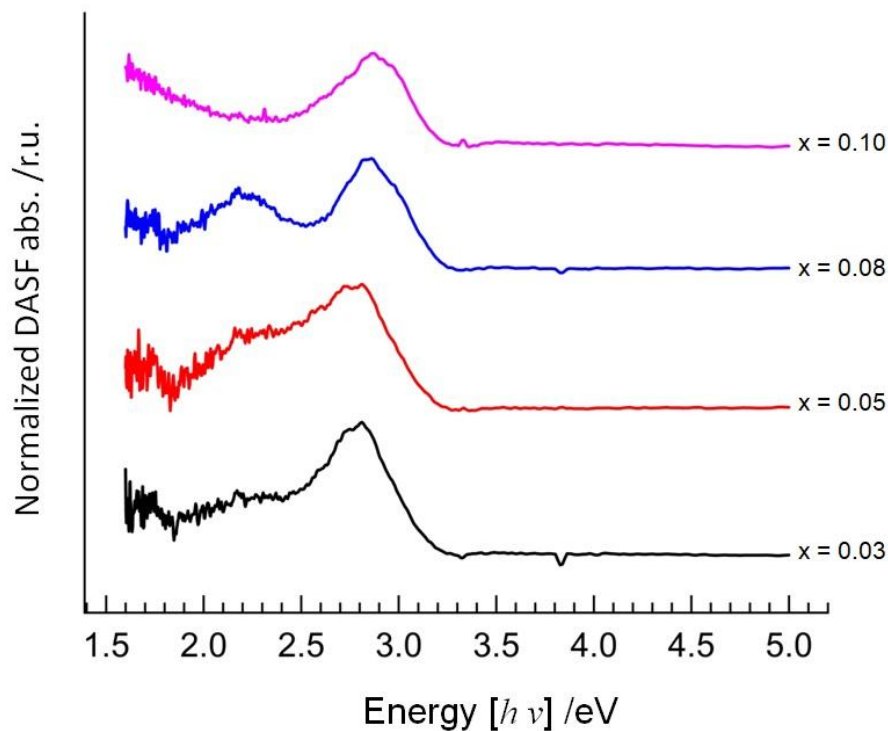
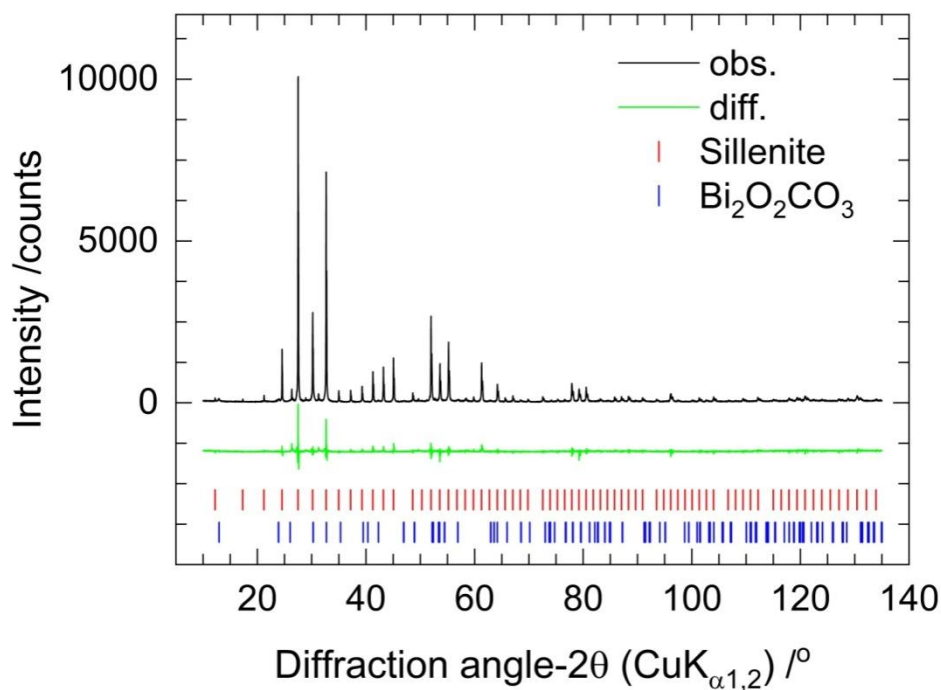


Figure S3.9: RATD plots of  $\text{Bi}_{12}(\text{Bi}^{3+}_{4/5-3x}\text{In}^{3+}_{5x})_{1/5-2x}\text{O}_{19.2+3x}$  for  $x = 0.05 - 0.10$ .



**Figure S3.10:** Calculated DASF absorbance spectra of  $\text{Bi}_{12}(\text{Bi}^{3+}_{4/5-3x}\text{In}^{3+}_{5x}\square_{1/5-2x})\text{O}_{19.2+3x}$  for  $x = 0.03 - 0.10$ .



**Figure S3.11:** X-ray powder diffraction data Rietveld pattern of  $x = 0.03$  sample exposed to open condition for 86 days.

## Chapter 4

### Stabilization of $(\text{Bi}_{1-x}\text{M}_x)_2\text{O}_3$ delta phase with rare-earth cations: structural, spectroscopic and thermal investigations for $M = \text{Y, Gd, Tb, Dy, Ho, Er, Tm, Yb, and Lu}$

#### Abstract

Series of high symmetric  $\delta$ – $(\text{Bi}_{1-x}\text{M}_x)_2\text{O}_3$  phases are synthesized by solid state method, where  $M = \text{Y, Gd, Tb, Dy, Ho, Er, Tm, Yb, and Lu}$ . Each solid solution comprises of members between  $x = 0.05$  and  $0.25$  with a chemical slice of  $0.05$ . Each sample is characterized by X-ray powder data diffraction followed by Rietveld refinement. The type of  $M^{3+}$ -cation and the compositional content ( $x$ ) play vital roles for the modification of low symmetric  $\beta$ –phase to high symmetric  $\delta$ –phase. The successive decrease in lattice parameter indicates the substitution of  $\text{Bi}^{3+}$  by smaller  $M^{3+}$  cations. The higher isotropic atomic displacement parameter of the oxygen atoms indicates a certain degree of static disorder. The  $\delta$ –phase is clearly identified by Raman spectra, and distinguishable from other structural phases with respect to the concentration of the compositional  $x$ -values. Moreover, broadening of some selective bands and the associated blue shifts support the structural modification. The direct band gap has reached a plateau at  $2.75(4)$  eV, and additional absorption band is identified due to anionic defect, and the change of the defect band gap with respect to  $x$  in  $(\text{Bi}_{1-x}\text{M}_x)_2\text{O}_3$  indicates the redistribution of oxygen. An additional endothermic peak before the respective decomposition temperature demonstrates the order  $\leftrightarrow$  disorder nature in the  $\delta$ –phase. The type of  $M^{3+}$ -cation and consecutive change of the Bi/ $M$ –O bond strengths explain the thermal stability of a given  $\delta$ –phase.

**Keywords:** Bismuth oxide, delta phase, disorder, oxygen vacancy, and bandgap.

## 1. Introduction

Bismuth oxide, the highly symmetric phase, has particularly come to the center of attention in ceramic field, as a solid electrolyte in the solid oxide fuel cell [1]. The polymorphism of  $\text{Bi}_2\text{O}_3$  is temperature dependent, where the thermal history clearly defines the appearance of  $\alpha$ -,  $\beta$ -,  $\gamma$ -, and  $\delta$ -phases [2, 3]. The  $\delta$ - $\text{Bi}_2\text{O}_3$  is a high symmetry phase (sp. gr.  $Fm\bar{3}m$ ,  $Z = 2$ ) and the crystal structure can be described as distorted  $\text{CaF}_2$  type [4], as depicted in **figure 4.1**. The statistical distribution of oxygen in anion sublattice keeps 25 % vacant sites in the structure. Both the ordering of the vacant sites and the complex distribution of oxygen sublattice fabricate the diffusion path for oxide ion conduction [5-8]. Three vacancy alignments, namely, in the direction of  $\langle 111 \rangle$ ,  $\langle 110 \rangle$ , and  $\langle 100 \rangle$  are known, leading to the estimated distance between the vacant sites as  $\sqrt{3}a/2$ ,  $\sqrt{2}a/2$  and  $a/2$  ( $a$  = lattice parameter), respectively [9]. The debate on the reliability of such oxygen vacancy orderings is still open [10]. The ideal anion site O(1) has an occupancy factor of 0.243. Another oxygen sublattice O(2), keeping 2.03 oxygen per unit cell, has been displaced from the tetrahedral site toward the central octahedral site along the  $\langle 111 \rangle$  directions (**Fig. 4.1b**). The O(1) is located at the center and O(2) close to the faces of the  $\text{OBi}_4$  tetrahedron. The  $\text{Bi}^{3+}$  cations hence form a framework, keeping a Bi–Bi distance of 400.26(3) pm which is longer than that of other polymorphs [5, 11, 12]. The ambient condition  $\alpha$ -form can be directly transformed into  $\delta$ -phase at 1033 K [5]. The  $\alpha \rightarrow \delta$  transformation requires a massive energy, which, however, occurs just before the solid-liquid phase transition [7]. The other phases appear after cooling the high temperature formed  $\delta$ -phase [2]. Ambient condition stabilization of the  $\beta$ -,  $\gamma$ - and  $\delta$ -phase is commonly accomplished by substituting bismuth by other cations in the  $\alpha$ -phase [13-15]. Neutron diffraction study on  $\delta$ -phase  $(\text{Bi}_{1-x}\text{Y}_x)_2\text{O}_3$  solid solution demonstrated cation ( $24e$  Wyckoff:  $x,0,0$ ) relaxation along the  $\langle 100 \rangle$  direction and presence of a small amount of interstitial oxy-

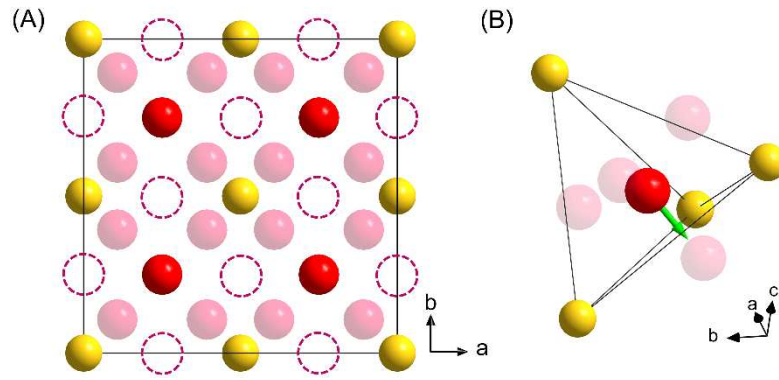


**Figure 4.1:** (A) Crystal structure of the representative  $\delta$ -phase  $(\text{Bi}_{0.87}\text{Gd}_{0.13})_2\text{O}_3$ , where the dotted circles represent the interstitial position (O3). (B) The green arrow indicates the distortive displacement of O(1) along the  $\langle 111 \rangle$  direction toward the O(2) position.

en (O3) at  $48i (\frac{1}{2}, y, y)$  [16, 17]. The O(3) is found to be located between two Bi/Y cations along the tetrahedral edge (**Fig. 4.1a - b**). The high isotropic displacement parameters of atoms in  $\delta$ - $\text{Bi}_2\text{O}_3$  structure at 1033 K indicates a certain degree of positional disordering at ambient condition [5, 16-19]. Many  $M^{n+}$ -cations are known to stabilize the  $\delta$ -phase at ambient condition, however, depends on the degree of substitution and the thermal history [4, 18-36]. The amount of  $\text{Bi}^{3+}$  substitution is apparently related to the size of the  $M^{n+}$ -cation. For instance, for a given  $\text{MO}_8$  coordination, the size of  $\text{Y}^{3+}$ - and most rare-earth  $M^{3+}$ -cations remains at around  $115.9 \pm 4$  pm [37]. This study investigates the successive substitution of  $\text{Bi}^{3+}$  by  $M^{3+}$  in the chemical formula  $(\text{Bi}_{1-x}\text{M}_x)_2\text{O}_3$ , with compositional  $x$ -value ranging from 0.05 to 0.25, and a maximum slice at  $x = 0.05$  for each  $M$ -series ( $M = \text{Y, Gd, Tb, Dy, Ho, Er, Tm, Yb, and Lu}$ ). It focuses on how the disorder in the oxygen sublattice of the  $\delta$ -phase changes upon the replacement of larger  $\text{Bi}^{3+}$  ions with smaller  $M^{3+}$  ions at the same Wyckoff site.

## 2. Experimental

### 2.1. Synthesis

All samples are prepared by mixing stoichiometric amount of  $\text{Bi}_2\text{O}_3$  and  $M_2\text{O}_3$  ( $M = \text{Y}$  and  $\text{Gd} - \text{Lu}$ ) in an agate mortar, and put into a corundum crucible. The solid mixture is heated at 923 K for 24 h followed by air quenching. Afterward, the grinding sample is further heated at 1073 K for 24 h followed by quenching down to room temperature.

### 2.2. Microscopy

Scanning electron microscopy (SEM) is carried out using a JMS-6510 (JEOL) equipped with an X-Flash 410-M detector (Bruker) for energy dispersive X-ray spectroscopy. A small amount of sample is taken on conducting carbon tabs and sputtered with gold for 20 s with a JFC-1200 coater (JEOL) followed by inserting them into the SEM chamber.

### 2.3. X-ray diffraction

X-ray powder diffraction (XRPD) pattern are recorded on a Bruker D8 Discover powder diffractometer using Bragg-Brentano geometry with  $\text{CuK}_{\alpha 1,2}$  ( $\lambda_{\text{K}\alpha 1} = 154.05929(5)$  pm,  $\lambda_{\text{K}\alpha 2} = 154.4414(2)$  pm) radiation. The measurements are taken at ambient condition with a step size of  $0.0167^\circ$  and a total data collection time of 75 s/step. The fundamental parameter approach, where the fundamental parameters are fitted against a  $\text{LaB}_6$  standard material, is applied for the Rietveld refinement using ‘Diffrac<sup>Plus</sup>Topas 6’ software (Bruker AXS GmbH, Karlsruhe, Germany). The starting lattice parameters and atomic coordinates are taken from the crystal structure of  $\beta$ - and  $\delta$ -phase [15, 16] (ICSD Coll. Code 83640 and 60198). During Rietveld refinements, the background, sample displacement, atomic coordinates, and occupancy parameters are optimized. In all cases, the isotropic displacement parameters between  $\text{Bi}^{3+}$  and  $M^{3+}$ , and between the oxygen atoms (O1, O2, O3) are constrained. During

the Rietveld refinements, bismuth has found on  $24e$  Wyckoff positions, and partially share the same site with  $M^{3+}$  cation. Successive refinement trials reveal mixed occupancy of  $\text{Bi}^{3+}$  and  $M^{3+}$ . The average crystallite size (ACS) and microstrain (MS) are calculated from the observed all X-ray reflections, using the fundamental approach, where ACS and MS are defined as  $L_{\text{Vol}}(\text{IB})$  and  $\varepsilon_0$  by the TOPAS software [38].

#### **2.4. Raman spectroscopy**

Raman spectra are recorded on a LabRam ARAMIS (Horiba JobinYvon, New Jersey) confocal Raman microscope with an excitation energy of 532 nm or 784 nm laser, where suitable laser (transparent region) is identified by the UV/Vis diffuse reflectance spectrum. A  $50\times$  objective, a moving grating of 1800 grooves/mm and a thermodynamically cooled CCD detector (Synapse,  $1024\times 256$  pixels) provide the spectral width of about  $3\text{ cm}^{-1}$  for 532 nm laser, and  $1\text{ cm}^{-1}$  for the 784 nm laser. The spectral positions are calibrated against the Raman mode of silicon at  $520.7\text{ cm}^{-1}$  before the measurement.

#### **2.5. UV/Vis diffuse reflectance spectroscopy**

UV/Vis diffuse reflectance spectra are recorded at room temperature on a Shimadzu UV-2600 (Shimadzu, Kyoto, Japan) spectrometer. Data are collected in the range between 190 nm to 850 nm with a step size of 1 nm.  $\text{BaSO}_4$  powder is used as the reference standard for baseline correction. The bandgap energies and the types of transition are determined using the RATD method described elsewhere [39].

#### **2.6. Thermogravimetric analysis**

TGA/DSC measurements are carried out using TGA/DSC 3+STARe System of Mettler Toledo. Each sample is measured with a heating rate of 10 K/min and a continuous  $\text{N}_2$  flow of



20 mL/min from 298 K to 1473 K. An amount of 10.0(1) mg of power sample is measured relative to an empty Al<sub>2</sub>O<sub>3</sub> crucible reference. The drift correction to the data is applied using an empty crucible measurement.

### 3. Results and Discussion

#### *Color shade*

Each solid solution of Y, Gd, Tb, Dy, Ho, Er, Tm, Yb, and Lu in the (Bi<sub>1-x</sub>M<sub>x</sub>)<sub>2</sub>O<sub>3</sub> series exhibits distinct colors that vary with the  $x$ -value, as shown in **figure S4.1** (Supplementary Information). An orange color is seen at lower  $x$ -values, while chromatic diversity appears for  $x \geq 0.10$ , with a yellowish hue at higher  $x$ -value. The color changes in the Y-series are consistent with previous reports [18].

#### *Microstructure*

Scanning electron micrographs (**Fig. S4.2 – S4.3**) show dense growth of micrometer-sized particles with irregular shapes and sizes. The calculated ACS exhibits a pseudo-linear relationship with the  $x$ -value (**Fig. S4.4a**), with a minimum of  $\sim 164(2)$  nm at  $x = 0.20$  and a maximum of  $\sim 290(4)$  nm at  $x = 0.23$  (**Tab. S4.1**). The low ACS at  $x = 0.20$  for Gd-series correlates with a high MS of 0.04(1) % (**Fig. S4.4b**), a trend also seen in  $x = 0.23$  for Tb-series.

#### *Crystal structure*

The pure  $\delta$ -phase appears in the Gd-, Tb-, Dy-, Ho-, Y-, Er-, Tm-, Yb-, and Lu-series at  $x = 0.13$ , 0.13, 0.13, 0.15, 0.18, 0.20, 0.20, 0.23, and 0.23, respectively (**Fig. S4.5 - S4.7**). All  $M$ -series solid solutions maintain the pure  $\delta$ -phase up to  $x = 0.25$  after meeting the initial  $x$ -value requirement for  $\delta$ -phase formation. The lowest possible composition for the  $\delta$ -phase formation is  $x = 0.13$ , with a pseudo-linear relationship observed between the  $x$ -value and the  $M^{3+}$  cation, indicating the amount of Bi<sup>3+</sup> substitution needed for the high-symmetry  $\delta$ -phase. Smaller  $M^{3+}$

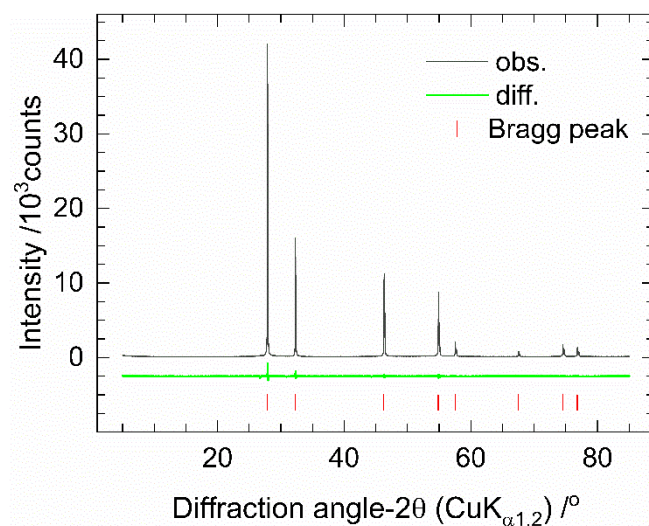


**Figure 4.2:** X-ray powder diffraction data Rietveld plot for pure  $\delta$ -phase at  $x = 0.13$  composition in  $(\text{Bi}_{1-x}\text{Gd}_x)_2\text{O}_3$ .

cations require higher  $\text{Bi}^{3+}$  substitution. Below the required  $x$ -value for  $\delta$ -phase, mixed  $\delta$ - and  $\beta$ -phase are present (**Tab. 4.1 and S4.2 – S4.9**). At  $x = 0.05$ , all solid solutions form a pure  $\beta$ -phase, as shown in the Rietveld refinement plot for the Gd-series at  $x = 0.05$  (**Fig. S4.8**), with associated structural parameters in **table 4.1**. In the  $\beta$ -phase, the lattice parameter ( $a$ ) increases while the  $c$ -lattice parameter decreases with the  $x$ -value (**Fig. S4.9**), reducing cell volume [40]. The opposite trend in lattice parameters of the  $\beta$ -phase with increasing  $x$ -value in solid solutions leads to the formation of the high-symmetry  $\delta$ -phase in each  $M$ -series. A representative Rietveld refinement plot for the  $\delta$ -phase at  $x = 0.13$  in the Gd-series is shown in **figure 4.2**, with structural parameters in **table 4.1**. Rietveld patterns for other  $M$ -series in the  $(\text{Bi}_{1-x}M_x)_2\text{O}_3$  solid solution for  $\delta$ -phase are in **figures S4.10 – S4.17**, and structural parameters for Tb, Dy, Ho, Y, Er, Tm, Yb, and Lu-series are in **tables S4.2 – S4.9**. **Figure 4.3** shows that the lattice parameter ( $a$ ) in the  $\delta$ -phase decreases linearly with increasing  $\text{Bi}^{3+}$  substitution ( $x$ -value). This trend indicates the incorporation of smaller  $M^{3+}$  cations in the  $(\text{Bi}_{1-x}M_x)_2\text{O}_3$  solid solution [37], as they share the same Wyckoff position. For example, at composition of  $x = 0.13$  for Gd-series,

**Table 4.1:** X-ray powder diffraction data Rietveld refined structural parameters for  $x = 0.05 - 0.25$  in  $(\text{Bi}_{1-x}\text{Gd}_x)_2\text{O}_3$ .

$x = 0.05$ , space group = $P4_2/nmc$						
Atom	Site	Occupancy	$x$	$y$	$z$	$B / 10^{-4} \text{ pm}^2$
Bi/Gd	8g	0.47/0.03(1)	0	0.256(1)	0.237(1)	1.41(3)
O1	8f	0.51(2)	0.300(3)	0.300(3)	0	2.10(3) <sup>a</sup>
O2	4d	0.42(2)	0	1/2	0.426(3)	2.10(3) <sup>a</sup>
O3	2a	0.11(3)	0	0	0	2.10(3) <sup>a</sup>
$x = 0.10$ , space group = $P4_2/nmc$ , $\beta$ -phase (%) = 36.8(2)						
Bi/Gd	8g	0.45/0.05(1)	0	0.251(1)	0.237(1)	1.58(3)
O1	8f	0.53(2)	0.305(3)	0.305(3)	0	3.10(3) <sup>b</sup>
O2	4d	0.39(2)	0	1/2	0.487(3)	3.10(3) <sup>b</sup>
O3	2a	0.10(3)	0	0	0	3.10(3) <sup>b</sup>
$x = 0.10$ , space group = $Fm\bar{3}m$ , $\delta$ -phase (%) = 63.2(2)						
Bi/Gd	24e	0.146/0.021(2)	0.055(2)	0	0	1.70(3)
O1	8c	0.020(2)	1/4	1/4	1/4	5.00(3) <sup>c</sup>
O2	32f	0.164(2)	0 292(3)	0 292(3)	0 292(3)	5.00(3) <sup>c</sup>
O3	48i	0.004(3)	1/2	0 320(3)	0 320(3)	5.00(3) <sup>c</sup>
$x = 0.13$ , space group = $Fm\bar{3}m$						
Bi/Gd	24e	0.142/0.024(1)	0.047(1)	0	0	1.67(2)
O1	8c	0.478(3)	1/4	1/4	1/4	2.60(3) <sup>d</sup>
O2	32f	0.049(1)	0 393(3)	0 393(3)	0 393(3)	2.60(3) <sup>d</sup>
O3	48i	0.012(3)	1/2	0 251(3)	0 251(3)	2.60(3) <sup>d</sup>
$x = 0.15$ , space group = $Fm\bar{3}m$						
Bi/Gd	24e	0.142/0.025(1)	0.045(1)	0	0	1.59(2)
O1	8c	0.465(3)	1/4	1/4	1/4	2.60(3) <sup>e</sup>
O2	32f	0.052(2)	0 371(3)	0 371(3)	0 371(3)	2.60(3) <sup>e</sup>
O3	48i	0.012(3)	1/2	0 251(3)	0 251(3)	2.60(3) <sup>e</sup>
$x = 0.25$ , space group = $Fm\bar{3}m$						
Bi/Gd	24e	0.125/0.042(1)	0.047(1)	0	0	1.67(2)
O1	8c	0.343(2)	1/4	1/4	1/4	5.20(1) <sup>f</sup>
O2	32f	0.083(2)	0 281(3)	0 281(3)	0 281(3)	5.20(1) <sup>f</sup>
O3	48i	0.013(3)	1/2	0 247(3)	0 247(3)	5.20(1) <sup>f</sup>

<sup>a,b,c,d,e,f</sup>Isotropic displacement parameter ( $B$ ) of O1, O2, and O3 with the same letter are linearly constraint to each other.

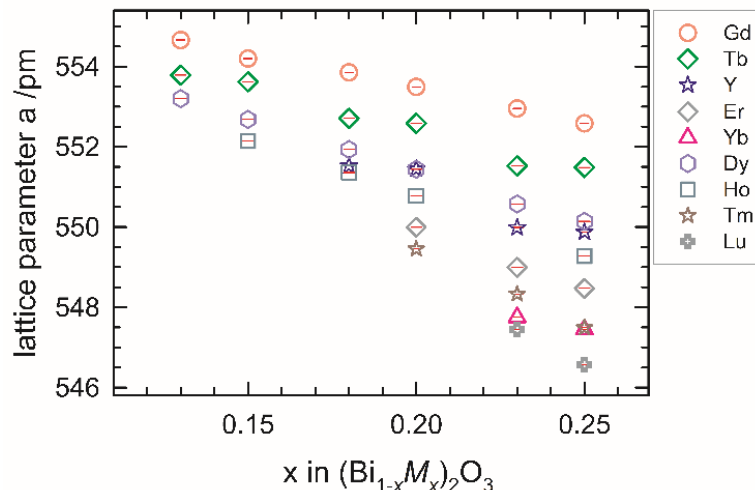


**Figure 4.3:** Evolution of the metric parameter ( $a$ ) with varying compositional  $x$  in  $(\text{Bi}_{1-x}\text{M}_x)_2\text{O}_3$ .

$a$  is 554.7(1) pm, about 2.1(1) pm larger than at  $x = 0.25$ . A similar trend is observed across all series, as shown in **figure 4.3**. For  $x = 0.25$ ,  $a$  values are 552.4(1) pm, 551.5(1) pm, 550.1(1) pm, 549.3(1) pm, 549.9(1) pm, 548.5(1) pm, 547.5(1) pm, 547.5(1) pm and 546.6(1) pm for Gd – Ho, Y, and Er – Lu series, respectively. The deviations between the initial  $\delta$ -phase composition and the last member ( $x = 0.25$ ) of the Tb-, Dy-, Ho-, Y-, Er-, Tm-, Yb-, and Lu-series are 2.3(1) pm, 2.8(1) pm, 2.9(1) pm, 1.6(1) pm, 1.5(1) pm, 2.0(1) pm, 0.3(1) pm, and 0.9(1) pm, respectively. The evaluated  $\langle \text{Bi}/\text{M}-\text{O} \rangle$  bond lengths for  $\delta$ -phase in all  $M$ -series are listed in **table S4.10**. The  $\langle \text{Bi}/\text{M}-\text{O}(1) \rangle$  bond length decreases linearly with increasing  $x$ -value (**Fig. 4.4**), while no clear trend is observed for  $\langle \text{Bi}/\text{M}-\text{O}(2) \rangle$  and  $\langle \text{Bi}/\text{M}-\text{O}(3) \rangle$  bond lengths (**Fig. S4.18** and **Tab. S4.10**). The  $\langle \text{Bi}/\text{M}-\text{O}(2) \rangle$  bond distances fluctuate within  $234 \pm 8$  pm, while  $\langle \text{Bi}/\text{M}-\text{O}(3) \rangle$  lengths are grouped into two ranges:  $250 \pm 10$  pm and  $200 \pm 10$  pm. This reflects the distorted sublattice positions of oxygen (O2, O3), with greater deviation at the interstitial O(3) position. The high isotropic displacement parameters (B) for O(2) and O(3) atoms further support the non-uniform ordering in the  $\delta$ -phase [41], and the O–O bond lengths exhibit irregular correlation even at 300 K [4, 40].

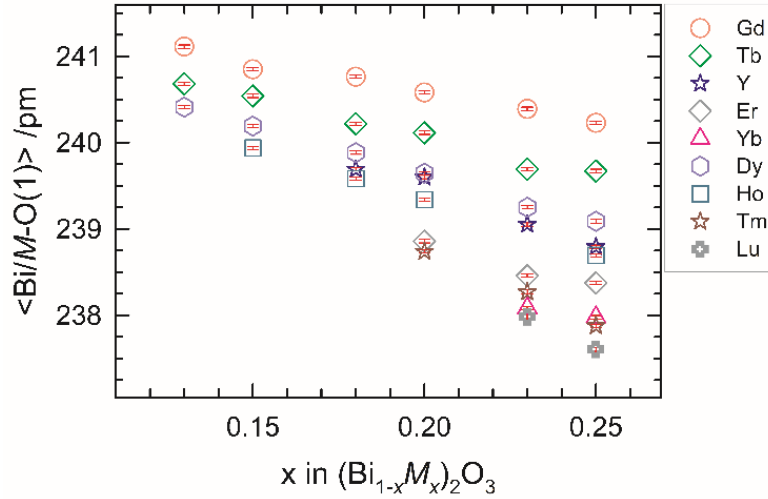


**Figure 4.4:** Evaluation of the  $\langle \text{Bi}/M\text{-O}(1) \rangle$  bond distances with varying the compositional  $x$ -value in  $(\text{Bi}_{1-x}\text{M}_x)_2\text{O}_3$  for different  $M$ -series.

### Spectroscopy

Accurate phase identification and positional disordering can be better understood through spectroscopic and diffraction techniques. Raman bands between  $110 \text{ cm}^{-1}$  and  $350 \text{ cm}^{-1}$  of low-symmetry phases are sharper than those of the  $\delta$ -phase [14, 42-44]. Minor phases in solid solut-

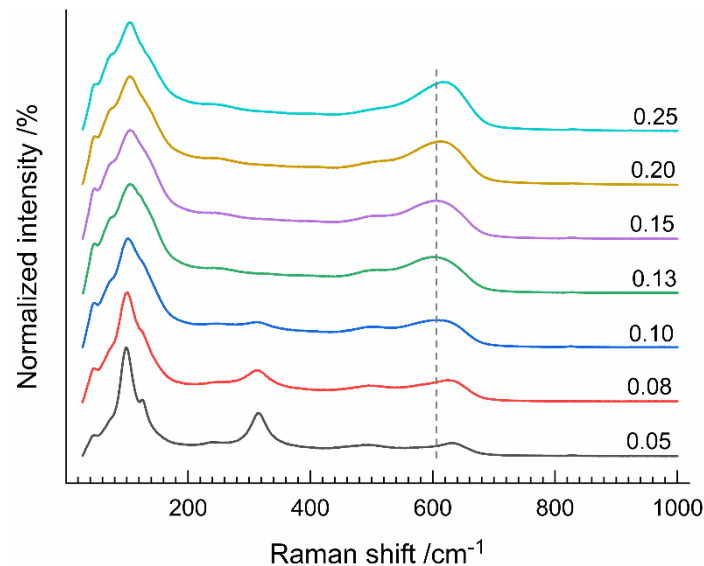


**Figure 4.5:** Raman spectra of  $(\text{Bi}_{1-x}\text{Gd}_x)_2\text{O}_3$  solid solutions with  $x$ -value ranging from 0.05 to 0.25, showing the blue shift of Bi-O stretching frequency (dotted line).

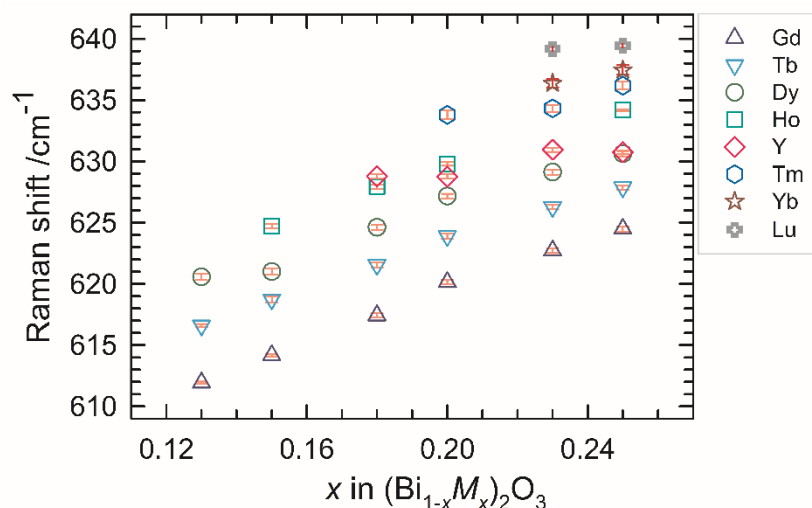


**Figure 4.6.** Variation of Bi–O stretching vibration frequencies with compositional  $x$ -value in  $(\text{Bi}_{1-x}\text{M}_x)_2\text{O}_3$  for all  $M$ -series.

ions can be identified by mapping these intense Raman bands [44, 45]. XRPD confirms the  $\beta$ -phase at  $x = 0.05$  in all  $M$ -series, while Raman spectra (**Fig. 4.5, S4.19 - S4.21**) probe phase identification and structural modifications. The  $\beta$ -phase shows Raman shifts at  $98(2) \text{ cm}^{-1}$ ,  $125(2) \text{ cm}^{-1}$ , and  $314(2) \text{ cm}^{-1}$  [46, 47], with the  $314(2) \text{ cm}^{-1}$  Raman band disappearing as the  $\delta$ -phase becomes dominant. This shift is attributed to Bi–O stretching in  $\text{BiO}_6$  octahedra in the  $\beta$ -phase [47]. The absence of this band indicates the pure  $\delta$ -phase, as observed in the Gd-series at  $x = 0.13$  (**Fig. 4.5**) and in other  $M$ -series (**Fig. S4.19 - S4.21**), matching XRPD analysis. The  $\delta$ -phase shows intense bands at  $104(2) \text{ cm}^{-1}$ , along with broad peaks between  $435(2) \text{ cm}^{-1}$  to  $692(2) \text{ cm}^{-1}$ , characteristic of the disorder in  $\text{BiO}_x$  polyhedra [42, 43, 48]. High-frequency bands are deconvoluted into two peaks, e.g.,  $498(2) \text{ cm}^{-1}$  and  $612(2) \text{ cm}^{-1}$  for Gd-series at  $x = 0.13$  (**Fig. S4.22**), where the  $498(2) \text{ cm}^{-1}$  band corresponds to asymmetric stretching and bending modes [44, 49], and the  $612(2) \text{ cm}^{-1}$  band to stretching of Bi–O bond [50-52]. The low-frequency bands at  $104(2) \text{ cm}^{-1}$ ,  $255(2) \text{ cm}^{-1}$ , and  $498(2) \text{ cm}^{-1}$  remain consistent across  $M$ -series (**Fig.4.5, S4.19 - S4.21**). A blue shift in the high-frequency band is observed from  $612(2) \text{ cm}^{-1}$  to  $625(2) \text{ cm}^{-1}$  as the composition changes from  $x = 0.13$  to 0.25 in the Gd-series

(**Fig. 4.6**). Blue shift of  $11\text{ cm}^{-1}$ ,  $10\text{ cm}^{-1}$ ,  $9\text{ cm}^{-1}$ ,  $2\text{ cm}^{-1}$ ,  $2\text{ cm}^{-1}$ , and  $1\text{ cm}^{-1}$  are observed in the Raman spectra from  $617(2)\text{ cm}^{-1}$ ,  $621(2)\text{ cm}^{-1}$ ,  $625(2)\text{ cm}^{-1}$ ,  $629(2)\text{ cm}^{-1}$ ,  $634(2)\text{ cm}^{-1}$ , and  $636(2)\text{ cm}^{-1}$  wavenumber for Tb-, Dy-, Ho-, Y-, Tm-, and Yb-series (**Fig. 4.6**). The Raman bands for shorter Bi–O (O2, O3) bonds dominates due to their higher covalency and polarizability [53]. Distortion in  $\text{BiO}_x$  polyhedra shifts the Bi–O stretching mode to higher wavenumbers [53]. The disorder in the oxygen sublattice increases the variation in Bi–O bond lengths, causing localized vibrations and broadening the Raman band in the high-frequency region [14, 43, 44, 48]. The characteristic  $M$ –O vibration of  $M_2\text{O}_3$  between  $350\text{ cm}^{-1}$  and  $395\text{ cm}^{-1}$  is obscured in Raman spectra [54].

A representative UV/Vis diffuse reflectance spectrum for the Gd-series at  $x = 0.13$  is shown in **figure 4.7**, with spectra for other  $M$ -series in **figures S4.23 – S4.27**. Tauc’s [55] and DASF [56] methods are used to calculate the electronic bandgap for each  $M$ -series, while RATD analysis helps determine the transition type and bandgap energy (**Tab. 4.2, S4.11, S4.12**). A direct bandgap of  $E_g = 2.68(2)\text{ eV}$  at  $x = 0.13$  for Gd-series, calculated by DASF, compares with a direct transition  $E_d = 2.73(3)\text{ eV}$  from Tauc’s analysis. The possible indirect transition bandgap energy  $E_i = 2.24(3)\text{ eV}$  significantly different from  $E_g$ . The same strategy is used to calculate  $E_g$ , with values listed in **table 4.2** for  $x = 0.05 – 0.25$ , suggesting a direct transition in the Gd-series. Similarly, other solid solutions of Y, Tb, Dy, Tm, Yb, and Lu show direct bandgap transitions (**Tab. S4.11, S4.12**). However, the  $E_g$  transition type in the Ho- and Er-series is unidentified due to additional electronic absorption bands, making separation from bandgap transition energy difficult in the DASF method (**Fig. S4.29, S4.30**). Only the  $E_d$  and  $E_i$  are calculated by Tauc’s analysis, and values are listed in **table 4.13**. The bandgap energy slightly increases with increasing  $x$ -value in  $(\text{Bi}_{1-x}\text{M}_x)_2\text{O}_3$ , as shown in **figure 4.8** and **S4.30**.  $E_g$

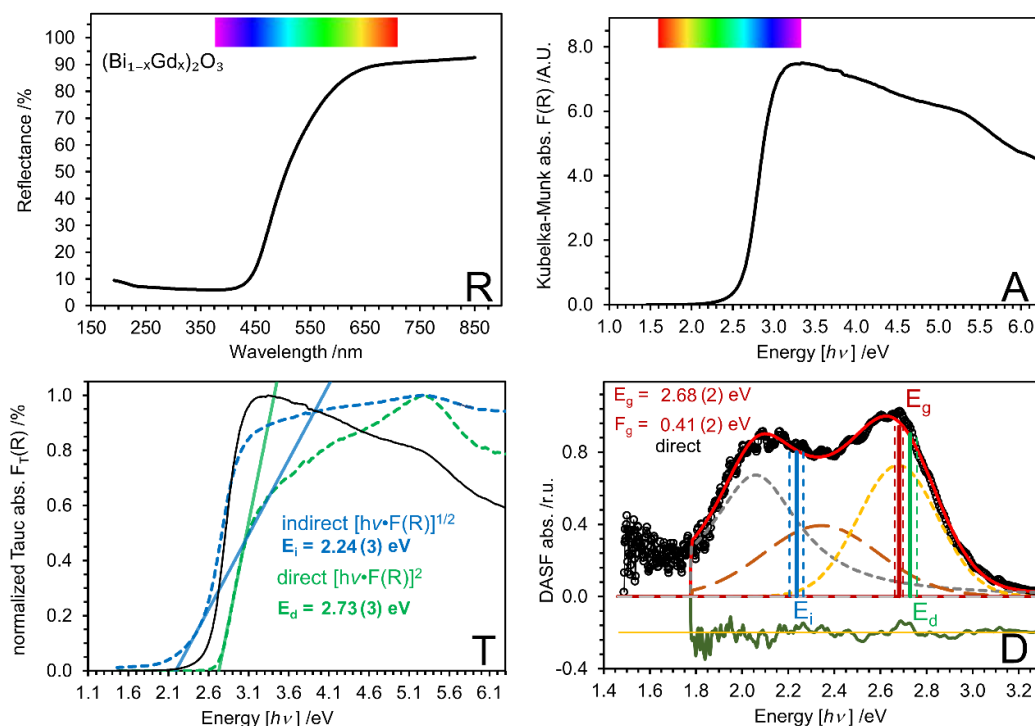


**Figure 4.7:** UV/Vis RATD plot containing reflectance spectrum (R), calculated absorbance spectrum (A), bandgap energies ( $E_g$ ) determined using the DASF method (D) and Tauc analysis (T) for direct ( $E_d$ ) and indirect ( $E_i$ ) transitions in  $(\text{Bi}_{1-x}\text{Gd}_x)_2\text{O}_3$  for  $x = 0.13$  composition.

reaches a plateau at 2.75(4) eV for the pure  $\delta$ -phase, corresponding to the reported direct bandgap energy [18, 31, 57].  $E_g$  for the  $\beta$ -phase is lower than that of the  $\delta$ -phase, with the dotted line in **figure 4.8** and **S4.30** representing the phase boundary at the corresponding  $x$ -value of  $M$ -series. In addition to  $E_g$ , an absorption band between 2.00(2) eV and 2.45(3) eV is identified in the DASF spectrum (**Fig. 4.7D** and **S4.23D – S4.27D**), which is assigned to anion defect transition energy ( $E^d$ ).  $E^d$  is a characteristic feature of the  $\delta$ -phase, linked to high ionic disorder in the oxide lattice (oxygen vacancy) [7, 8, 14, 58]. The variation of  $E^d$  in  $(\text{Bi}_{1-x}\text{M}_x)_2\text{O}_3$  solid solutions (**Fig. 4.8** and **S4.30**) shows a pseudo-Voigt type distribution, with peak maxima appearing at the pure  $\delta$ -phase. The low symmetric  $\beta$ -phase is closely related to the high symmetric  $\delta$ -phase, where the vacant oxygen sites are fully ordered [3].



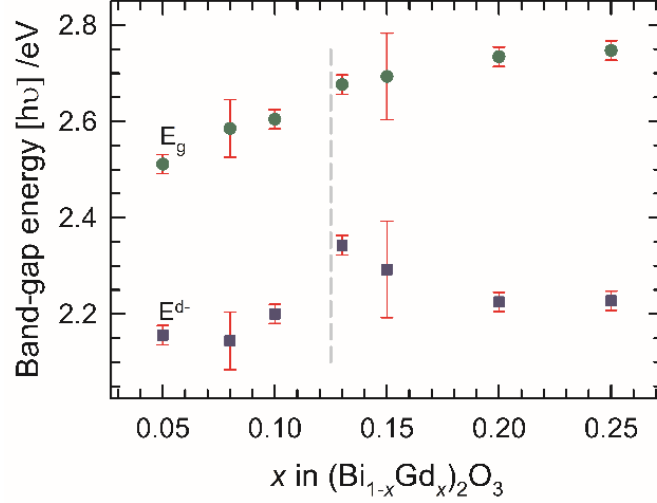


**Figure 4.8:** Determined  $E_g$  (circle, bandgap) and  $E^{d-}$  (square, anionic defect) transition energies for the  $(\text{Bi}_{1-x}\text{Gd}_x)_2\text{O}_3$  solid solution as a variation of  $x$ -value, with the dotted line denoting the phase boundary between  $\beta$ - and  $\delta$ -phases.

**Table 4.2:** Bandgap energies calculated from UV/Vis diffuse reflectance spectroscopic data of  $(\text{Bi}_{1-x}\text{Gd}_x)_2\text{O}_3$  using the RATD methods [39]. Respective value for  $x = 0$  is taken from the given literature.

$x$	DASF fitting			Tauc fitting		Type
	$E_g/\text{eV}$	$F_g/\text{eV}$	$E^{d-}/\text{eV}$	$E_d/\text{eV}$	$E_i/\text{eV}$	
0	--	--	--	--	2.50 [59]	Indirect
0	--	--	--	3.55 [57]	--	Direct
0.05	2.51(2)	0.51(2)	2.16(2)	2.58(3)	2.09(3)	Direct
0.08	2.59(5)	0.48(4)	2.14(6)	2.63(3)	2.14(3)	Direct
0.10	2.60(2)	0.53(2)	2.20(2)	2.72(3)	2.14(3)	Direct
0.13	2.68(2)	0.41(2)	2.34(2)	2.73(3)	2.24(3)	Direct
0.15	2.69(8)	0.46(8)	2.29(9)	2.77(3)	2.18(3)	Direct
0.20	2.73(2)	0.36(2)	2.22(2)	2.78(3)	2.16(3)	Direct
0.25	2.75(2)	0.39(2)	2.23(2)	2.79(3)	2.15(3)	Direct

$E_g$ ,  $E^{d-}$  and  $F_g$  refer to bandgap energy, anionic defect transition, and band flatness, respectively, obtained from the fitting of the DASF plots.  $E_d$  and  $E_i$ , respectively, represent direct and indirect transition energies determined from the Tauc plots.

### Thermal analysis

Thermogravimetric analysis and respective DSC curves for  $(\text{Bi}_{1-x}\text{M}_x)_2\text{O}_3$  solid solutions at  $x = 0.25$  are shown in **figure 4.9**. The first inflection point in TGA data marks the onset decomposition temperature at 1482(2) K, 1486(2) K, 1468(2) K, 1502(2) K, 1482(2) K, 1479(2) K, 1478(2) K, and 1460(2) K for Gd, Tb, Ho, Y, Er, Tm, Yb, and Lu, respectively. The decomposition temperature slightly decreases with a smaller cationic radius from  $\text{Gd}^{3+}$  to  $\text{Lu}^{3+}$ , reflecting the bond strength of the M–O bond [60]. The heat flow curves show an additional endothermic peak around 873 K, before the decomposition temperature, indicating an order  $\leftrightarrow$  disorder structural modification in  $\delta$ -phase [41].

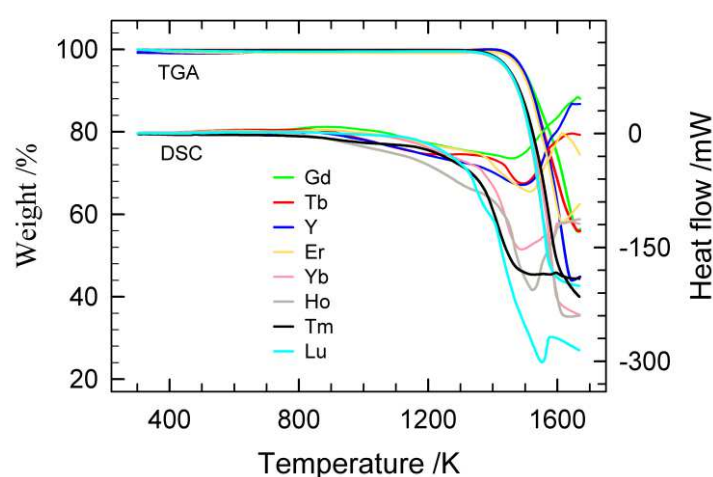


**Figure 4.9:** Thermogravimetric analysis of  $(\text{Bi}_{1-x}\text{M}_x)_2\text{O}_3$  solid solution at  $x = 0.25$  composition for  $M = \text{Y}$  and Gd - Lu.

### 4. Conclusions

The high temperature metastable  $\delta$ - $\text{Bi}_2\text{O}_3$  is stabilized at ambient condition by substituting  $\text{Bi}^{3+}$  cation by some rare-earth cations. The amount of substitution depends on the size of the RE-cation. By replacing the  $\text{Bi}^{3+}$  by the RE-cation the solid solutions gradually transform from low-symmetry into high-symmetry phase along with redistribution of the oxygen positions. The phase purity of each sample is confirmed by X-ray powder diffraction and complemented

by Raman spectroscopy. The characteristic Bi–O vibration in the  $\beta$ - and  $\delta$ -phase clearly separates the phase boundary for compositional  $x$ -value. The electronic transition calculated by the DASF approach indicates the oxygen vacancy. Band gap has reached a plateau at 2.75(4) eV for all nine investigated series. The low bandgap and the oxygen disordering in these solid solutions could be interesting materials for photocatalysis and solid state electrolysis.

## References

- [1] S. Hui, J. Roller, S. Yick, X. Zhang, C. Decès-Petit, Y. Xie, R. Maric, D. Ghosh, A brief review of the ionic conductivity enhancement for selected oxide electrolytes, *J. Power Sources* 172(2) (2007) 493-502. Doi:10.1016/j.jpowsour.2007.07.071
- [2] H.A. Harwig, J.W. Weenk, Phase relations in bismuthsesquioxide, *Z. anorg. allg. Chem.* 444 (1978) 167-177. Doi:10.1002/zaac.19784440119
- [3] H.A. Harwig, On the structure of bismuthsesquioxide: the  $\alpha$ ,  $\beta$ ,  $\gamma$ , and  $\delta$ -phase, *Z. anorg. allg. Chem.* 444 (1978) 151-166. Doi:10.1002/zaac.19784440118
- [4] M. Gambino, F. Giannici, A. Longo, S.D. Tommaso, F. Labat, A. Martorana, Dopant clusterization and oxygen coordination in Ta-doped bismuth oxide: a structural and computational insight into the mechanism of anion conduction, *J. Phys. Chem. C* 119(47) (2015) 26367-26373. Doi:10.1021/acs.jpcc.5b09449
- [5] S. Hull, S.T. Norberg, M.G. Tucker, S.G. Eriksson, C.E. Mohn, S. Stølen, Neutron total scattering study of the  $\delta$  and  $\beta$  phases of  $\text{Bi}_2\text{O}_3$ , *Dalton Trans.* (40) (2009) 8737-8745. Doi:10.1039/B910484B
- [6] N. Sammes, G. Tompsett, H. Näfe, F. Aldinger, Bismuth based oxide electrolytes—structure and ionic conductivity, *J. Eur. Ceram. Soc.* 19(10) (1999) 1801-1826. Doi:10.1016/S0955-2219(99)00009-6
- [7] P. Shuk, H.-D. Wiemhöfer, U. Guth, W. Gijpeld, M. Greenblatt, Oxide ion conducting solid electrolytes based on  $\text{Bi}_2\text{O}_3$ , *Solid State Ionics* 89 (1996) 179-196. Doi:10.1016/0167-2738(96)00348-7
- [8] D.S. Aidhy, J.C. Nino, S.B. Sinnott, E.D. Wachsman, S.R. Phillpot, Vacancy-ordered structure of cubic bismuth oxide from simulation and crystallographic analysis, *J. Am. Ceram. Soc.* 91(7) (2008) 2349-2356. Doi:10.1111/j.1551-2916.2008.02463.x
- [9] M. Leszczynska, X. Liu, W. Wrobel, M. Malys, M. Krynski, S.T. Norberg, S. Hull, F. Krok, I. Abrahams, Thermal variation of structure and electrical conductivity in  $\text{Bi}_4\text{YbO}_{7.5}$ , *Chem. Mater.* 25(3) (2013) 326-336. Doi:10.1021/cm302898m
- [10] A. Matsumoto, Y. Koyama, I. Tanaka, Structures and energetics of  $\text{Bi}_2\text{O}_3$  polymorphs in a defective fluorite family derived by systematic first-principles lattice dynamics calculations, *Phys. Rev. B* 81(9) (2010) 094117. Doi:10.1103/PhysRevB.81.094117

- [11] S.F. Radaev, V.I. Simonov, Structural features of  $\gamma$ -phase  $\text{Bi}_2\text{O}_3$  and its place in the sillenite family, *Acta Cryst. B* 48 (1992) 604-609. Doi:10.1107/S0108768192003847
- [12] G. Malmros, The crystal structure of  $\alpha$ - $\text{Bi}_2\text{O}_3$ , *Acta Chem. Scand* 24 (1970) 384-396. Doi:10.3891/acta.chem.scand.24-0384
- [13] J.C. Boivin, G. Mairesse, Recent material developments in fast oxide ion conductors, *Chem. Mater.* 10(10) (1998) 2870-2888. Doi:10.1021/cm980236q
- [14] M.I. Hossain, M.M. Murshed, T.M. Gesing, Indium containing sillenite semiconductor: Synthesis, structural, spectroscopic and thermogravimetric analysis, *J. Am. Ceram. Soc.* 106(10) (2023) 6268-6278. Doi:10.1111/jace.19231
- [15] J. Ducke, M. Trömel, D. Hohlwein, P. Kizler, Yttrium and titanium bismuthates with structures related to  $\beta$ - $\text{Bi}_2\text{O}_3$ , *Acta Cryst.* 52(6) (1996) 1329-1331. Doi:10.1107/S0108270195011267
- [16] P.D. Battle, C.R.A. Catlow, J. Drennan, A.D. Murray, The structural properties of the oxygen conducting  $\delta$  phase of  $\text{Bi}_2\text{O}_3$ , *J. Phys. C: Solid State Phys.* 16(17) (1983) L561-L566. Doi:10.1088/0022-3719/16/17/003
- [17] P.D. Battle, C.R.A. Catlow, J.W. Heap, L.M. Moroney, Structural and dynamical studies of  $\delta$ - $\text{Bi}_2\text{O}_3$  oxide ion conductors: I. The structure of  $(\text{Bi}_2\text{O}_3)_{1-x}(\text{Y}_2\text{O}_3)_x$  as a function of  $x$  and temperature, *J. Solid State Chem.* 63(1) (1986) 8-15. Doi:10.1016/0022-4596(86)90146-5
- [18] X. Liu, A. Staubitz, T.M. Gesing, Thermochromic behavior of yttrium-substituted bismuth oxides, *ACS Appl. Mater. Interfaces* 11(36) (2019) 33147-33156. Doi:10.1021/acsami.9b11450
- [19] R.K. Datta, J.P. Meehan, The system  $\text{Bi}_2\text{O}_3$ - $\text{R}_2\text{O}_3$  (R= Y, Gd), *Z. Anorg. Allg. Chem.* 383(3) (1971) 328-337.
- [20] Y.-C. Wu, Y.-T. Huang, H.-Y. Yang, Crystallization mechanism and photocatalytic performance of vanadium-modified bismuth oxide through precipitation processes at room temperature, *CrystEngComm* 18(36) (2016) 6881-6888. Doi:10.1039/C6CE00954A
- [21] H. Sudrajat, Chemical state and local structure of V species incorporated in  $\delta$ - $\text{Bi}_2\text{O}_3$  photocatalysts, *J. Mater. Sci.* 53(2) (2018) 1088-1096. Doi:10.1007/s10853-017-1565-9
- [22] Y. Lu, L. Chen, Y. Huang, H. Cheng, S.I. Kim, H.J. Seo, Optical properties and visible light-driven photocatalytic activity of  $\text{Bi}_{11}\text{VO}_{19}$  nanoparticles with  $\delta$ - $\text{Bi}_2\text{O}_3$ -structure, *J. Alloys Compd.* 640 (2015) 226-232. Doi:10.1016/j.jallcom.2015.04.046
- [23] H. Sudrajat, S. Hartuti, Boosting electron population in  $\delta$ - $\text{Bi}_2\text{O}_3$  through iron doping for improved photocatalytic activity, *Advanced Powder Technology* 30(5) (2019) 983-991. Doi:10.1016/j.appt.2019.02.012
- [24] Y.-C. Wu, Y.-W. Chang, S.-F. Wang, Electrical properties and microstructural analysis of aliovalent-ion ( $\text{Y}^{3+}$ ,  $\text{Nb}^{5+}$ )-doped bismuth-based solid-oxide electrolyte, *Ferroelectrics* 455(1) (2013) 123-128. Doi:10.1080/00150193.2013.845486
- [25] T. Kikuchi, Y. Kitami, M. Yokoyama, H. Sakai, Pseudo-binary system  $\text{Bi}_2\text{O}_3$ - $\text{TeO}_2$  in air, *J. Mater. Sci.* 24 (1989) 4275-4278. Doi:10.1007/BF00544499
- [26] G.A. Lovas, I. Dódonny, L. Pöppl, Z. Szaller, On the phase transitions of  $\text{Bi}_2\text{Te}_4\text{O}_{11}$ , *J. Solid State Chem.* 135(2) (1998) 175-181. Doi:10.1006/jssc.1997.7594

- [27] S.E. Lin, W.C.J. Wei, Long-term degradation of Ta<sub>2</sub>O<sub>5</sub>-doped Bi<sub>2</sub>O<sub>3</sub> systems, *J. Eur. Ceram. Soc.* 31(16) (2011) 3081-3086. Doi:10.1016/j.jeurceramsoc.2011.04.015
- [28] L. Bourja, B. Bakiz, A. Benlhachemi, M. Ezahri, J.C. Valmalette, S. Villain, J.R. Gavarrí, Structural and raman vibrational studies of CeO<sub>2</sub>-Bi<sub>2</sub>O<sub>3</sub> oxide system, *Adv. Mater. Sci. Eng.* 2009 (2009) 1-4. Doi:10.1155/2009/502437
- [29] Y. Huang, G. Zhou, D. Wei, Z. Fan, H.J. Seo, Phase-formation and luminescence properties of Eu<sup>3+</sup>-doped Bi<sub>2</sub>O<sub>3</sub> on synthetic process, *J. Lumin.* 220 (2020) 116970. Doi:10.1016/j.jlumin.2019.116970
- [30] N.O. Kalaycioglu, E. Çırçır, Measurement and properties of the oxide ionic conductivity of  $\beta$ - and  $\delta$ -Phases in the binary (Bi<sub>2</sub>O<sub>3</sub>)<sub>1-x</sub>(Tb<sub>4</sub>O<sub>7</sub>)<sub>x</sub> system, *Synthesis and Reactivity in Inorganic, Metal-Organic, and Nano-Metal Chemistry* 42(3) (2012) 398-401. Doi:10.1080/15533174.2011.611565
- [31] S. Bandyopadhyay, A. Dutta, Thermal, optical and dielectric properties of phase stabilized  $\delta$ -Dy-Bi<sub>2</sub>O<sub>3</sub> ionic conductors, *J. Phys. Chem. Solids* 102 (2017) 12-20. Doi:10.1016/j.jpcs.2016.11.001
- [32] A. Concha-Balderrama, H.A. Martinez-Rodriguez, G. Rojas-George, H.E. Esparza-Ponce, V. Orozco-Carmona, P. Pizá-Ruiz, M.H. Bocanegra-Bernal, A. Reyes-Rojas, Enhanced Ionic transport and compressive residual stress in Er-doped Bi<sub>2</sub>O<sub>3</sub> with lower Er<sup>3+</sup> concentrations, *J. Electron. Mater.* 47 (2018) 5422-5432. Doi:10.1007/s11664-018-6441-0
- [33] A. Dapčević, D. Poleti, J. Rogan, A. Radojković, M. Radović, G. Branković, A new electrolyte based on Tm<sup>3+</sup>-doped  $\delta$ -Bi<sub>2</sub>O<sub>3</sub>-type phase with enhanced conductivity, *Solid State Ionics* 280 (2015) 18-23. Doi:10.1016/j.ssi.2015.08.004
- [34] H.O. Torun, S. Cakar, E. Ersoy, O. Turkoglu, The bulk electrical conductivity properties of  $\delta$ -Bi<sub>2</sub>O<sub>3</sub> solid electrolyte system doped with Yb<sub>2</sub>O<sub>3</sub>, *J. Therm. Anal. Calorim.* 122 (2015) 525-536. Doi:10.1007/s10973-015-4785-8
- [35] E. Öztürk, N.O. Kalaycioglu, Synthesis, characterization and oxide ionic conductivity of binary  $\delta$ -(Bi<sub>2</sub>O<sub>3</sub>)<sub>1-x</sub>(Lu<sub>2</sub>O<sub>3</sub>)<sub>x</sub> system, *J. Chin. Chem. Soc.* 60(6) (2013) 605-607. Doi:10.1002/jccs.201200540
- [36] P. Meenakshi, K. Promila, U. Sitharaman, R. Nagarajan, Evaluation of solid solution formation between ThO<sub>2</sub> and  $\delta$ -Bi<sub>2</sub>O<sub>3</sub> by molecular precursor route, *Mater. Res. Bull.* 107 (2018) 66-73. Doi:10.1016/j.materresbull.2018.07.001
- [37] R.D. Shannon, Revised effective ionic radii and systematic studies of interatomic distances in halides and chalcogenides, *Acta Cryst.* A32 (1976) 751-767. Doi:10.1107/S0567739476001551
- [38] D. Balzar, N. Audebrand, M.R. Daymond, A. Fitch, A. Hewat, J.I. Langford, A.L. Bail, D. Louër, O. Masson, C.N. McCowan, N.C. Popa, P.W. Stephens, B.H. Toby, Size-strain line-broadening analysis of the ceria round-robin sample, *J. Appl. Crystallogr.* 37(6) (2004) 911-924. Doi:10.1107/s0021889804022551
- [39] T.M. Gesing, M.M. Murshed, S. Schuh, O. Thüringer, K. Krämer, T. Neudecker, C.B. Mendive, L. Robben, Nano-crystalline precursor formation, stability, and transformation to mullite-type visible-light photocatalysts, *J. Mater. Sci.* (2022) 1-20. Doi:10.1007/s10853-022-07854-w

- [40] P. Goel, M.K. Gupta, R. Mittal, S.J. Skinner, S. Mukhopadhyay, S. Rols, S.L. Chaplot, Phonons and oxygen diffusion in  $\text{Bi}_2\text{O}_3$  and  $(\text{Bi}_{0.7}\text{Y}_{0.3})_2\text{O}_3$ , *J. Phys.: Condens. Matter* 32(33) (2020) 334002. Doi:10.1088/1361-648X/ab88f8
- [41] S. Boyapati, E.D. Wachsman, B.C. Chakoumakos, Neutron diffraction study of occupancy and positional order of oxygen ions in phase stabilized cubic bismuth oxides, *Solid State Ionics* 138(3-4) (2001) 293-304. Doi:10.1016/S0167-2738(00)00792-X
- [42] M. Ahila, E. Subramanian, D.P. Padiyan, Influence of annealing on phase transformation and specific capacitance enhancement in  $\text{Bi}_2\text{O}_3$ , *J. Electroanal. Chem.* 805 (2017) 146-158. Doi:10.1016/j.jelechem.2017.10.037
- [43] R. Sharma, N. Benshalom, M. Asher, T.M. Brenner, A. Kossi, O. Yaffe, R. Korobko, Dynamic disorder in Bi sub-lattice of  $\delta\text{-Bi}_2\text{O}_3$ , *Cond-mat.mtrl-sci* (2022) 1-6. Doi:10.48550/arXiv.2205.13289
- [44] A. Rubbens, M. Drache, P. Roussel, J.P. Wignacourt, Raman scattering characterization of bismuth based mixed oxides with  $\text{Bi}_2\text{O}_3$  related structures, *Mater. Res. Bull.* 42(9) (2007) 1683-1690. Doi:10.1016/j.materresbull.2006.11.036
- [45] S.C. Hebert, K. Stowe, Synthesis and Characterization of Bismuth-Cerium Oxides for the Catalytic Oxidation of Diesel Soot, *Materials* 13(6) (2020) 1369. Doi:10.3390/ma13061369
- [46] A.L. Pereira, J.A. Sans, R. Vilaplana, O. Gomis, F. Manjón, P. Rodríguez-Hernández, A. Muñoz, C. Popescu, A. Beltran, Isostructural second-order phase transition of  $\beta\text{-Bi}_2\text{O}_3$  at high pressures: an experimental and theoretical study, *J. Phys. Chem. C* 118(40) (2014) 23189-23201. Doi:10.1021/jp507826j
- [47] C. Díaz-Guerra, P. Almodóvar, M. Camacho-López, S. Camacho-López, J. Piqueras, Formation of  $\beta\text{-Bi}_2\text{O}_3$  and  $\delta\text{-Bi}_2\text{O}_3$  during laser irradiation of Bi films studied in-situ by spatially resolved Raman spectroscopy, *J. Alloys Compd.* 723 (2017) 520-526. Doi:10.1016/j.jallcom.2017.06.263
- [48] R.J. Betsch, W.B. White, Vibrational spectra of bismuth oxide and the sillenite-structure bismuth oxide derivatives, *Spectrochim. Acta A Mol. Biomol. Spectrosc.* 34(5) (1978) 505-514. Doi:10.1016/0584-8539(78)80047-6
- [49] A. Pereira, O. Gomis, J. Sans, J. Pellicer-Porres, F. Manjón, A. Beltran, P. Rodríguez-Hernández, A. Muñoz, Pressure effects on the vibrational properties of  $\alpha\text{-Bi}_2\text{O}_3$ : an experimental and theoretical study, *J. Phys.: Condens. Matter* 26(22) (2014) 225401. Doi:10.1088/0953-8984/26/22/225401
- [50] S. Saha, S. Chanda, A. Dutta, U. Kumar, R. Ranjan, T. Sinha, Dielectric relaxation and anti-ferromagnetic coupling of  $\text{BiEuO}_3$  and  $\text{BiGdO}_3$ , *Journal of magnetism and magnetic materials* 360 (2014) 80-86. Doi:10.1016/j.jmmm.2014.01.075
- [51] L. Ermakova, V. Strekalovskii, E. Vovkotrub, V. Bamburov, Structural Transformations in a  $\text{Bi}_2\text{O}_3$  Crystal and in  $\text{Bi}_2\text{O}_3$ -Based Solid Solutions in the Temperature Interval 25–750°C, *J. Appl. Spectrosc.* 69 (2002) 152-154. Doi:10.1023/A:1015396716886
- [52] S. Bandyopadhyay, A. Dutta, Microstructural interpretation of vibrational properties and ionic transport mechanism in Dy stabilized  $\delta\text{-Bi}_2\text{O}_3$ , *J. Alloys Compd.* 682 (2016) 80-88. Doi:10.1016/j.jallcom.2016.04.256

- [53] F. D.Hardcastle, I. E.Wachs, The molecular structure of bismuth oxide by Raman spectroscopy, *J. Solid State Chem.* 97(2) (1992) 319-331. Doi:10.1016/0022-4596(92)90040-3
- [54] A. Ubaldini, M.M. Carnasciali, Raman characterisation of powder of cubic RE<sub>2</sub>O<sub>3</sub> (RE= Nd, Gd, Dy, Tm, and Lu), Sc<sub>2</sub>O<sub>3</sub> and Y<sub>2</sub>O<sub>3</sub>, *J. Alloys Compd.* 454(1-2) (2008) 374-378. Doi:10.1016/j.jallcom.2006.12.067
- [55] J. Tauc, R. Grigorovici, A. Vancu, Optical properties and electronic structure of amorphous germanium, *Phys. Status Solidi B* 15(2) (1966) 627-637. Doi:10.1002/pssb.19660150224
- [56] D. Souri, Z.E. Tahan, A new method for the determination of optical band gap and the nature of optical transitions in semiconductors, *Appl. Phys. B* 119(2) (2015) 273-279. Doi:10.1007/s00340-015-6053-9
- [57] J. Xie, L. Li, C. Tian, C. Han, D. Zhao, Template-free synthesis of hierarchical constructed flower-like  $\delta$ -Bi<sub>2</sub>O<sub>3</sub> microspheres with photocatalytic performance, *Micro Nano Lett.* 7(7) (2012) 651-653. Doi:10.1049/mnl.2012.0201
- [58] H. Deng, W. Hao, H. Xu, C. Wang, Effect of intrinsic oxygen vacancy on the electronic structure of  $\gamma$ -Bi<sub>2</sub>O<sub>3</sub>: First-principles calculations, *J. Phys. Chem. C* 116(1) (2012) 1251-1255. Doi:10.1021/jp2086895
- [59] J. Zhang, Q. Han, X. Wang, J. Zhu, G. Duan, Synthesis of  $\delta$ -Bi<sub>2</sub>O<sub>3</sub> microflowers and nanosheets using CH<sub>3</sub>COO(BiO) self-sacrifice precursor, *Mater. Lett.* 162 (2016) 218-221. Doi:10.1016/j.matlet.2015.10.024
- [60] J.G. Speight, *Lange's handbook of chemistry*, 17 ed., McGraw-Hill Education 2017.

## Supplementary Information

### Stabilization of $(\text{Bi}_{1-x}\text{M}_x)_2\text{O}_3$ delta phase with rare-earth cations: structural, spectroscopic and thermal investigations for $M = \text{Y}$ , $\text{Gd}$ , $\text{Tb}$ , $\text{Dy}$ , $\text{Ho}$ , $\text{Er}$ , $\text{Tm}$ , $\text{Yb}$ , and $\text{Lu}$

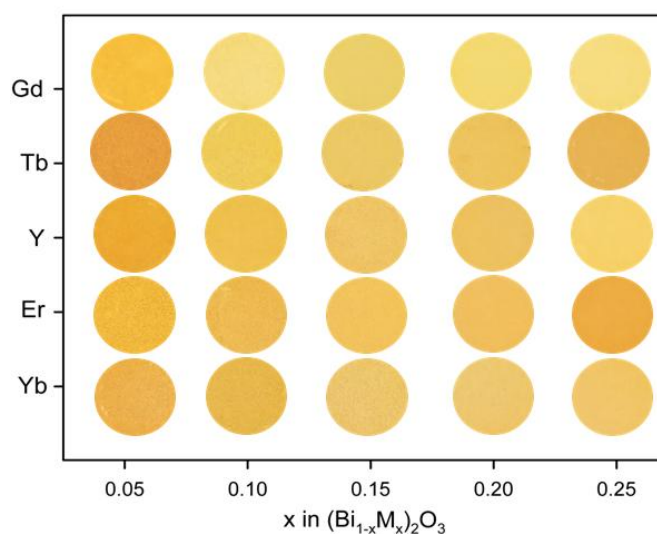


**Figure S4.1:** Selective sample color variation in  $(\text{Bi}_{1-x}\text{M}_x)_2\text{O}_3$  for  $x = 0.05 - 0.25$ .

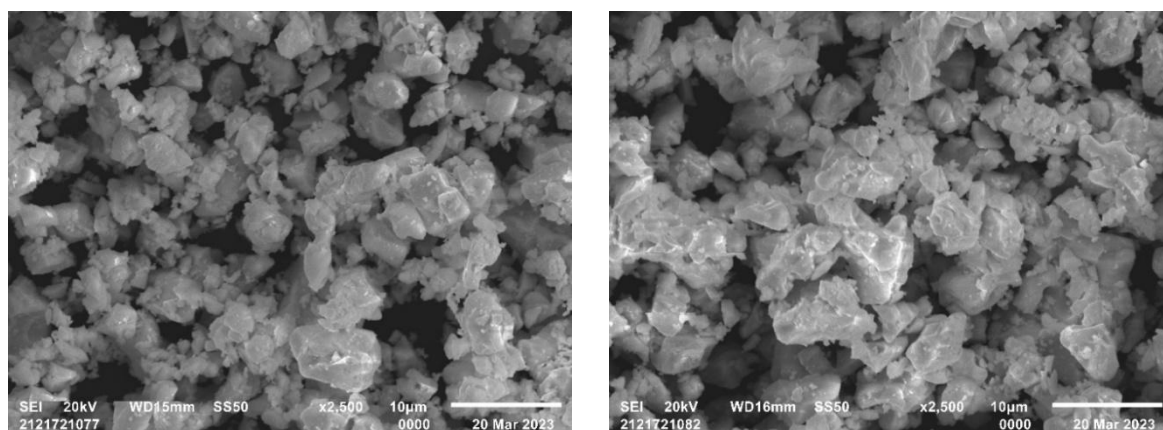


**Figure S4.2:** Scanning electron micrographs of  $(\text{Bi}_{1-x}\text{M}_x)_2\text{O}_3$  for  $M = \text{Gd}$  (left) and  $\text{Tb}$  (right) at  $x = 0.15$ .



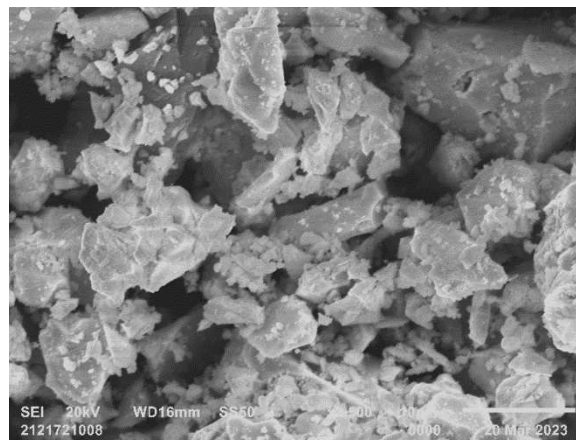
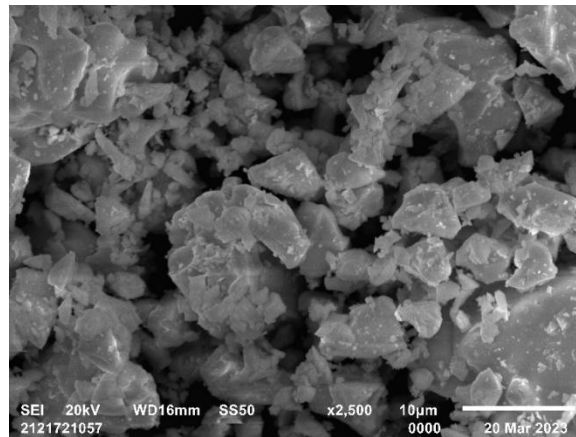
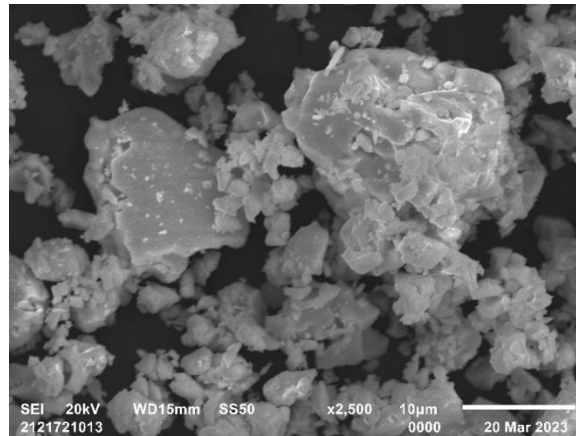


**Figure S4.3:** Scanning electron micrographs of  $(\text{Bi}_{1-x}\text{M}_x)_2\text{O}_3$  for  $M = \text{Y}$  (up), Er, and Yb (down) at  $x = 0.15$ .

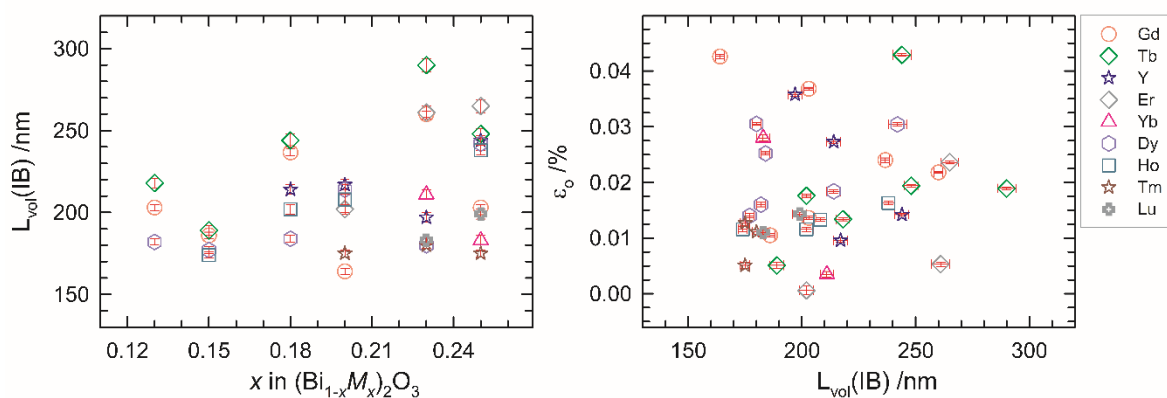


**Figure S4.4:** Variation of average crystallite size ( $L_{\text{vol}}(\text{IB})$ ) and micro-strain ( $\epsilon_0$ ) as a function of compositional changes in  $(\text{Bi}_{1-x}\text{M}_x)_2\text{O}_3$  for the pure  $\delta$ -phase.

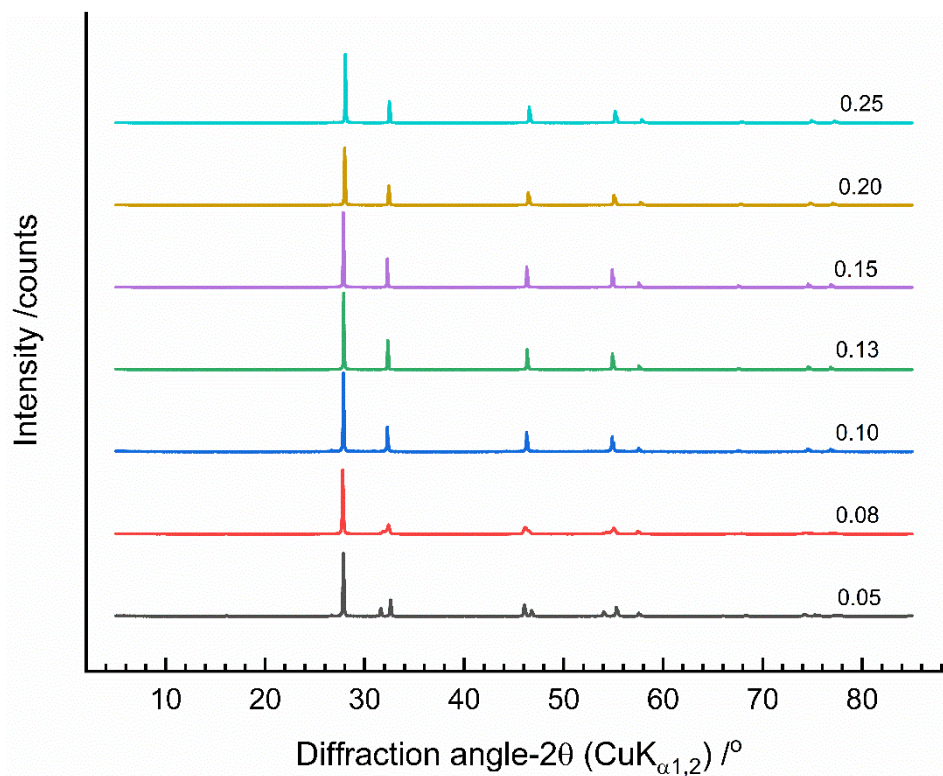


**Figure S4.5:** X-ray powder diffraction patterns for the Gd-series of  $(\text{Bi}_{1-x}\text{Gd}_x)_2\text{O}_3$ , illustrating the variations in structural characteristics as the compositional  $x$ -value changes.

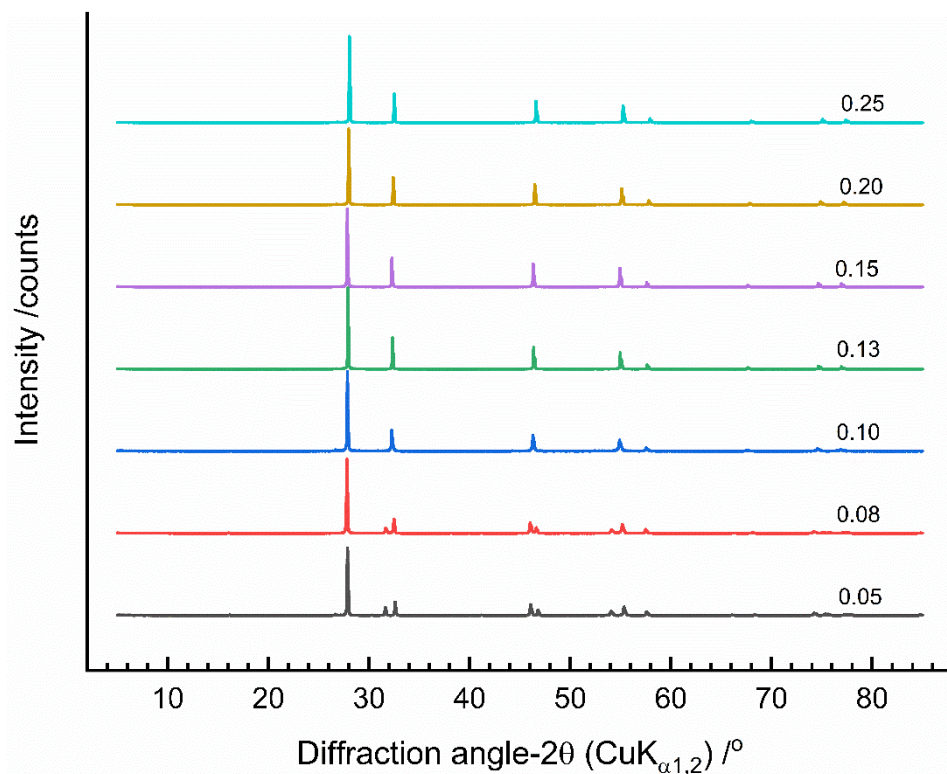


**Figure S4.6:** X-ray powder diffraction patterns for the Tb-series of  $(\text{Bi}_{1-x}\text{Tb}_x)_2\text{O}_3$ , illustrating the variations in structural characteristics as the compositional  $x$ -value changes.

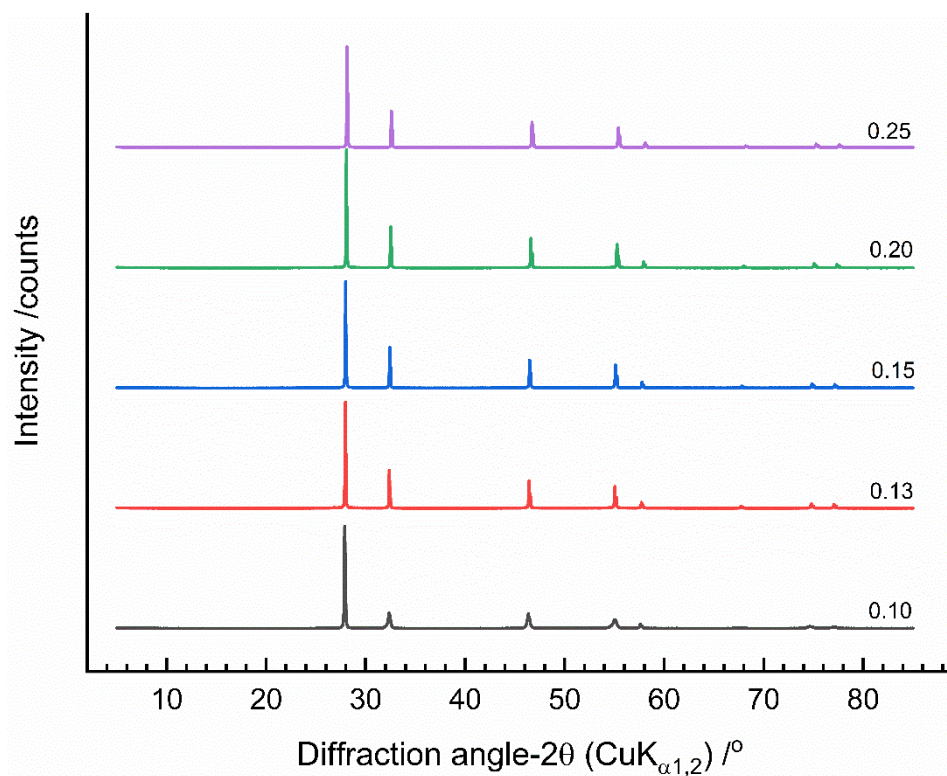


**Figure S4.7:** X-ray powder diffraction patterns for the Dy-series of  $(\text{Bi}_{1-x}\text{Dy}_x)_2\text{O}_3$ , illustrating the variations in structural characteristics as the compositional  $x$ -value changes.

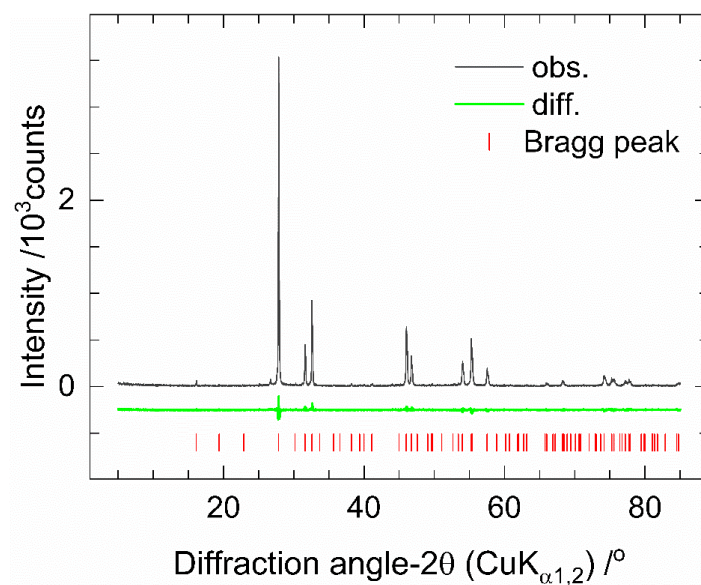


**Figure S4.8:** X-ray powder diffraction data Rietveld pattern for pure  $\beta$ -phase at  $x = 0.05$  composition in  $(\text{Bi}_{1-x}\text{Gd}_x)_2\text{O}_3$ .

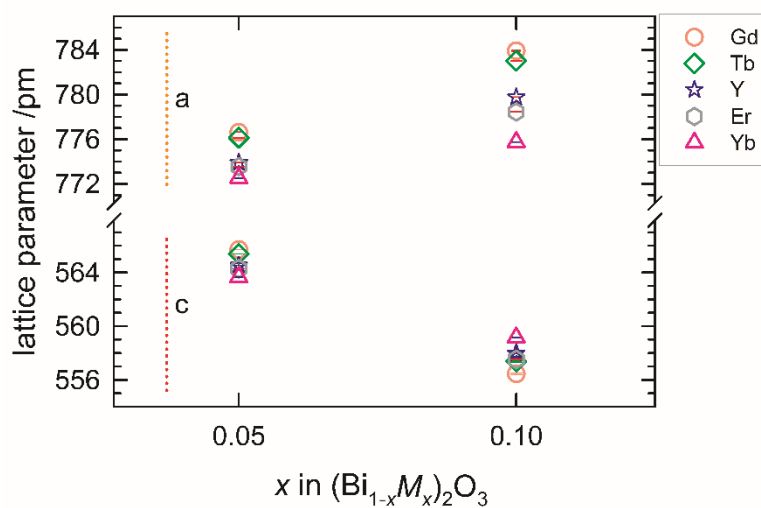


**Figure S4.9:** Variation of  $a$ - and  $c$ -lattice parameters as a function of compositional  $x$  in different  $M$ -series of  $(\text{Bi}_{1-x}\text{M}_x)_2\text{O}_3$ .

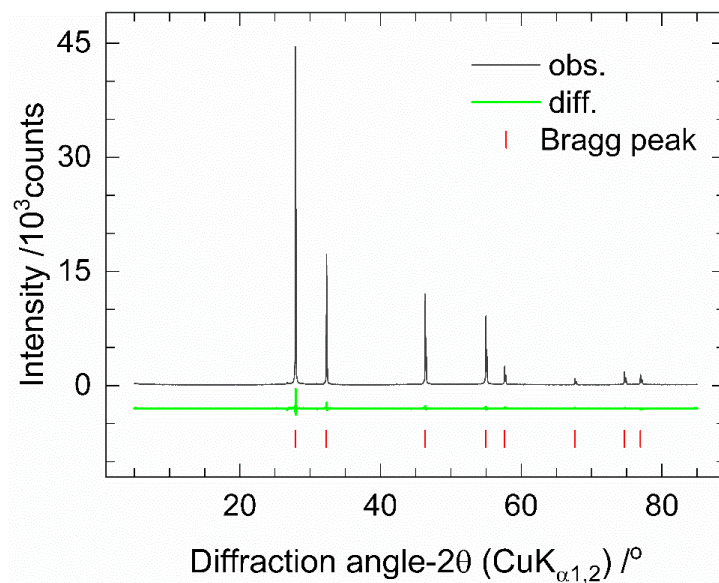


**Figure S4.10:** X-ray powder diffraction data Rietveld plot for pure  $\delta$ -phase at  $x = 0.13$  composition in  $(\text{Bi}_{1-x}\text{Tb}_x)_2\text{O}_3$ .

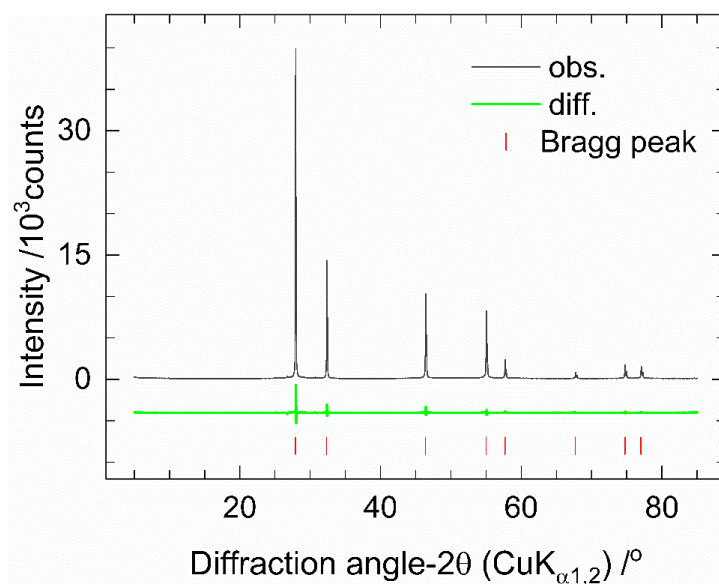


**Figure S4.11:** X-ray powder diffraction data Rietveld plot for pure  $\delta$ -phase at  $x = 0.13$  composition in  $(\text{Bi}_{1-x}\text{Dy}_x)_2\text{O}_3$ .



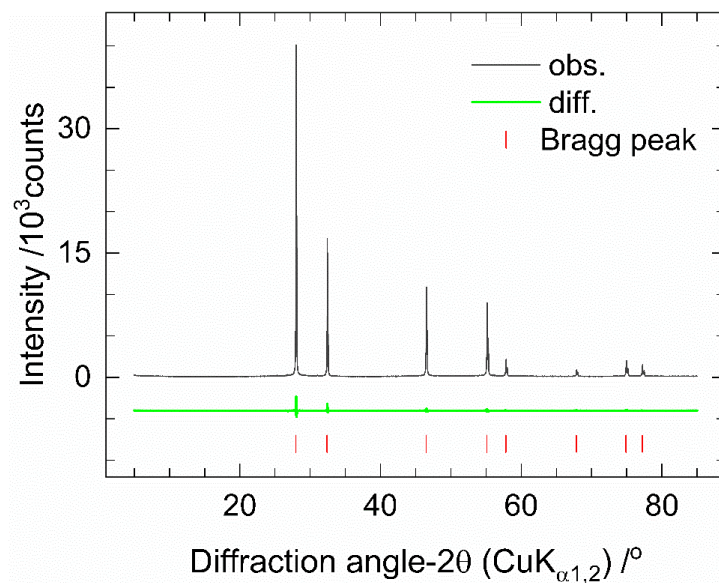


**Figure S4.12:** X-ray powder diffraction data Rietveld plot for pure  $\delta$ -phase at  $x = 0.15$  composition in  $(\text{Bi}_{1-x}\text{Ho}_x)_2\text{O}_3$ .

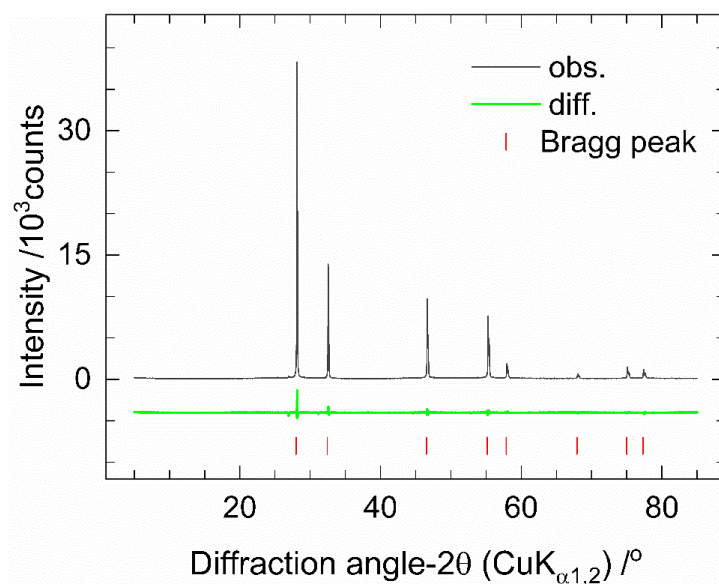


**Figure S4.13:** X-ray powder diffraction data Rietveld plot for pure  $\delta$ -phase at  $x = 0.18$  composition in  $(\text{Bi}_{1-x}\text{Y}_x)_2\text{O}_3$ .

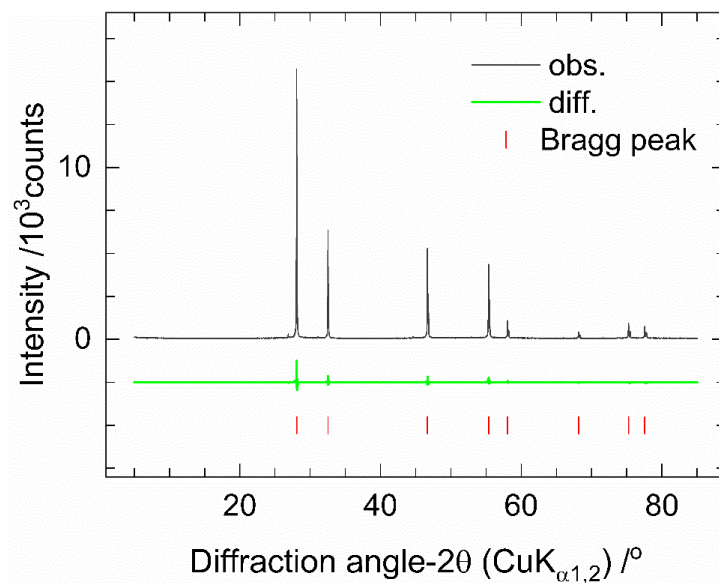


**Figure S4.14:** X-ray powder diffraction data Rietveld plot for pure  $\delta$ -phase at  $x = 0.20$  composition in  $(\text{Bi}_{1-x}\text{Er}_x)_2\text{O}_3$ .

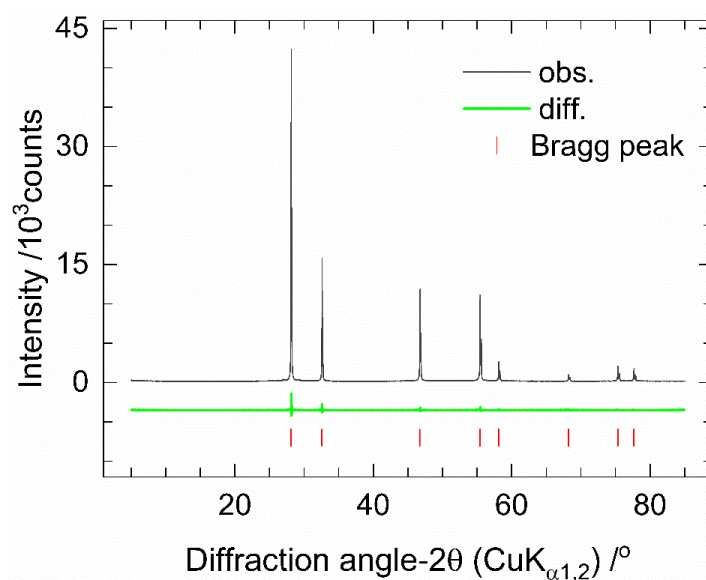


**Figure S4.15:** X-ray powder diffraction data Rietveld plot for pure  $\delta$ -phase at  $x = 0.20$  composition in  $(\text{Bi}_{1-x}\text{Tm}_x)_2\text{O}_3$ .

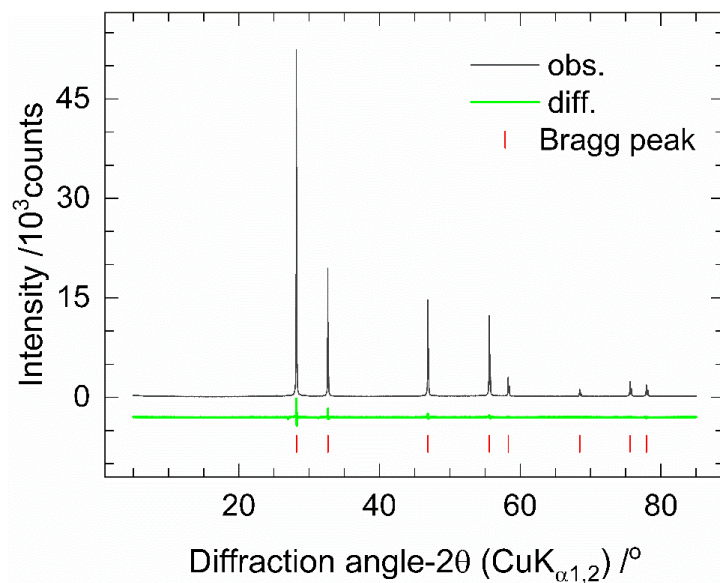


**Figure S4.16:** X-ray powder diffraction data Rietveld plot for pure  $\delta$ -phase at  $x = 0.23$  composition in  $(\text{Bi}_{1-x}\text{Yb}_x)_2\text{O}_3$ .

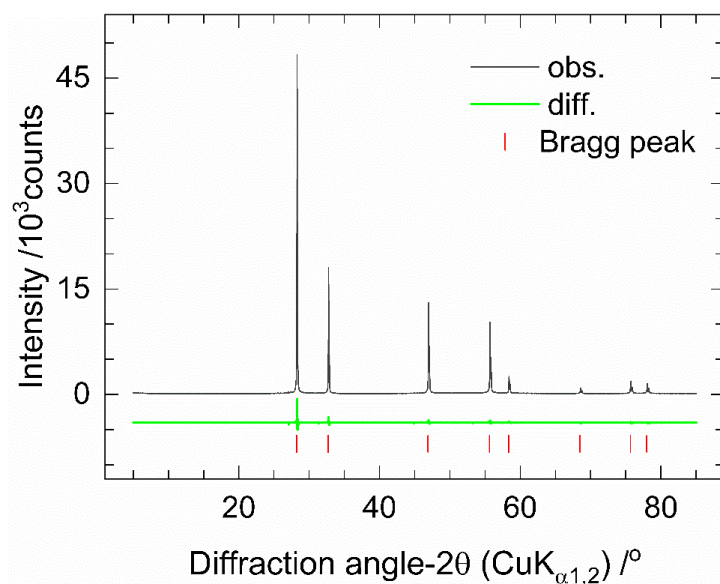


**Figure S4.17:** X-ray powder diffraction data Rietveld plot for pure  $\delta$ -phase at  $x = 0.23$  composition in  $(\text{Bi}_{1-x}\text{Lu}_x)_2\text{O}_3$ .



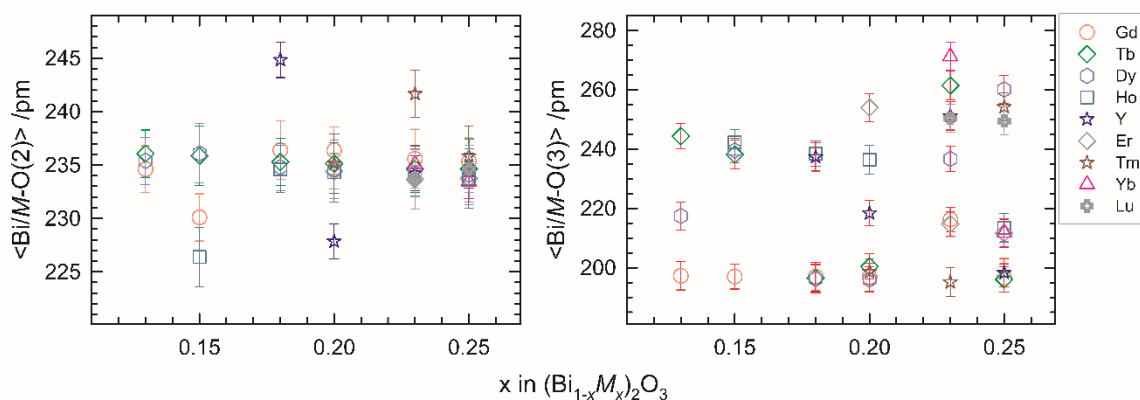


**Figure S4.18:** Variation of  $\langle \text{Bi}/\text{M}-\text{O}(2) \rangle$  and  $\langle \text{Bi}/\text{M}-\text{O}(3) \rangle$  bond distances with increasing compositional  $x$ -value in  $(\text{Bi}_{1-x}\text{M}_x)_2\text{O}_3$  for all  $M$ -series.

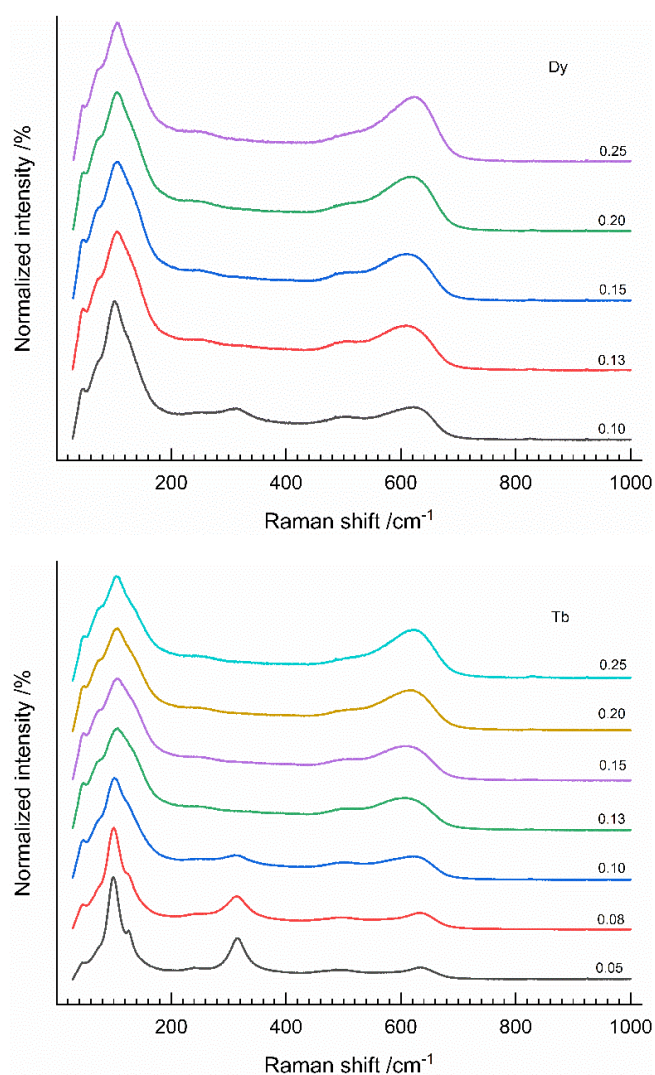


**Figure S4.19:** Raman spectra of  $(\text{Bi}_{1-x}\text{M}_x)_2\text{O}_3$  for  $M = \text{Tb}$  and  $\text{Dy}$  as a variation of compositional  $x$ -value.

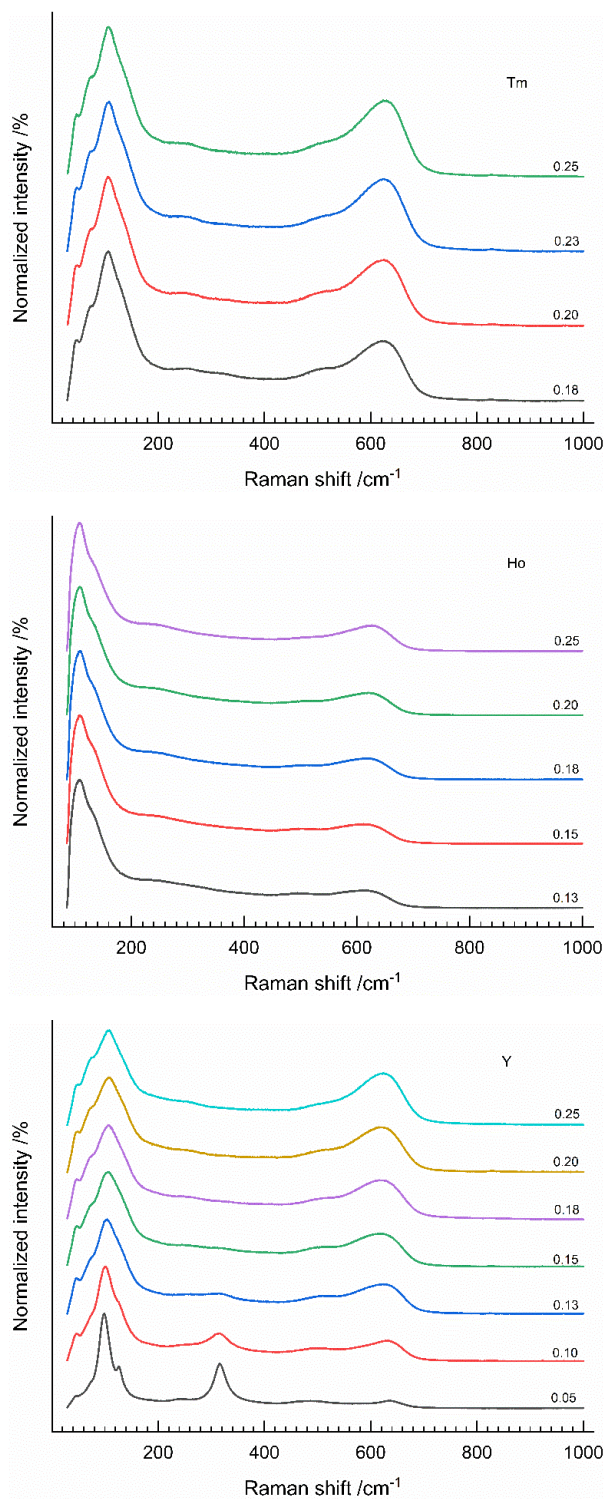


**Figure S4.20:** Raman spectra of  $(\text{Bi}_{1-x}\text{M}_x)_2\text{O}_3$  for  $M = \text{Y}, \text{Ho},$  and  $\text{Tm}$  as a variation of compositional  $x$ -value.

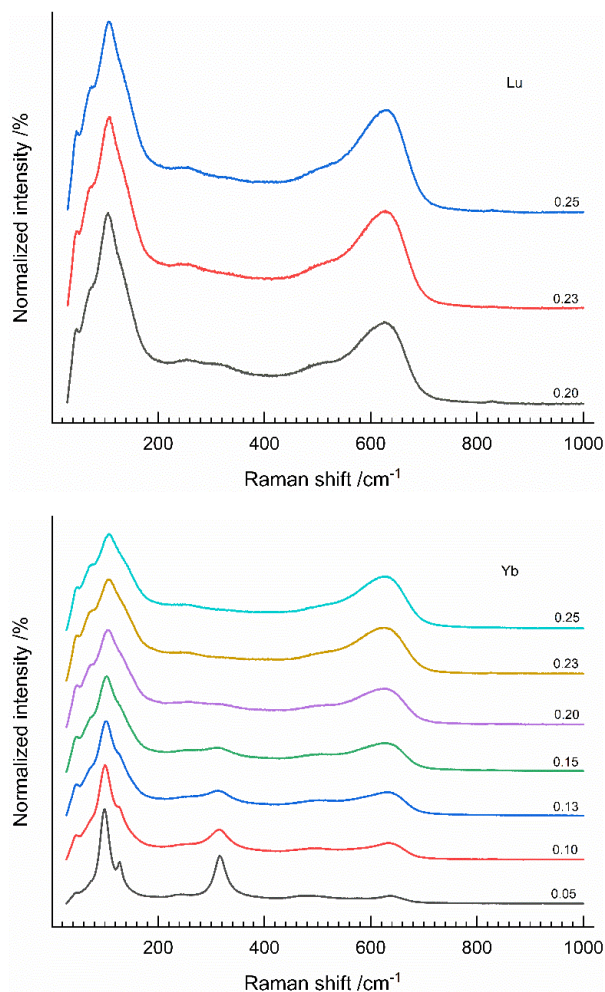


**Figure S4.21:** Raman spectra of  $(\text{Bi}_{1-x}\text{M}_x)_2\text{O}_3$  for  $M = \text{Yb}$  and  $\text{Lu}$  as a variation of compositional  $x$ -value.

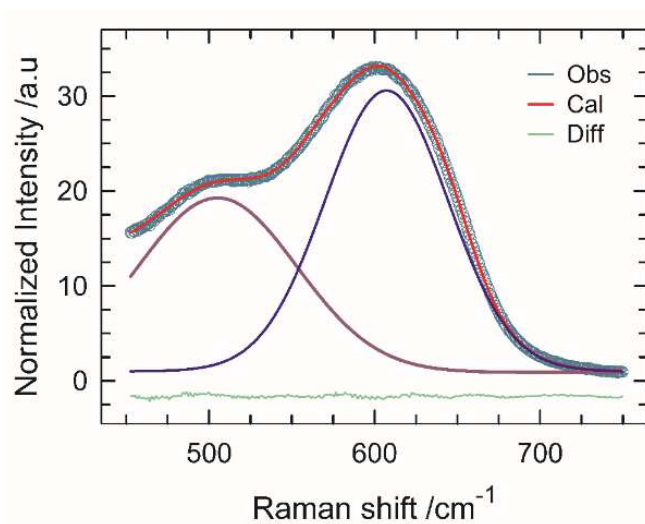


**Figure S4.22:** Representative Raman spectrum peak fitting of different Bi–O vibrations for  $x = 0.13$  compositional value in  $(\text{Bi}_{1-x}\text{Gd}_x)_2\text{O}_3$ .

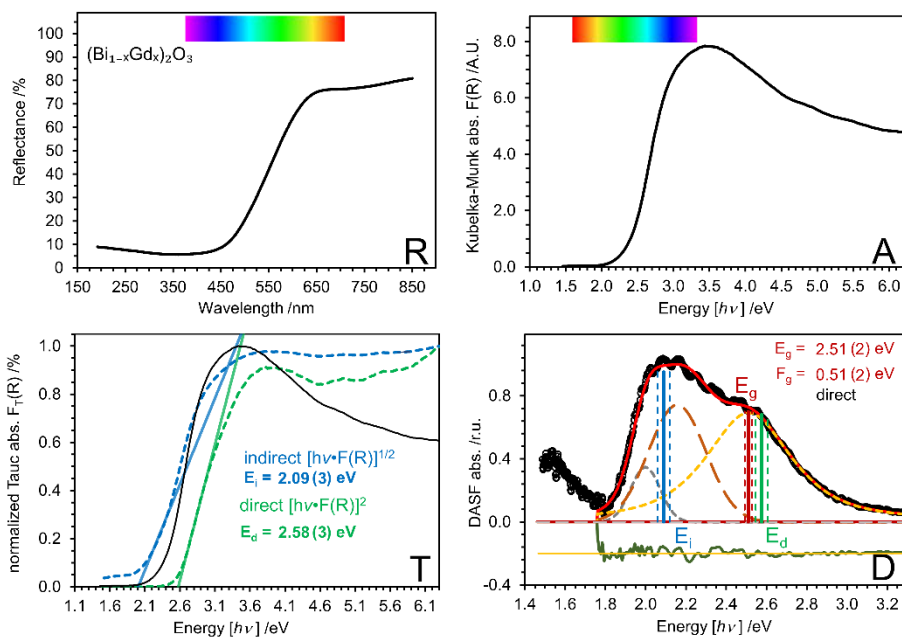


**Figure S4.23:** UV/Vis RATD plot containing reflectance spectrum (R), calculated absorbance spectrum (A), bandgap energies ( $E_g$ ) determined using the DASf method (D) and Tauc analysis (T) for direct ( $E_d$ ) and indirect ( $E_i$ ) transitions in  $(\text{Bi}_{1-x}\text{Gd}_x)_2\text{O}_3$  for  $x = 0.05$  composition.

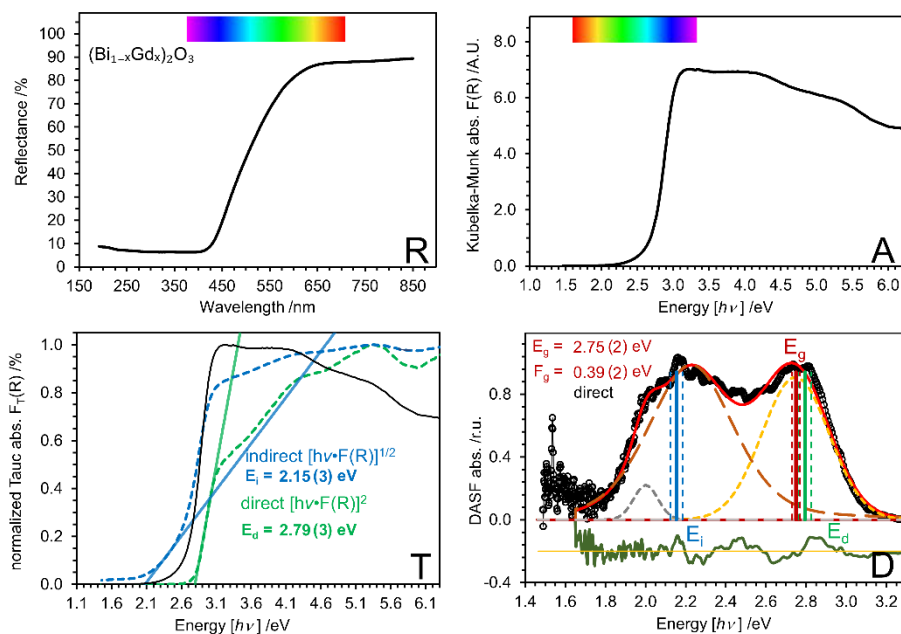


**Figure S4.24:** UV/Vis RATD plot containing reflectance spectrum (R), calculated absorbance spectrum (A), bandgap energies ( $E_g$ ) determined using the DASf method (D) and Tauc analysis (T) for direct ( $E_d$ ) and indirect ( $E_i$ ) transitions in  $(\text{Bi}_{1-x}\text{Gd}_x)_2\text{O}_3$  for  $x = 0.25$  composition.



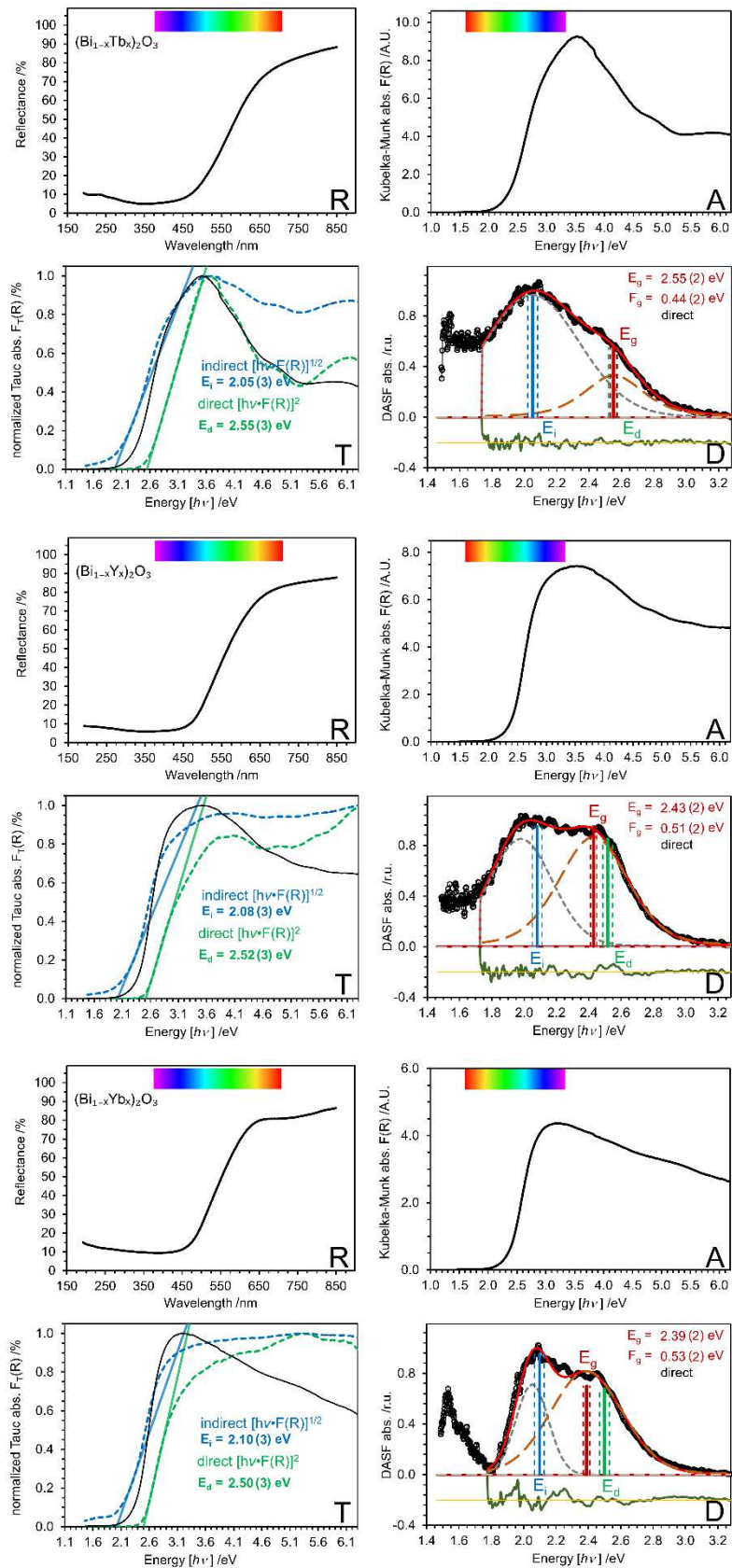


Figure S4.25: RATD plots of  $x = 0.05$  in  $(\text{Bi}_{1-x}\text{M}_x)_2\text{O}_3$  solid solution for  $M = \text{Tb}$ ,  $\text{Y}$ , and  $\text{Yb}$ .

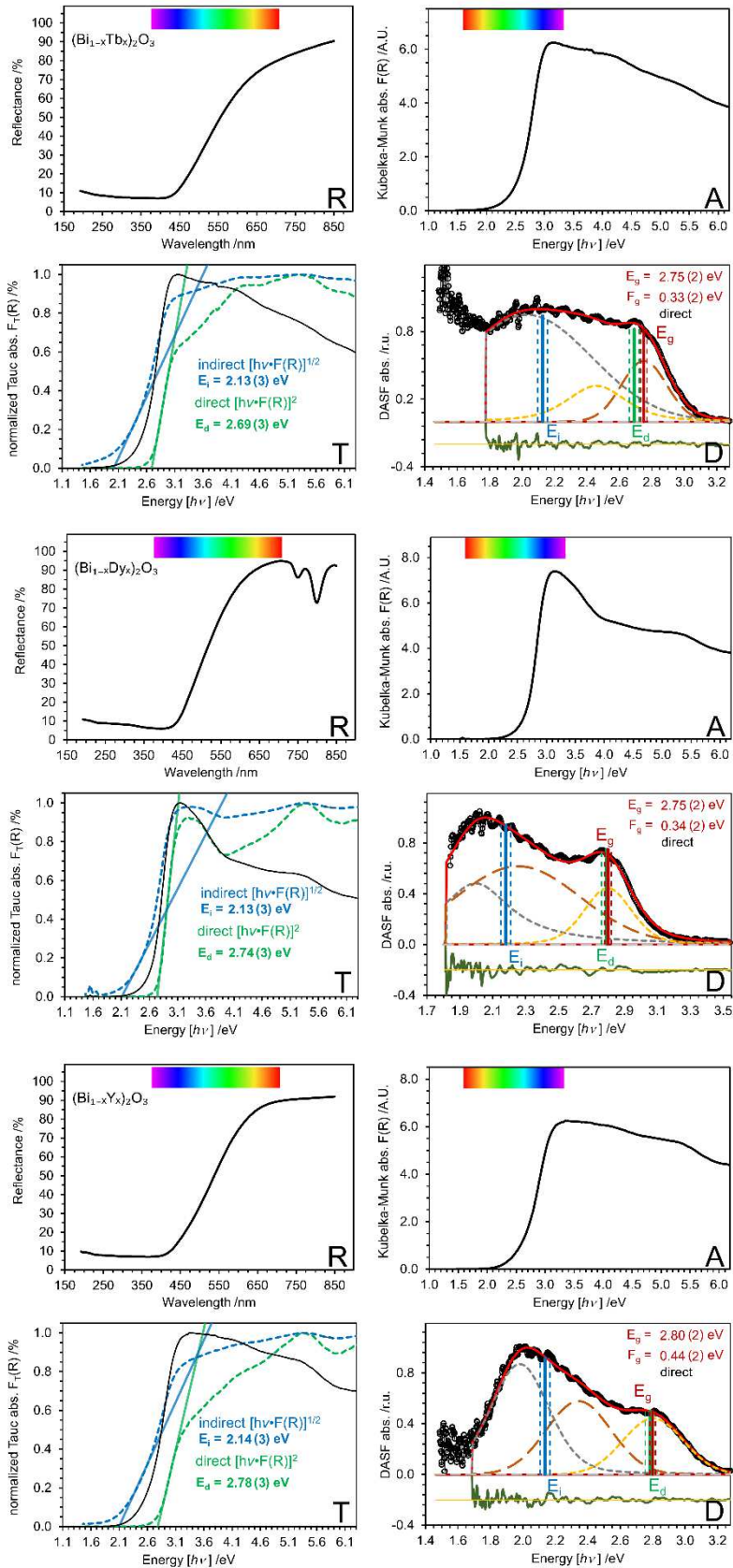


Figure S4.26: RATD plots of  $x = 0.25$  in  $(\text{Bi}_{1-x}\text{M}_x)_2\text{O}_3$  solid solution for  $M = \text{Tb}$ ,  $\text{Dy}$ , and  $\text{Y}$ .

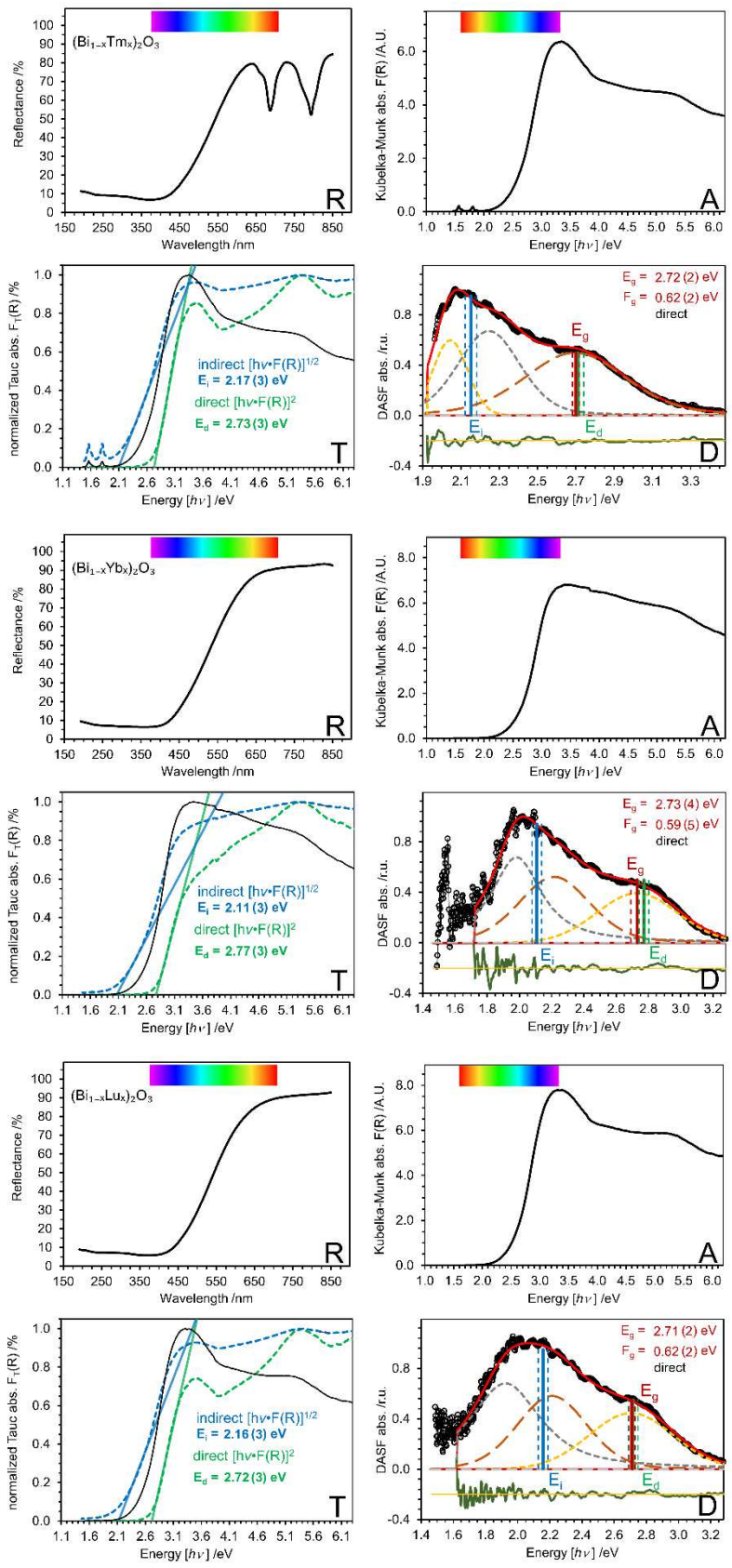
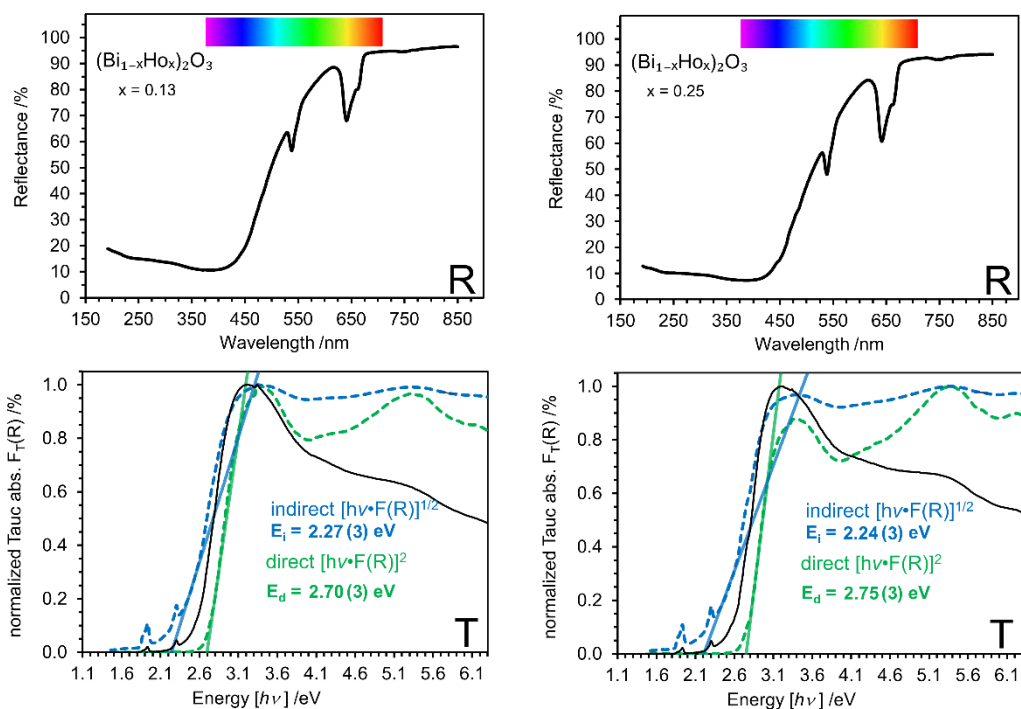
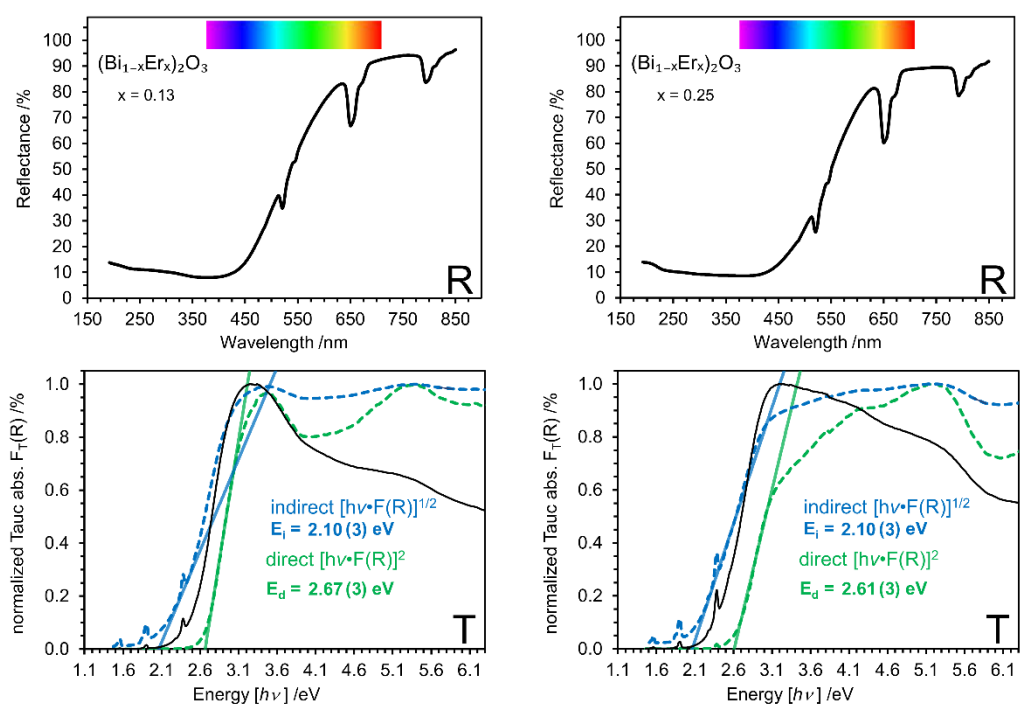


Figure S4.27: RATD plots of  $x = 0.25$  in  $(\text{Bi}_{1-x}\text{M}_x)_2\text{O}_3$  solid solution for  $M = \text{Tm}, \text{Yb},$  and  $\text{Lu}$ .



**Figure S4.28:** UV/Vis plot containing reflectance spectrum (R) and Tauc analysis (T) for direct ( $E_d$ ) and indirect ( $E_i$ ) transitions in  $(\text{Bi}_{1-x}\text{Ho}_x)_2\text{O}_3$  for  $x = 0.13$  and  $0.25$ .



**Figure S4.29:** UV/Vis plot containing reflectance spectrum (R) and Tauc analysis (T) for direct ( $E_d$ ) and indirect ( $E_i$ ) transitions in  $(\text{Bi}_{1-x}\text{Er}_x)_2\text{O}_3$  for  $x = 0.13$  and  $0.25$ .



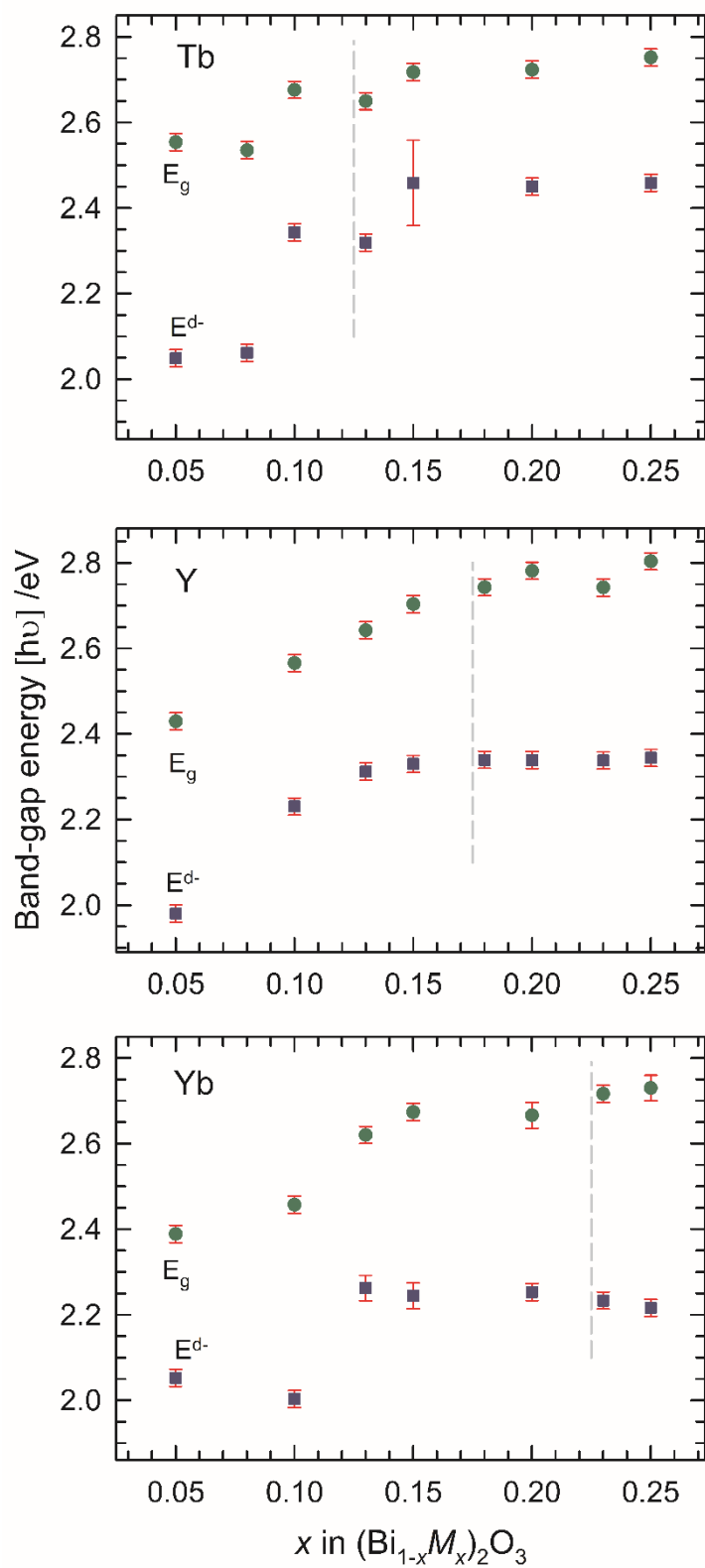


**Figure S4.30:** Determined  $E_g$  (circle, bandgap) and  $E^{d-}$  (diamond, anionic defect) transition energies for the  $(\text{Bi}_{1-x}\text{M}_x)_2\text{O}_3$  solid solution of Tb, Y, and Yb, with the dotted line representing the phase boundary between  $\beta$ - and  $\delta$ -phases.

**Table S4.1:** Average crystallite size and microstrain of the  $(\text{Bi}_{1-x}\text{M}_x)_2\text{O}_3$   $\delta$ -phases obtained from X-ray powder data Rietveld refinements.

<b><math>L_{\text{vol}}(\text{IB}) / \text{nm}</math></b>									
$x$	Y	Gd	Tb	Dy	Ho	Er	Tm	Yb	Lu
0.13	--	203(2)	218(3)	182(2)	274(3)	--	--	--	--
0.15	221(4)	186(2)	189(3)	177(2)	174(2)	210(4)	--	--	--
0.18	214(3)	236(2)	244(4)	184(2)	202(3)	--	--	--	--
0.20	217(3)	164(2)	202(2)	214(3)	208(3)	202(3)	175(2)	188(3)	242(3)
0.23	197(3)	260(3)	290(4)	180(2)	--	261(4)	180(2)	211(3)	183(2)
0.25	244(3)	203(2)	248(3)	242(3)	238(3)	265(4)	175(2)	183(3)	199(3)
<b><math>\epsilon / \%</math></b>									
0.13	--	0.014(1)	0.013(1)	0.016(1)	0.018(1)	--	--	--	--
0.15	0.027(1)	0.011(1)	0.005(1)	0.014(1)	0.012(1)	0.007(1)	--	--	--
0.18	0.027(1)	0.024(1)	0.043(1)	0.025(1)	0.012(1)	--	--	--	--
0.20	0.010(1)	0.043(1)	0.018(1)	0.018(1)	0.013(1)	0.001(1)	0.005(1)	0.014(1)	0.020(1)
0.23	0.036(1)	0.022(1)	0.019(1)	0.031(1)	--	0.005(1)	0.011(1)	0.004(1)	0.011(1)
0.25	0.014(1)	0.037(1)	0.019(1)	0.030(1)	0.016(1)	0.024(1)	0.013(1)	0.028(2)	0.014(1)

**Table S4.2:** X-ray powder diffraction data Rietveld refined structural parameter for  $x = 0.05 - 0.25$  in  $(\text{Bi}_{1-x}\text{Tb}_x)_2\text{O}_3$ .

$x = 0.05$ , space group = $P4_2/nmc$						
Atom	Site	Occupancy	$x$	$y$	$z$	$B / 10^{-4} \text{ pm}^2$
Bi/Tb	8g	0.48/0.03(1)	0	0.256(1)	0.239(2)	1.37(3)
O1	8f	0.49(2)	0.299(3)	0.299(3)	0	1.85(3) <sup>a</sup>
O2	4d	0.48(2)	0	1/2	0.388(3)	1.85(3) <sup>a</sup>
O3	2a	0.09(3)	0	0	0	1.85(3) <sup>a</sup>
$x = 0.10$ , space group = $P4_2/nmc$ , $\beta$ -phase (%) = 35.9(2)						
Bi/Tb	8g	0.45/0.05(1)	0	0.250(2)	0.246(3)	1.58(3)
O1	8f	0.50(2)	0.294(3)	0.294(3)	0	4.93(3) <sup>b</sup>
O2	4d	0.46(2)	0	1/2	0.402(1)	4.93(3) <sup>b</sup>
O3	2a	0.09(3)	0	0	0	4.93(3) <sup>b</sup>
$x = 0.10$ , space group = $Fm\bar{3}m$ , $\delta$ -phase (%) = 64.1(2)						
Bi/Tb	24e	0.142/0.025(1)	0.057(3)	0	0	1.76(3)
O1	8c	0.038(3)	1/4	1/4	1/4	5.48(3) <sup>c</sup>
O2	32f	0.159(3)	0.276(3)	0.276(3)	0.276(3)	5.48(3) <sup>c</sup>
O3	48i	0.012(3)	1/2	0.249(3)	0.249(3)	5.48(3) <sup>c</sup>
$x = 0.13$ , space group = $Fm\bar{3}m$						
Bi/Tb	24e	0.144/0.023(1)	0.046(1)	0	0	1.59(2)
O1	8c	0.315(1)	1/4	1/4	1/4	5.00(3) <sup>d</sup>
O2	32f	0.090(3)	0.310(2)	0.310(2)	0.310(2)	5.00(3) <sup>d</sup>
O3	48i	0.011(2)	1/2	0.105(3)	0.105(3)	5.00(3) <sup>d</sup>
$x = 0.15$ , space group = $Fm\bar{3}m$						
Bi/Tb	24e	0.142/0.024(1)	0.044(1)	0	0	1.50(2)
O1	8c	0.280(1)	1/4	1/4	1/4	4.10(3) <sup>e</sup>
O2	32f	0.099(3)	0.308(3)	0.308(3)	0.308(3)	4.10(3) <sup>e</sup>
O3	48i	0.011(3)	1/2	0.145(3)	0.145(3)	4.10(3) <sup>e</sup>
$x = 0.25$ , space group = $Fm\bar{3}m$						
Bi/Tb	24e	0.121/0.046(1)	0.045(1)	0	0	1.56(2)
O1	8c	0.216(3)	1/4	1/4	1/4	4.89(2) <sup>f</sup>
O2	32f	0.115(3)	0.290(3)	0.290(3)	0.290(3)	4.89(2) <sup>f</sup>
O3	48i	0.013(3)	1/2	0.252(3)	0.252(3)	4.89(2) <sup>f</sup>

<sup>a,b,c,d,e,f</sup>Isotropic displacement parameter ( $B$ ) of O1, O2, and O3 with the same letter are linearly constraint to each other.

**Table S4.3:** X-ray powder diffraction data Rietveld refined structural parameter for  $x = 0.10 - 0.25$  in  $(\text{Bi}_{1-x}\text{Dy}_x)_2\text{O}_3$ .

$x = 0.10$ , space group = $P4_2/nmc$ , $\beta$ -phase (%) = 32.8(2)						
Atom	Site	Occupancy	$x$	$y$	$z$	$B / 10^{-4} \text{ pm}^2$
Bi/Dy	8g	0.45/0.05(2)	0	0.253(2)	0.245(2)	1.15(3)
O1	8f	0.49(2)	0.291(3)	0.291(3)	0	4.20(3) <sup>a</sup>
O2	4d	0.47(2)	0	1/2	0.494(1)	4.20(3) <sup>a</sup>
O3	2a	0.09(3)	0	0	0	4.20(3) <sup>a</sup>
$x = 0.10$ , space group = $Fm\bar{3}m$ , $\delta$ -phase (%) = 67.2(2)						
Bi/Dy	24e	0.133/0.034(1)	0.052(2)	0	0	1.55(3)
O1	8c	0.036(3)	1/4	1/4	1/4	4.78(3) <sup>b</sup>
O2	32f	0.159(3)	0.274(3)	0.274(3)	0.274(3)	4.78(3) <sup>b</sup>
O3	48i	0.013(3)	1/2	0.249(3)	0.249(3)	4.78(3) <sup>b</sup>
$x = 0.13$ , space group = $Fm\bar{3}m$						
Bi/Dy	24e	0.145/0.022(1)	0.045(1)	0	0	1.58(2)
O1	8c	0.248(3)	1/4	1/4	1/4	5.00(3) <sup>c</sup>
O2	32f	0.107(3)	0.299(3)	0.299(3)	0.299(3)	5.00(3) <sup>c</sup>
O3	48i	0.020(3)	1/2	0.329(3)	0.329(3)	5.00(3) <sup>c</sup>
$x = 0.15$ , space group = $Fm\bar{3}m$						
Bi/Dy	24e	0.141/0.026(1)	0.045(1)	0	0	1.58(2)
O1	8c	0.320(3)	1/4	1/4	1/4	4.80(3) <sup>d</sup>
O2	32f	0.089(3)	0.317(2)	0.317(2)	0.317(2)	4.80(3) <sup>d</sup>
O3	48i	0.019(3)	1/2	0.369(3)	0.369(3)	4.80(3) <sup>d</sup>
$x = 0.20$ , space group = $Fm\bar{3}m$						
Bi/Dy	24e	0.133/0.033(1)	0.045(1)	0	0	1.55(2)
O1	8c	0.278(3)	1/4	1/4	1/4	4.35(3) <sup>e</sup>
O2	32f	0.099(3)	0.300(3)	0.300(3)	0.300(3)	4.35(3) <sup>e</sup>
O3	48i	0.012(3)	1/2	0.353(3)	0.353(3)	4.35(3) <sup>e</sup>
$x = 0.25$ , space group = $Fm\bar{3}m$						
Bi/Dy	24e	0.121/0.046(1)	0.046(1)	0	0	1.58(2)
O1	8c	0.310(3)	1/4	1/4	1/4	4.58(2) <sup>f</sup>
O2	32f	0.091(3)	0.288(3)	0.288(3)	0.288(3)	4.58(2) <sup>f</sup>
O3	48i	0.011(3)	1/2	0.433(3)	0.433(3)	4.58(2) <sup>f</sup>

<sup>a,b,c,d,e,f</sup>Isotropic displacement parameter ( $B$ ) of O1, O2, and O3 with the same letter are linearly constraint to each other.

**Table S4.4:** X-ray powder diffraction data Rietveld refined structural parameter for  $x = 0.13 - 0.25$  in  $(\text{Bi}_{1-x}\text{Ho}_x)_2\text{O}_3$ .

$x = 0.13$ , space group = $P4_2/nmc$ , $\beta$ -phase (%) = 26.1(2)						
Atom	Site	Occupancy	$x$	$y$	$z$	$B / 10^{-4} \text{ pm}^2$
Bi/Ho	8g	0.43/0.07(2)	0	0.249(2)	0.240(2)	1.44(3)
O1	8f	0.57(2)	0.296(3)	0.296(3)	0	4.80(3) <sup>a</sup>
O2	4d	0.31(2)	0	1/2	0.530(3)	4.80(3) <sup>a</sup>
O3	2a	0.10(3)	0	0	0	4.80(3) <sup>a</sup>
$x = 0.13$ , space group = $Fm\bar{3}m$ , $\delta$ -phase (%) = 73.9(2)						
Bi/Ho	24e	0.145/0.022(1)	0.050(3)	0	0	1.50(3)
O1	8c	0.170(3)	1/4	1/4	1/4	3.00(3) <sup>b</sup>
O2	32f	0.127(3)	0 310(3)	0 310(3)	0 310(3)	3.00(3) <sup>b</sup>
O3	48i	0.016(3)	1/2	0 440(3)	0 440(3)	3.00(3) <sup>b</sup>
$x = 0.15$ , space group = $Fm\bar{3}m$						
Bi/Ho	24e	0.143/0.024(1)	0.045(1)	0	0	1.57(2)
O1	8c	0.335(3)	1/4	1/4	1/4	4.10(3) <sup>c</sup>
O2	32f	0.080(3)	0 339(3)	0 339(3)	0 339(3)	4.10(3) <sup>c</sup>
O3	48i	0.014(3)	1/2	0 388(3)	0 388(3)	4.10(3) <sup>c</sup>
$x = 0.18$ , space group = $Fm\bar{3}m$						
Bi/Ho	24e	0.136/0.031(1)	0.045(1)	0	0	1.54(2)
O1	8c	0.290(3)	1/4	1/4	1/4	3.40(3) <sup>d</sup>
O2	32f	0.097(3)	0 299(3)	0 299(3)	0 299(3)	3.40(3) <sup>d</sup>
O3	48i	0.014(3)	1/2	0 366(3)	0 366(3)	3.40(3) <sup>d</sup>
$x = 0.20$ , space group = $Fm\bar{3}m$						
Bi/Ho	24e	0.133/0.033(1)	0.045(1)	0	0	1.56(2)
O1	8c	0.250(3)	1/4	1/4	1/4	4.00(3) <sup>e</sup>
O2	32f	0.106(3)	0 296(3)	0 296(3)	0 296(3)	4.00(3) <sup>e</sup>
O3	48i	0.014(3)	1/2	0 350(3)	0 350(3)	4.00(3) <sup>e</sup>
$x = 0.25$ , space group = $Fm\bar{3}m$						
Bi/Ho	24e	0.124/0.042(1)	0.045(1)	0	0	1.56(2)
O1	8c	0.204(3)	1/4	1/4	1/4	4.17(2) <sup>f</sup>
O2	32f	0.118(3)	0 286(3)	0 286(3)	0 286(3)	4.17(2) <sup>f</sup>
O3	48i	0.011(3)	1/2	0 309(3)	0 309(3)	4.17(2) <sup>f</sup>

<sup>a,b,c,d,e,f</sup>Isotropic displacement parameter ( $B$ ) of O1, O2, and O3 with the same letter are linearly constraint to each other.

**Table S4.5:** X-ray powder diffraction data Rietveld refined structural parameter for  $x = 0.05 - 0.25$  in  $(\text{Bi}_{1-x}\text{Y}_x)_2\text{O}_3$ .

$x = 0.05$ , space group = $P4_2/nmc$						
Atom	Site	Occupancy	$x$	$y$	$z$	$B / 10^{-4} \text{ pm}^2$
Bi/Y	8g	0.48/0.02	0	0.255(1)	0.238(2)	1.30(2)
O1	8f	0.46(2)	0.304(1)	0.304(1)	0	1.60(3) <sup>a</sup>
O2	4d	0.54(2)	0	1/2	0.404(3)	1.60(3) <sup>a</sup>
O3	2a	0.08(3)	0	0	0	1.60(3) <sup>a</sup>
$x = 0.15$ , space group = $P4_2/nmc$ , $\beta$ -phase (%) = 7.7(2)						
Bi/Y	8g	0.87/0.13(1)	0	0.248(3)	0.265(3)	1.22(3)
O1	8f	0.51(2)	0.235(3)	0.235(3)	0	4.26(3) <sup>b</sup>
O2	4d	0.47(2)	0	1/2	0.474(3)	4.26(3) <sup>b</sup>
O3	2a	0.04(3)	0	0	0	4.26(3) <sup>b</sup>
$x = 0.15$ , space group = $Fm\bar{3}m$ , $\delta$ -phase (%) = 92.3(2)						
Bi/Y	24e	0.142/0.025(1)	0.045(3)	0	0	1.28(2)
O1	8c	0.100(3)	1/4	1/4	1/4	4.57(3) <sup>c</sup>
O2	32f	0.144(3)	0.298(3)	0.298(3)	0.298(3)	4.57(3) <sup>c</sup>
O3	48i	0.017(3)	1/2	0.253(3)	0.253(3)	4.57(3) <sup>c</sup>
$x = 0.18$ , space group = $Fm\bar{3}m$						
Bi/Y	24e	0.134/0.032(1)	0.045(1)	0	0	1.56(2)
O1	8c	0.309(3)	1/4	1/4	1/4	2.90(3) <sup>d</sup>
O2	32f	0.092(3)	0.327(2)	0.327(2)	0.327(2)	2.90(3) <sup>d</sup>
O3	48i	0.013(2)	1/2	0.356(3)	0.356(3)	2.90(3) <sup>d</sup>
$x = 0.23$ , space group = $Fm\bar{3}m$						
Bi/Y	24e	0.130/0.037(1)	0.047(1)	0	0	1.64(2)
O1	8c	0.320(1)	1/4	1/4	1/4	3.20(3) <sup>e</sup>
O2	32f	0.089(3)	0.307(2)	0.307(2)	0.307(2)	3.20(3) <sup>e</sup>
O3	48i	0.012(2)	1/2	0.390(3)	0.390(3)	3.20(3) <sup>e</sup>
$x = 0.25$ , space group = $Fm\bar{3}m$						
Bi/Y	24e	0.128/0.046(1)	0.039(1)	0	0	1.67(2)
O1	8c	0.278(3)	1/4	1/4	1/4	2.80(3) <sup>f</sup>
O2	32f	0.099(3)	0.310(2)	0.310(2)	0.310(2)	2.80(3) <sup>f</sup>
O3	48i	0.003(3)	1/2	0.286(3)	0.286(3)	2.80(3) <sup>f</sup>

<sup>a,b,c,d,e,f</sup>Isotropic displacement parameter ( $B$ ) of O1, O2, and O3 with the same letter are linearly constraint to each other.

**Table S4.6:** X-ray powder diffraction data Rietveld refined structural parameter for  $x = 0.05 - 0.25$  in  $(\text{Bi}_{1-x}\text{Er}_x)_2\text{O}_3$ .

$x = 0.05$ , space group = $P4_2/nmc$						
Atom	Site	Occupancy	$x$	$y$	$z$	$B / 10^{-4} \text{ pm}^2$
Bi/Er	8g	0.48/0.02(2)	0	0.255(1)	0.237(1)	1.22(3)
O1	8f	0.50(3)	0.317(3)	0.317(3)	0	1.40(3) <sup>a</sup>
O2	4d	0.46(3)	0	1/2	0.402(3)	1.40(3) <sup>a</sup>
O3	2a	0.09(3)	0	0	0	1.40(3) <sup>a</sup>
$x = 0.15$ , space group = $P4_2/nmc$ , $\beta$ -phase (%) = 6.6(2)						
Bi/Er	8g	0.43/0.07(2)	0	0.248(3)	0.250(1)	1.25(3)
O1	8f	0.53(3)	0.295(3)	0.295(3)	0	4.20(3) <sup>b</sup>
O2	4d	0.38(3)	0	1/2	0.475(3)	4.20(3) <sup>b</sup>
O3	2a	0.10(3)	0	0	0	4.20(3) <sup>b</sup>
$x = 0.15$ , space group = $Fm\bar{3}m$ , $\delta$ -phase (%) = 93.4(2)						
Bi/Er	24e	0.132/0.035(1)	0.045(1)	0	0	1.28(2)
O1	8c	0.250(3)	1/4	1/4	1/4	3.70(3) <sup>c</sup>
O2	32f	0.105(3)	0 313(3)	0 313(3)	0 313(3)	3.70(3) <sup>c</sup>
O3	48i	0.015(3)	1/2	0 401(3)	0 401(3)	3.70(3) <sup>c</sup>
$x = 0.20$ , space group = $Fm\bar{3}m$						
Bi/Er	24e	0.131/0.035(1)	0.041(1)	0	0	1.35(2)
O1	8c	0.390(3)	1/4	1/4	1/4	1.20(3) <sup>d</sup>
O2	32f	0.072(3)	0 309(3)	0 309(3)	0 309(3)	1.20(3) <sup>d</sup>
O3	48i	0.016(2)	1/2	0 412(3)	0 412(3)	1.20(3) <sup>d</sup>
$x = 0.23$ , space group = $Fm\bar{3}m$						
Bi/Er	24e	0.122/0.045(1)	0.042(1)	0	0	1.40(2)
O1	8c	0.300(3)	1/4	1/4	1/4	2.10(3) <sup>e</sup>
O2	32f	0.094(3)	0 300(3)	0 300(3)	0 300(3)	2.10(3) <sup>e</sup>
O3	48i	0.012(3)	1/2	0 321(3)	0 321(3)	2.10(3) <sup>e</sup>
$x = 0.25$ , space group = $Fm\bar{3}m$						
Bi/Er	24e	0.122/0.045(1)	0.046(1)	0	0	1.56(2)
O1	8c	0.260(3)	1/4	1/4	1/4	2.60(3) <sup>f</sup>
O2	32f	0.104(3)	0 310(2)	0 310(2)	0 310(2)	2.60(3) <sup>f</sup>
O3	48i	0.012(3)	1/2	0 290(3)	0 290(3)	2.60(3) <sup>f</sup>

<sup>a,b,c,d,e,f</sup>Isotropic displacement parameter ( $B$ ) of O1, O2, and O3 with the same letter are linearly constraint to each other.

**Table S4.7:** X-ray powder diffraction data Rietveld refined structural parameter for  $x = 0.18 - 0.25$  in  $(\text{Bi}_{1-x}\text{Tm}_x)_2\text{O}_3$ .

$x = 0.18$ , space group = $P4_2/nmc$ , $\beta$ -phase (%) = 12.4(2)						
Atom	Site	Occupancy	$x$	$y$	$z$	$B / 10^{-4} \text{ pm}^2$
Bi/Tm	8g	0.41/0.09(2)	0	0.249(2)	0.240(2)	1.44(3)
O1	8f	0.49(2)	0.296(3)	0.296(3)	0	4.80(3) <sup>a</sup>
O2	4d	0.48(2)	0	1/2	0.529(3)	4.80(3) <sup>a</sup>
O3	2a	0.09(3)	0	0	0	4.80(3) <sup>a</sup>
$x = 0.18$ , space group = $Fm\bar{3}m$ , $\delta$ -phase (%) = 87.6(2)						
Bi/Tm	24e	0.145/0.022(1)	0.047(3)	0	0	1.53(3)
O1	8c	0.151(3)	1/4	1/4	1/4	3.41(3) <sup>b</sup>
O2	32f	0.131(3)	0 310(3)	0 310(3)	0 310(3)	3.41(3) <sup>b</sup>
O3	48i	0.011(3)	1/2	0 499(3)	0 499(3)	3.41(3) <sup>b</sup>
$x = 0.20$ , space group = $Fm\bar{3}m$						
Bi/Tm	24e	0.143/0.024(1)	0.044(1)	0	0	1.48(2)
O1	8c	0.296(3)	1/4	1/4	1/4	1.72(3) <sup>c</sup>
O2	32f	0.095(3)	0 322(2)	0 322(2)	0 322(2)	1.72(3) <sup>c</sup>
O3	48i	0.014(3)	1/2	0 203(3)	0 203(3)	1.72(3) <sup>c</sup>
$x = 0.23$ , space group = $Fm\bar{3}m$						
Bi/Tm	24e	0.129/0.038(1)	0.045(1)	0	0	1.50(2)
O1	8c	0.260(3)	1/4	1/4	1/4	1.45(3) <sup>d</sup>
O2	32f	0.103(3)	0 309(3)	0 309(3)	0 309(3)	1.45(3) <sup>d</sup>
O3	48i	0.016(3)	1/2	0 237(3)	0 237(3)	1.45(3) <sup>d</sup>
$x = 0.25$ , space group = $Fm\bar{3}m$						
Bi/Tm	24e	0.122/0.045(1)	0.044(1)	0	0	1.48(2)
O1	8c	0.365(3)	1/4	1/4	1/4	2.50(3) <sup>e</sup>
O2	32f	0.077(3)	0 335(2)	0 335(2)	0 335(2)	2.50(3) <sup>e</sup>
O3	48i	0.016(3)	1/2	0 421(3)	0 421(3)	2.50(3) <sup>e</sup>

<sup>a,b,c,d,e</sup>Isotropic displacement parameter ( $B$ ) of O1, O2, and O3 with the same letter are linearly constraint to each other.



**Table S4.8:** X-ray powder diffraction data Rietveld refined structural parameter for  $x = 0.05 - 0.25$  in  $(\text{Bi}_{1-x}\text{Yb}_x)_2\text{O}_3$ .

$x = 0.05$ , space group = $P4_2/nmc$						
Atom	Site	Occupancy	$x$	$y$	$z$	$B / 10^{-4} \text{ pm}^2$
Bi/Yb	8g	0.48/0.02(1)	0	0.255(1)	0.237(2)	0.99(2)
O1	8f	0.49(2)	0.310(1)	0.310(1)	0	1.30(3) <sup>a</sup>
O2	4d	0.48(2)	0	1/2	0.375(3)	1.30(3) <sup>a</sup>
O3	2a	0.09(3)	0	0	0	1.30(3) <sup>a</sup>
$x = 0.20$ , space group = $P4_2/nmc$ , $\beta$ -phase (%) = 17.9(2)						
Bi/Yb	8g	0.40/0.10(1)	0	0.248(3)	0.253(3)	1.43(3)
O1	8f	0.50(2)	0.267(3)	0.267(3)	0	3.50(3) <sup>b</sup>
O2	4d	0.46(2)	0	1/2	0.570(3)	3.50(3) <sup>b</sup>
O3	2a	0.08(3)	0	0	0	3.50(3) <sup>b</sup>
$x = 0.20$ , space group = $Fm\bar{3}m$ , $\delta$ -phase (%) = 82.1(2)						
Bi/Yb	24e	0.142/0.025(1)	0.048(1)	0	0	1.54(3)
O1	8c	0.160(3)	1/4	1/4	1/4	4.58(3) <sup>c</sup>
O2	32f	0.128(3)	0 308(3)	0 308(3)	0 308(3)	4.58(3) <sup>c</sup>
O3	48i	0.013(3)	1/2	0 292(3)	0 292(3)	4.58(3) <sup>c</sup>
$x = 0.23$ , space group = $Fm\bar{3}m$						
Bi/Yb	24e	0.130/0.039(1)	0.046(1)	0	0	1.58(2)
O1	8c	0.344(1)	1/4	1/4	1/4	3.00(3) <sup>d</sup>
O2	32f	0.083(3)	0 329(3)	0 329(3)	0 329(3)	3.00(3) <sup>d</sup>
O3	48i	0.012(2)	1/2	0 481(3)	0 481(3)	3.00(3) <sup>d</sup>
$x = 0.25$ , space group = $Fm\bar{3}m$						
Bi/Yb	24e	0.129/0.037(1)	0.047(1)	0	0	1.59(2)
O1	8c	0.311(3)	1/4	1/4	1/4	3.47(3) <sup>e</sup>
O2	32f	0.091(3)	0 312(2)	0 312(2)	0 312(2)	3.47(3) <sup>e</sup>
O3	48i	0.011(3)	1/2	0 300(3)	0 300(3)	3.47(3) <sup>e</sup>

<sup>a,b,c,d,e</sup>Isotropic displacement parameter ( $B$ ) of O1, O2, and O3 with the same letter are linearly constraint to each other.

**Table S4.9:** X-ray powder diffraction data Rietveld refined structural parameter for  $x = 0.20 - 0.25$  in  $(\text{Bi}_{1-x}\text{Lu}_x)_2\text{O}_3$ .

$x = 0.20$ , space group = $P4_2/nmc$ , $\beta$ -phase (%) = 15.5(2)						
Atom	Site	Occupancy	$x$	$y$	$z$	$B / 10^{-4} \text{ pm}^2$
Bi/Lu	8g	0.40/0.10(2)	0	0.249(3)	0.243(3)	0.82(3)
O1	8f	0.51(3)	0.270(3)	0.270(3)	0	3.30(3) <sup>a</sup>
O2	4d	0.44(3)	0	1/2	0.490(3)	3.30(3) <sup>a</sup>
O3	2a	0.07(3)	0	0	0	3.30(3) <sup>a</sup>
$x = 0.20$ , space group = $Fm\bar{3}m$ , $\delta$ -phase (%) = 84.5(2)						
Bi/Lu	24e	0.133/0.034(1)	0.048(1)	0	0	1.53(3)
O1	8c	0.110(3)	1/4	1/4	1/4	4.18(3) <sup>b</sup>
O2	32f	0.140(3)	0.289(3)	0.289(3)	0.289(3)	4.18(3) <sup>b</sup>
O3	48i	0.012(3)	1/2	0.248(3)	0.248(3)	4.18(3) <sup>b</sup>
$x = 0.23$ , space group = $Fm\bar{3}m$						
Bi/Lu	24e	0.126/0.041(1)	0.047(1)	0	0	1.59(2)
O1	8c	0.360(3)	1/4	1/4	1/4	2.60(3) <sup>c</sup>
O2	32f	0.079(3)	0.315(3)	0.315(3)	0.315(3)	2.60(3) <sup>c</sup>
O3	48i	0.009(2)	1/2	0.394(3)	0.394(3)	2.60(3) <sup>c</sup>
$x = 0.25$ , space group = $Fm\bar{3}m$						
Bi/Lu	24e	0.125/0.041(1)	0.047(1)	0	0	1.60(2)
O1	8c	0.347(3)	1/4	1/4	1/4	2.90(3) <sup>d</sup>
O2	32f	0.084(3)	0.329(2)	0.329(2)	0.329(2)	2.90(3) <sup>d</sup>
O3	48i	0.007(2)	1/2	0.389(3)	0.389(3)	2.90(3) <sup>d</sup>

<sup>a,b,c,d</sup>Isotropic displacement parameter ( $B$ ) of O1, O2, and O3 with the same letter are linearly constraint to each other.

**Table S4.10:** Average Bi/*M*–O bond distances of the (Bi<sub>1-*x*</sub>*M<sub>x</sub>*)<sub>2</sub>O<sub>3</sub>  $\delta$ -phases obtained from X-ray powder data Rietveld refinements.

<b>&lt;Bi/<i>M</i>–O(1)&gt; /pm</b>									
<i>x</i>	Y	Gd	Tb	Dy	Ho	Er	Tm	Yb	Lu
0.13	--	241.1(1)	240.7(1)	240.4(1)	--	--	--	--	--
0.15	--	240.9(1)	240.5(1)	240.2(1)	239.9(1)	--	--	--	--
0.18	239.7(1)	240.8(1)	240.2(1)	239.9(1)	239.6(1)	--	--	--	--
0.20	239.6(1)	240.6(1)	240.1(1)	239.6(1)	239.3(1)	238.9(1)	238.7(1)	--	--
0.23	239.1(1)	240.4(1)	239.7(1)	239.3(1)	--	238.5(1)	238.3(1)	238.1(1)	238.0(1)
0.25	238.8(1)	240.2(1)	239.7(1)	239.1(1)	238.7(1)	238.4(1)	237.9(1)	238.0(1)	237.6(1)
<b>&lt;Bi/<i>M</i>–O(2)&gt; /pm</b>									
0.13	--	234.6(1)	236.1(1)	235.4(1)	--	--	--	--	--
0.15	--	230.1(1)	235.9(1)	236.1(1)	226.4(1)	--	--	--	--
0.18	244.8(1)	236.4(1)	235.3(1)	234.8(1)	234.6(1)	--	--	--	--
0.20	227.9(1)	236.4(1)	235.1(1)	234.6(1)	234.3(1)	234.4(1)	235.1(1)	--	--
0.23	234.2(1)	235.6(1)	234.6(1)	234.3(1)	--	233.6(1)	241.7(1)	235.1(1)	233.6(1)
0.25	234.5(1)	235.3(1)	234.6(1)	234.1(1)	233.7(1)	233.7(1)	235.8(1)	233.5(1)	234.6(1)
<b>&lt;Bi/<i>M</i>–O(3)&gt; /pm</b>									
0.13	--	197.3(1)	244.3(1)	217.4(1)	--	--	--	--	--
0.15	--	197.0(1)	238.1(1)	239.5(1)	242.3(1)	--	--	--	--
0.18	237.3(1)	197.0(1)	196.5(1)	196.2(1)	238.4(1)	--	--	--	--
0.20	218.4(1)	196.8(1)	200.4(1)	196.0(1)	236.4(1)	254.0(1)	198.6(1)	--	--
0.23	251.1(1)	216.2(1)	261.4(1)	236.6(1)	--	214.7(1)	195.1(1)	271.2(1)	250.4(1)
0.25	198.3(1)	196.6(1)	196.1(1)	260.1(1)	213.5(1)	211.6(1)	254.1(1)	211.8(1)	249.4(1)

**Table S4.11:** Bandgap energies calculated from UV/Vis diffuse reflectance spectroscopic data of  $(\text{Bi}_{1-x}\text{M}_x)_2\text{O}_3$  for  $M = \text{Tb}, \text{Dy},$  and  $\text{Y}$  using the RATD methods.

<b>Tb</b>						
DASF fitting				Tauc fitting		Type
$x$	$E_g$	$F_g$	$E^{d-}$	$E_d$	$E_i$	
0.05	2.55(2)	0.44(2)	2.05(2)	2.55(3)	2.05(3)	Direct
0.08	2.53(2)	0.61(2)	2.06(2)	2.60(3)	2.12(3)	Direct
0.10	2.68(2)	0.45(2)	2.34(2)	2.67(3)	2.16(3)	Direct
0.13	2.65(2)	0.42(2)	2.32(2)	2.70(3)	2.08(3)	Direct
0.15	2.72(2)	0.40(5)	2.46(9)	2.75(3)	2.17(3)	Direct
0.20	2.72(2)	0.35(2)	2.45(2)	2.70(3)	2.13(3)	Direct
0.25	2.75(2)	0.33(2)	2.46(2)	2.69(3)	2.13(3)	Direct
<b>Dy</b>						
0.10	2.56(2)	0.51(2)	2.22(2)	2.65(3)	2.24(3)	Direct
0.13	2.68(2)	0.42(2)	2.25(2)	2.73(3)	2.22(3)	Direct
0.15	2.69(2)	0.44(2)	2.23(2)	2.75(3)	2.21(3)	Direct
0.20	2.72(2)	0.39(2)	2.20(2)	2.74(3)	2.22(3)	Direct
0.25	2.75(2)	0.34(2)	2.20(2)	2.74(3)	2.13(3)	Direct
<b>Y</b>						
0.05	2.43(2)	0.51(2)	1.98(2)	2.52(3)	2.08(3)	Direct
0.10	2.57(2)	0.53(2)	2.23(2)	2.65(3)	2.19(3)	Direct
0.13	2.64(2)	0.42(2)	2.31(2)	2.67(3)	2.18(3)	Direct
0.15	2.70(2)	0.48(2)	2.33(2)	2.74(3)	2.14(3)	Direct
0.18	2.74(2)	0.40(2)	2.34(2)	2.75(3)	2.16(3)	Direct
0.20	2.78(2)	0.43(2)	2.34(2)	2.79(3)	2.16(3)	Direct
0.23	2.74(2)	0.44(2)	2.34(2)	2.71(3)	2.14(3)	Direct
0.25	2.80(2)	0.44(2)	2.34(2)	2.78(3)	2.14(3)	Direct

$E_g$ ,  $E^{d-}$  and  $F_g$  refer to bandgap energy, anionic defect transition, and band flatness in eV, respectively, obtained from the fitting of the DASF plots. The  $E_d$  and  $E_i$ , respectively represent direct and indirect transition in eV determined from the Tauc plots.

**Table S4.12:** Bandgap energies calculated from UV/Vis diffuse reflectance spectroscopic data of  $(\text{Bi}_{1-x}\text{M}_x)_2\text{O}_3$  for  $M = \text{Tm}, \text{Yb},$  and  $\text{Lu}$  using the RATD methods.

<b>Tm</b>						
DASF fitting				Tauc fitting		Type
$x$	$E_g$	$F_g$	$E^{d-}$	$E_d$	$E_i$	
0.18	2.69(2)	0.57(2)	2.27(2)	2.70(3)	2.16(3)	Direct
0.20	2.70(2)	0.58(2)	2.27(2)	2.72(3)	2.16(3)	Direct
0.23	2.73(2)	0.57(2)	2.27(2)	2.72(3)	2.15(3)	Direct
0.25	2.72(2)	0.62(2)	2.27(2)	2.73(3)	2.17(3)	Direct
<b>Yb</b>						
0.05	2.39(2)	0.53(2)	2.05(2)	2.50(3)	2.10(3)	Direct
0.10	2.46(2)	0.66(2)	2.00(2)	2.67(3)	2.14(3)	Direct
0.13	2.62(2)	0.49(2)	2.26(3)	2.68(3)	2.11(3)	Direct
0.15	2.67(2)	0.48(2)	2.24(2)	2.71(3)	2.13(3)	Direct
0.20	2.67(2)	0.59(5)	2.25(2)	2.76(3)	2.11(3)	Direct
0.23	2.72(2)	0.49(2)	2.23(2)	2.71(3)	2.09(3)	Direct
0.25	2.73(4)	0.59(5)	2.22(2)	2.77(3)	2.11(3)	Direct
<b>Lu</b>						
0.20	2.69(2)	0.51(2)	2.17(2)	2.73(3)	2.15(3)	Direct
0.23	2.70(2)	0.64(2)	2.20(2)	2.74(3)	2.15(3)	Direct
0.25	2.71(2)	0.62(2)	2.21(2)	2.72(3)	2.16(3)	Direct

$E_g$ ,  $E^{d-}$  and  $F_g$  refer to bandgap energy, anionic defect transition, and band flatness in eV, respectively, obtained from the fitting of the DASF plots. The  $E_d$  and  $E_i$ , respectively represent direct and indirect transition in eV determined from the Tauc plots.

**Table S4.13:** Bandgap energies calculated from UV/Vis diffuse reflectance spectroscopic data of  $(\text{Bi}_{1-x}\text{M}_x)_2\text{O}_3$  for  $M = \text{Ho}$  and  $\text{Er}$  using the Tauc fitting.

$x$	<b>Ho</b>		<b>Er</b>	
	$E_d$	$E_i$	$E_d$	$E_i$
0.13	2.70(3)	2.27(3)	2.67(3)	2.10(3)
0.15	2.75(3)	2.27(3)	2.69(3)	2.10(3)
0.18	2.75(3)	2.26(3)	--	--
0.20	2.75(3)	2.26(3)	2.68(3)	2.13(3)
0.25	2.75(3)	2.24(3)	2.61(3)	2.10(3)

The  $E_d$  and  $E_i$ , respectively represent direct and indirect transition in eV determined from the Tauc plots.

## Chapter 5

### Impact of $M^{n+}$ charge and size on $\delta$ -phases formation: structural and spectroscopic investigations with $M = \text{Cr}$ and $\text{Ta}$

#### Abstract

The  $\delta$ -phase of  $\text{Bi}_2\text{O}_3$  is stabilized at ambient condition by substituting  $\text{Bi}^{3+}$  with small size cations, specifically  $\text{Cr}^{3+}$  and  $\text{Ta}^{5+}$ , following the formula  $(\text{Bi}_{1-x}\text{M}^{n+}_x)_2\text{O}_{3+(n-3)x}$ . The substitution produces two distinct series: one with Cr and the other with Ta. The Cr-series is studied at compositions  $x = 0.15, 0.20, 0.25, 0.27,$  and  $0.30$ , whereas the Ta-series is examined at  $x = 0.05, 0.10, 0.15, 0.20, 0.25, 0.27,$  and  $0.30$ . During synthesis at  $1273 \text{ K}$ , the  $\text{Cr}^{3+}$  cation is oxidized to  $\text{Cr}^{6+}$ , resulting in a mixed oxidation state. The portion of  $\text{Cr}^{3+}$  and  $\text{Cr}^{6+}$  are identified by X-ray photoelectron spectroscopy. The solid solution of Cr-series is identified as  $\delta$ -phase within the compositional range of  $x = 0.15$  to  $0.30$  by X-ray powder diffraction technique. The three-dimensional incommensurate structural modulation reflects the complexity of this high symmetric phase. The lattice parameters of Cr-series remain unchanged throughout the entire compositional range of  $x = 0.15$  to  $0.30$ . The Ta-series exhibits both  $\beta$ - and  $\delta$ -phase at low  $x$ -values, while a pure  $\delta$ -phase is identified at the  $x = 0.25$  solid solution. The lattice parameter decreases with increasing substitution level. All phases are verified by the X-ray powder diffraction and Raman spectroscopy. A strong Raman shift at  $314(2) \text{ cm}^{-1}$  serves as an indicator of the  $\beta$ -phase, while the disappearance of this Raman band in a mixed solid solution indicates the formation of pure  $\delta$ -phase. The bandgap energy of pure  $\delta$ -phase is investigated using UV/Vis diffuse reflectance spectroscopy, revealing bandgaps of  $2.27(2) \text{ eV}$  and  $2.93(2) \text{ eV}$  at the  $x = 0.25$  composition for Cr- and Ta-series, respectively. Anionic and cationic defect absorption bands are identified in Cr-series, with an irreversible trend across the composition

$x$ -value. Only an anionic absorption band is found in the Ta-series, and the presence of this band in both series indicates oxygen vacancies in the  $\delta$ -phase.

**Keywords:** Bismuth oxide, delta phase, oxygen vacancy, oxidation state, and bandgap.

## 1. Introduction

The structural phase transition from low-symmetric to high-symmetric phase is a notable feature for accommodating defects within the overall structure. This attribute of bismuth oxide phases highlights their potential as semiconductor [1], solid electrolyte [2, 3], and ferroelectric material [4]. Internal phase transition in bismuth oxide is examined through their occurrence at various temperatures [5-7] and the substitution of  $\text{Bi}^{3+}$  with other  $M^{n+}$  cation [1, 8, 9]. The choice of phase is influenced by the cationic size, as discussed in **chapter 6**. Comparable-sized cations with different charges ( $M^{n+}$ ) affect the degree of phase stabilization. Transition metals  $\text{Cr}^{3+}$  and  $\text{Ta}^{5+}$  are suitable candidates due to their nearly identical cationic sizes within six-fold coordination [10]. Understanding phase formation at different temperatures and structural modification by substitution  $\text{Bi}^{3+}$  with other  $M^{n+}$  cation ( $M = \text{Cr}, \text{Ta}$ ) is essential. For example,  $\text{Bi}_6\text{Cr}_2\text{O}_{15}$  is a thermochromic material where  $\text{Cr}^{3+}$  ion is oxidized to  $\text{Cr}^{6+}$  during synthesis at 923 K in an open condition [11]. The compound crystallizes in space group  $Ccc2$  (no. 37) with the lattice parameters  $a = 1230.18(2)$  pm,  $b = 1987.49(2)$  pm, and  $c = 588.16(1)$  pm [11]. The isolated  $\text{CrO}_4^{2-}$  tetrahedron is connected within  $\text{Bi}(2)/\text{Bi}(3)\text{-O-Cr}$  framework. The  $\text{Bi}(1)\text{-O}$  bond lengths in the first coordination sphere range from 213 pm to 234 pm, while  $\text{Bi}(1)/\text{Bi}(2)\text{-O}$  bond lengths range from 209 pm to 221 pm, and short 163 - 168 pm bonds are found in  $\text{CrO}_4^{2-}$  tetrahedron [11].  $\text{Bi}_{14}\text{CrO}_{24}$ , which crystallizes in space group  $I4/m$  (no. 87), has a deep red color and is synthesized at 1023 K in open condition [12]. Its lattice parameters



are  $a = 868.4(1)$  pm and  $c = 1723.8(1)$  pm. The  $\text{CrO}_4^{2-}$  tetrahedron is weakly connected via the Bi(2)–O–Cr linkage, with Bi(2)–O(6,7) bonds measuring 282.14 pm and 288.08 pm [12]. Bi(1)–O bond lengths range from 235.12 pm to 273.07 pm, while Bi(3)–O bonds range from 208.57 pm to 274.96 pm [12]. A series of  $\text{Bi}_{1-x}\text{Cr}_x\text{O}_{1.5+1.5x}$  with average fluorite-type ( $\delta$ - $\text{Bi}_2\text{O}_3$ ) structure in space group  $Fm\bar{3}m$  (no. 225) is synthesized at 1223 K followed by direct quenching in water [13]. Compositions  $x = 0.05, 0.10,$  and  $0.15$  show three-dimensional incommensurate modulation, with satellite reflections described by atomic modulation functions and periodic nodal surfaces [13]. Lattice parameters are  $a = 558.67(3)$  pm,  $559.05(2)$  pm, and  $560.25(3)$  pm for  $x = 0.05, 0.10,$  and  $0.15,$  respectively [13].  $\text{Bi}^{3+}$  and  $\text{Cr}^{6+}$  share the same Wyckoff position, and  $\text{CrO}_4^{2-}$  tetrahedron in sixfold coordination is confirmed by infrared spectroscopy. Further investigation of the  $\text{Bi}_{1-x}\text{Cr}_x\text{O}_{1.5+1.5x}$  series at higher substitution levels remains open, with  $\text{Cr}^{3+}$  oxidation to  $\text{Cr}^{6+}$  occurring between 923 K and 1223 K. Low-level substitution of  $\text{Bi}^{3+}$  by  $\text{Ta}^{5+}$  in  $(\text{Bi}^{3+}_{1-x}\text{Ta}^{5+}_x)_2\text{O}_{3+2x}$  solid solution that crystallize in space group  $P4_2/nmc$  (no. 137) as  $\beta$ -phase, with an example at 8% substitution showing lattice parameters  $a = 770.69(6)$  pm and  $c = 567.35(5)$  pm [9]. The  $\delta$ -phase appears at  $x = 0.20$  composition in  $(\text{Bi}^{3+}_{1-x}\text{Ta}^{5+}_x)_2\text{O}_{3+2x}$  [14, 15] but is not further confirmed by spectroscopy. In the  $\delta$ -phase, atoms exhibit irregular shifts from their ideal positions, with identical ions showing different coordination [16, 17]. This behavior, known as anti-glass disorder [9], is reflected in the high atomic displacement parameter. In this investigation, the general formula  $(\text{Bi}^{3+}_{1-x}\text{M}^{n+}_x)_2\text{O}_{3+(n-3)x}$  is used for the successive substitution of  $\text{Bi}^{3+}$  by  $\text{M}^{n+}$  ( $M = \text{Cr}$  and  $\text{Ta}$ ). This study focuses on the appearance of  $\delta$ -phase, considering the effects of cationic charge and size.

## **2. Experimental**

### **2.1. Synthesis**

All samples are prepared by mixing stoichiometric amounts of  $\text{Bi}_2\text{O}_3$  and metal oxide ( $\text{Cr}_2\text{O}_3$  or  $\text{Ta}_2\text{O}_5$ ) in an agate mortar and placed in a platinum or corundum crucible. The Cr-series is heated at 1273 K for 2 minutes, quenched in an icy water bath, and dried at 373 K for 24 h. The Ta-series solid solution is heated at 923 K for 24 h, air-quenched, ground, then reheated at 1073 K for 24 h and quenched to room temperature.

### **2.2. Microscopy**

Scanning electron microscopy (SEM) is performed using a JMS-6510 (JEOL) with a X-Flash 410-M detector (Bruker) for energy dispersive X-ray spectroscopy (EDX) analysis. Samples are placed on conducting carbon tabs, gold-sputtered for 20 s with a JFC-1200 coater (JEOL), and then inserted into the SEM chamber.

### **2.3. X-ray photoelectron spectroscopy**

X-ray photoelectron spectroscopy (XPS) measurements have been performed on a Specs GmbH customized spectrometer, equipped with a Phoibos 150 hemispherical electron analyzer and a 1D-DLD Detector. Monochromatized Al radiation ( $E = 1486.6$  eV) operated at 15 kV and 200 W has been used for excitation, and the pressure in the analysis chamber was about  $10^{-10}$  mbar. An electron flood gun has been used to compensate for charging. All spectra have been referenced to the C1s peak at a value of 284.5 eV. The spectrometer was operated in Medium Area Mode. The survey spectrum has been collected at a pass energy of 50 eV, and the high-resolution spectra were measured at 20 eV.

## 2.4. X-ray diffraction

X-ray powder diffraction (XRPD) patterns are recorded on a Bruker D8 Discover powder diffractometer using Bragg-Brentano geometry with  $\text{CuK}_{\alpha 1,2}$  ( $\lambda_{\text{K}\alpha 1} = 154.05929(5)$  pm,  $\lambda_{\text{K}\alpha 2} = 154.4414(2)$  pm) radiation. The measurements are taken at ambient condition with a step size of  $0.0167^\circ$  and a total data collection time of 75 s/step. The fundamental parameter approach, where the fundamental parameters are fitted against a  $\text{LaB}_6$  standard material, is applied for the Rietveld refinement using 'Diffrac<sup>Plus</sup>Topas 6' software (Bruker AXS GmbH, Karlsruhe, Germany). The starting lattice parameters and atomic coordinates are taken from the crystal structure of  $\beta$ - and  $\delta$ -phase [3, 9] (ICSD Coll. Code 83640 and 60198,  $Z = 2$ ). During Rietveld refinements, the background, sample displacement, atomic coordinates, and occupancy parameters are optimized. In all cases, the isotropic displacement parameters between  $\text{Bi}^{3+}$  and  $M^{n+}$ , and between the oxygen atoms (O1, O2, O3) are constrained. During the Rietveld refinements, bismuth has found on  $24e$  Wyckoff positions, and partially share the same site with  $M^{n+}$  cation. Successive refinement trials reveal mixed occupancy of  $\text{Bi}^{3+}$  and  $M^{n+}$ . The average crystallite size (ACS) and microstrain (MS) are calculated from the observed all X-ray reflections, using the fundamental approach, where ACS and MS are defined as  $L_{\text{Vol}}(\text{IB})$  and  $\varepsilon_0$  by the TOPAS software [18].

## 2.5. Raman spectroscopy

Raman spectra are recorded on a LabRam ARAMIS (Horiba JobinYvon, New Jersey) confocal Raman microscope with an excitation energy of 784 nm and 532 nm laser for Cr- and Ta-series, respectively. Where suitable laser (transparent region) is identified by the UV/Vis diffuse reflectance spectrum. A  $50\times$  objective, a moving grating of 1800 grooves/mm and a thermodynamically cooled CCD detector (Synapse,  $1024\times 256$  pixels) provide the spectral

width of about  $1\text{ cm}^{-1}$  for 784 nm laser and  $3\text{ cm}^{-1}$  for the 532 nm laser. The spectral positions are calibrated against the Raman mode of silicon at  $520.7\text{ cm}^{-1}$  before the measurement.

## 2.6. UV/Vis diffuse reflectance spectroscopy

UV/Vis diffuse reflectance spectra are recorded at room temperature on a Shimadzu UV-2600 (Shimadzu, Kyoto, Japan) spectrometer. Data are collected in the range between 190 nm to 850 nm with a step size of 1 nm.  $\text{BaSO}_4$  powder is used as the reference standard for baseline correction. The bandgap energies and the types of transition are determined using the RATD method described elsewhere [19].

## 3. Results and Discussion

### *Crystal structure*

Micrometer-sized particles are observed in the SEM image (Fig. 5.1), appearing as a solidified mass without distinct shapes. The calculated ACS and MS for the  $\delta$ -phase in the Cr- and Ta-

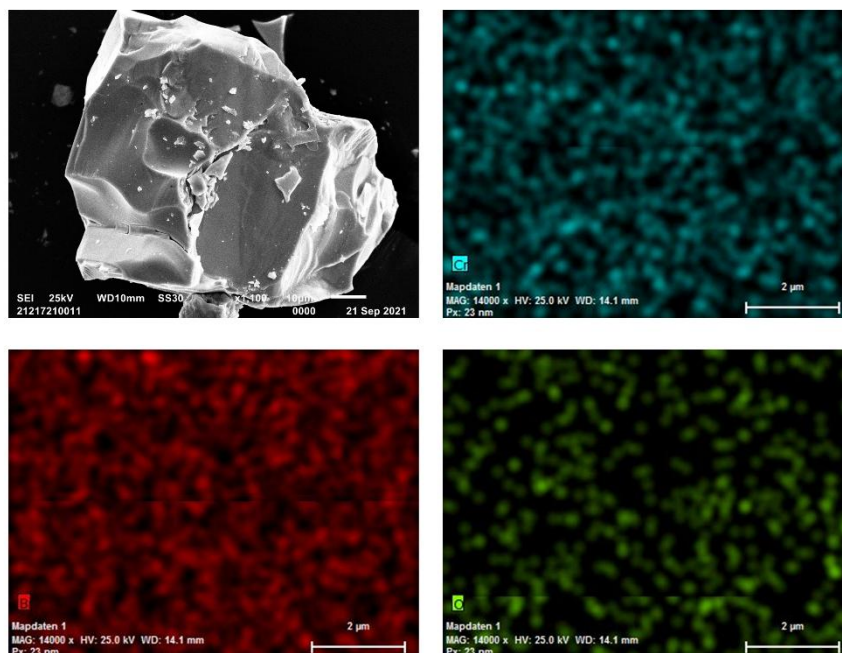


**Figure 5.1:** Scanning electron micrograph and EDX spectrum of Bi, Cr, and O for  $x = 0.15$  composition in  $(\text{Bi}^{3+}_{1-x}\text{Cr}^{n+}_x)_2\text{O}_{3+(n-3)x}$ .

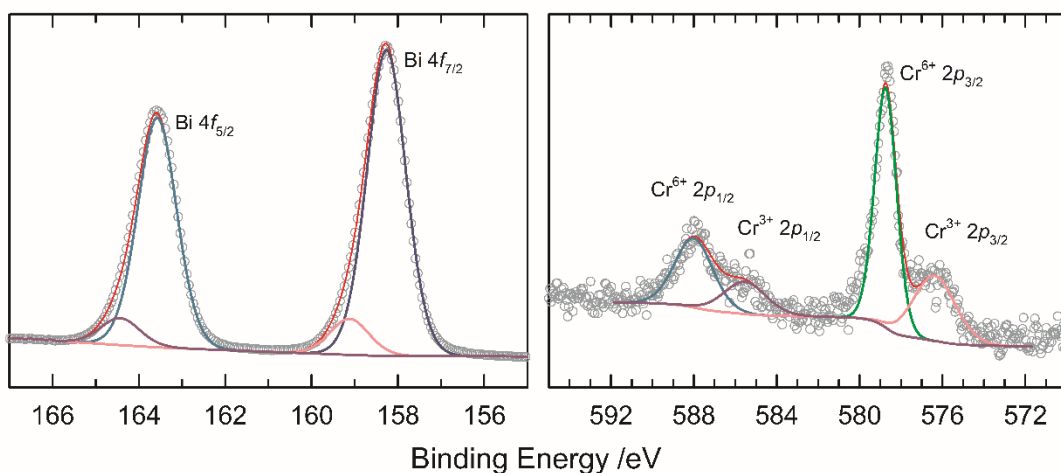


**Figure 5.2:** X-ray photoelectron spectra and peak fitting of Bi 4*f* and Cr 2*p* for  $x = 0.15$  composition in  $(\text{Bi}^{3+}_{1-x}\text{Cr}^{n+}_x)_2\text{O}_{3+(n-3)x}$ .

series of  $(\text{Bi}^{3+}_{1-x}\text{M}^{n+}_x)_2\text{O}_{3+(n-3)x}$  are  $55.85 \pm 4.75$  nm and  $0.031 \pm 0.008$ , respectively (**Tab. S5.1**, supplementary information). EDX analysis shows an atomic composition of 83% Bi and 17% Cr for  $x = 0.15$ , matching the nominal composition. XPS spectra for the  $x = 0.15$  compound are displayed in **figures 5.2 and S5.1**. The Bi 4*f* spectrum shows peaks at 158.27(1) eV ( $4f_{7/2}$ ) and 163.58(1) eV ( $4f_{5/2}$ ) with a spin-orbital separation of 5.3(1) eV (**Fig. 5.2a**), indicating  $\text{Bi}^{3+}$  cations [20]. Two components with their  $4f_{7/2}$  branch at 159.12(1) eV and 158.27(1) eV correspond to Bi–O–Bi and Bi–O–Cr bonds, respectively [21]. The Cr 2*p* spectrum reveals  $\text{Cr}^{6+}$  and  $\text{Cr}^{3+}$  oxidation states (**Fig. 5.2b**), with  $\text{Cr}^{6+}$  as the dominant species. Peaks at 578.74(1) eV and 576.38(1) eV confirm the presence of  $\text{Cr}^{6+} 2p_{3/2}$  and  $\text{Cr}^{3+} 2p_{3/2}$ , respectively [22].

The XRPD patterns for Cr- and Ta-series of  $(\text{Bi}^{3+}_{1-x}\text{M}^{n+}_x)_2\text{O}_{3+(n-3)x}$  are presented in **figure 5.3**. XRPD data Rietveld refinements confirm phase purity in the Cr-series for  $x = 0.15$  to 0.30, although extra reflections are observed between  $2\theta$  angle of  $7^\circ$  and  $40^\circ$  (**Fig. 5.3a**). This incommensurate three-dimensional modulation is reported elsewhere for  $x = 0.05$ , 0.10, and 0.15 [13]. Similar observations are noted in the Mo- and W-series, discussed in **chapter 6**. **Figure 5.4** shows representative Rietveld refinement plots for  $x = 0.15$  and 0.30, and the crystal

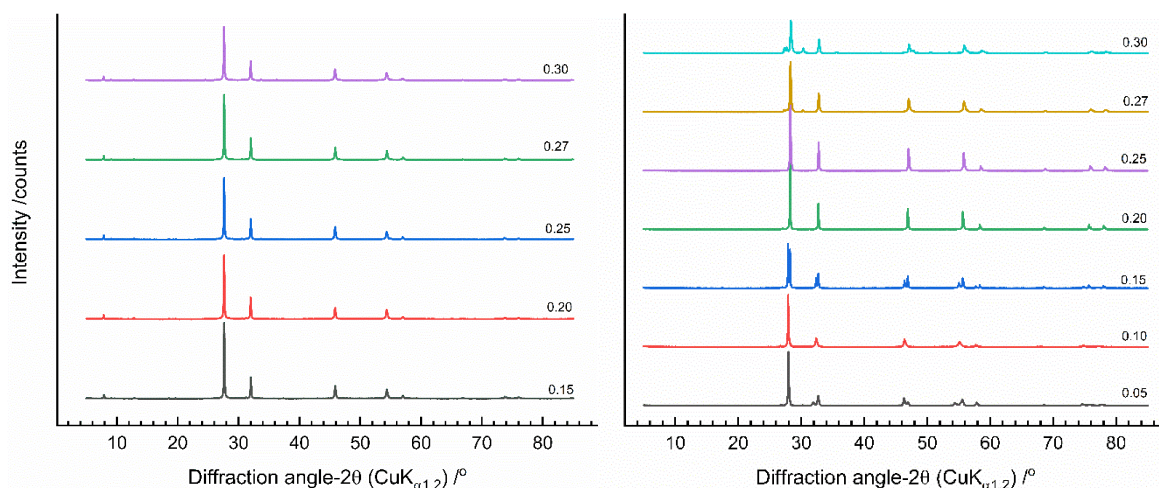


**Figure 5.3:** X-ray powder diffraction data of Cr-series (left) and Ta-series (right) at different  $x$ -value in  $(\text{Bi}^{3+}_{1-x}\text{M}^{n+}_x)_2\text{O}_{3+(n-3)x}$ .

structure parameters are listed in **table 5.1**. XPS analysis identifies both  $\text{Cr}^{6+}$  and  $\text{Cr}^{3+}$  oxidation states in  $x = 0.15$  composition, leading to independent occupancy parameter refinement during XRPD data Rietveld refinement for compositions  $x = 0.15$  to 0.30. The chemical formula for each solid solution is provided in **table 5.1**. XRPD data Rietveld refinements of Ta-series indicate that the  $\delta$ -phase is pure only at  $x = 0.25$  (**Fig. 5.5**). Mixed phases of  $\beta$ - and  $\delta$ -phase are observed between  $x = 0.05$  and 0.20 (**Fig. 5.3b, S5.2**). Beyond  $x = 0.25$ , low symmetric triclinic structure [23] with space group  $P\bar{1}$  (no. 2) coexist with the  $\delta$ -phase (**Fig. 5.3b, S5.3**). The crystal structure parameters are detailed in **table 5.2**.

The lattice parameter ( $a$ ) of the  $(\text{Bi}^{3+}_{1-x}\text{Cr}^{n+}_x)_2\text{O}_{3+(n-3)x}$  series ranges from 559.82(2) pm to 560.18(3) pm (**Tab. 5.1**), consistent with previous reports in literature [13]. The complex incommensurate structural modulation may explain the unusual trends in  $a$ . At  $x = 0.15$ , the comparison of  $a$  (560.03(2) pm for Cr-series and 547.37(2) pm for Ta-series) highlights the structural complexity of the Cr-series. Despite  $\text{Ta}^{5+}$  having a larger cationic size than  $\text{Cr}^{6+}$  and  $\text{Cr}^{3+}$  [10], the Ta-series exhibits smaller  $a$  compared to the Cr-series. The Ta-series shows a linear decrease in  $a$  for the  $\delta$ -phase (**Fig. 5.6a**), with values of 551.83(3) pm at  $x = 0.05$  and

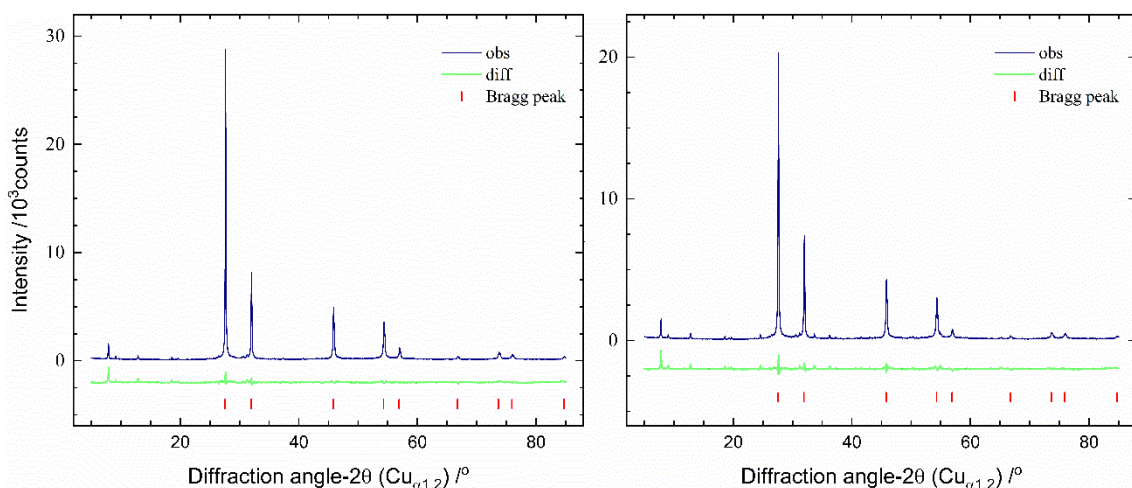


**Figure 5.4:** X-ray powder diffraction data Rietveld plot of  $x = 0.15$  (left) and  $0.30$  (right) compositional value in  $(\text{Bi}^{3+}_{1-x}\text{Cr}^{n+}_x)_2\text{O}_{3+(n-3)x}$ .

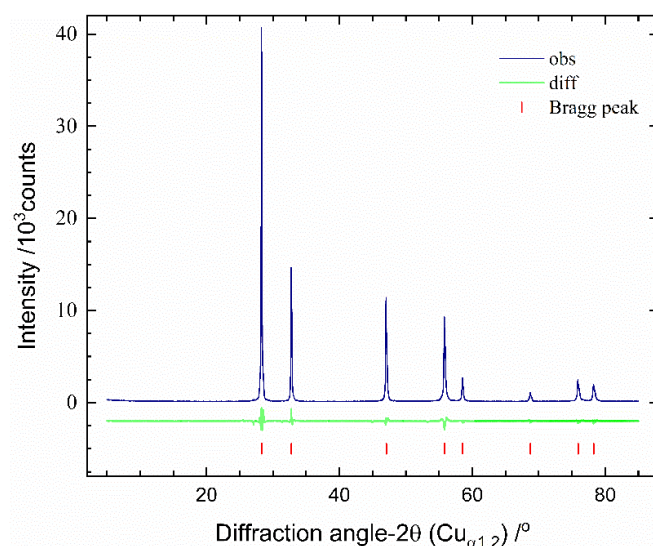


**Figure 5.5:** X-ray powder diffraction data Rietveld plot of  $x = 0.25$  in  $(\text{Bi}^{3+}_{1-x}\text{Ta}^{5+}_x)_2\text{O}_{3+2x}$ .

545.79(2) pm at  $x = 0.25$ . A similar trend is observed in the low-symmetry  $\beta$ -phase (**Fig.S5.4**) between  $x = 0.05$  and  $0.20$ , where  $\beta$ -phase appears as an impurity. These changes in lattice parameters indicate structural modifications due to  $\text{Bi}^{3+}$  substitution, with a noticeable saturation for  $\delta$ -phase observed between  $x = 0.27$  and  $0.30$  (**Fig.5.6a**). The formation of pure  $\delta$ -phase at  $x = 0.25$  and the onset of impurities starting at  $x = 0.27$  suggest that the  $\delta$ -phase of Ta-series reaches its maximum  $\text{Bi}^{3+}$  substitution at  $x = 0.25$ . The bond topology in  $\text{Bi}/\text{MO}_x$  pol-



**Table 5.1:** X-ray powder diffraction data Rietveld refined structural parameter for  $x = 0.15 - 0.30$  in  $(\text{Bi}^{3+}_{1-x}\text{Cr}^{n+}_x)_2\text{O}_{3+(n-3)x}$ .

$x = 0.15$ , space group = $Fm\bar{3}m$ , $a = 560.03(2)$ pm, $(\text{Bi}^{3+}_{1.70}\text{Cr}^{3+}_{0.015}\text{Cr}^{6+}_{0.285})\text{O}_{3.428}$						
Atom	Site	Occupancy	$x$	$y$	$z$	$B / 10^{-4} \text{ pm}^2$
Bi/Cr	$24e$	0.142/0.025(1)	0.063(2)	0	0	1.71(3)
O1	$8c$	0.310(3)	1/4	1/4	1/4	3.40(3) <sup>a</sup>
O2	$32f$	0.092(3)	0 302(3)	0 302(3)	0 302(3)	3.40(3) <sup>a</sup>
O3	$48i$	0.030(3)	1/2	0 300(3)	0 300(3)	3.40(3) <sup>a</sup>
$x = 0.20$ , space group = $Fm\bar{3}m$ , $a = 560.09(2)$ pm, $(\text{Bi}^{3+}_{1.60}\text{Cr}^{3+}_{0.020}\text{Cr}^{6+}_{0.380})\text{O}_{3.570}$						
Bi/Cr	$24e$	0.133/0.033(1)	0.064(2)	0	0	1.69(3)
O1	$8c$	0.356(3)	1/4	1/4	1/4	4.50(3) <sup>b</sup>
O2	$32f$	0.080(3)	0 346(3)	0 346(3)	0 346(3)	4.50(3) <sup>b</sup>
O3	$48i$	0.036(3)	1/2	0 268(3)	0 268(3)	4.50(3) <sup>b</sup>
$x = 0.25$ , space group = $Fm\bar{3}m$ , $a = 560.16(2)$ pm, $(\text{Bi}^{3+}_{1.50}\text{Cr}^{3+}_{0.025}\text{Cr}^{6+}_{0.475})\text{O}_{3.713}$						
Bi/Cr	$24e$	0.125/0.041(1)	0.064(2)	0	0	1.76(3)
O1	$8c$	0.410(3)	1/4	1/4	1/4	3.44(3) <sup>c</sup>
O2	$32f$	0.670(3)	0 313(2)	0 313(2)	0 313(2)	3.44(3) <sup>c</sup>
O3	$48i$	0.042(3)	1/2	0 333(3)	0 333(3)	3.44(3) <sup>c</sup>
$x = 0.27$ , space group = $Fm\bar{3}m$ , $a = 559.82(2)$ pm, $(\text{Bi}^{3+}_{1.46}\text{Cr}^{3+}_{0.027}\text{Cr}^{6+}_{0.513})\text{O}_{3.770}$						
Bi/Cr	$24e$	0.122/0.045(1)	0.064(1)	0	0	1.75(3)
O1	$8c$	0.364(3)	1/4	1/4	1/4	3.70(3) <sup>d</sup>
O2	$32f$	0.077(3)	0 337(2)	0 337(2)	0 337(2)	3.70(3) <sup>d</sup>
O3	$48i$	0.045(3)	1/2	0 281(3)	0 281(3)	3.70(3) <sup>d</sup>
$x = 0.30$ , space group = $Fm\bar{3}m$ , $a = 560.18(2)$ pm, $(\text{Bi}^{3+}_{1.40}\text{Cr}^{3+}_{0.030}\text{Cr}^{6+}_{0.570})\text{O}_{3.855}$						
Bi/Cr	$24e$	0.117/0.050(1)	0.064(1)	0	0	1.73(3)
O1	$8c$	0.375(3)	1/4	1/4	1/4	4.00(3) <sup>e</sup>
O2	$32f$	0.075(3)	0 348(3)	0 348(3)	0 348(3)	4.00(3) <sup>e</sup>
O3	$48i$	0.048(3)	1/2	0 299(3)	0 299(3)	4.00(3) <sup>e</sup>

<sup>a,b,c,d,e</sup>Isotropic displacement parameter ( $B$ ) of O1, O2, and O3 with the same letter are linearly constraint to each other.



**Table 5.2:** X-ray powder diffraction data Rietveld refined structural parameter for  $x = 0.05 - 0.30$  in  $(\text{Bi}^{3+}_{1-x}\text{Ta}^{5+}_x)_2\text{O}_{3+2x}$ .

$x = 0.05$ , space group = $P4_2/nmc$ , $a = 773.72(2)$ pm, $c = 561.59(2)$ pm, $\beta$ -phase (%) = 83.4(3)						
Atom	Site	Occupancy	$x$	$y$	$z$	$B / 10^{-4} \text{ pm}^2$
Bi/Ta	8g	0.475/0.025(1)	0	0.252(3)	0.236(2)	1.77(3)
O1	8f	0.459(2)	0.365(3)	0.365(3)	0	3.50(3) <sup>a</sup>
O2	4d	0.522(2)	0	1/2	0.452(4)	3.50(3) <sup>a</sup>
O3	2a	0.220(2)	0	0	0	3.50(3) <sup>a</sup>
$x = 0.05$ , space group = $Fm\bar{3}m$ , $a = 551.83(3)$ pm, $\delta$ -phase (%) = 16.6(3)						
Bi/Ta	24e	0.158/0.008(1)	0.035(2)	0	0	1.22(3)
O1	8c	0.308(3)	1/4	1/4	1/4	1.26(3) <sup>b</sup>
O2	32f	0.082(3)	0.262(3)	0.262(3)	0.262(3)	1.26(3) <sup>b</sup>
O3	48i	0.023(3)	1/2	0.390(3)	0.390(3)	1.26(3) <sup>b</sup>
$x = 0.20$ , space group = $Fm\bar{3}m$ , $a = 547.31(2)$ pm, $\delta$ -phase (%) = 72.8(3)						
Bi/Ta	24e	0.133/0.033(1)	0.028(1)	0	0	1.16(2)
O1	8c	0.311(3)	1/4	1/4	1/4	3.50(3) <sup>c</sup>
O2	32f	0.093(3)	0.301(2)	0.301(2)	0.301(2)	3.50(3) <sup>c</sup>
O3	48i	0.027(3)	1/2	0.315(3)	0.315(3)	3.50(3) <sup>c</sup>
$x = 0.25$ , space group = $Fm\bar{3}m$ , $a = 545.79(2)$ pm, $\delta$ -phase (%) = 100.0(1)						
Bi/Ta	24e	0.125/0.042(1)	0.026(2)	0	0	1.17(2)
O1	8c	0.321(2)	1/4	1/4	1/4	4.30(3) <sup>d</sup>
O2	32f	0.089(3)	0.304(3)	0.304(3)	0.304(3)	4.30(3) <sup>d</sup>
O3	48i	0.033(2)	1/2	0.288(3)	0.288(3)	4.30(3) <sup>d</sup>
$x = 0.27$ , space group = $Fm\bar{3}m$ , $a = 545.37(2)$ pm, $\delta$ -phase (%) = 88.6(1)						
Bi/Ta	24e	0.122/0.045(1)	0.033(1)	0	0	1.15(2)
O1	8c	0.431(2)	1/4	1/4	1/4	4.30(3) <sup>e</sup>
O2	32f	0.065(3)	0.296(3)	0.296(3)	0.296(3)	4.30(3) <sup>e</sup>
O3	48i	0.032(3)	1/2	0.270(3)	0.270(3)	4.30(3) <sup>e</sup>
$x = 0.30$ , space group = $Fm\bar{3}m$ , $a = 545.36(2)$ pm, $\delta$ -phase (%) = 62.2(2)						
Bi/Ta	24e	0.117/0.050(1)	0.032(1)	0	0	1.16(2)
O1	8c	0.399(3)	1/4	1/4	1/4	4.80(3) <sup>f</sup>
O2	32f	0.068(3)	0.276(3)	0.276(3)	0.276(3)	4.80(3) <sup>f</sup>
O3	48i	0.037(3)	1/2	0.300(3)	0.300(3)	4.80(3) <sup>f</sup>

<sup>a,b,c,d,e,f</sup>Isotropic displacement parameter ( $B$ ) of O1, O2, and O3 with the same letter are linearly constraint to each other.

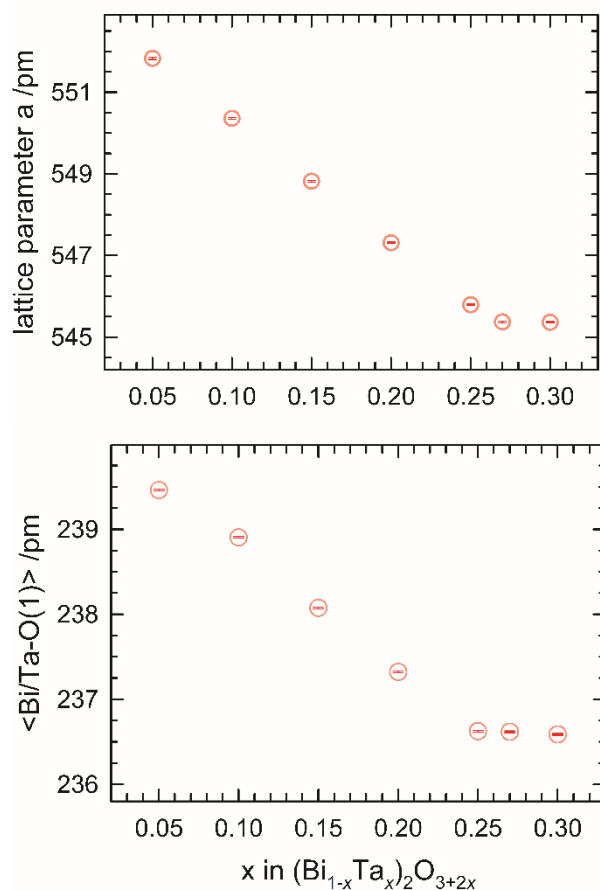


**Figure 5.6:** Evolution of metric parameter (up) and average  $\langle \text{Bi/Ta-O}(1) \rangle$  bond distances (down) in metal oxide polyhedra of  $(\text{Bi}^{3+}_{1-x}\text{Ta}^{5+}_x)_2\text{O}_{3+2x}$  with varying compositional  $x$  value for the  $\delta$ -phase.

hedra is quite diverge, with O(1) occupying the ideal anionic lattice position of the  $\delta$ -phase, defined by a  $\text{CaF}_2$ -type high-symmetry structure [3]. The displacement of oxygen position along  $\langle 111 \rangle$  direction from O(1) creates O(2) position, while O(3) serves as an interstitial site between O(1) and O(2) [3, 17]. Details of the  $\delta$ -phase are discussed in **chapter 4**. The bond lengths of  $\text{Bi}/M\text{-O}$  are provided in **table 5.3** for  $M = \text{Cr}$  and Ta. For the compositions of  $(\text{Bi}^{3+}_{1-x}\text{Cr}^{n+}_x)_2\text{O}_{3+(n-3)x}$  at  $x = 0.15$  to  $0.30$ , the  $\text{Bi}/\text{Cr-O}(1)$  bond length is stable at  $244.24 \pm 0.07$  pm, reflecting a similar trend in the lattice parameter. The  $\text{Bi}/\text{Cr-O}(2)$  and  $\text{Bi}/\text{Cr-O}(3)$  bond lengths vary from  $234.72 \pm 4.27$  pm and  $214.54 \pm 5.76$  pm (**Tab. 5.3**), respectively. The shorter  $\text{Bi}/\text{Cr-O}(3)$  bond length likely indicates the tetrahedral coordination of  $\text{Cr}^{6+}$  cation. The  $\delta$ -pha-

**Table 5.3:** Average Bi/*M*–O bond distances of the  $(\text{Bi}^{3+}_{1-x}\text{M}^{n+}_x)_2\text{O}_{3+(n-3)x}$   $\delta$ -phases obtained from X-ray powder data Rietveld refinements.

<b>&lt;Bi/<i>M</i>–O(1)&gt; /pm</b>		
<i>x</i>	Cr	Ta
0.05	--	239.46(1)
0.10	--	238.90(1)
0.15	244.19(2)	238.07(1)
0.20	244.31(2)	237.32(1)
0.25	244.30(2)	236.63(1)
0.27	244.17(2)	236.62(1)
0.30	244.33(2)	236.59(1)
<b>&lt;Bi/<i>M</i>–O(2)&gt; /pm</b>		
0.05	--	239.64(1)
0.10	--	229.38(1)
0.15	238.41(3)	233.53(2)
0.20	230.89(3)	240.87(2)
0.25	238.99(3)	240.56(2)
0.27	230.44(3)	239.38(2)
0.30	230.96(3)	237.50(2)
<b>&lt;Bi/<i>M</i>–O(3)&gt; /pm</b>		
0.05	--	252.68(2)
0.10	--	251.10(1)
0.15	216.44(3)	250.39(2)
0.20	208.78(3)	213.92(2)
0.25	220.31(3)	195.57(2)
0.27	215.57(3)	194.02(2)
0.30	216.49(3)	193.37(2)

se's parent structure contains defects from the lone electron pair of  $\text{Bi}^{3+}$ , which is balanced by 25% vacant anionic sites [5], allowing for the prevalent tetrahedral coordination of  $\text{Cr}^{6+}$  within the Bi/*MO*<sub>*x*</sub> polyhedral geometry [9, 16, 17]. The bond length of Bi/Ta–O(1) decreases with increasing substitution from  $x = 0.05$  to 0.25 in the  $(\text{Bi}^{3+}_{1-x}\text{Ta}^{5+}_x)_2\text{O}_{3+2x}$  series, as illustrated in **figure 5.6b**. At  $x = 0.05$  and 0.25, the Bi/Ta–O(1) bond lengths are 239.46(1) pm and 236.63(1) pm (**Tab. 5.3**), respectively, with a saturation observed between  $x = 0.25$  and 0.30. The Bi/Ta–O(2) and Bi/Ta–O(3) bond lengths vary from  $235.13 \pm 5.74$  pm and

245.09 ± 7.59 pm, respectively. While the Bi/*M*-O(2) bond lengths (for *M* = Cr and Ta) are comparable, the Bi/Ta-O(3) bond length is greater than that of Bi/Cr-O(3), suggesting a larger coordination polyhedron around the Ta<sup>5+</sup> cation.

### Spectroscopy

Raman spectroscopy provides structural information by probing internal and external modes of a crystal [24, 25]. External modes, appearing in the low-frequency region, correspond to the translation and vibration of molecular units within the lattice. Internal modes, found in the high-frequency region, represent the normal vibrations of the molecular units. **Figure 5.7** shows the Raman spectra for the Cr- and Ta-series. XRPD identifies each composition ( $x = 0.15 - 0.30$ ) of  $(\text{Bi}^{3+}_{1-x}\text{Cr}^{n+}_x)_2\text{O}_{3+(n-3)x}$  as  $\delta$ -phase, with the Raman spectra revealing structural complexity. The convoluted Raman bands (**Fig. 5.7a**) show peak maxima at 103(1) cm<sup>-1</sup>, 131(1) cm<sup>-1</sup>, 332(1) cm<sup>-1</sup>, 361(1) cm<sup>-1</sup>, 569(1) cm<sup>-1</sup>, and 828(1) cm<sup>-1</sup> wavenumber. The low-frequency bands at 103(1) cm<sup>-1</sup> and 131(1) cm<sup>-1</sup> correspond to bismuth and oxygen lattice vibrations [25-27]. The 332(1) cm<sup>-1</sup> and 361(1) cm<sup>-1</sup> bands are attributed to the asymmetric stretching of Cr<sup>3+</sup>O<sub>x</sub>

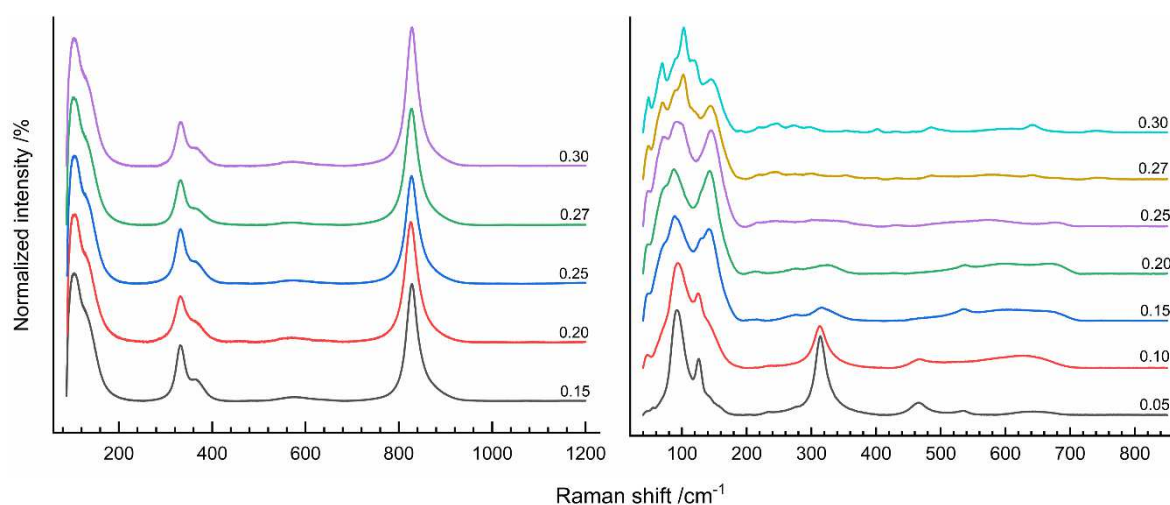


**Figure 5.7:** Raman spectra of  $(\text{Bi}^{3+}_{1-x}\text{M}^{n+}_x)_2\text{O}_{3+(n-3)x}$ , where *M* = Cr (left) and Ta (right), with respect to compositional *x*-value.

polyhedra [28, 29], while the 569(1)  $\text{cm}^{-1}$  band indicates symmetric stretching vibration of Bi–O bond [25-27]. The Raman shift at 828(1)  $\text{cm}^{-1}$  corresponds to the stretching vibration of  $\text{Cr}^{6+}\text{O}_4$  tetrahedra, suggesting slight distortion in the  $\delta$ -phase. For comparison,  $\text{CrO}_4$  in  $\text{K}_2\text{Cr}_2\text{O}_7$  (solid state) exhibits a perfect tetrahedron with a stretching band at 874(2)  $\text{cm}^{-1}$ , but a red shift to 848(2)  $\text{cm}^{-1}$  occurs in aqueous solution due to tetrahedral distortion [30]. Similarly, the Raman shift at 828(1)  $\text{cm}^{-1}$  implies  $\text{Cr}^{6+}\text{O}_4$  in a distorted tetrahedral environment. Both  $\delta$ - and  $\beta$ -phase are identified in Ta-series at  $x = 0.05$ , with XRPD analysis indicating 83.4% of  $\beta$ -phase (**Tab. 5.2**). The Raman spectrum of  $x = 0.05$  also confirms the  $\beta$ -phase in  $(\text{Bi}^{3+}_{1-x}\text{Ta}^{5+}_x)_2\text{O}_{3+2x}$  (**Fig. 5.7b**), showing characteristic Raman bands at 92(2)  $\text{cm}^{-1}$ , 125(2)  $\text{cm}^{-1}$ , 314(2)  $\text{cm}^{-1}$ , and 465(2)  $\text{cm}^{-1}$ , with weaker peak at 534(2)  $\text{cm}^{-1}$  and 641(2)  $\text{cm}^{-1}$  [31, 32]. At  $x = 0.25$ , pure  $\delta$ -phase is identified by XRPD analysis, with the  $\delta$ -phase content increasing as  $x$ -value rises from 0.05 (**Tab. 5.2**). The 314(2)  $\text{cm}^{-1}$  Raman band steadily weakens with increasing  $x$ -value, reflecting the disappearance of the  $\beta$ -phase and highlighting phase separation between  $\beta$ - and  $\delta$ -phases, discussed in **chapter 4**. At  $x = 0.25$ , pure  $\delta$ -phase exhibits intense Raman bands below 200  $\text{cm}^{-1}$  wavenumber, characteristic of external modes [33], which are sharper than internal modes (**Fig. 5.7b**). Weak peaks at 320(2)  $\text{cm}^{-1}$  and 550(2)  $\text{cm}^{-1}$  correspond to Bi–O stretching [33], with the red-shifted 550(2)  $\text{cm}^{-1}$  Raman band indicating structural distortion in the  $\text{BiO}_x$  polyhedra.

The UV/Vis diffuse reflectance spectrum of  $(\text{Bi}^{3+}_{1-x}\text{Cr}^{n+}_x)_2\text{O}_{3+(n-3)x}$  at  $x = 0.15$  composition is shown in **figure 5.8**, while spectra for  $x = 0.20 - 30$  are in **figure S5.5 – S5.6**. For  $(\text{Bi}^{3+}_{1-x}\text{Ta}^{5+}_x)_2\text{O}_{3+2x}$ , the pure  $\delta$ -phase at  $x = 0.25$  is displayed in **figure S5.7**. The electronic bandgap  $E_g$  is determined using Tauc's [34] and DASF methods [35], alongside RATD analysis [19] for bandgap energy and transition type, with results summarized in **table 5.4**. For  $x = 0.15$  composition in Cr-series, DASF yields  $E_g = 2.21(2)$  eV, close to direct transition bandgap ener-

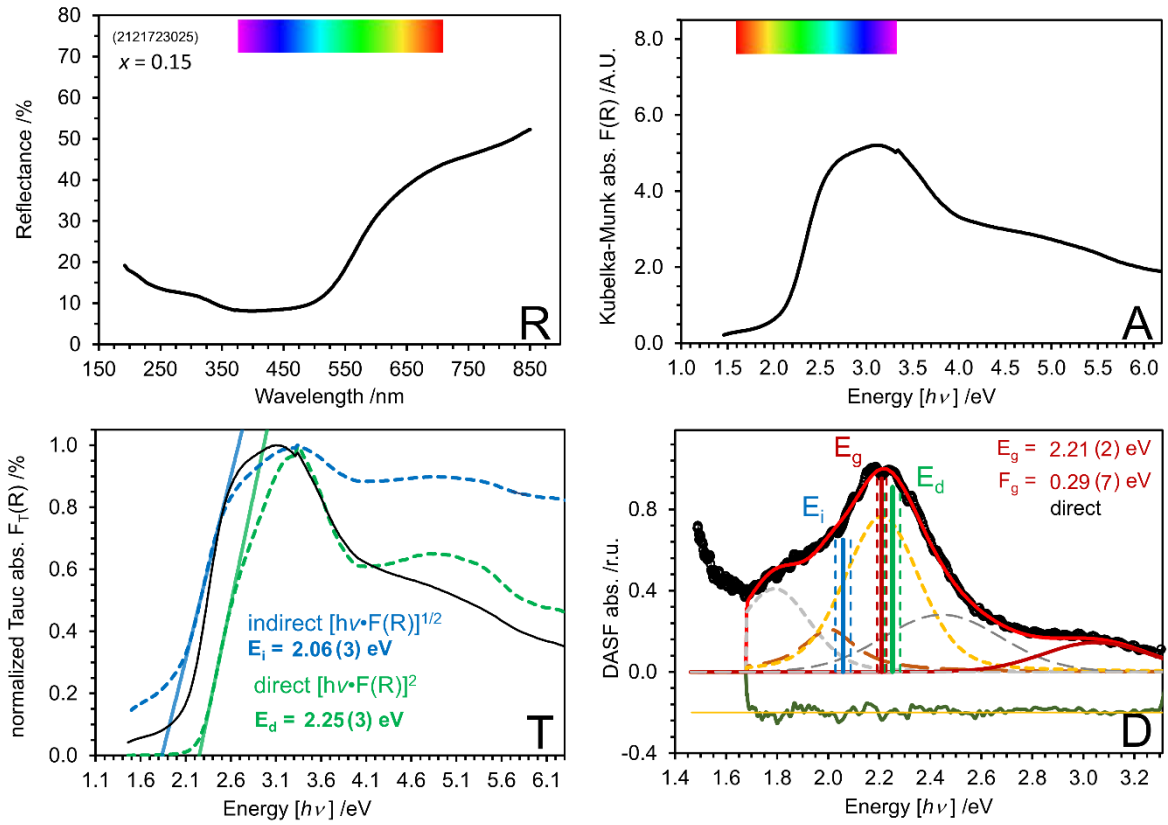


**Figure 5.8:** UV/Vis RATD plot containing reflectance spectrum (R), calculated absorbance spectrum (A), bandgap energies ( $E_g$ ) determined using the DASf method (D) and Tauc analysis (T) for direct ( $E_d$ ) and indirect ( $E_i$ ) transitions in  $(\text{Bi}^{3+}_{1-x}\text{Cr}^{n+})_2\text{O}_{3+(n-3)x}$  at  $x = 0.15$  composition.

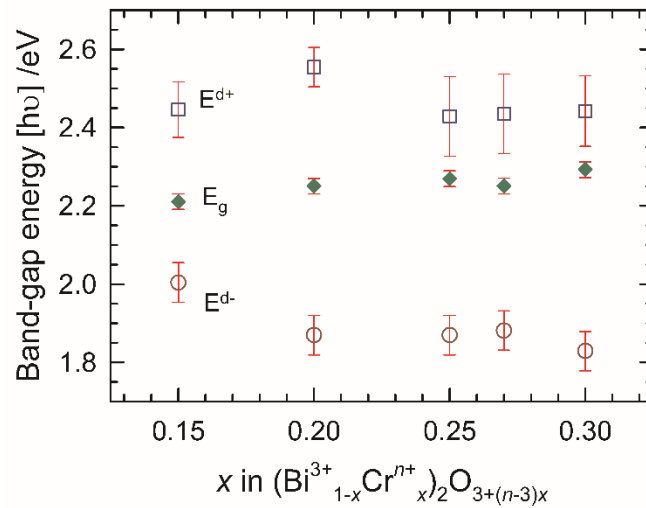


**Figure 5.9:** Determined  $E_g$  (diamond, bandgap),  $E^{d+}$  (square, cationic defect), and  $E^{d-}$  (circle, anionic defect) transition energies for the  $(\text{Bi}^{3+}_{1-x}\text{Cr}^{n+})_2\text{O}_{3+(n-3)x}$  solid solution.

**Table 5.4:** Bandgap energies calculated from UV/Vis diffuse reflectance spectroscopic data of  $(\text{Bi}^{3+}_{1-x}\text{M}^{n+}_x)_2\text{O}_{3+(n-3)x}$  using the RATD methods [19], where  $M = \text{Cr}$  and  $\text{Ta}$ . Respective value for  $x = 0$  is taken from the given literature.

$M$	DASF fitting					Tauc fitting		Type
	$x$	$E_g/\text{eV}$	$F_g/\text{eV}$	$E^{d+}/\text{eV}$	$E^{d-}/\text{eV}$	$E_d/\text{eV}$	$E_i/\text{eV}$	
Cr	0	--	--	--	--	--	2.50 [39]	Indirect
	0	--	--	--	--	3.55 [40]	--	Direct
	0.15	2.21(2)	0.29(7)	2.45(7)	2.00(5)	2.25(3)	2.06(3)	Direct
	0.20	2.25(2)	0.30(4)	2.55(5)	1.87(5)	2.29(3)	2.09(3)	Direct
	0.25	2.27(2)	0.18(8)	2.43(5)	1.87(5)	2.29(3)	2.11(3)	Direct
	0.27	2.25(2)	0.25(5)	2.43(5)	1.88(5)	2.29(3)	2.10(3)	Direct
Ta	0.30	2.29(2)	0.06(5)	2.44(6)	1.83(5)	2.28(3)	2.15(3)	Direct
	0.25	2.93(2)	0.38(2)	--	1.95(2)	2.99(3)	2.55(6)	Direct

$E_g$ ,  $E^{d+}$ ,  $E^{d-}$ , and  $F_g$  refer to bandgap energy, cationic defect transition, anionic defect transition, and band flatness, respectively, obtained from the fitting of the DASF plots.  $E_d$  and  $E_i$ , respectively, represent direct and indirect transition energies determined from the Tauc plots.

gy  $E_d = 2.25(3)$  eV from Tauc's method, whereas the indirect bandgap  $E_i = 2.06(3)$  eV deviates (**Fig. 5.8D**). All solid solutions indicate a direct transition  $E_g$  (**Tab. 5.4**). In addition to  $E_g$ , defect bands  $E^{d-}$  (anionic defect) and  $E^{d+}$  (cationic defect) are identified (**Fig. 5.8D, S5.5D – S5.7D**). As  $x$ -value increases,  $E_g$  rises, while  $E^{d-}$  decreases (**Fig. 5.9**).  $E^{d+}$  approaches  $E_g$ , and  $E^{d-}$  moves further away, highlighting structural modification (**Fig. 5.9**) [6]. For  $(\text{Bi}^{3+}_{1-x}\text{Ta}^{5+}_x)_2\text{O}_{3+2x}$  at  $x = 0.25$ , the direct bandgap  $E_g$  is 2.93(2) eV, with only  $E^{d-}$  defect at 1.95(2) eV (**Fig S5.7**). Low-energy  $E^{d-}$  defect in both Cr- and Ta-series correspond to oxygen vacancies in the  $\delta$ -phase [1, 6, 15].

#### 4. Conclusions

The study explores the substitution of  $\text{Bi}^{3+}$  cation with  $\text{Cr}^{3+}$  and  $\text{Ta}^{5+}$  in solid solution represented by the formula  $(\text{Bi}^{3+}_{1-x}\text{M}^{n+}_x)_2\text{O}_{3+(n-3)x}$ . Two series, the Cr-series and Ta-series, are

synthesized with compositions ranging from  $x = 0.15$  to  $0.30$  for Cr and  $x = 0.05$  to  $0.30$  for Ta. During synthesis at  $1273\text{ K}$ ,  $\text{Cr}^{3+}$  cation oxidizes to  $\text{Cr}^{6+}$ , resulting in mixed oxidation states confirmed by X-ray photoelectron spectroscopy. Structural analysis indicates that all Cr-series compositions exhibit  $\delta$ -phase, while the Ta-series displays  $\delta$ -phase only at  $x = 0.25$ . The Ta-series shows a linear trend in lattice parameters with increasing  $x$ -value, whereas the Cr-series maintains a larger, unchanged lattice parameter, suggesting incommensurate structure formation. Raman spectroscopy further confirms tetrahedral coordination for  $\text{Cr}^{6+}$  and highlights structural distortions. Both series feature low direct bandgaps, with oxygen vacancies contributing to anionic defect band, influencing their electronic properties.

## References

- [1] M.I. Hossain, M.M. Murshed, T.M. Gesing, Indium containing sillenite semiconductor: Synthesis, structural, spectroscopic and thermogravimetric analysis, *J. Am. Ceram. Soc.* 106(10) (2023) 6268-6278. Doi:10.1111/jace.19231
- [2] S. Hui, J. Roller, S. Yick, X. Zhang, C. Decès-Petit, Y. Xie, R. Maric, D. Ghosh, A brief review of the ionic conductivity enhancement for selected oxide electrolytes, *J. Power Sources* 172(2) (2007) 493-502. Doi:10.1016/j.jpowsour.2007.07.071
- [3] P.D. Battle, C.R.A. Catlow, J. Drennan, A.D. Murray, The structural properties of the oxygen conducting  $\delta$  phase of  $\text{Bi}_2\text{O}_3$ , *J. Phys. C: Solid State Phys.* 16(17) (1983) L561-L566. Doi:10.1088/0022-3719/16/17/003
- [4] E. Subbarao, A family of ferroelectric bismuth compounds, *J. Phys. Chem. Solids* 23(6) (1962) 665-676. Doi:10.1016/0022-3697(62)90526-7
- [5] S. Hull, S.T. Norberg, M.G. Tucker, S.G. Eriksson, C.E. Mohn, S. Stølen, Neutron total scattering study of the  $\delta$  and  $\beta$  phases of  $\text{Bi}_2\text{O}_3$ , *Dalton Trans.* (40) (2009) 8737-8745. Doi:10.1039/B910484B
- [6] H.A. Harwig, On the structure of bismuthsesquioxide: the  $\alpha$ ,  $\beta$ ,  $\gamma$ , and  $\delta$ -phase, *Z. anorg. allg. Chem.* 444 (1978) 151-166. Doi:10.1002/zaac.19784440118
- [7] H.A. Harwig, J.W. Weenk, Phase relations in bismuthsesquioxide, *Z. anorg. allg. Chem.* 444 (1978) 167-177. Doi:10.1002/zaac.19784440119
- [8] J.C. Boivin, G. Mairesse, Recent material developments in fast oxide ion conductors, *Chem. Mater.* 10(10) (1998) 2870-2888. Doi:10.1021/cm980236q
- [9] J. Ducke, M. Trömel, D. Hohlwein, P. Kizler, Yttrium and titanium bismuthates with structures related to  $\beta$ - $\text{Bi}_2\text{O}_3$ , *Acta Cryst.* 52(6) (1996) 1329-1331. Doi:10.1107/S0108270195011267



- [10] R.D. Shannon, Revised effective ionic radii and systematic studies of interatomic distances in halides and chalcogenides, *Acta Cryst.* A32 (1976) 751-767. Doi:10.1107/S0567739476001551
- [11] J. Grins, S. Esmaeilzadeh, S. Hull, Structure and Ionic Conductivity of  $\text{Bi}_6\text{Cr}_2\text{O}_{15}$ , a New Structure Type Containing  $(\text{Bi}_{12}\text{O}_{14})_n^{8n+}$  Columns and  $\text{CrO}_2^{-4}$  Tetrahedra, *J. Solid State Chem.* 163(1) (2002) 144-150. Doi:10.1006/jssc.2001.9385
- [12] S. Warda, W. Pietzuch, W. Massa, U. Kesper, D. Reinen, Color and constitution of  $\text{Cr}^{\text{VI}}$ -doped  $\text{Bi}_2\text{O}_3$  phases: the structure of  $\text{Bi}_{14}\text{CrO}_{24}$ , *J. Solid State Chem.* 149(2) (2000) 209-217. Doi:10.1006/jssc.1999.8469
- [13] S. Esmaeilzadeh, S. Lundgren, U. Hålenius, J. Grins,  $\text{Bi}_{1-x}\text{Cr}_x\text{O}_{1.5+1.5x}$ ,  $0.05 \leq x \leq 0.15$ : A New High-Temperature Solid Solution with a Three-Dimensional Incommensurate Modulation, *J. Solid State Chem.* 156(1) (2001) 168-180. Doi:10.1006/jssc.2000.8978
- [14] M. Struzik, M. Malys, W. Wrobel, I. Abrahams, F. Krok, J.R. Dugas, Ordered fluorite phases in the  $\text{Bi}_2\text{O}_3$ - $\text{Ta}_2\text{O}_5$  system: a structural and electrical investigation, *Solid State Ionics* 202(1) (2011) 22-29. Doi:10.1016/j.ssi.2011.08.009
- [15] W. Zhou, Superstructures and band gaps of bismuth tantalum oxide solid solutions, *Adv. Mater.* 2(9) (1990) 414-420. Doi:10.1002/adma.19900020906
- [16] M. Gambino, F. Giannici, A. Longo, S.D. Tommaso, F. Labat, A. Martorana, Dopant clusterization and oxygen coordination in Ta-doped bismuth oxide: a structural and computational insight into the mechanism of anion conduction, *J. Phys. Chem. C* 119(47) (2015) 26367-26373. Doi:10.1021/acs.jpcc.5b09449
- [17] P.D. Battle, C.R.A. Catlow, J.W. Heap, L.M. Moroney, Structural and dynamical studies of  $\delta$ - $\text{Bi}_2\text{O}_3$  oxide ion conductors: I. The structure of  $(\text{Bi}_2\text{O}_3)_{1-x}(\text{Y}_2\text{O}_3)_x$  as a function of  $x$  and temperature, *J. Solid State Chem.* 63(1) (1986) 8-15. Doi:10.1016/0022-4596(86)90146-5
- [18] D. Balzar, N. Audebrand, M.R. Daymond, A. Fitch, A. Hewat, J.I. Langford, A.L. Bail, D. Louër, O. Masson, C.N. McCowan, N.C. Popa, P.W. Stephens, B.H. Toby, Size-strain line-broadening analysis of the ceria round-robin sample, *J. Appl. Crystallogr.* 37(6) (2004) 911-924. Doi:10.1107/s0021889804022551
- [19] T.M. Gesing, M.M. Murshed, S. Schuh, O. Thüringer, K. Krämer, T. Neudecker, C.B. Mendive, L. Robben, Nano-crystalline precursor formation, stability, and transformation to mullite-type visible-light photocatalysts, *J. Mater. Sci.* (2022) 1-20. Doi:10.1007/s10853-022-07854-w
- [20] S. Singh, R.K. Sahoo, N.M. Shinde, J.M. Yun, R.S. Mane, W. Chung, K.H. Kim, Asymmetric faradaic assembly of  $\text{Bi}_2\text{O}_3$  and  $\text{MnO}_2$  for a high-performance hybrid electrochemical energy storage device, *RSC Adv.* 9(55) (2019) 32154-32164. Doi:10.1039/C9RA06331E
- [21] B. Oprea, T. Radu, S. Simon, XPS investigation of atomic environment changes on surface of  $\text{B}_2\text{O}_3$ - $\text{Bi}_2\text{O}_3$  glasses, *J. Non-Cryst. Solids* 379 (2013) 35-39. Doi:10.1016/j.jnoncrsol.2013.07.024
- [22] O. Cortazar-Martínez, J.-A. Torres-Ochoa, J.-G. Raboño-Borbolla, A. Herrera-Gomez, Oxidation mechanism of metallic chromium at room temperature, *Appl. Surf. Sci.* 542 (2021) 148636. Doi:10.1016/j.apsusc.2020.148636

- [23] C.D. Ling, J.G. Thompson, R.L. Withers, S. Schmid, Modeling and Rietveld-Refinement of the Crystal Structure of  $\text{Bi}_4\text{Ta}_2\text{O}_{11}$  Based on That of  $\text{Bi}_7\text{Ta}_3\text{O}_{18}$ , *J. Solid State Chem.* 142(1) (1999) 33-40. Doi:10.1006/jssc.1998.7980
- [24] W.G. Fateley, F.R. Dollish, *Infrared and Raman selection rules for molecular and lattice vibrations: the correlation method*, New York: Wiley-Interscience (1972).
- [25] R. Sharma, N. Benshalom, M. Asher, T.M. Brenner, A. Kossi, O. Yaffe, R. Korobko, Dynamic disorder in Bi sub-lattice of  $\delta\text{-Bi}_2\text{O}_3$ , *Cond-mat.mtrl-sci* (2022) 1-6. Doi:10.48550/arXiv.2205.13289
- [26] M. Ahila, E. Subramanian, D.P. Padiyan, Influence of annealing on phase transformation and specific capacitance enhancement in  $\text{Bi}_2\text{O}_3$ , *J. Electroanal. Chem.* 805 (2017) 146-158. Doi:10.1016/j.jelechem.2017.10.037
- [27] A. Rubbens, M. Drache, P. Roussel, J.P. Wignacourt, Raman scattering characterization of bismuth based mixed oxides with  $\text{Bi}_2\text{O}_3$  related structures, *Mater. Res. Bull.* 42(9) (2007) 1683-1690. Doi:10.1016/j.materresbull.2006.11.036
- [28] B.M. Weckhuysen, I.E. Wachs, R.A. Schoonheydt, Surface chemistry and spectroscopy of chromium in inorganic oxides, *Chem. Rev.* 96(8) (1996) 3327-3350. Doi:10.1021/cr940044o
- [29] J. Mougín, T. Le Bihan, G. Lucazeau, High-pressure study of  $\text{Cr}_2\text{O}_3$  obtained by high-temperature oxidation by X-ray diffraction and Raman spectroscopy, *J. Phys. Chem. Solids* 62(3) (2001) 553-563. Doi:10.1016/S0022-3697(00)00215-8
- [30] B.M. Weckhuysen, I.E. Wachs, Raman spectroscopy of supported chromium oxide catalysts. Determination of chromium-oxygen bond distances and bond orders, *J. Chem. Soc., Faraday Trans.* 92(11) (1996) 1969-1973. Doi:10.1039/FT9969201969
- [31] A.L. Pereira, J.A. Sans, R. Vilaplana, O. Gomis, F. Manjón, P. Rodríguez-Hernández, A. Muñoz, C. Popescu, A. Beltrán, Isostructural second-order phase transition of  $\beta\text{-Bi}_2\text{O}_3$  at high pressures: an experimental and theoretical study, *J. Phys. Chem. C* 118(40) (2014) 23189-23201. Doi:10.1021/jp507826j
- [32] C. Díaz-Guerra, P. Almodóvar, M. Camacho-López, S. Camacho-López, J. Piqueras, Formation of  $\beta\text{-Bi}_2\text{O}_3$  and  $\delta\text{-Bi}_2\text{O}_3$  during laser irradiation of Bi films studied in-situ by spatially resolved Raman spectroscopy, *J. Alloys Compd.* 723 (2017) 520-526. Doi:10.1016/j.jallcom.2017.06.263
- [33] F. D.Hardcastle, I. E.Wachs, The molecular structure of bismuth oxide by Raman spectroscopy, *J. Solid State Chem.* 97(2) (1992) 319-331. Doi:10.1016/0022-4596(92)90040-3
- [34] J. Tauc, R. Grigorovici, A. VanCu, Optical properties and electronic structure of amorphous germanium, *Phys. Status Solidi B* 15(2) (1966) 627-637. Doi:10.1002/pssb.19660150224
- [35] D. Souri, Z.E. Tahan, A new method for the determination of optical band gap and the nature of optical transitions in semiconductors, *Appl. Phys. B* 119(2) (2015) 273-279. Doi:10.1007/s00340-015-6053-9
- [36] P. Shuk, H.-D. Wiemhöfer, U. Guth, W. Gijpeld, M. Greenblatt, Oxide ion conducting solid electrolytes based on  $\text{Bi}_2\text{O}_3$ , *Solid State Ionics* 89 (1996) 179-196. Doi:10.1016/0167-2738(96)00348-7

- [37] H. Deng, W. Hao, H. Xu, C. Wang, Effect of intrinsic oxygen vacancy on the electronic structure of  $\gamma$ - $\text{Bi}_2\text{O}_3$ : First-principles calculations, *J. Phys. Chem. C* 116(1) (2012) 1251-1255. Doi:10.1021/jp2086895
- [38] D.S. Aidhy, J.C. Nino, S.B. Sinnott, E.D. Wachsman, S.R. Phillpot, Vacancy-ordered structure of cubic bismuth oxide from simulation and crystallographic analysis, *J. Am. Ceram. Soc.* 91(7) (2008) 2349-2356. Doi:10.1111/j.1551-2916.2008.02463.x
- [39] J. Zhang, Q. Han, X. Wang, J. Zhu, G. Duan, Synthesis of  $\delta$ - $\text{Bi}_2\text{O}_3$  microflowers and nanosheets using  $\text{CH}_3\text{COO}(\text{BiO})$  self-sacrifice precursor, *Mater. Lett.* 162 (2016) 218-221. Doi:10.1016/j.matlet.2015.10.024
- [40] J. Xie, L. Li, C. Tian, C. Han, D. Zhao, Template-free synthesis of hierarchical constructed flower-like  $\delta$ - $\text{Bi}_2\text{O}_3$  microspheres with photocatalytic performance, *Micro Nano Lett.* 7(7) (2012) 651-653. Doi:10.1049/mnl.2012.0201

## Supplementary Information

### Impact of $M^{n+}$ charge and size on $\delta$ -phases formation: structural and spectroscopic investigations with $M = \text{Cr}$ and $\text{Ta}$

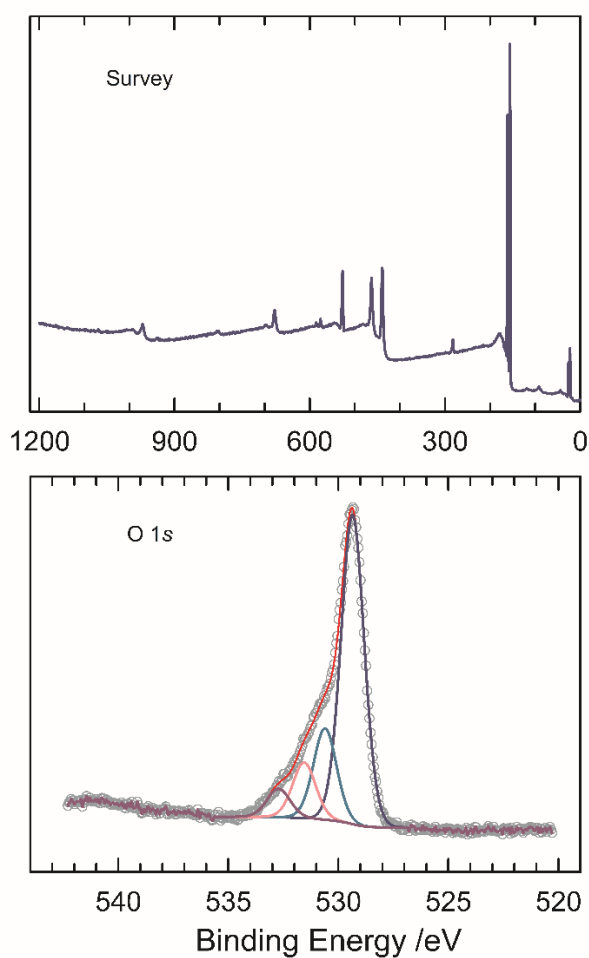


**Figure S5.1:** XPS survey spectra for  $x = 0.15$  composition in  $(\text{Bi}^{3+}_{1-x}\text{Cr}^{n+}_x)_2\text{O}_{3+(n-3)x}$  and peak fitting of O 1s.

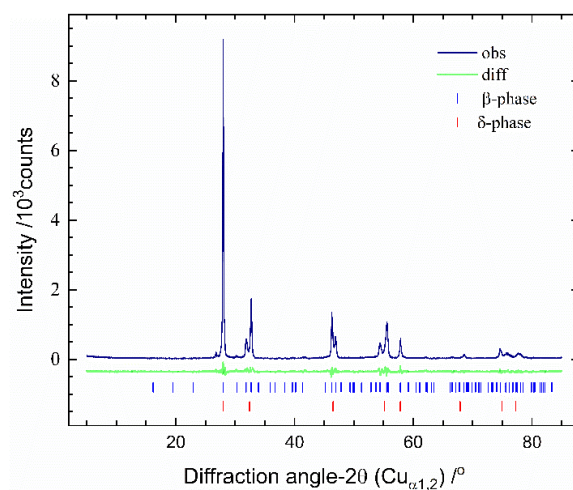


**Figure S5.2:** X-ray powder diffraction data Rietveld pattern for  $x = 0.05$  in  $(\text{Bi}^{3+}_{1-x}\text{Ta}^{5+}_x)_2\text{O}_{3+2x}$ .

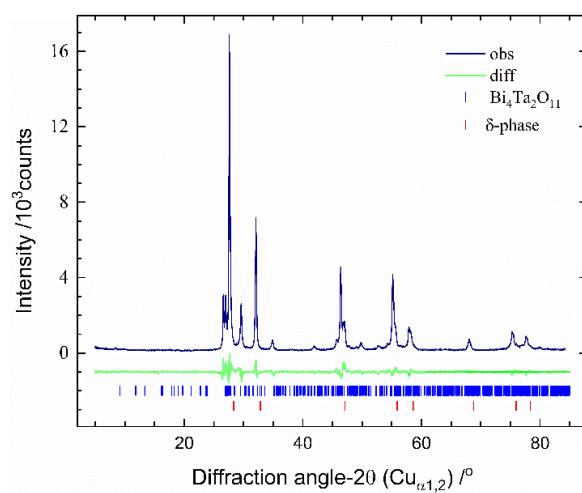


**Figure S5.3:** X-ray powder diffraction data Rietveld pattern for  $x = 0.30$  in  $(\text{Bi}^{3+}_{1-x}\text{Ta}^{5+}_x)_2\text{O}_{3+2x}$ .

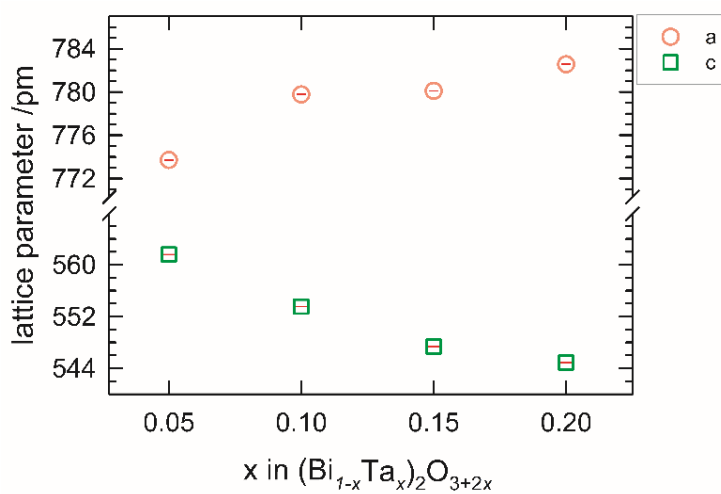


**Figure S5.4:** Evolution of metric parameter of  $(\text{Bi}^{3+}_{1-x}\text{Ta}^{5+}_x)_2\text{O}_{3+2x}$  in changing the compositional  $x$  value for  $\beta$ -phase.

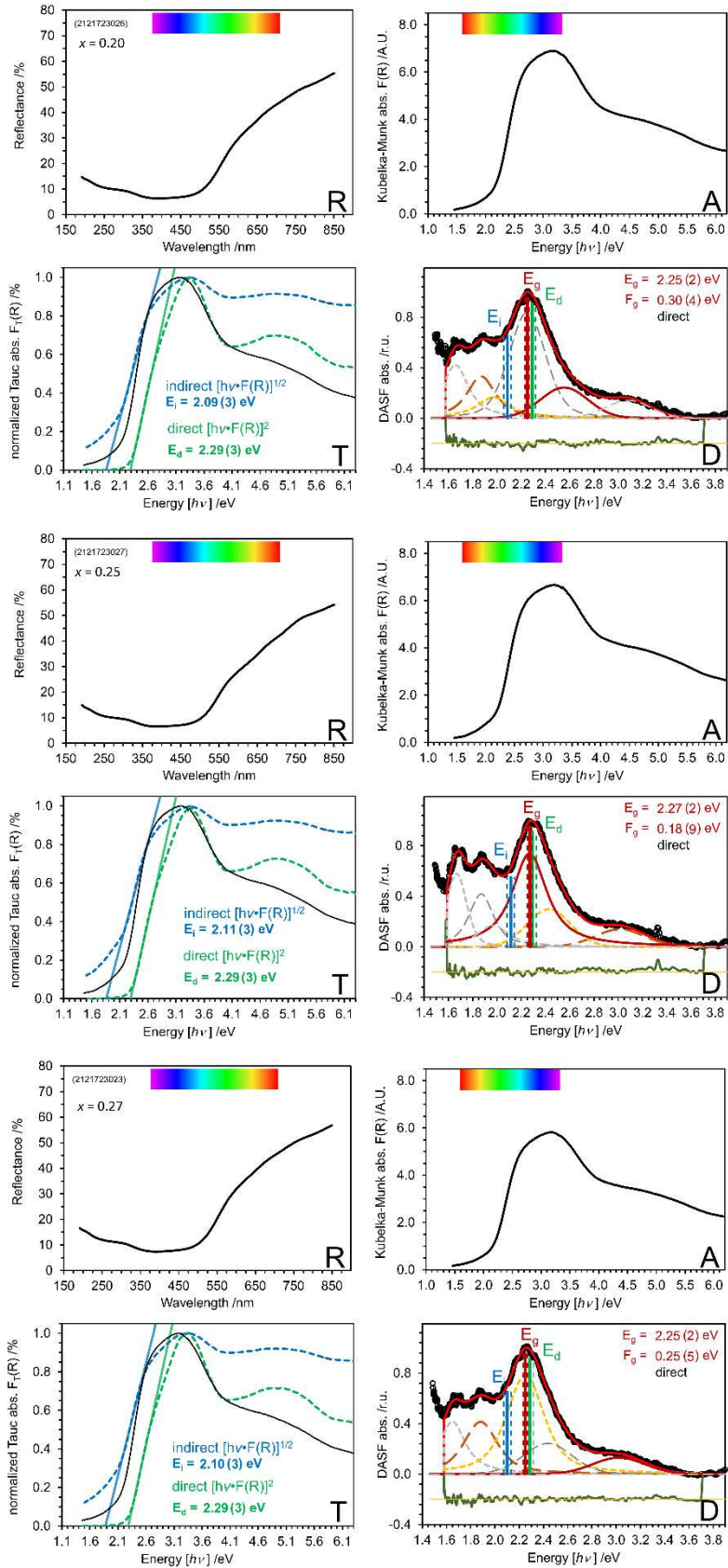


**Figure S5.5:** UV/Vis RATD plot containing reflectance spectrum (R), calculated absorbance spectrum (A), bandgap energies ( $E_g$ ) determined using the DASF method (D) and Tauc analysis (T) for direct ( $E_d$ ) and indirect ( $E_i$ ) transitions in  $(\text{Bi}^{3+}_{1-x}\text{Cr}^{n+}_x)_2\text{O}_{3+(n-3)x}$  for  $x = 0.20 - 0.27$ .

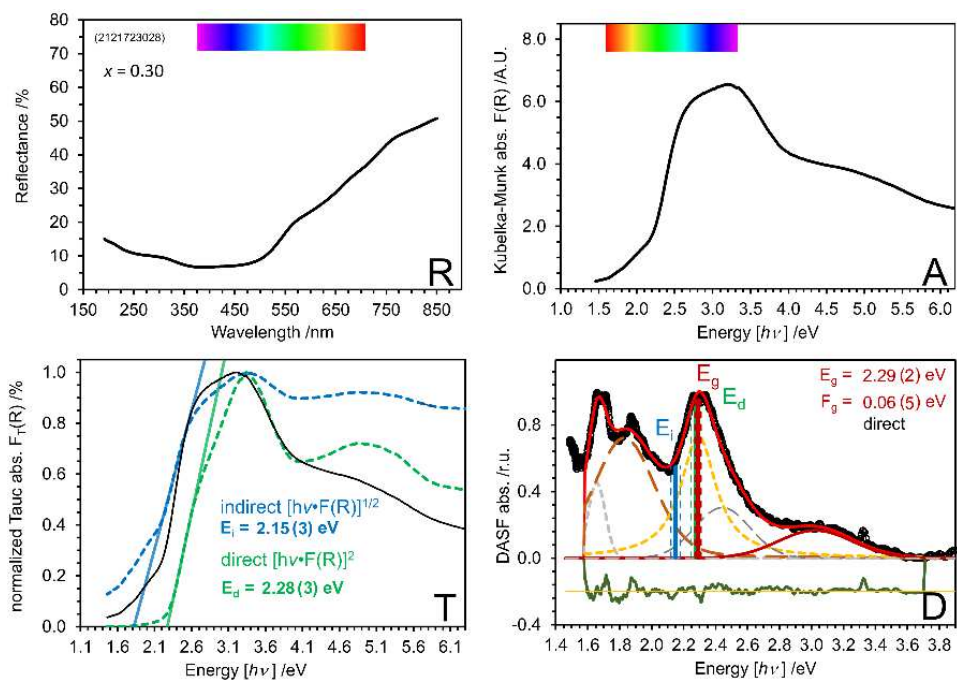


**Figure S5.6:** UV/Vis RATD plot containing reflectance spectrum (R), calculated absorbance spectrum (A), bandgap energies ( $E_g$ ) determined using the DASF method (D) and Tauc analysis (T) for direct ( $E_d$ ) and indirect ( $E_i$ ) transitions in  $(\text{Bi}^{3+}_{1-x}\text{Cr}^{n+}_x)_2\text{O}_{3+(n-3)x}$  for  $x = 0.30$ .

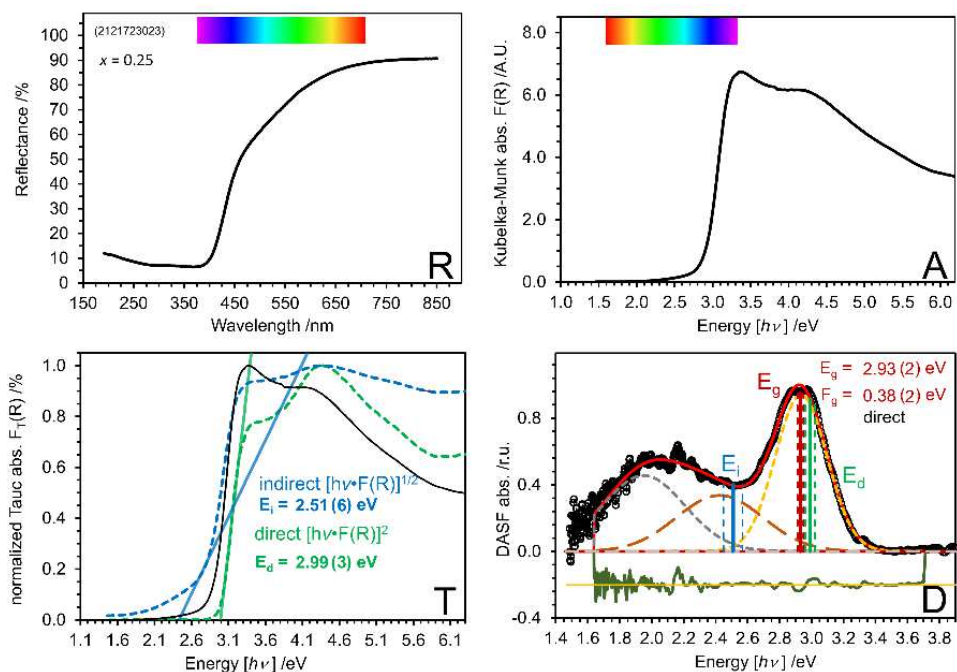


**Figure S5.7:** UV/Vis RATD plot containing reflectance spectrum (R), calculated absorbance spectrum (A), bandgap energies ( $E_g$ ) determined using the DASF method (D) and Tauc analysis (T) for direct ( $E_d$ ) and indirect ( $E_i$ ) transitions in  $(\text{Bi}^{3+}_{1-x}\text{Ta}^{5+}_x)_2\text{O}_{3+2x}$  for  $x = 0.25$ .

**Table S5.1:** Average crystallite size and microstrain of the  $(\text{Bi}_{1-x}\text{M}^{n+})_2\text{O}_{3+(n-3)x}$   $\delta$ -phases obtained from X-ray powder data Rietveld refinements.

$x$	<b>Cr</b>		<b>Ta</b>	
	$L_{\text{vol}}(\text{IB})$ /nm	$\varepsilon$ /%	$L_{\text{vol}}(\text{IB})$ /nm	$\varepsilon$ /%
0.05	-	-	26.7(4)	0.277(3)
0.10	-	-	79.0(4)	0.375(4)
0.15	60.6(4)	0.031(2)	103.2(4)	0.023(4)
0.20	58.2(4)	0.034(2)	144.0(4)	0.032(1)
0.25	54.4(4)	0.029(2)	63.9(2)	0.018(2)
0.27	51.6(4)	0.007(4)	40.6(3)	0.048(3)
0.30	51.1(4)	0.042(2)	38.9(3)	0.038(2)



## Chapter 6

### Synthesis of $\delta$ -phase $(\text{Bi}_{1-x}\text{M}^{n+})_2\text{O}_{3+(n-3)x}$ : exploring suitable foreign cation for $\text{Bi}^{3+}$ substitution

The size of foreign cationic ( $M^{n+}$ ) species is a critical factor in the formation of the  $\delta$ -phase. The choice of  $M^{n+}$  and various synthesis methods provide significant opportunities for  $\delta$ -phase synthesis. This discussion is divided into three sections based on the types of  $M^{n+}$  cations: metals and metalloids, rare earth metals, and transition metals. Each section will cover specific synthesis routes for  $M^{n+}$  and their temperature profiles. For clarity, we will use the general formula  $(\text{Bi}_{1-x}\text{M}^{n+})_2\text{O}_{3+(n-3)x}$ , where 'n' accounts for the additional oxygen needed for overall charge balancing in the presence of the  $M^{n+}$  cation.

#### *Metals and metalloids*

##### **$\text{Al}^{3+}$ , $\text{Ga}^{3+}$ , and $\text{Ge}^{4+}$**

Polycrystalline samples with compositions ranging from  $x = 0.05$  to  $0.80$  are prepared via solid-state synthesis. Metal oxides ( $M = \text{Al}, \text{Ga}, \text{Ge}$ ) and  $\text{Bi}_2\text{O}_3$  are mixed in an agate mortar, placed in a corundum crucible, and heated at  $1073 \text{ K}$  for  $24 \text{ h}$ , followed by air quenching. The resulting powders are ground and analyzed by X-ray powder diffraction (XRPD), as shown in **figures 6.1 - 6.3**. For  $x = 0.20, 0.40,$  and  $0.60$ , the samples exhibit mixed phases, with the major phase being orthorhombic ( $Pb\text{am}$ , no. 55) [1] and the minor phase cubic sillenite ( $\gamma$ -phase,  $I23$ , no. 197) [2, 3]. A small amount of  $\alpha$ -phase ( $P2_1/c$ , no. 14) is identified for  $x = 0.05$  in the  $\text{Ge}^{4+}$ -series. At  $x = 0.80$ , the structure crystallizes fully into the orthorhombic crystal system ( $Pb\text{am}$ , no. 55) [1]. Low  $x$  values favor the formation of the  $\gamma$ -phase [1, 3], while increasing  $x$  promotes the orthorhombic structure.

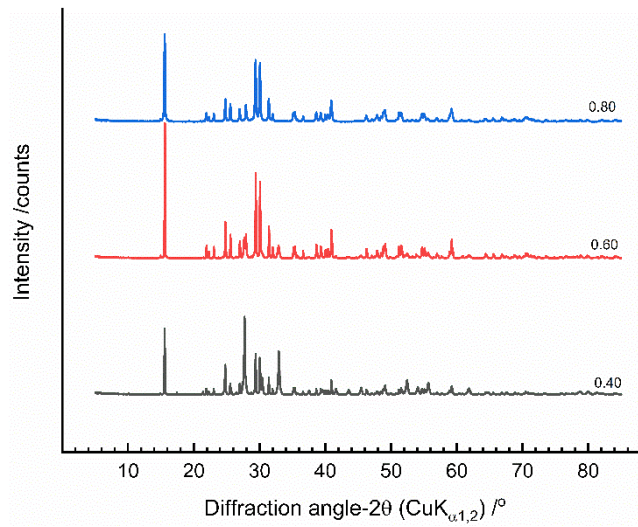


**Figure 6.1:** X-ray powder diffraction data of  $x = 0.40, 0.60,$  and  $0.80$  for  $(\text{Bi}_{1-x}\text{Al}_x)_2\text{O}_3$ .

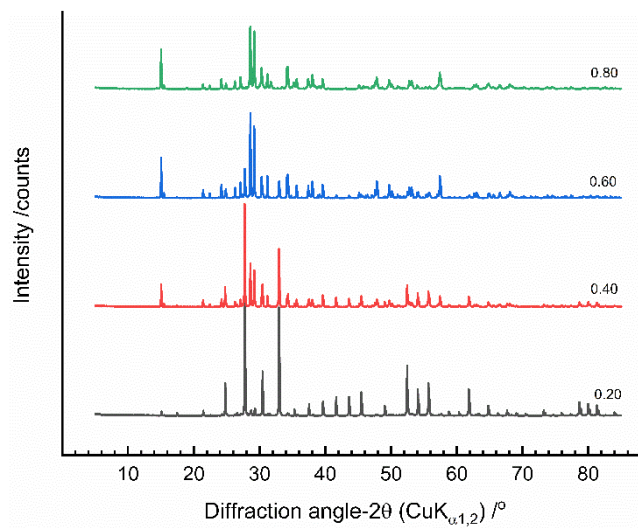


**Figure 6.2:** X-ray powder diffraction data of  $x = 0.20, 0.40, 0.60,$  and  $0.80$  for  $(\text{Bi}_{1-x}\text{Ga}_x)_2\text{O}_3$ .

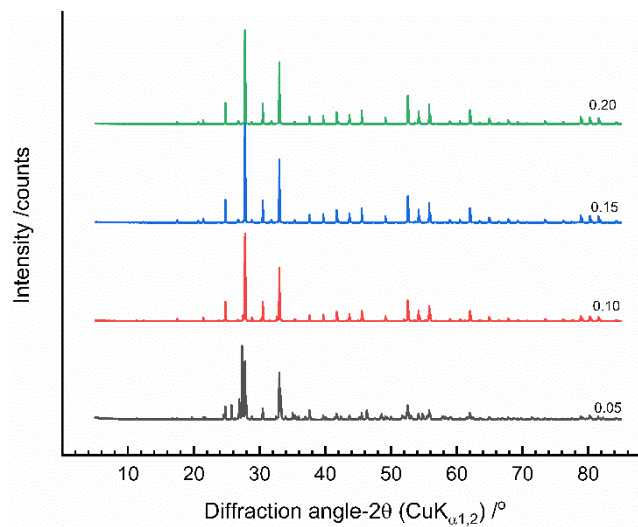


**Figure 6.3:** X-ray powder diffraction data of  $x = 0.05, 0.10, 0.15,$  and  $0.20$  for  $(\text{Bi}_{1-x}\text{Ge}_x)_2\text{O}_{3+x}$ .

## Sn<sup>4+</sup>

Samples of  $(\text{Bi}_{1-x}\text{Sn}_x)_2\text{O}_{3+x}$  with  $x = 0.05, 0.10, 0.15, 0.20,$  and  $0.25$  are prepared using solid-state synthesis.  $\text{SnO}_2$  and  $\text{Bi}_2\text{O}_3$  are mixed in an agate mortar, placed in a corundum crucible, and heated in two stages: first at 923 K for 24 h, followed by intermediate grinding, then at 1073 K for another 24 h. The samples are quenched in an ice-water bath immediately after heating. XRPD analysis (**Fig. 6.4**) reveals that all compositions ( $x = 0.05 - 0.25$ ) crystallize into the low-symmetry  $\alpha$ -phase.

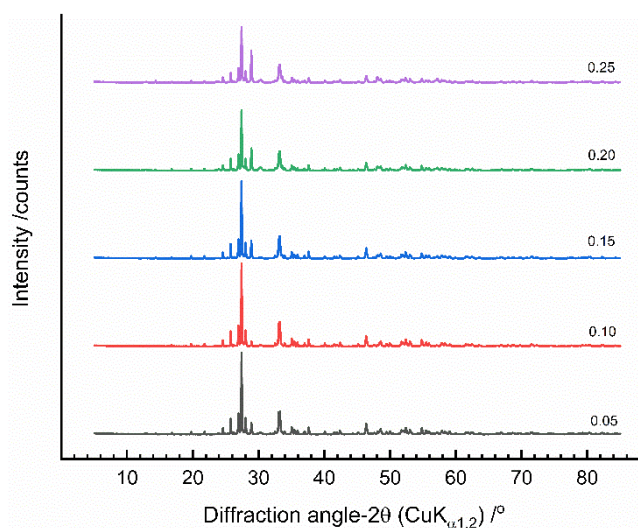


**Figure 6.4:** X-ray powder diffraction data of  $x = 0.05 - 0.25$  for  $(\text{Bi}_{1-x}\text{Sn}_x)_2\text{O}_{3+x}$ .

## Sb<sup>3+</sup>

An orange polycrystalline sample of  $x = 0.17$  for  $(\text{Bi}_{1-x}\text{Sb}_x)_2\text{O}_3$  is synthesized by solid state method.  $\text{Sb}_2\text{O}_3$  and  $\text{Bi}_2\text{O}_3$  are mixed in an agate mortar, placed in a corundum crucible, and heated in three stages: 923 K and 983 K for 24 h each, with intermediate air quenching and grinding, followed by 1213 K for 24 h and air quenching. XRPD analysis (**Fig. 6.5**) shows that the sample crystallizes into the  $\alpha$ -phase at all stages, with a small amount of  $\beta$ -phase ( $P4_2/nmc$ , no. 137) appearing after the final heating.

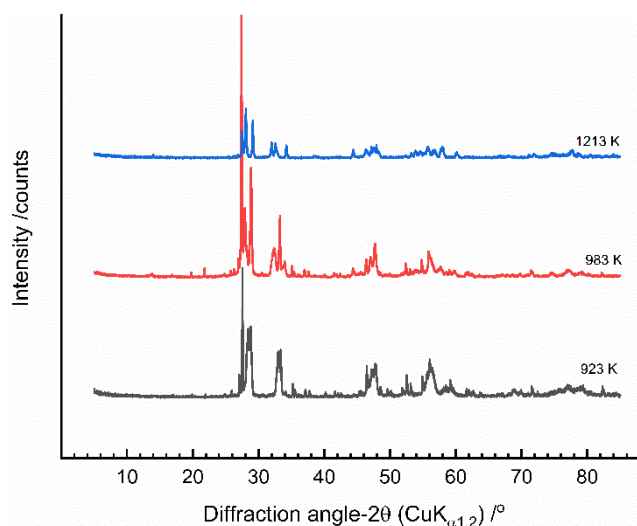


**Figure 6.5:** X-ray powder diffraction data of  $x = 0.17$  for  $(\text{Bi}_{1-x}\text{Sb}_x)_2\text{O}_3$  at three different stages of synthesis.

### $\text{Te}^{4+}$

Polycrystalline samples of  $(\text{Bi}_{1-x}\text{Te}_x)_2\text{O}_{3+x}$  with  $x = 0.05$  to  $0.25$  (in  $0.05$  intervals) are synthesized via solid-state method.  $\text{TeO}_2$  and  $\text{Bi}_2\text{O}_3$  are mixed in an agate mortar, placed in a corundum crucible, and heated at  $983$  K for  $18$  h. The final products are ground and analyzed by XRPD (Fig. 6.6). Previous studies report  $\delta$ -phase ( $Fm\bar{3}m$ , no. 225) at  $x = 0.75$  [4]. Here,  $x = 0.05$  to  $0.25$  is chosen to investigate initial structural modifications using a slower heating

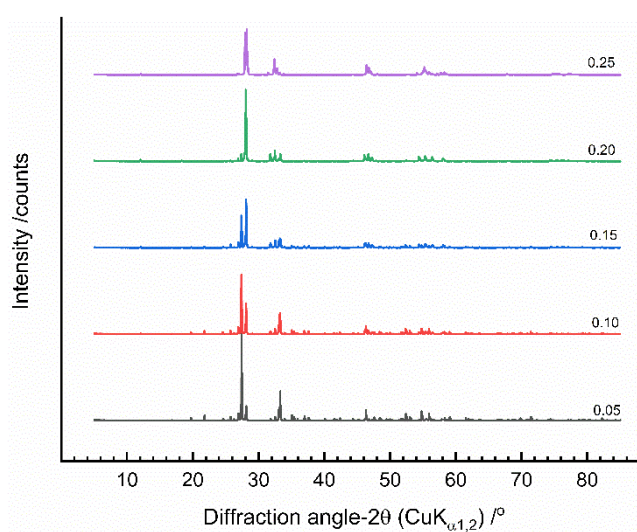


**Figure 6.6:** X-ray powder diffraction data of  $x = 0.05 - 0.25$  for  $(\text{Bi}_{1-x}\text{Te}_x)_2\text{O}_{3+x}$ .

rate due to the lower melting point of  $\text{TeO}_2$  compared to  $\text{Bi}_2\text{O}_3$ . Compositions  $x = 0.05$  to  $0.15$  show mixed phases, with  $\alpha$ -phase as the major component [5] and a minor orthorhombic phase [6]. Pure orthorhombic structure appears at  $x = 0.20$ , while  $\delta$ - and orthorhombic phases are both present at  $x = 0.25$ .

### *Rare earth metals*

#### **$\text{La}^{3+}$ , $\text{Ce}^{3+}$ , and $\text{Eu}^{3+}$**

La- and Eu-series samples are prepared via solid-state synthesis, while the Ce-series is synthesized using the glycerin method. All samples are finally heated at 1073 K for 24 h. XRPD analysis, shown in **figures 6.7 - 6.9**, is used to study the powder samples. In the La-series, changes in the XRPD patterns (**Fig. 6.7**) indicate structural modifications with increasing  $x$ -value.

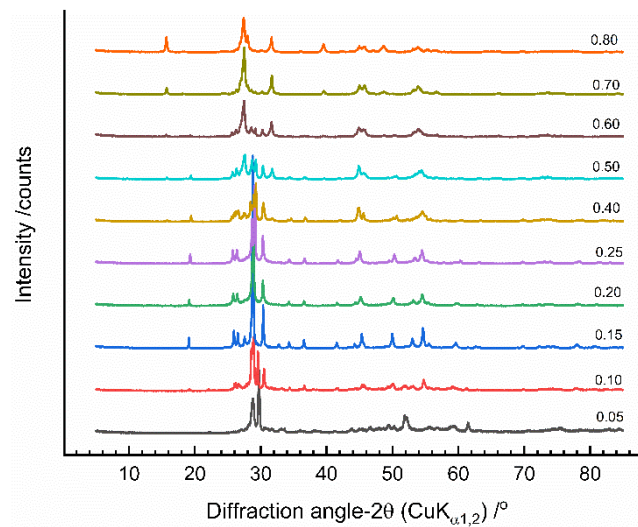


**Figure 6.7:** X-ray powder diffraction data of  $x = 0.05 - 0.80$  for  $(\text{Bi}_{1-x}\text{La}_x)_2\text{O}_3$ .

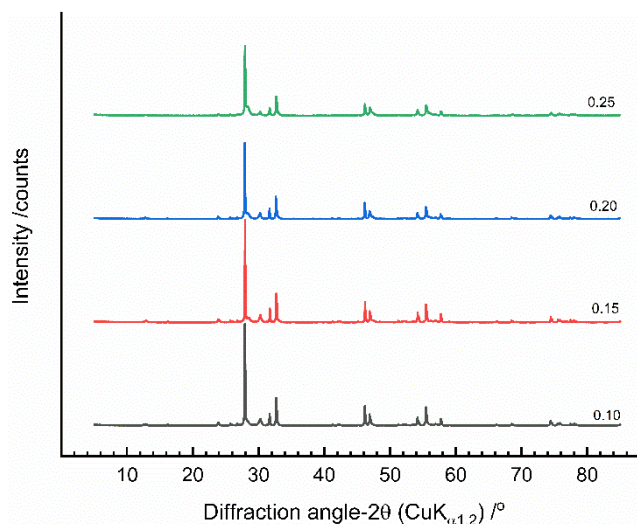


**Figure 6.8:** X-ray powder diffraction data of  $x = 0.05, 0.15, 0.20,$  and  $0.25$  for  $(\text{Bi}_{1-x}\text{Ce}_x)_2\text{O}_3$ .

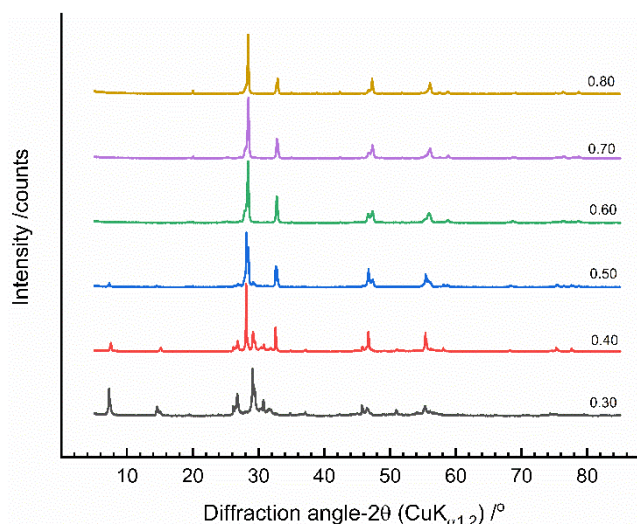


**Figure 6.9:** X-ray powder diffraction data of  $x = 0.30 - 0.80$  for  $(\text{Bi}_{1-x}\text{Eu}_x)_2\text{O}_3$ .

At  $x = 0.20$  and  $0.25$ , solid solutions crystallize into rhombohedral structure ( $R\bar{3}m$ , no. 166) [7]. However, as  $x$  increases, the rhombohedral structure transitions to a hexagonal structure ( $P6_3/m$ , no. 176) [8]. In the Ce-series (**Fig. 6.8**), the  $\beta$ -phase is present across all compositions, along with  $\text{Bi}_2\text{O}_2\text{CO}_3$ , which suggests incomplete burning of residual products from the glycerin method. The Eu-series, studied for  $x = 0.30$  to  $0.80$  (**Fig. 6.9**), shows mixed phases with additional reflections at  $7.27^\circ$  and  $14.58^\circ$  ( $2\theta$ ) for  $x = 0.30$  to  $0.50$ . The  $\delta$ -phase becomes



the dominant phase for  $x = 0.40$  to  $0.50$ , coexisting with the rhombohedral structure ( $R\bar{3}m$ , no. 166). At  $x = 0.70$  and  $0.80$ , solid solutions adopt the  $\text{Eu}_2\text{O}_3$ -type cubic structure ( $Ia\bar{3}$ , no. 206).

### *Transition metals*

#### $\text{Sc}^{3+}$

Polycrystalline samples of  $(\text{Bi}_{1-x}\text{Sc}_x)_2\text{O}_3$  are synthesized via solid-state method.  $\text{Sc}_2\text{O}_3$  and  $\text{Bi}_2\text{O}_3$  are mixed in an agate mortar, placed in a corundum crucible, and heated at  $1073\text{ K}$  for  $24\text{ h}$ , followed by air quenching. The powder samples ( $x = 0.05 - 0.90$ ) are analyzed by XRPD, as shown in **figure 6.10**. Compositions from  $x = 0.05$  to  $0.60$  crystallize into the  $\alpha$ -phase, while  $\beta$ -phase and  $\text{Sc}_2\text{O}_3$ -type structure are detected at  $x = 0.80$  and  $0.90$ . The  $\beta$ -phase reaches saturation at  $x = 0.80$ , with increasing  $x$  further promoting  $\text{Sc}_2\text{O}_3$  as impurity.

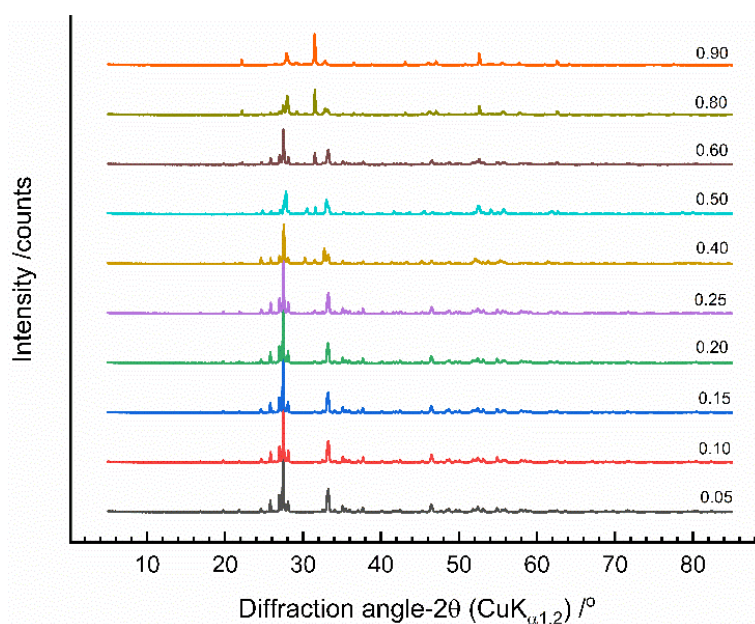


**Figure 6.10:** X-ray powder diffraction data of  $x = 0.05 - 0.90$  for  $(\text{Bi}_{1-x}\text{Sc}_x)_2\text{O}_3$ .

## Ti<sup>4+</sup>

(Bi<sub>1-x</sub>Ti<sub>x</sub>)<sub>2</sub>O<sub>3+x</sub> samples with  $x = 0.20$ ,  $0.60$ , and  $0.80$  are synthesized via solid-state method. TiO<sub>2</sub> and Bi<sub>2</sub>O<sub>3</sub> are mixed in an agate mortar, placed in a corundum crucible, and heated at 1073 K for 18 h, followed by air quenching. XRPD analysis (**Fig. 6.11**) reveals that the samples crystallize into three distinct single phases: the  $\gamma$ -phase at  $x = 0.20$ , an orthorhombic Bi<sub>4</sub>Ti<sub>3</sub>O<sub>12</sub>-type (*B2cb*) at  $x = 0.60$  [9], and a monoclinic Bi<sub>2</sub>Ti<sub>4</sub>O<sub>11</sub>-type (*C2/c*) at  $x = 0.80$  [10].

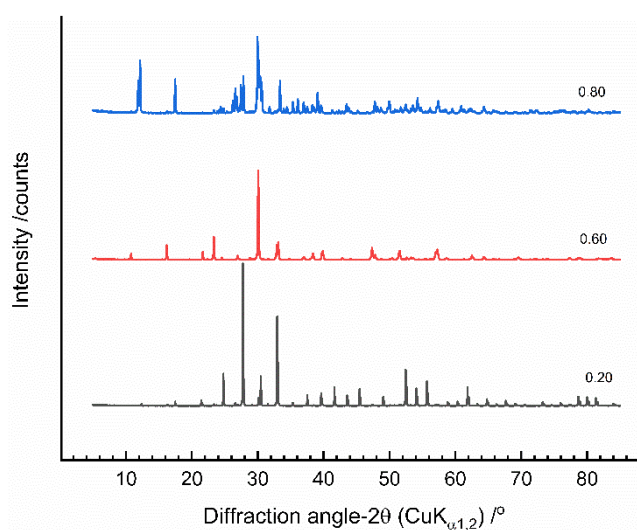


**Figure 6.11:** X-ray powder diffraction data of  $x = 0.20$ ,  $0.60$ , and  $0.80$  for (Bi<sub>1-x</sub>Ti<sub>x</sub>)<sub>2</sub>O<sub>3+x</sub>.

## Zr<sup>4+</sup>

Polycrystalline samples of (Bi<sub>1-x</sub>Zr<sub>x</sub>)<sub>2</sub>O<sub>3+x</sub> with  $x = 0.14$  and  $0.20$  are synthesized via solid-state method. ZrO<sub>2</sub> and Bi<sub>2</sub>O<sub>3</sub> are mixed in an agate mortar, placed in a corundum crucible, and heated in two stages: first at 923 K, then at 1073 K for 24 h, with intermediate air quenching and grinding. XRPD analysis (**Fig. 6.12**) shows that the  $x = 0.14$  sample crystallizes into mixed phases, with  $\delta$ -phase as the major component and a small amount of  $\alpha$ -phase. The  $x = 0.20$  sample forms  $\gamma$ -phase with minor  $\alpha$ -phase impurities.



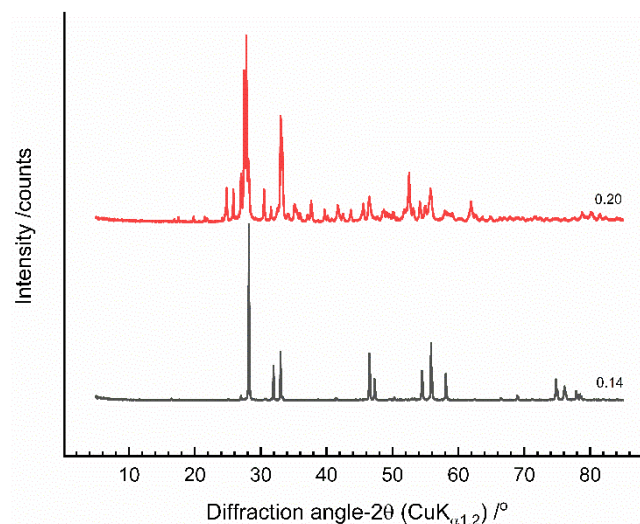


**Figure 6.12:** X-ray powder diffraction data of  $x = 0.14$  and  $0.20$  for  $(\text{Bi}_{1-x}\text{Zr}_x)_2\text{O}_{3+3x}$ .

### **Mo<sup>6+</sup> and W<sup>6+</sup>**

Two series of compounds,  $(\text{Bi}_{1-x}\text{Mo}_x)_2\text{O}_{3+3x}$  and  $(\text{Bi}_{1-x}\text{W}_x)_2\text{O}_{3+3x}$ , are synthesized via solid-state method.  $\text{MoO}_3$  or  $\text{WO}_3$  and  $\text{Bi}_2\text{O}_3$  are mixed in an agate mortar, placed in a corundum crucible, and heated in two stages: first at 923 K for 24 h, followed by 1073 K for eight days, with intermediate air quenching and grinding.

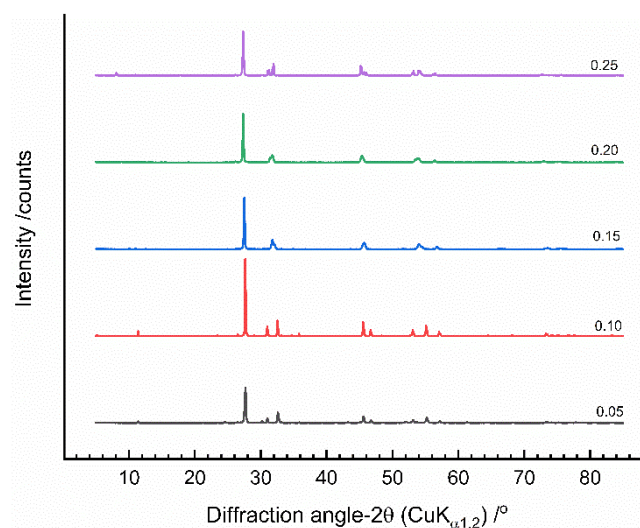


**Figure 6.13:** X-ray powder diffraction data of  $x = 0.05 - 0.25$  for  $(\text{Bi}_{1-x}\text{Mo}_x)_2\text{O}_{3+3x}$ .

The powder samples are analyzed by XRPD (**Fig. 6.13-6.14**). In Mo-series (**Fig. 6.13**), compositions from  $x = 0.10$  to 0.25 crystallize as single phases. At  $x = 0.05$ , two phases are present: a major  $\gamma$ -phase and a minor tetragonal structure ( $I4/m$ , no. 87). The  $x = 0.10$  sample also forms a single tetragonal phase ( $I4/m$ , no. 87). Compositions  $x = 0.15$  and 0.20 crystallize into  $\delta$ -phase with extra reflections at low  $2\theta$ -angle (**Fig. 6.13**). The  $x = 0.25$  sample adopts an orthorhombic structure ( $Pccn$ , no. 56). In W-series (**Fig. 6.14**), the  $x = 0.10$  sample also exhibits a tetragonal phase ( $I4/m$ , no. 87). At  $x = 0.15$ , mixed phases appear, including a tetragonal structure ( $I4_1/a$ , no. 88), which becomes a pure phase at higher  $x$ -value. Extra reflections at low  $2\theta$ -angle are observed (**Fig. 6.14**), indicative of an incommensurate structure, as discussed in **chapter 5**.

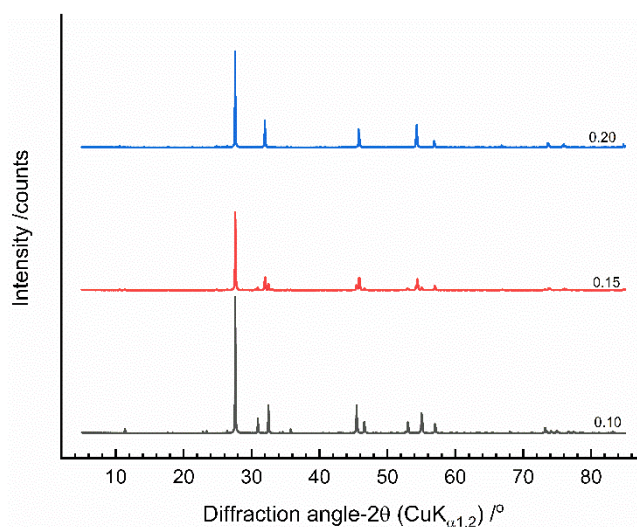


**Figure 6.14:** X-ray powder diffraction data of  $x = 0.10, 0.15,$  and  $0.20$  for  $(\text{Bi}_{1-x}\text{W}_x)_2\text{O}_{3+3x}$ .

The studied  $M^{n+}$  foreign cations can be categorized into three groups based on cation size and the resulting phase formation, following the formula  $(\text{Bi}_{1-x}M^{n+}_x)_2\text{O}_{3+(n-3)x}$ .  $\text{Te}^{4+}$  and  $\text{Eu}^{3+}$ , with ionic sizes similar to  $\text{Bi}^{3+}$  [11], favor  $\delta$ -phase formation at specific compositions (**Fig. 6.6, 6.8**). Cations with ionic sizes smaller than 90 pm typically stabilize the  $\gamma$ -type structure at low

compositions ( $x \leq 0.10$ ). The  $\beta$ -type structure, closely related to the  $\delta$ -phase, often coexists with it.

## References

- [1] I. Abrahams, A. Bush, G. Hawkes, T. Nunes, Structure and oxide ion conductivity mechanism in  $\text{Bi}_2\text{Al}_4\text{O}_9$  by combined X-ray and high-resolution neutron powder diffraction and  $^{27}\text{Al}$  solid state NMR, *J. Solid State Chem.* 147(2) (1999) 631-636. Doi:10.1006/jssc.1999.8427
- [2] R.V.K. Mangalam, R. Ranjith, A. Iyo, A. Sundaresan, S.B. Krupanidhi, C.N.R. Rao, Ferroelectricity in  $\text{Bi}_{26-x}\text{M}_x\text{O}_{40-8}$  ( $\text{M} = \text{Al}$  and  $\text{Ga}$ ) with the  $\gamma$ - $\text{Bi}_2\text{O}_3$  structure, *Solid State Commun.* 140(1) (2006) 42-44. Doi:10.1016/j.ssc.2006.07.015
- [3] T.I. Mel'nikova, G.M. Kuz'micheva, N.B. Bolotina, V.B. Rybakov, Y.V. Zubavichus, N.V. Sadovskaya, E.A. Mar'ina, Structural features of compounds of the sillenite family, *Crystallogr. Rep.* 59(3) (2014) 353-361. Doi:10.1134/s1063774514030134
- [4] G.A. Lovas, I. Dódony, L. Pöppel, Z. Szaller, On the phase transitions of  $\text{Bi}_2\text{Te}_4\text{O}_{11}$ , *J. Solid State Chem.* 135(2) (1998) 175-181. Doi:10.1006/jssc.1997.7594
- [5] T. Kikuchi, Y. Kitami, M. Yokoyama, H. Sakai, Pseudo-binary system  $\text{Bi}_2\text{O}_3$ - $\text{TeO}_2$  in air, *J. Mater. Sci.* 24 (1989) 4275-4278. Doi:10.1007/BF00544499
- [6] T. Kikuchi, T. Hatano, S. Horiuchi, Phases with fluorite superstructures in the pseudo-ternary system  $\text{PbO}$ - $\text{Bi}_2\text{O}_3$ - $\text{TeO}_2$ , *J. Mater. Sci. Lett.* 9(J. Mater. Sci.) (1990) 580-582. Doi:10.1007/BF00725883
- [7] A. Watanabe, M. Drache, J. Wignacourt, P. Conflant, J. Boivin, The dependence of polymorphism on the ionic radius of  $\text{Ln}^{3+}$  ( $\text{Ln} = \text{La-Er, Y}$ ) in the oxide ion conductors  $\text{Bi}_{0.775}\text{Ln}_{0.225}\text{O}_{1.5}$ , *Solid State Ionics* 67(1-2) (1993) 25-28. Doi:10.1016/0167-2738(93)90304-L
- [8] M. Atoji, D.E. Williams, Deuterium positions in lanthanum deuterioxide by neutron diffraction, *J. Chem. Phys.* 31(2) (1959) 329-331. Doi:10.1063/1.1730351
- [9] C.H. Hervoches, P. Lightfoot, A variable-temperature powder neutron diffraction study of ferroelectric  $\text{Bi}_4\text{Ti}_3\text{O}_{12}$ , *Chem. Mater.* 11(11) (1999) 3359-3364. Doi:10.1021/cm991090d
- [10] V. Kahlenberg, H. Böhm, The structures of  $\alpha$ - and  $\beta$ - $\text{Bi}_2\text{Ti}_4\text{O}_{11}$ , *Acta Cryst.* B51(1) (1995) 11-18.
- [11] R.D. Shannon, Revised effective ionic radii and systematic studies of interatomic distances in halides and chalcogenides, *Acta Cryst.* A32 (1976) 751-767. Doi:10.1107/S0567739476001551

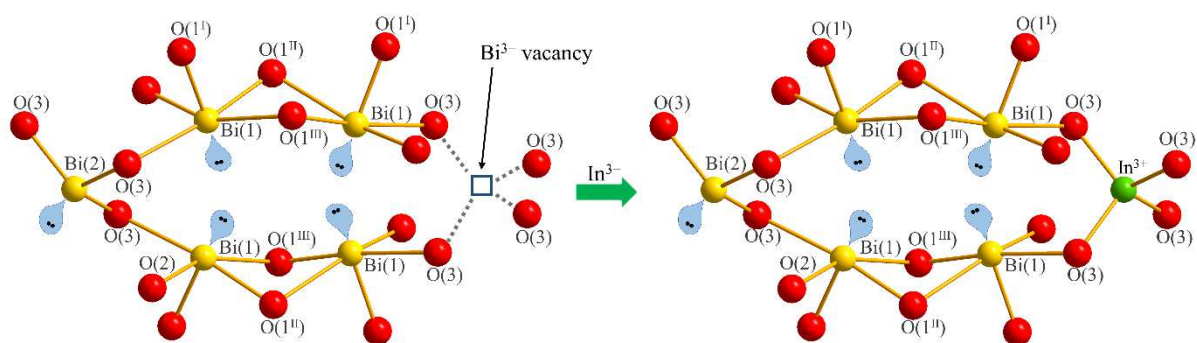
## Outlook

In this dissertation, several structures of bismuth oxide, including  $\gamma$ - (sillenite),  $\alpha$ -,  $\beta$ -, and  $\delta$ - phases, are reported and investigated. The incorporation of  $\text{In}^{3+}$  cations in the sillenite structure of  $\text{Bi}_{12}(\text{Bi}^{3+}_{4/5-3x}\text{In}^{3+}_{5x}\square_{1/5-2x})\text{O}_{19.2+3x}$  is primarily confined to the Bi-cation vacancy in the tetrahedral site. Despite reports suggesting a maximum indium incorporation of  $x = 0.10$ , structural and spectroscopic analysis in this study shows that indium substitution above  $x = 0.08$  leads to partial replacement in the octahedral site. The study reveals how subtle changes in indium concentration impact the crystal chemical properties of sillenite-type  $\text{Bi}_2\text{O}_3$ . The stereochemical activity of the lone electron pair of  $\text{Bi}^{3+}$  cations appears to induce distortions in the polyhedral sites, as indicated by the Wang-Liebau eccentricity parameter and complemented by bond valence sums and Raman shift analysis. The variation in optical bandgap with respect to  $\text{In}^{3+}$  content in the sillenites reflects the substitution behavior, which aids in understanding the optoelectronic properties. In the case of the metastable  $\delta$ - $\text{Bi}_2\text{O}_3$  phase, substitution of  $\text{Bi}^{3+}$  with rare-earth (RE) cations stabilizes the phase at ambient conditions. The extent of substitution depends on the size of the RE-cation, causing a gradual transformation of the solid solution from low- to high-symmetry phases, along with oxygen position redistribution. Phase purity is confirmed through X-ray powder diffraction and Raman spectroscopy, with distinct Bi–O vibrations in the  $\beta$ - and  $\delta$ -phases identifying the phase boundary for compositional  $x$ -values. The calculated electronic transition using the DASF approach indicates oxygen vacancies, and the bandgap stabilizes at 2.75(4) eV for all nine investigated series. The low bandgap and oxygen disorder make these solid solutions promising for photocatalysis and solid-state electrolysis. Furthermore, the study examines  $\text{Bi}^{3+}$  substitution with  $\text{Cr}^{3+}$  and  $\text{Ta}^{5+}$  in solid solutions,  $(\text{Bi}^{3+}_{1-x}\text{M}^{n+}_x)_2\text{O}_{3+(n-3)x}$ , synthesized with varying  $x$ -values for Cr (0.15 to 0.30) and Ta (0.05 to 0.30). The Cr-series, synthesized at

1273 K, shows  $\text{Cr}^{3+}$  oxidation to  $\text{Cr}^{6+}$ , confirmed by X-ray photoelectron spectroscopy, with all compositions exhibiting the  $\delta$ -phase. In contrast, the Ta-series only reaches the  $\delta$ -phase at  $x = 0.25$ , with lattice parameters showing linear trends for Ta but maintaining a larger, unchanged parameter for Cr, suggesting incommensurate structure formation. Raman spectroscopy reveals tetrahedral coordination for  $\text{Cr}^{6+}$  and structural distortions, while both series exhibit low direct bandgaps, influenced by oxygen vacancies contributing to anionic defect bands, shaping their electronic properties.

## Appendix

**Figure A1:** Abstract figure for the published manuscript titled as “Indium containing sillenite semiconductor: Synthesis, structural, spectroscopic and thermogravimetric analysis”, Journal of the American Ceramic Society 106(10) (2023) 6268-6278. DOI: 10.1111/jace.19231.



# Curriculum Vitae

## Md Imran Hossain

Albrecht-Thaer-Weg 22g, D-37075 Göttingen

Email: mdimran@uni-bremen.de

### Education

---

PhD student | 2021 to 2024

Institute of Inorganic Chemistry and Crystallography, University of Bremen, Bremen, Germany

MS in Physical Chemistry | 2017 (held in 2018)

Department of Chemistry, University of Dhaka, Dhaka, Bangladesh

BS (Honors) Major in Chemistry, Minor in Physics and Mathematics | 2016 (held in 2017)

Department of Chemistry, University of Dhaka, Dhaka, Bangladesh

Higher Secondary School Certificate | 2011

Bogra Cantonment Public School & College, Bogra, Bangladesh

Secondary School Certificate | 2009

Betil High School, Sirajganj, Bangladesh

### Research Skills

---

Solid State Chemical Crystallography at University of Bremen, Germany | 2020 to 2024

- Solid state synthesis and characterization
- X-ray diffraction, Raman spectroscopy, SEM, EDX, XPS, and TGA-DSC
- Thermal expansion modeling

Electrochemistry at Material Chemistry Research Laboratory, Bangladesh | 2017 to 2020

- Electrocatalytic splitting of water
- Electrical double layer structure and supercapacitor electrode
- Scanning electrochemical microscopy, FTIR and UV-Vis spectroscopy

Quantum Chemistry at the Red Green Research Centre, Bangladesh | 2018

- IR, and VCD spectral simulation of amino acids in gas and solvent phase by DFT

## Experience in Software

TOPAS (v. 6), LabSpec (v. 5.78.24), LAMP (v. 8.5), OriginPro (2018), MATLAB (R2013a), SigmaPlot (v. 10.0), and Microsoft Office

## Job Experience

---

- Scientific Coworker | January 2021 to January 2024  
Institute of Inorganic Chemistry and Crystallography, University of Bremen  
Leobener Straße 7, D-28359 Bremen, Germany
- Quality Control Officer | November 2020 to December 2020  
Advanced Chemical Industries Limited (ACI)  
Hajeegonj Road 7, Godnyl, Narayangonj, Bangladesh
- Research Fellow | September 2019 to June 2020  
Bose Centre for Advanced Study and Research in Natural Sciences  
Department of Chemistry, University of Dhaka, Dhaka-1000, Bangladesh
- Assistant Researcher | March 2019 to August 2019  
University Grants Commission, Department of Chemistry, University of Dhaka  
Dhaka-1000, Bangladesh

## Organizational Affiliations

---

- Researcher | 2021 to 2024  
Institute of Inorganic Chemistry and Crystallography, University of Bremen,  
Germany  
Website: [www.ckfs.uni-bremen.de](http://www.ckfs.uni-bremen.de)
- Researcher | 2017 to 2020  
Material Chemistry Research Laboratory, University of Dhaka, Bangladesh  
Website: [www.matchemdu.edu.bd](http://www.matchemdu.edu.bd)

## Publications

---

- **M. I. Hossain**, M. M. Murshed, Th. M. Gesing, Indium containing sillenite semiconductor: Synthesis, structural, spectroscopic and thermogravimetric analysis, *J. Am. Ceram. Soc.* 106(10) (2023) 6268-6278. Doi: 10.1111/jace.19231
- M. J. Propa, **M. I. Hossain**, A. Ahmed, Carbon stock and respiration of rhizosphere soils of Sal (*Shorea Robusta* Roxb. Ex. Gaertn. F.) in relation to some environmental variables of different Sal forest stands of Bangladesh, *Bangladesh J. Bot.* 50(3) (2021) 685-693. Doi: 10.3329/bjb.v50i3.55849
- **M. I. Hossain**, T. Debnath, M. Y. A. Mollah, M. A. B. H. Susan, M. M. Islam, Highly robust, novel aluminum counter cation-based monophosphate tungsten bronze electrocatalysts for oxygen evolution in acidic solution, *RSC Advances* 11(18) (2021) 10681-10687. Doi:10.1039/d1ra00699a



- **Master thesis**, Electrochemical Splitting of Water by Polyoxometalate Catalyst, Department of Chemistry, University of Dhaka, Dhaka-1000, Bangladesh, **2019**.

## Awards

---

**2018** | Best Poster Award (1<sup>st</sup> position) in *Bangladesh Chemical Congress, Dhaka, Bangladesh*

## Conference Presentation

---

1. **M. I. Hossain**, M. M. Murshed, Th. M. Gesing. “Synthesis and spectroscopic characterization of  $(\text{Bi}_{1-x}\text{M}_x)_2\text{O}_3$  (M = Y, Gd, Er, Tb, Yb)” *31<sup>st</sup> Annual Meeting of the German Crystallographic Society (DGK)*, March 27-30, **2023**, Frankfurt am Main, Germany.
2. **M. I. Hossain**, M. M. Murshed, Th. M. Gesing. “Synthesis and characterization of indium-containing sillenite” *30<sup>th</sup> Annual Meeting of the German Crystallographic Society (DGK)*, March 14-17, **2022**, Munich, Germany.
3. M. Saha, **M. I. Hossain**, M. A. B. H. Susan, M. M. Islam. “Hetero-structured polyoxometalate electrocatalysts for oxygen evolution reaction in acidic media” *6<sup>th</sup> Conference of Bangladesh Crystallographic Association*, January 15-16, **2021**, Dhaka, Bangladesh.
4. T. Ahmed, **M. I. Hossain**, M. K. B. Islam, M. Y. A. Mollah, M. A. B. H. Susan, M. M. Islam. “Effect of magnetic field on electrochemical oxygen evolution reaction catalyzed by nickel ferrites in alkaline medium” *International Conference on Recent Advances in Chemistry*, February 7-8, **2020**, Dhaka, Bangladesh.
5. M. Saha, **M. I. Hossain**, T. Debnath, M. Y. A. Mollah, M. A. B. H. Susan, M. M. Islam. “Polyoxometalate based electrocatalysts for oxygen evolution reaction in acidic medium” *International Conference on Recent Advances in Chemistry*, February 7-8, **2020**, Dhaka, Bangladesh.
6. **M. I. Hossain**, T. Debnath, M. Y. A. Mollah, M. A. B. H. Susan, M. M. Islam. “Electrocatalytic oxygen evolution at aluminium based monophosphate tungsten bronze in acidic media” *International Conference on Recent Advances in Chemistry*, February 7-8, **2020**, Dhaka, Bangladesh.
7. T. Ahmed, M. K. B. Islam, **M. I. Hossain**, M. Y. A. Mollah, M. A. B. H. Susan, M. M. Islam. “Oxygen evolution reaction at spinel compounds fabricated graphite electrode in alkaline medium” *International Conference on Advanced Functional Materials*, January 23-25, **2020**, Nagpur, India.
8. T. Ahmed, M. K. B. Islam, **M. I. Hossain**, M. Y. A. Mollah, M. A. B. H. Susan, M. M. Islam. “Oxygen evolution reaction at nickel ferrite-modified graphite electrode in alkaline medium” *5<sup>th</sup> Conference of Bangladesh Crystallographic Association*, January 25-26, **2019**, Dhaka, Bangladesh.
9. **M. I. Hossain**, T. Debnath, M. Y. A. Mollah, M. A. B. H. Susan, M. M. Islam. “Electrocatalytic oxygen evolution reaction at aluminium-based polyoxometalates

modified graphite electrode” 5<sup>th</sup> Conference of Bangladesh Crystallographic Association, January 25-26, 2019, Dhaka, Bangladesh.

10. **M. I. Hossain**, T. Debnath, M. Y. A. Mollah, M. A. B. H. Susan, M. M. Islam. “Electrochemical splitting of water by polyoxometalate catalyst” *Bangladesh Chemical Congress*, October 17-19, 2018, Dhaka, Bangladesh.

## Volunteering Experience

---

- Volunteer | 2017  
International Seminar Camp 2017: Tuning Thermal Properties for Smart Applications, Gazipur, Dhaka, Bangladesh  
Website: [www.matchemdu.edu.bd](http://www.matchemdu.edu.bd)
- Volunteer | 2018  
4<sup>th</sup> Conference of Bangladesh Crystallographic Association, University of Dhaka, Dhaka-1000, Bangladesh  
Website: [www.bd-ca.org](http://www.bd-ca.org)

## Research Interests

---

Polymorphism of Bi<sub>2</sub>O<sub>3</sub>, defects in crystal structure, cation and oxygen vacancy, structure property relation, electrocatalysis, water splitting, and supercapacitor.